ΕΘΝΙΚΟ ΜΕΤΣΟΒΙΟ ΠΟΛΥΤΕΧΝΕΙΟ
ΣΧΟΛΗ ΕΦΑΡΜΟΣΜΕΝΩΝ ΜΑΘΗΜΑΤΙΚΩΝ
ΚΑΙ ΦΥΣΙΚΩΝ ΕΠΙΣΤΗΜΩΝ

Μέτρηση της παραγωγής των J/ψ και $\psi(2S)$ μεσονίων και μελέτη της διάσπασης του $\chi_b \to J/\psi J/\psi$ με τον ανιχνευτή ATLAS στον LHC

ΔΙΔΑΚΤΟΡΙΚΗ ΔΙΑΤΡΙΒΗ

ΚΩΝΣΤΑΝΤΙΝΟΥ Σ. ΚΑΡΑΚΩΣΤΑ

Διπλωματούχου Φυσικού Εφαρμογών Ε.Μ.Π.

ΕΠΙΒΛΕΠΩΝ :
Γ. ΤΣΙΠΟΛΙΤΗΣ
Καθηγητής Ε.Μ.Π.

ΑΘΗΝΑ, Ιούλιος 2015

ΕΘΝΙΚΟ ΜΕΤΣΟΒΙΟ ΠΟΛΥΤΕΧΝΕΙΟ
ΣΧΟΛΗ ΕΦΑΡΜΟΣΜΕΝΩΝ ΜΑΘΗΜΑΤΙΚΩΝ
ΚΑΙ ΦΥΣΙΚΩΝ ΕΠΙΣΤΗΜΩΝ

Μέτρηση της παραγωγής των J/ψ και $\psi(2S)$ μεσονίων και μελέτη της διάσπασης του $\chi_b \to J/\psi J/\psi$ με τον ανιχνευτή ATLAS στον LHC

ΔΙΔΑΚΤΟΡΙΚΗ ΔΙΑΤΡΙΒΗ

ΚΩΝΣΤΑΝΤΙΝΟΥ Σ. ΚΑΡΑΚΩΣΤΑ

Διπλωματούχου Φυσικού Εφαρμογών Ε.Μ.Π.

ΤΡΙΜΕΛΗΣ ΣΥΜΒΟΥΛΕΥΤΙΚΗ ΕΠΙΤΡΟΠΗ:

1. Γ. Τσιπολίτης, Καθ. Ε.Μ.Π.
2. Θ. Αλεξόπουλος, Καθ. Ε.Μ.Π.
3. Ευ. Γαζής, Καθ. Ε.Μ.Π.

ΕΠΤΑΜΕΛΗΣ ΕΞΕΤΑΣΤΙΚΗ ΕΠΙΤΡΟΠΗ:

1. Γ. Τσιπολίτης, Καθ. Ε.Μ.Π.
2. Θ. Αλεξόπουλος, Καθ. Ε.Μ.Π.
3. Ευ. Γαζής, Καθ. Ε.Μ.Π.
4. Σ. Μαλτέζος, Αν. Καθ. Ε.Μ.Π.
5. Κ. Κουσουρής, Επ. Καθ. Ε.Μ.Π.
6. Κ. Φουντάς, Καθ. Παν. Ιωαννίνων
7. Χ. Μάρκου, Ερευν. Α' Ε.Κ.Ε.Φ.Ε. 'Δημόκριτος'

ΑΘΗΝΑ, Ιούλιος 2015

Measurement of the production of the J/ψ and $\psi(2S)$ mesons and study of the decay $\chi_b \to J/\psi J/\psi$ with the ATLAS detector at LHC

KONSTANTINOS KARAKOSTAS

A dissertation submitted in fulfillment of the requirements
for the degree of Doctor of Philosophy in Physics

ATHENS, July 2015

To my family
and the people who understood me

Contents

Outline

There have been almost forty years since the discovery of the quark-antiquark bound state (charmonium), the J/ψ [1, 2] and still, the knowledge on how this quarkonium state is produced in hadronic interactions is incomplete. Over this period several experiments studied these states (not only J/ψ but also many other that were subsequently identified) with a variety of sophisticated approaches providing increasingly precise measurements. The situation though, has become more vague since none of the theoretical approaches can describe adequately the available data.

The start of the Large Hadron Collider (LHC) [3] at CERN, capable of delivering unprecedentedly high luminosities and high energy collisions to its experiments, grants a unique opportunity to significantly advance our understanding of charmonium production.

This thesis is aiming to include the work contributed by the author in the context of the ATLAS experiment (A Toriodal LHC ApparatuS) [4] for the several measurements of the production of J/ψ and $\psi(2S)$ quarkonium states along to the study of the decay of $\chi_{b0} \to J/\psi J/\psi$.

In Chapter 1, the basic elements of the Standard Model are described including the production mechanisms of the quarkonia states. The relevant theoretical production models are summarized.

The LHC and the ATLAS detector are described briefly in Chapter 2. The accelerator complex, where ATLAS and the other experiments are able to perform their physics searches, is outlined. The basic subsystems of ATLAS on which the physics program is relied are identified and the basic components of the detector are described.

A detector of such size requires a powerful and adaptive automated system for the control, supervision and monitoring of its various components and subsystems. The work of the author on the Detector Control System is described in Chapter 3. That involves the development and maintenance of the control system of the Power Supplies for the Monitored Drift Tubes. The SCADA software used is described along with the tools developed by the author for the configuration and the optimization of the system.

The production rates of prompt and non-prompt J/ψ and $\psi(2S)$ mesons (non-prompt mesons coming from long-lived b-hadrons) are measured using 11.4fb^{-1} of data collected with the ATLAS experiment at the LHC, in proton-proton collisions at $\sqrt{s} = 8$ TeV are described in Chapter 4. The production cross-sections for both prompt and non-prompt sources, ratios of $\psi(2S)$ to J/ψ production, and fractions

of non-prompt to inclusive production for J/ψ and $\psi(2\mathrm{S})$ are measured double-differentially as a function of meson p_{T} and rapidity. These measurements are made in a restricted fiducial volume and extrapolated to the full kinematic phase space. Then they are compared to a variety of theoretical predictions.

In Chapter 5 a blinded analysis studying the decay of $\chi_{\mathrm{b}} \to J/\psi J/\psi \to \mu^+\mu^-\mu^+\mu^-$is described. A first time study of its kind on LHC era, setting a limit on both observed signal events and $\mathcal{B}\left(\chi_{b0} \to J/\psi J/\psi\right)$, performed using $11.4\mathrm{fb}^{-1}$ of proton-proton collision data at $\sqrt{s} = 8$ TeV recorded by the ATLAS experiment at the LHC.

Finally, the contribution of the author in the analysis performed on the search for the rare decay $B_s^0 \to \mu^+\mu^-$ is described in appendix A.

Περίληψη

Έχουν περάσει σχεδόν σαράντα χρόνια από την ανακάλυψη της πρώτης δέσμιας κατάστασης quark-antiquark (charmonium), του J/ψ [1, 2] και ακόμα η γνώση σχετικά με το πώς αυτό το $c\bar{c}$ μεσόνιο παράγεται σε αδρονικές αλληλεπιδράσεις είναι ελλιπής. Κατά την περίοδο αυτήν πολλά πειράματα έχουν μελετήσει αυτές τις καταστάσεις, (όχι μόνο το J/ψ αλλά και πολλά άλλα quarkonium που προσδιορίστηκαν μεταγενέστερα), με ποικιλία εκλεπτισμένων προσεγγίσεων, παρέχοντας ολοένα και περισσότερο ακριβείς μετρήσεις. Παρ'ολα αυτά η κατάσταση έχει γίνει πιο ασαφής καθώς καμία από τις θεωρητικές προσεγγίσεις δεν έχει περιγράψει επαρκώς τα διαθέσιμα δεδομένα.

Η έναρξη λειτουργίας του Μεγάλου Επιταχυντή Αδρονίων (Large Hadron Collider – LHC) [3] στο CERN, ικανού να παρέχει άνευ προηγουμένου συγκρούσεις υψηλών ενεργειών και υψηλής φωτεινότητας στα πειράματά του, παρέχει μια μοναδική ευκαιρία στην βελτίωση της κατανόησης μας της παραγωγής των $c\bar{c}$ μεσονίων.

Αυτή η διατριβή έχει ως στόχο να περιγράψει το έργο με το οποίο συνέβαλε ο συγγραφέας, στα πλαίσια του πειράματος ATLAS (A Toroidal LHC ApparatuS) [4], για τις διάφορες μετρήσεις της παραγωγής των J/ψ και $\psi(2\mathrm{S})$ μεσονίων καθώς επίσεις και την μελέτη της διάσπαση του μεσονίου $\chi_{b0} \to J/\psi J/\psi$. Ακολουθεί μια συνοπτική περιγραφή των περιεχομένων αυτού του κειμένου.

Στο Κεφάλαιο 1, περιγράφονται τα βασικά στοιχεία του Καθιερωμένου Προτύπου (Standard Model) συμπεριλαμβανομένων και των μηχανισμών παραγωγής των heavy quarkonium καταστάσεων. Επιπλέον, συνοψίζονται τα σχετικά θεωρητικά μοντέλα παραγωγής.

Ο επιταχυντής LHC και ο ανιχνευτής ATLAS περιγράφονται εν συντομία στο Κεφάλαιο 2. Το σύμπλεγμα των επιταχυντών, στο οποίο το πείραμα ATLAS καθώς και τα άλλα πειράματα είναι σε θέση να εκτελούν τις έρευνες φυσικής, σκιαγραφείται. Τα βασικά υποσυστήματα του ATLAS, στα οποία στηρίχθηκε το πρόγραμμα φυσικής του πειράματος ταυτοποιούνται και περιγράφονται.

Ένα φασματόμετρο τέτοιου μεγέθους απαιτεί ένα ισχυρό και ευπροσάρμοστο αυτοματοποιημένο σύστημα για τον έλεγχο, την επίβλεψη και την επιτήρηση των διαφόρων υποσυστημάτων και επιμέρους ανιχνευτών. Στο Κεφάλαιο 3 περιγράφεται η συνεισφορά του συγγραφέα στο Σύστημα Ελέγχου του Ανιχνευτή (Detector Control System). Αυτό συμπεριλαμβάνει την ανάπτυξη και την συντήρηση ενός συστήματος ελέγχου των τροφοδοτικών τάσεων για τους ανιχνευτές αερίου (Monitored Drift Tubes) του μιονικού ανιχνευτή. Το SCADA λογισμικό που χρησιμοποιήθηκε, περιγράφεται σε συνδυασμό με τα εργαλεία που αναπτύχθηκαν από τον συγγραφέα για τη διαμόρφωση και την βελτιστοποίηση του συστήματος αυτού.

Στο Κεφάλαιο 4 περιγράφονται οι ρυθμοί παραγωγής των prompt και non-prompt J/ψ και $\psi(2S)$ μεσονίων (τα non-prompt μεσόνια προέρχονται από b-αδρόνια μεγάλης διάρκειας ζωής) μετρώνται χρησιμοποιώντας συνολικά 11.4fb^{-1} των δεδομένων που συλλέχθηκαν μέσω του πειράματος ATLAS στο LHC , σε συγκρούσεις πρωτονίων – πρωτονίων σε ενέργεια κέντρου μάζας $\sqrt{s} = 8$ TeV. Οι μετρήσεις των ρυθμών παραγωγής και για τις δύο τις πηγές (prompt και non-prompt) των J/ψ και $\psi(2S)$ μεσονίων καθώς ακόμα, οι λόγοι παραγωγής των $\psi(2S)$ ως προς τα J/ψ και οι λόγοι των non-prompt ρυθμών παραγωγής μετριώνται σε δύο διαστάσεις συναρτήση της ορμής των μεσονίων και της ωκύτητας. Σύγκριση των μετρούμενων ποσοτήτων με τα επικρατέστερα θεωρητικά μοντέλα λαμβάνει χώρα στα πλαίσια αυτής της ανάλυσης.

Στο Κεφάλαιο 5 γίνεται μελέτη της σπάνιας δίασπασης $\chi_{\text{b}} \to J/\psi J/\psi \to \mu^+\mu^-\mu^+\mu^-$ με χρήση των δεδομένων του ATLAS που συλλέχθηκαν το 2012 απο σύγκρουση πρωτονίων σε ενέργεια κέντρου μάζας $\sqrt{s} = 8$ TeV. Πειραματική επιβεβαίωση του καναλιού αυτού δεν έχει γίνει ακόμα ενώ η παρούσα ανάλυση ειναι η πρώτη στο είδος της για το LHC.

Τέλος, η συμμετοχή του συγγραφέα στης ανάλυση της σπάνιας διάσπασης του $B_s^0 \to \mu^+\mu^-$ περιγράφεται στο παράρτημα A.

Chapter 1

Motivation

There are questions that have puzzled man since the dawn of humanity: "*What is the world made of*?" and "*What holds it together*?".

Gradually people have come to realize that the whole observed universe is made of only a few, fundamental, non composite, building blocks.

A combination of the theoretical and experimental efforts took place over the last decades, driven by the need to shed light upon the intrinsic properties of these basic building blocks of matter and how they interact with each other. The Particle Physics manages to prove experimentally that everything in our world is build from elementary particles.

The Particle Physics managed to prove the theoretical predictions that the physical system of the observable universe is made of N elementary particles. In addition, the dynamics of this system are described by the interactions of these elementary building blocks. When this knowledge was expressed in a strict mathematical formalism, the Standard Model was born.

1.1 The Standard Model

The Standard Model of particle physics (SM), proposed by Glashow, Salam and Weinberg in the sixties [5–7]. Its symmetry group [5, 7, 8] is described by $SU(3)_C \otimes SU(2)_L \otimes U(1)_Y$ representing the current model of strong interactions via the $SU(3)_C$ and the unification of the electromagnetic and weak interactions into the electroweak via the $SU(2)_L \otimes U(1)_Y$.

The Standard Model describes all of the known fundamental particles along with their interactions via three out of the four interactions of nature: electromagnetism, the weak interaction and the strong interaction. Gravity (which is the forth interaction) plays no significant role at the energy scale of particle physics, as far as the current experimental results suggest. Therefore, gravity is not yet included in the Standard Model.

In the current context all matter is made out of two kinds of elementary particles: quark and leptons, while the interactions of these being mediated by several gauge bosons. The quarks and the leptons are spin $1/2$ particles and they obey the

Fermi-Dirac statistics and they are named fermions. The mediators of the interactions between the fermions, are integer-spin particles which obey the Bose-Einstein statistics, hence they are bosons.

Table 1.1: There are three generations of leptons, each consisting of a charged and a neutral one. The quoted masses are the cited averages or limits set according to Reference [9].

Generation	Lepton	Mass [MeV]	Charge
I	e	0.511	-1
	ν_e	$< 0.26 \cdot 10^{-3}$	0
II	μ	105.69	-1
	ν_μ	< 0.19	0
III	τ	1776.99	-1
	ν_τ	< 18.2	0

The theoretical model encompasses three "generations" of particles each containing a pair of leptons, a pair of quarks (as well as their antiparticles), and the gauge bosons. For the leptons, each generation is composed by the charged lepton (e, μ and τ) differing only in mass (mass is increasing in every generation with respect to the previous one) and its neutrino partner (ν_e, ν_μ and ν_τ respectively). There are all pointlike with $r < 10^{-17}$ cm. In Table 1.1 the three lepton generations are shown along with their masses and charge. Among them only the e (first generation) is stable while the μ and the τ, are unstable and decay to other particles.

Table 1.2: The six quark flavors form three generations. The quoted masses are the cited averages or limits set according to Reference [9].

Generation	Quark (Name–Symbol)	Mass [GeV]	Charge
I	Up–u	$< 2.3 \cdot 10^{-3}$	$+2/3$
	Down–d	$< 4.8 \cdot 10^{-3}$	$-1/3$
II	Charm–c	1.275 ± 0.025	$+2/3$
	Strange–s	$(95 \pm 5) \cdot 10^{-3}$	$-1/3$
III	Top–t	173.2 ± 0.7	$+2/3$
	Bottom–b	4.18 ± 0.03	$-1/3$

The quarks carry fractional charge ($+2/3$ or $-1/3$). Similarly to the leptons, there are six flavors of quarks divided into three generations. Some basic information about them including the world-average mass are shown in Table 1.2. Every quark comes in three colors: "red", "blue", "green".

Table 1.3: Bosons mediate the fundamental forces of nature and mass is being created by the Higgs field.The quoted masses are the cited averages or limits set according to Reference [9].

Name	Symbol	Mass [GeV]	Spin	Interaction mediated
Photon	γ	0	1	Electromagnetism
W boson	$W^{\pm}$	80.385 ± 0.015	1	Weak interaction
Z boson	Z	91.1876 ± 0.0021	1	Weak interaction
Gluon	g	0	1	Strong interaction
Higgs boson	H	125.7 ± 0.4	0	Mass
Graviton	G	$< 7 \times 10^{-41}$ [10]	2	Gravitation

The SM describes three of the four fundamental interactions: electromagnetic, the weak and the strong interaction. In addition to the these interactions, the mechanism that describes how the particles gain mass has been incorporated in the SM via the the Brout, Englert, Higgs mechanism [11–14]. This mechanism requires the existence of a spin zero boson, the Higgs boson, which has been observed by the ATLAS and CMS experiments [15–17].

The electromagnetic interaction acts between electrically charged particles. It is responsible of keeping the electrons around the nuclei and links the atoms to form molecule structures, it is described by the Quantum Electrodynamics (QED). The mediator of the electromagnetic force is the spin-1 massless photon.

The weak interaction, is responsible for nuclear β-decays, as well as absorption and emission of neutrinos. It has three gauge boson mediators: $W^{\pm}$ and Z, which are massive with spin 1.

The strong interaction is acting between quarks, and keeps them inside the hadrons. It is described by the Quantum Chromodynamics (QCD), with eight massless, spin-1 gluons (g) as mediators. In Table 1.3 the gauge bosons are presented along with their mass, charge and the interaction type they correspond to.

Finally, the gravitational interaction incarnates between all types of particles and is by far the weakest. Its mediator is the graviton (G), a purely theoretical (for the moment) spin-2 boson.

Quarks are held together via the strong interaction and create the hadrons. The hadrons are categorized into two families, mesons and baryons. Mesons are composed of a quark–antiquark pair with integer spin, while baryons are composed of a triplet of quarks with half-integer spin.

1.2 From Quarks Towards Quarkonium

Before the aforementioned formation of the Standard Model and QCD a great uncertainty was covering the formation of many hadrons that had been discovered during the fifties. At a first approach, Murray Gell-Mann became "Mendeleev" of elementary particle physics, who introduced the so-called *"Eightfold Way"* in

1961 [18]. The grouping of particles was proposed independently also by Yuval Ne'eman. Based on this, the particles were grouped depending on their properties (charge and strangeness[1]) into geometrical patterns (in example hexagonal or triangular arrays).

The placing of particles in this way could give insight for the "missing" particles (particles that were proposed by the model but not observed yet), as well as some information about them, like the mass and the lifetime. Due to this model the suggestion arose that the structure of the patterns could be explained by the existence of some fundamental particles now known as quarks, and from which hadrons are constructed. This was the birth of the quark model, independently proposed by Murray Gell-Mann [19] and George Zweig [20].

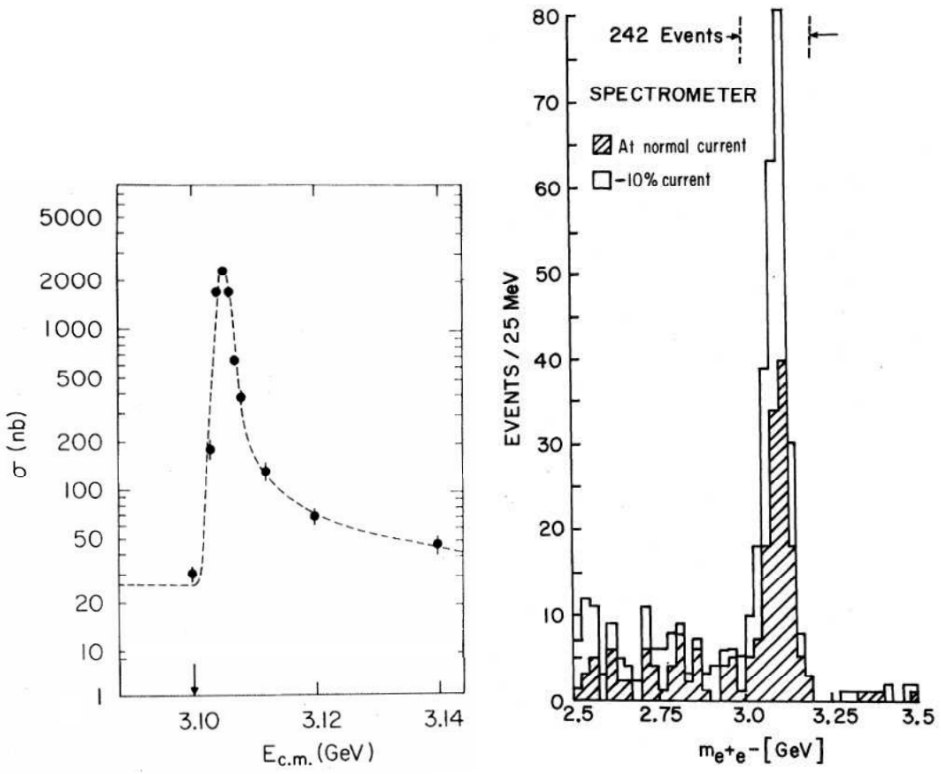

(a) SLAC J/ψ (b) BNL J/ψ

Figure 1.1: Observation of J/ψ in Stanford Linear Accelerator Center (e^+e^- collisions) in cross-section versus centre-of-mass energy with J/ψ going to a hadronic final state [1] at (a) and the first observation of J/ψ in 1974 from Brookhaven National Laboratory (p^+Be collisions) in di-electron mass spectrum [2] in (b).

The discovery in late 1974 of a resonance at 3.1 GeV performed simultaneously from Stanford Linear Accelerator Center (SLAC) [1] and Brookhaven National Lab-

[1]The strangeness of a particle is a quantum number defined as: $S = -(n_s - n_{\bar{s}})$ where n_s represents the number of strange quarks (s) and $n_{\bar{s}}$ represents the number of strange antiquarks (s).

oratory (BNL) [2] (see Figure 1.1) confirming the presence of a new particle, the J/ψ, which eventually evolved the quark model and secured its place among the emerging theories.

In the same di-electron decay mode, the discovery of the $\psi(2S)$ followed the discovery of the J/ψ. From the decay of $\psi(2S)$, seen via the detection of the radiated photon, the χ_c states were discovered later. Not so long after these discoveries, in 1977, a further narrow state with a mass of around 9.5 GeV was observed decaying into $\mu^+\mu^-$ at Fermilab [21]. This new state was the $\Upsilon(1S)$ and provided the first evidence for a heavier quark, the b-quark (called bottom or beauty).

These mesons bound states of charm–anticharm are called charmonia and they belong to the greater family of quarkonia. Quarkonium is a sub-atomic system composed of a heavy quark q and its antiquark $\bar{q}$, bound by the strong interaction. They belong to the meson family of hadrons but they gain their own sub-classification due to the fact that, the mass differences of the charm (c) and bottom (b) quarks compared to the light (u, d, s) quarks are three orders of magnitude and endues the quarkonia family with properties that differ significantly from those of the mesons with light quarks.

Any heavy quarkonium system is allowed to contain a charm and anticharm ($c\bar{c}$) quark pair (known as charmonium) or a bottom and antibottom ($b\bar{b}$) quark pair (known as bottomonium). No top and antitop ($t\bar{t}$) -proposed as toponium- state has been observed[2] .

The quarkonium states are typically characterized according to the total spin of the quark–antiquark system S, the orbital angular momentum L, and the total angular momentum ($\vec{J} = \vec{L} + \vec{S}$) of the system J. The charge conjugation symmetry C is given by $C = (-1)^{L+S}$ while the parity P of the quark–antiquark system is given by $P = (-1)^{L+1}$. Parity and charge conjugation are both conserved quantities in the strong and electromagnetic decays of the quarkonium states. The spectroscopic notation $n^{2S+1}L_J$, where n is the principal quantum number, is often used to denote the quarkonium states.

All quarkonium states belonging to the regime with mass below the open-flavor-hadron threshold decay have to be narrow states decaying either via the electromagnetic or the strong interactions to lower mass states, charged leptons or light hadrons in order or be kinematically allowed. This threshold for the charmonia states is $m_{D\bar{D}} \sim 3.7$ GeV while for the bottomonia states is $m_{B\bar{B}} \sim 10.6$ GeV.

All expected charmonium states below the allowed $D\bar{D}$ threshold have been observed experimentally. On the other hand, for bottomonium states this is not the case since there are states below the $B\bar{B}$ mass threshold like $\eta_b(2S)$, $\eta_b(3S)$ which have not yet been observed.

Figures 1.2 and 1.3 provide an illustrative summary of the experimentally observed (solid lines) and some of the predicted (dashed lines) spectrum of charmonium and bottomonium states respectively.

[2]The large mass of the top (t) quark disfavors it from forming a quarkonium system, since it decays through the electroweak interaction before a bound state can form.

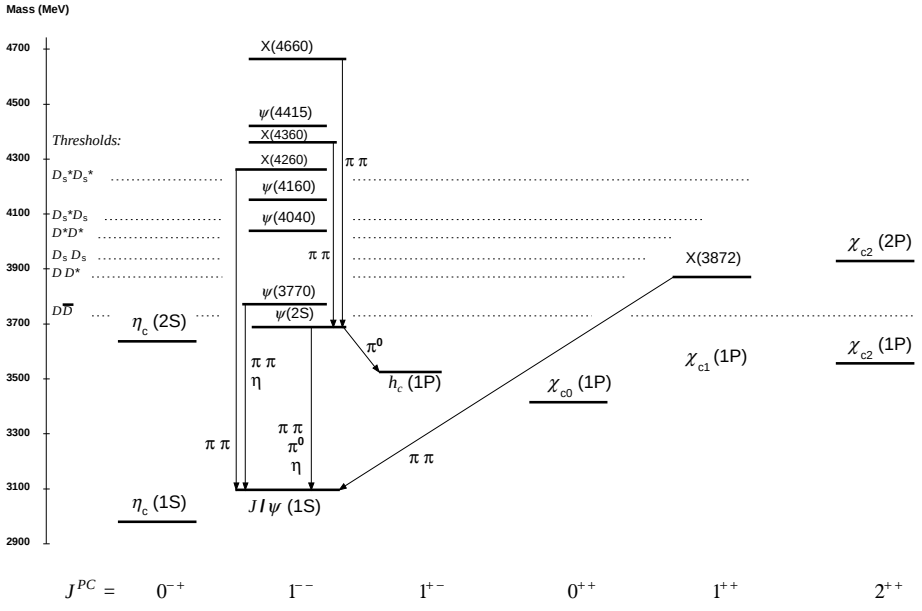

Figure 1.2: The level scheme of the $c\bar{c}$ states showing experimentally established states with solid lines. Singlet states are called η_c and h_c, triplet states ψ and χ_{cJ}, and unassigned charmonium-like states X. In parentheses it is given the radial quantum number and the orbital angular momentum and specifies the states with all their quantum numbers. Only observed hadronic transitions are shown; the single photon transitions $\psi(nS) \to \gamma\eta_c(mP)$, $\psi(nS) \to \gamma\chi_{cJ}(mP)$ and $\chi_{cJ}(1P) \to \gamma J/\psi$ are omitted for clarity [9].

1.3 Production of Quarkonia

The production mechanism for the quarkonium states can be factorized into two distinguishable parts. The production of a quark–antiquark pair is the first part and is described by perturbative QCD. The second part is describes the formation of a physical bound state using the quark–antiquark pair. Several non-perturbative QCD approaches and models have been proposed, without establishing a successful one, in order to explain the properties of all quarkonium states production.

Precise measurements of quarkonia is the tool of testing and -at the same time- improving the existing theoretical models. The key to accomplish this is to exploit extensive regimes using large quantities of data with a delicate and elegant way as in the analyses presented in Chapters 4 and 5. In the following sections the dominant production models are briefly presented.

1.3.1 Potential Models

Following a basic approach, one could correlate the quark–antiquark system to the positronium. Like the positronium, the quarkonium states have various spin states with accompanied energies which could benefit the hadronic dynamic with

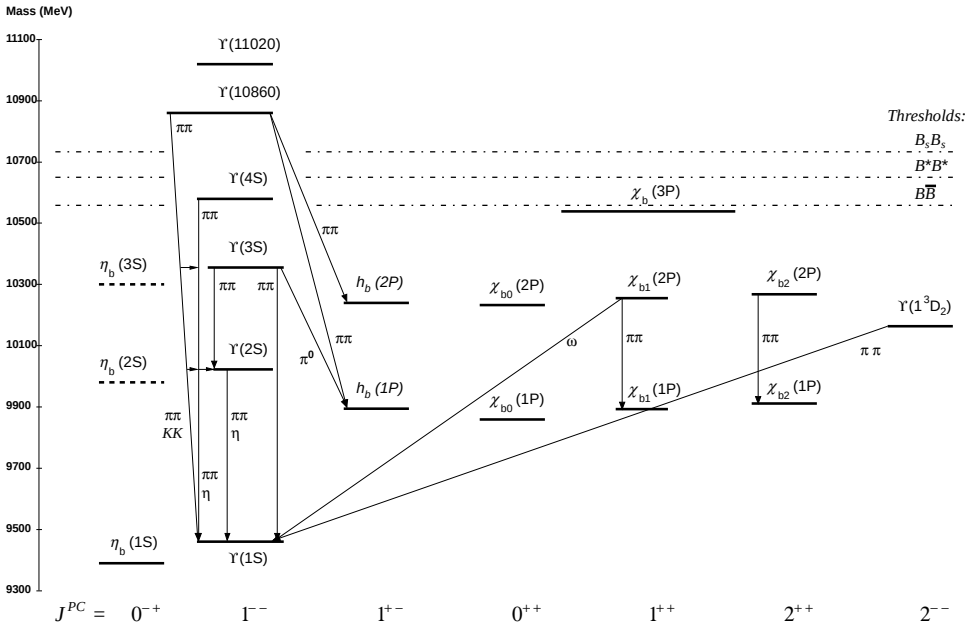

Figure 1.3: The level scheme of the $b\bar{b}$ states showing experimentally established states with solid lines. Singlet states are called η_b and h_b, triplet states Υ and χ_{bJ}. In parentheses it is sufficient to give the radial quantum number and the orbital angular momentum and specifies the states with all their quantum numbers. E.g., $h_b(2P)$ means 2^1P_1 with $n = 2,\ L = 1,\ S = 0,\ J = 1,\ PC = +-$. The figure shows observed hadronic transitions. The single photon transitions $\Upsilon(nS) \rightarrow \gamma\, \eta_b(mS),\ \Upsilon(nS) \rightarrow \gamma\chi_{bJ}(mP)$ and $\chi_{bJ}(nP) \rightarrow \gamma\Upsilon(mS)$ are omitted for clarity [9].

any knowledge gained from them.

In the simplest model one can assume that the quark dynamics are determined by treating the quarkonia as a non-relativistic system. The exchange of gluons between the interacting quarks of the system works like an analogy to the electromagnetic interaction in QED. The potential that could be used for the quarkonia system is then analogous to the Coulomb one:

$$V_{EM}(r) = -\frac{\alpha_{EM}}{r}$$

where r is the distance between the two interacting bodies.

Of course a potential of this form could not be applied effectively on the quark–antiquark system due to confinement [22–25] . In order to model also the confinement of the quarks into the potential it is necessary a linear (non-zero at large distances) term to be added resulting in a form of the potential like the one shown in Equation 1.1,

$$V(r) = -\frac{\alpha}{r} + f(r). \tag{1.1}$$

Various and peculiar formulations of this simplest model have been studies by several groups. The most known alteration of the potential from Equation 1.1 is the Cornell potential [26] shown in Equation 1.2,

$$V(r) = -\frac{\alpha}{r} + \frac{r}{b} \tag{1.2}$$

with the numerical coefficients a = 0.52, b = 2.34 GeV^{-1}.

1.3.2 The Colour Evaporation Model

The Colour Evaporation Model (CEM) [27, 28], a relatively simple model, is one of the earliest models for the heavy quarkonium production. It was proposed few years after the discovery of the first heavy quarkonium, the J/ψ and despite its simplicity it behaved rather successfully describing many of the main features of the quarkonium production.

In the CEM, no correlation of the quantum numbers of color and angular momentum between the initial state of $q\bar{q}$ and the final physical state of quarkonium is taken into account. The $q\bar{q}$ pair will transform, during the binding process, into the desired final physical state (color singlet state) altering its quantum numbers by soft gluon emission. Based on this model, any $q\bar{q}$ pair can form a quarkonium under the only limitation that its invariant mass is below the open-flavor-threshold, $m_{D\bar{D}}$ for charmonium state and $m_{B\bar{B}}$ for bottomonium state.

The proposed, by this model, cross-section for a production of a quarkonium state X is predicted to be proportional, by a factor f_X, to the total rate of production of heavy quarks ($\hat{\sigma}_{Onia}$) with invariant mass between twice the heavy quark masses ($2m_c$ for charmonium, $2m_b$ for bottomonium) and the threshold for open-flavor meson production ($m_{D\bar{D}}$ for charmonium, $m_{B\bar{B}}$ for bottomonium) and is given by Equation 1.3,

$$\hat{\sigma}_X = f_X \cdot \hat{\sigma}_{Onia}. \tag{1.3}$$

The parameter f_X is dedicated for each quarkonium state, colliding particles and energy and it is determined after fit to the data.

1.3.3 The Color Singlet Model

About the same time as the CEM, the Color Singlet Model (CSM) [29, 30] was proposed. The CSM adopts the exact opposite approach than CEM and it assumes that any given physical quarkonium state is produced only from quark–antiquark pairs that they already have the proper quantum numbers (color and spin).

Therefore, the final quarkonium state produced can be derived only from a specific configuration of the quark–antiquark pair, in particular, the quark–antiquark pair is required to have the exact same color and spin state as the final quarkonium formed. That boils down to the requirement that also the quark–antiquark pair must be produced in a color singlet state.

1.3.4 The NRQCD – Colour Octet Model

During the nineties, the Colour Octet Model (COM) [31] was proposed. Similarly to CEM, the COM treats the quark–antiquark pair without the restrictions that CSM had introduced. Based on this model the quark–antiquark pairs are not obliged to be produced with the final quantum numbers of the physical quarkonium but they can evolve into it through radiation of soft gluons.

The difference between CEM and COM is that, for the later, the framework of Non-Relativistic QCD (NRQCD) is used, treating the quarkonium as an approximately non-relativistic system. In this approximation the production is described by two distinguishable parts.

The first one is fully calculable and it describes the short distance cross-section. On the other hand, the second one describes the Long Distance Matrix Elements (LDMEs) [32] which are extracted from fits to the experimental data, and can hence describe the cross-sections and differential spectra reasonably well by construction. The LDMEs illustrate the probabilities for a given quark–antiquark pair with certain quantum numbers to evolve into the desired quarkonium state.

1.4 Quarkonium Phenomenology

In hadronic collisions the quarkonia production can be separated in two distinguishable processes, the direct production and the feed-down. Directly produced quarkonia originate from the hard scattering while feed-down produced quarkonia from the decay of other higher-mass quarkonium states or long-lived b-hadrons.

Experimentally treating the quarkonium production, if its decay chain includes long-lived particles such as b-hadrons, then this quarkonium is called non-prompt on the other case it is called prompt. This separation is essential as the two processes are described with different theoretical approaches. Comparisons between experimental results and theoretical predictions are meaningful only when the non-prompt and prompt categorization takes place.

The charmonium production at hadron colliders is generally studied with the J/ψ, $\psi(2\mathrm{S})$ and χ_{cJ} states, with the preferable, from the experimentalist point of view, state for studies to be the J/ψ. Correspondingly, for the bottomonium production, the typical probes are the $\Upsilon(nS)$ and $\chi_b(nP)$ states with the $\Upsilon(nS)$ states, to act in analogous to the J/ψ, being the favored and most studied.

The bottomonium states are much heavier than the charmonium (expected since the b quark is almost four times heaver than the c quark) which enables them not only to decay into light hadrons but also charmonium states. Moreover, double charmonium production can happen via bottomonium decays too.

1.4.1 Spin Alignment Polarization

The polarization of the quarkonium system is a quite important parameter since it is sensitive to its production mechanisms. It can be measured experimentally using the angular distributions of the quarkonium decay products. A typical system used for the measurement of quarkonium polarization can be found in Figure 1.4.

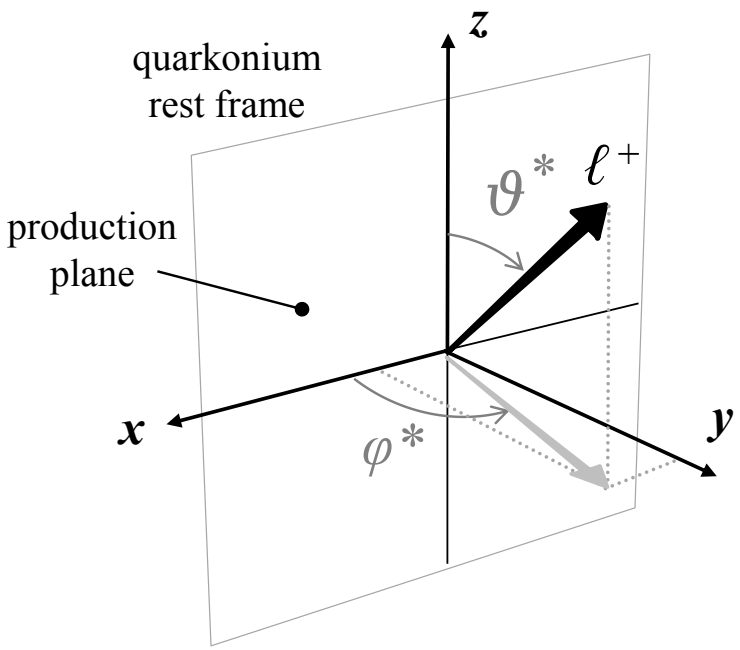

Figure 1.4: The coordinate system for the measurement of a two-body decay angular distribution in the quarkonium rest frame. Figure from reference [33].

Working on the quarkonium rest frame the polar angle θ^* is chosen to be the one between the positive lepton and the polarization axis z, the azimuthal angle, ϕ^*, between the positive lepton and the production plane.

The angular distribution of the quarkonia is described by:

$$\frac{\mathrm{d}^2 N}{\mathrm{d}\cos\theta^* \mathrm{d}\phi^*} \propto 1 + \lambda_\theta \cos^2\theta^* + \lambda_\phi \sin^2\theta^* \cos 2\phi^* + \lambda_{\theta\phi} \sin 2\theta^* \cos\phi^* \tag{1.4}$$

where the coefficients $\lambda_\theta,\ \lambda_\phi,\ \lambda_{\theta\phi}$ in Equation 1.4 are related to the spin density matrix elements of the dimuon spin wave function.

Seven extreme cases that lead to the largest possible variations of the polarization are identified. These cases, described in Table 1.4, are typically used in order to define a range in which the results coming from quarkonium states may vary under any physically allowed spin-alignment assumptions.

Table 1.4: Values of the angular coefficients describing the considered spin-alignment scenaria.

	Angular coefficients		
	λ_θ	λ_ϕ	$\lambda_{\theta\phi}$
Isotropic *(typical central value)*	0	0	0
Longitudinal	-1	0	0
Transverse positive	$+1$	$+1$	0
Transverse zero	$+1$	0	0
Transverse negative	$+1$	-1	0
Off-(λ_θ–λ_ϕ)-plane positive	0	0	$+0.5$
Off-(λ_θ–λ_ϕ)-plane negative	0	0	-0.5

Chapter 2

The ATLAS experiment at the LHC

The ATLAS detector (A Toriodal LHC ApparatuS) [4] is designed to study proton-proton as well as heavy ion collisions at the Large Hadron Collider (LHC) [3]. The LHC accelerator complex, together with the experiments was built to study particle collisions at energies significantly higher than the ones that have been achieved to date.

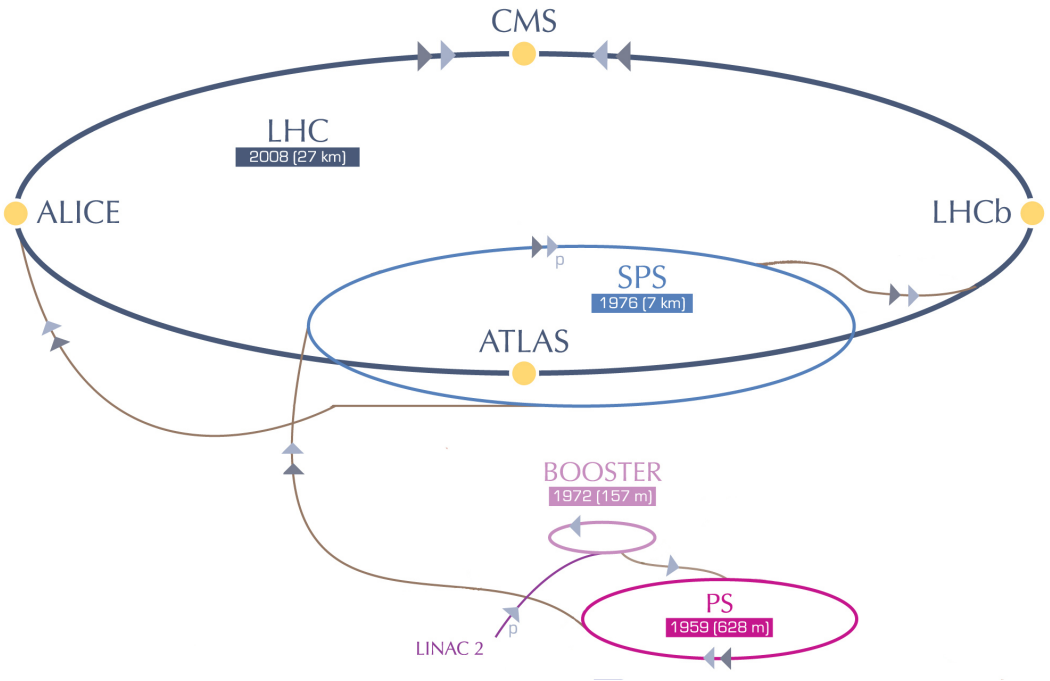

Figure 2.1: The full acceleration complex for the LHC proton-proton collisions along with the four major experiments (ALICE, ATLAS, CMS and LHCb).

2.1 The LHC complex

The LHC [3] is the newest hadron particle accelerator. It was built in a tunnel which is in average 100 meters underground (depending on the inclination of the surface varying from 50 up to 175 meters) and 26.7 kilometers in circumference. It is hosted in the same tunnel that was used by the Large Electron Positron (LEP) collider from 1989 – 2000 at the Swiss-French border in Geneva - Switzerland at a laboratory called the "Conseil Européen pour la Recherche Nucléaire" (European Council for Nuclear Research), CERN. It consists of eight arcs and eight straight sections and its plane is inclined with 1.4 % slope.

The acceleration procedure is split amongst several stages. To begin with, the proton source is a simple bottle of hydrogen gas. An electric field is used to strip hydrogen atoms of their electrons to yield protons. After their production the protons are accelerated in a 50 MeV linear accelerator (LINAC). Following down the acceleration chain, the 1.4 GeV Proton Synchrotron (PS) booster followed by the 25 GeV PS deliver beam bunches of $1.15 \cdot 10^{11}$ protons with 50 ns distance to each other to the 6.9 km Super Proton Synchrotron (SPS). At this point of the acceleration chain the beam bunches are accelerated up to $450\mathrm{GeV}$ and are finally injected into the LHC, which handles the focusing, the final acceleration and eventually the collisions at the interaction points of the individual experiments with a bunch crossing rate of 40 MHz on designed energy (14 TeV).

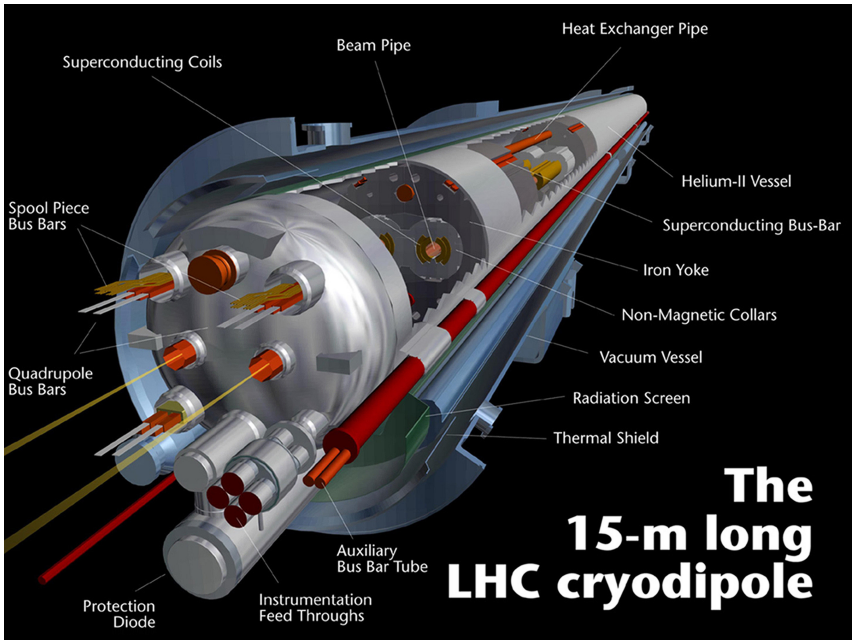

Figure 2.2: This computer-generated image of a LHC dipole magnet shows some of the parts vital for the operation of these components. The magnets must be cooled to 1.9 K ($-270.3°$C) so that the superconducting coils can produce the required 8 T magnetic field strength.

The beam has a bunch structure with a time interval of 50 ns ($\sim$ 15 m). This

structure has been adopted in order to have a number of interactions per crossing within certain limits, to maximize the luminosity and keep close track of the beam parameters.

A total amount of 9600 magnets of different varieties and sizes are used to drive the beams around the accelerator. Those include 1232 dipole magnets 15 meters in length which bend the beams (shown in Figure 2.2), and 392 quadrupole magnets, each 5-7 meters long, which used for focusing and beam corrections. The acceleration of the beams is taken care of by 400 MHz Radio-Frequency (RF) cavities.

The magnets have Niobium-Titanium (Nb-Ti) coils providing fields up to 8.33 T with a current of nearly 12 kA. The magnet and the beam lines are housed in the same cryostat and the system is cooled down to 1.9 K using super-fluid Helium (He). Just prior to the collision points, another type of magnet is used to "squeeze" the particles closer together to increase the probability of having a collision.

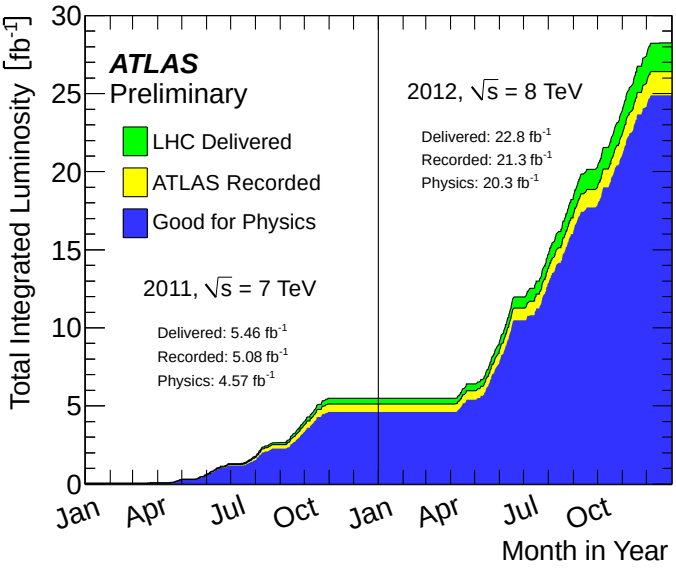

Figure 2.3: Cumulative luminosity versus time delivered to and for pp collisions at 7 and 8 TeV centre-of-mass energy in 2011 and 2012.

The LHC is also capable of accelerating lead (Pb) ions to deliver both lead-lead and proton-lead collisions. It has four interactions points (IP), shown in Figure 2.1, each one accommodating a particle physics experiment. The ATLAS and CMS (Compact Muon Solenoid) are general purpose experiments designed for high-luminosity operation and are equipped to study a wide range of phenomena including precise measurement of Standard Model processes and searches for evidence of New Physics.

Additionally, two dedicated experiments, ALICE (A Large Ion Collider Experiment) and LHCb are designed for lower luminosity operation $(\sim 10^{30}\ \mathrm{cm}^{-2}\ \mathrm{s}^{-1})$. Both of them are specially equipped for targeted physics searches: ALICE specializes on heavy ion and quark-gluon plasma physics, LHCb on b-quark physics and

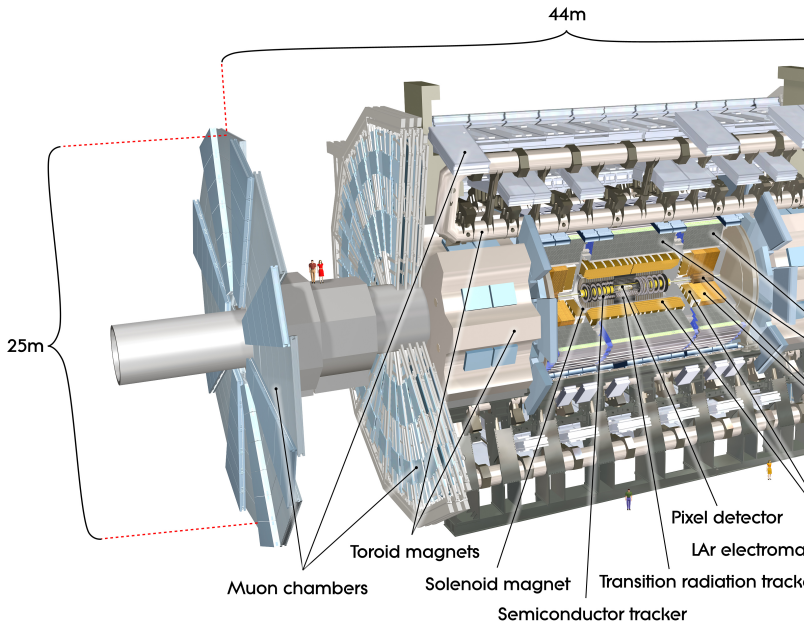

Figure 2.4: A detailed computer-generated image of the ATLAS detector and it's sub-systems. The ATLAS detector is one the two general purpose detectors located at the LHC. It consists of three sub-detector systems: the Inner Detector, the Calorimeters and the Muon Spectrometer.

CP violation measurements.

By design, the LHC will accelerate proton beams to a center-of-mass energy $\sqrt{s} = 14\,\text{TeV}$ and lead (Pb) ion beams to $\sqrt{s} = 2.8\,\text{TeV}$. It should reach a luminosity of $10^{34}\,\text{cm}^{-2}\text{s}^{-1}$ and $10^{27}\,\text{cm}^{-2}\text{s}^{-1}$ respectively [34]. During 2011 LHC delivered $5.6\,\text{fb}^{-1}$ of proton-proton collisions at $\sqrt{s} = 7\,\text{TeV}$ and ATLAS recorded $5.2\,\text{fb}^{-1}$ reaching a peak instantaneous luminosity of 3.65×10^{33} $\text{cm}^{-2}\text{s}^{-1}$. In 2012 the energy increased to $\sqrt{s} = 8$ TeV, LHC had delivered $23.2\,\text{fb}^{-1}$ and ATLAS recorded $21.7\,\text{fb}^{-1}$. A peak luminosity record of $7.73 \times 10^{33}\,\text{cm}^{-2}\text{s}^{-1}$ had been reached during 2012. In Figure 2.3 the cumulative luminosity versus time is shown for 2011 and for 2012, including delivered by LHC (green), recorded by ATLAS (yellow), and certified to be good quality data (blue) during stable beams.

2.2 The ATLAS detector

The ATLAS detector is 44 m in length and 25 m in height and it weights 7000 tons [4], making it the largest particle detector constructed up to now. The experiment is a collaboration involving roughly 3000 physicists from over 174 institutions in 38 countries.

With respect to the Interaction Point (IP), ATLAS is forward-backward symmetric. It is divided in two regions, barrel and end-caps. In the barrel region where the

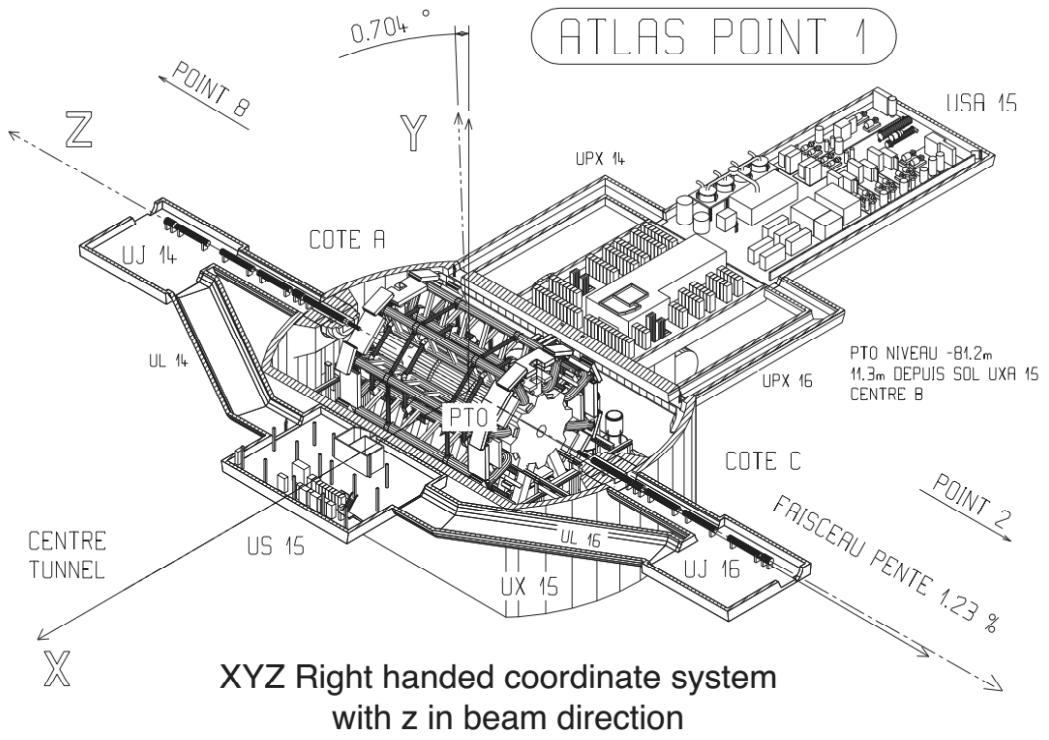

Figure 2.5: The coordinate system of the ATLAS detector.

modules disposed into concentric layers with respect to the beam axis while in end-cap regions the detectors form disks to increase the detector coverage. ATLAS is mainly composed of six subsystems: the magnet system, the Inner Detector, the Calorimeters, the Muon Spectrometer, the trigger and the data acquisition system. A schematic illustration of ATLAS detector can be found on Figure 2.4.

2.2.1 The ATLAS coordinate system

The coordinate system of ATLAS is a right-handed coordinate system with the x-axis pointing towards the center of the LHC tunnel, and the z-axis along the tunnel. The side of ATLAS detector pointing lying towards positive z is called side-A while the other, being on negative z is side-C. The y-axis is slightly tilted with respect to the vertical due to the general tilt of the tunnel. The coordinate system is shown in Figure 2.5. The pseudorapidity of particles from the primary vertex is defined as

$$\eta = -ln\left(tan\frac{\theta}{2}\right) \tag{2.1}$$

where θ is the polar angle of the particle direction measured from the positive z-axis. Transverse momentum, p_T , is defined as the momentum perpendicular to the LHC beam axis.

2.2.2 Magnet system

The ATLAS experiment has a very peculiar magnet system [35] which named the experiment itself. It has been designed to provide magnetic field over a large region ($|\eta| < 3$) and to allow the inner tracker and the Muon Spectrometer to perform measurements of the charged particles momenta. The ATLAS magnet system is sketched in Figure 2.6.

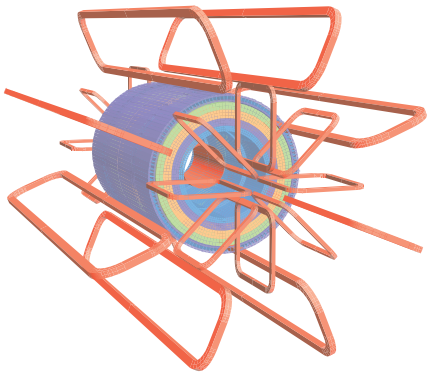

Figure 2.6: The geometry of magnet windings and tile calorimeter steel. The eight barrel toroid coils, with the end-cap coils interleaved are visible. The solenoid winding lies inside the volume of the calorimeter. The tile calorimeter is modeled by four layers with different magnetic properties, plus an outside return yoke. For the sake of clarity the forward shielding disk is not displayed.

ATLAS features a unique hybrid system of four large superconducting magnets. This magnetic system is 22 m in diameter and 26 m in length, with a stored energy of 1.6 GJ. The ATLAS magnets system is sketched in Figure 2.6.
This huge system is composed of:

- a central solenoid, providing a 2 T solenoidal field in the tracker
- three superconducting air-core toroid systems (one in the barrel and two in the end-caps), each made of eight coils, providing a toroidal field up to 4T in the Muon Spectrometer.

The central solenoid is 5.3 m long and has a diameter of 2.4 m; the end-caps toroids, placed at both sides of the solenoid, are 5 m long and have an external diameter and an internal bore of 10.7 m and 1.65 m respectively. The end-cap coils, assembled radially and symmetrically around the beam axis, are shifted by 22.5° in ϕ with respect to the barrel coils. Magnets are kept at low temperature by the liquid helium flowing through tubes welded to the coils at a temperature of $4^\circ\ K$.

2.2.3 Inner Detector

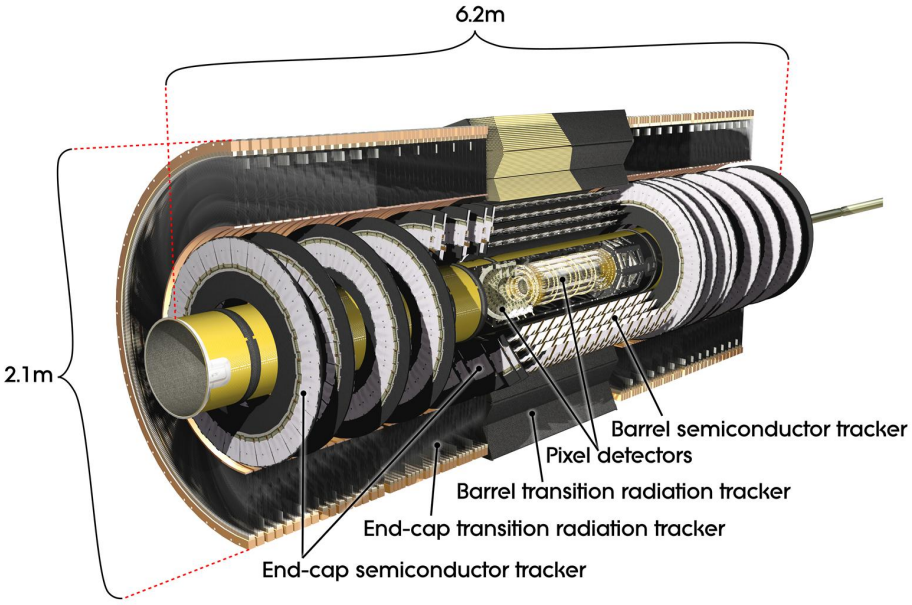

Figure 2.7: The ATLAS Inner Detector. From inner to outer layers it consists of the Pixel Detector, the Semi-Conductor Tracker and the Transition Radiation Tracker. It is about 6 m long and 2 m in diameter.

The Inner Detector (ID) [36,37] is a tracking detector with three different subsystems (see Figure 2.7): Pixel Detector, Semi-Conductor Tracker (SCT) and Transition Radiation Tracker (TRT). Modern physics analyses require excellent momentum and impact parameter measurements, therefore the detectors close to the beam line have to be radiation hard, especially in the high pile-up environment of the LHC which increases dramatically the radiation dose to the subsystems.

The three systems consist of two high resolution pixel and silicon strip detectors and one straw tube detector with transition radiation capabilities for electron identification and pion rejection.

Each detector is divided into one central barrel region and two end cap regions with full hermetic coverage in an η region of $|\eta| < 2.5$. Each particle produces an average of 3 pixel, 8 SCT and 36 TRT hits.

Pixel Detector

The Pixel Detector is the innermost detector. It has three layers in the barrel and three discs in each end-cap region assuring at least 3 measurements over the whole acceptance. The barrel layers are located at radial distances of 50.5, 88.5 and 122.5 mm and the discs at distances of $\pm$ 495, 580, 650 mm as can be seen in Figures 2.8 and 2.9 respectively. The system covers a region of $|\eta| < 2.5$.

The Pixel detector has a very high granularity with a total of 80 million pixel

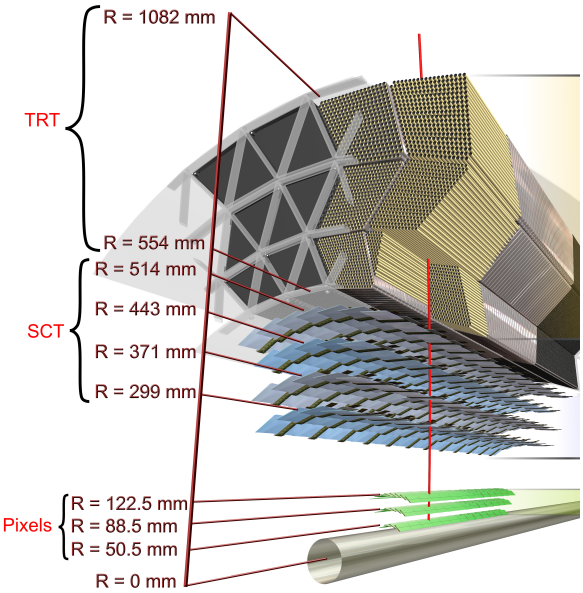

Figure 2.8: A drawing showing the sensors and the structural elements traversed by a charged track of 10 GeV in p_{T}in the barrel inner detector (η=0.3). The track traverses successively the beryllium beam-pipe, the three cylindrical silicon-pixel layers with individual sensor elements of 50×400 μm^2, the four cylindrical double layers (one axial and one with a stereo angle of 40 mrad) of barrel SCT of pitch 80μm, and approximatey 36 axial straws of 4 mm diameter contained in the barrel transition-radiation tracker modules within their support structure.

elements mounted on 1456 modules in the barrel and 144 in each end-cap. A module has 46080 pixels. The high precision measurements in the Pixel Detector guarantee good pattern recognition and determine mostly the performance of the whole Inner Detector in terms of the impact parameter resolution and the ability to find short lived particles.

The pixel elements have a size of 50 μm in rϕ and 400 μm in z direction. Each module is 62.4 mm long and 21.4 mm wide. The readout chips, which are mounted directly on the modules, are analogue to allow for charge weighted clustering which improves the resolution and assures noise reduction. The information is buffered on the module until the Level 1 trigger decision is taken (see section 2.2.6). The first layer - being closest to the beam pipe - has to withstand high radiation levels. Due to an insertable design it is possible and foreseen to exchange the innermost layer after a few years of operation in order to maintain an excellent performance.

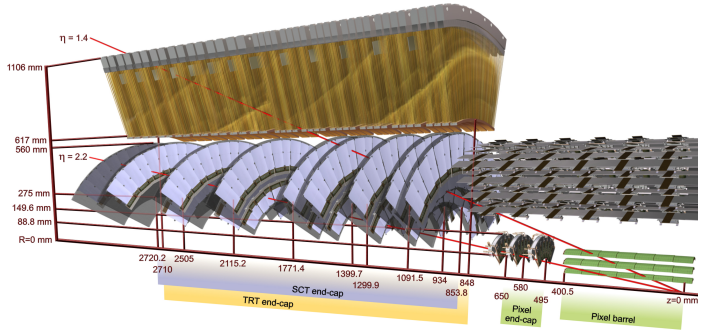

Figure 2.9: A drawing showing the sensors and the structural elements traversed by two charged tracks of 10 GeV in p_{T}in the end-cap inner detector (η= 1.4 and 2.2). The end-cap track at η= 1.4 traverses successively the beryllium beam-pipe, the three cylindrical silicon-pixel layers with individual sensor elements of 50×400 μm^2, four of the disks with double layers (one radial and one with a stereo angle of 40 mrad) of end-cap silicon-microstrip sensors (SCT) of pitch $\sim$ 80 μm, and approximately 40 straws of 4 mm diameter contained in the end-cap transition radiation tracker wheels. While on end-cap track at η=2.2 traverses successively the beryllium beam-pipe, only the first of the cylindrical silicon-pixel layers, two end-cap pixel disks and the last four disks of the end-cap SCT. The coverage of the end-cap TRT does not exceed $|\eta|$= 2.

Semi-Conductor Tracker

The middle detector of the three Inner Detector subsystems is the Semi-Conductor Tracker. It consists of 4 layers in the barrel region and 9 discs in each end-cap region. The layers consist of two detector modules mounted back-to-back at a small angle of 40 mrad to obtain the z measurement. There are 4224 back-to-back modules in the barrel and 1976 in each end-cap. The 4 double layers are mounted at radial distances of 301, 373, 445 and 516 mm while the 9 discs at z distances between $\pm$ 85 cm and $\pm$272 cm. It covers a region of $|\eta| < 2.5$.

Each module has a size of 6.3 $\times$ 6.4 cm and holds 780 readout strips each with 80 μm pitch. The total covered area is 61 m^2 and accommodates about 6.2 million readout channels. It is a high granularity tracking detector which adds a maximum of 8 precision measurements to the 3 hits of the Pixel Detector. It contributes significantly to the pattern recognition capabilities and momentum and impact parameter resolution of the Inner Detector. The read out chips are again mounted on the modules and the digital hit information is buffered until Level 1 trigger has drawn its decision.

Transition Radiation Tracker

The outermost layer of the Inner Detector is the Transition Radiation Tracker. The TRT is based on multiwire proportional chamber technology and was chosen so as to cheaply provide extended continuous tracking in the Inner Detector. The barrel section, located at radial distances from 554 mm up to 1082 mm, contains 50000

straw detectors, 144 cm long and of 4 mm diameter, parallel to the beam axis within $|\eta| < 0.7$. The TRT end-cap, at z distances between ± 84.8 cm and ± 271 cm, contains an additional 320000 straws aligned radially, of 37 cm in length, covering $0.7 < |\eta| < 2.5$.

The straws are filled with a gas mixture of Xe : CO_2 : CF_4 – (70 : 20 : 10) such that a charged particle traversing the gas causes ionization which is detected on the wire readout. Using a threshold of collected charge and timing information to determine track hits and their position TRT is capable only of providing rϕ information. TRT adds on average 36 hits to the measurements of the Pixel and SCT.

2.2.4 Calorimeters

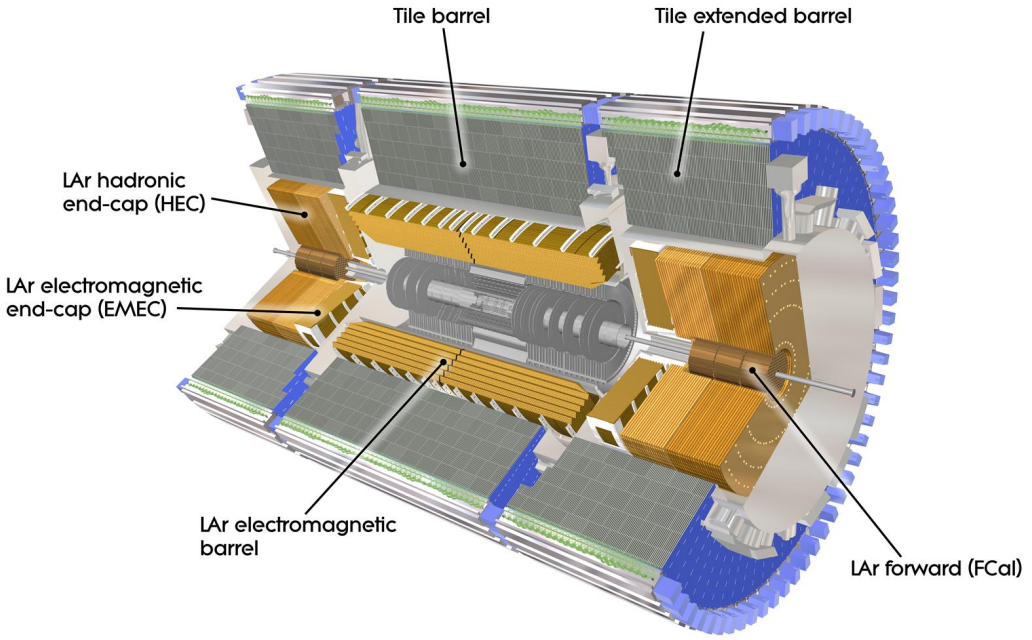

Figure 2.10: The calorimeter system measures the energy and the position of particles by sampling the energy deposit in them. It comprises the Electromagnetic and the Hadronic Calorimeters.

Surrounding the Inner Detector and solenoid is the electromagnetic and hadronic calorimeters [38, 39], measuring the energy of both charged and neutral particles, providing pseudorapidity coverage up to $|\eta| = 4.9$. An overview of the ATLAS calorimetry system is given in Figure 2.10.

Electromagnetic Calorimeter

The ATLAS Electromagnetic Calorimeter (ECAL) has been built to reconstruct the energy of particles that interact via the electromagnetic interaction like electrons,

photons and hadrons. In order to achieve that it makes use of the interaction of electrons and photons with matter to provide excellent performance in terms of energy and position resolution.

The ECAL is a lead – liquid Argon (LAr) detector with accordion-shaped kapton electrodes and lead absorber plates over its full coverage. The calorimeter is divided into a barrel part ($|\eta| < 1.475$) and two end-cap components ($1.375 < |\eta| < 3.2$).

Particles passing through the ECAL lose energy in the lead absorber which causes them to radiate photons (bremsstrahlung). These photons are converted into electron-positron pairs which initiate a cascade/shower. The secondary particles ionize the liquid-argon and free electrons from the ionization are attracted by the high voltage field and the produced signal is registered on the copper electrodes. Liquid argon was chosen as the active detector medium due to its linear behavior and intrinsic radiation hardness.

The resolution provided by the ECAL is σ(E)/E=10 %/$\sqrt{E}\oplus$0.7 % and the angular one $\sigma_\theta = 55\,\text{mrad}/\sqrt{E\,(\text{GeV})}$. The barrel part of ECAL is sharing the same cryostat unit with the solenoid magnet, as described in Section 2.2.2, while the two end-cap calorimeters are housed in their own.

Hadronic Calorimeter

The Hadronic Calorimeter surrounds the Electromagnetic Calorimeter. It has an outer radius of 4.25 m and a length of 12.2 m. In the barrel region ($|\eta| < 1.7$) it uses a novel approach with plastic scintillators embedded in the iron absorber. The incoming particles initiate showers in the absorber and the secondary particles excite atoms in the scintillators which then radiate photons. These photons are transmitted to photo-multipliers which convert the light into an electric signal. In the end caps ($1.5 < |\eta| < 3.2$) the hadron calorimeter makes also use of the more radiation hard liquid-argon as active material. The calorimeters extend up to $|\eta| = 4.9$ to cover the very forward regions. To achieve this, additional calorimeters are mounted at a distance of 4.7 m from the interaction point in z and as close as possible in rϕ (some centimeters). This region is under high exposure to radiation and therefore the LAr technology has been used for both the Electromagnetic and Hadronic Calorimeter. The former is made of copper while the latter of tungsten. The design energy resolution of the hadron calorimeter is $\sigma(E)/E = 50\,\%/\sqrt{E}\oplus 3\,\%$ and $\sigma(E)/E = 100\,\%/\sqrt{E}\oplus 10\,\%$ in the forward region.

2.2.5 Muon Spectrometer

In the outer part of ATLAS the Muon Spectrometer (MS) is located [40]. Its goal is to identify, measure and trigger muons. The MS has the capability by design to provide standalone measurement of muons independently to the measurements of the Inner Detector. MS uses four different technologies, as shown in Figure 2.11. Two of its subdetectors are used to provide precision measurements, the Monitored Drift Tubes (MDT) and the Cathode Strip Chambers (CSC), while the rest, the Resistive Plate Chambers (RPC) and the Thin Gap Chambers (TGC), provide

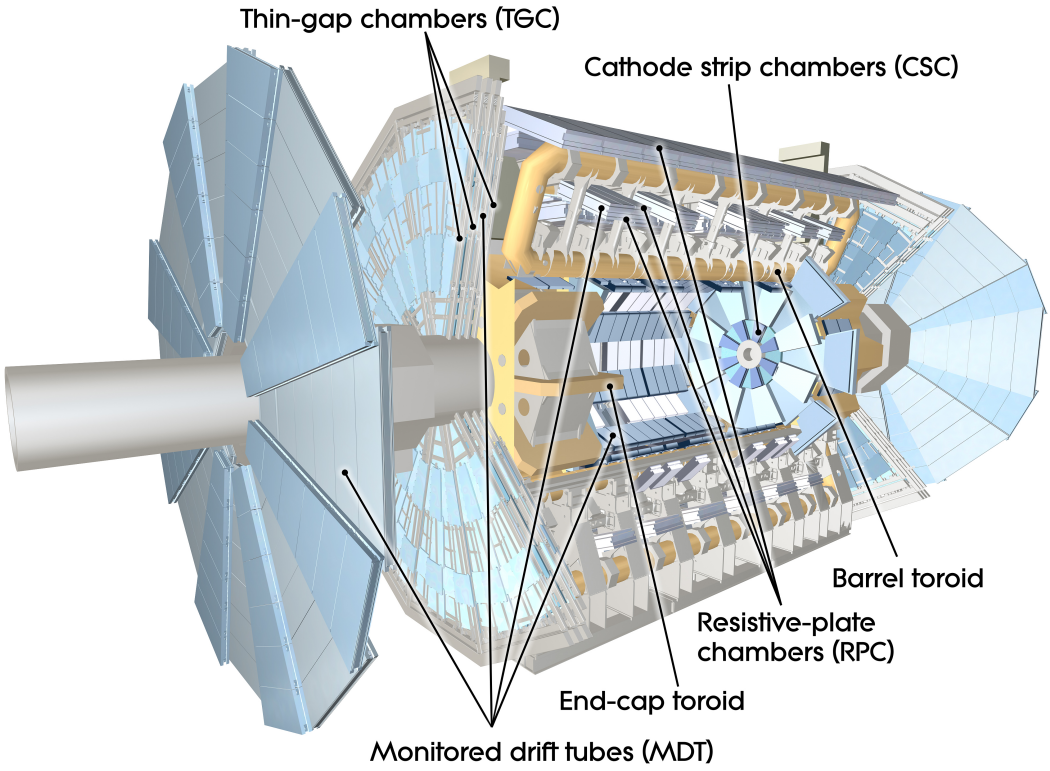

Figure 2.11: The Muon Spectrometer intends to identify, measure and trigger muons. It contains four detector technologies: the Monitored Drift Tubes, the Cathode Strip Chambers, the Resistive Plate Chambers and the Thin Gap Chambers.

triggering information. Similar to the other systems, the MS is also segmented into a barrel ($|\eta| < 1.05$) and two end-caps regions ($1.05 < |\eta| < 2.7$).

Resistive Plate Chambers

The RPCs are located in the barrel region covering up to $|\eta|$ = 1.05. They consist of three layers of chambers and they are located below and above their respective MDT partner. They present excellent characteristics for a trigger system; in fact, they provide a fast momentum estimation (at the level of $\sim$ 2 ns) for the hardware-based trigger and necessary timing information for the MDT chambers. Moreover, they provide the ϕ coordinate measurements with a precision of $\sim$ 1 cm which is fundamental in the muon track reconstruction as MDTs cannot measure the ϕ coordinate.

The chambers are made by two parallel highly resistive plates separated by insulating spacers in order to form a 2 mm gas gap filled with $C_2H_2F_4$: Iso-C_4H_{10} : SF_6 (94.7 : 5 : 0.3 %) as gas mixture. The plates are covered with readout strips at their back which are orthogonal to each other in order to achieve an $\eta - \phi$ measurement.

The operational electric field is about 4.9 kV/mm.

Thin Gap Chambers

For the muon trigger in the region of $1.05 < |\eta| < 2.4$ the TGC have been chosen. The reason is their very good rate capability, timing resolution and aging characteristics.

Apart from the triggering, their second functionality is the determination of the second, azimuthal, coordinate to complement the measurement of the MDT chambers in the radial direction.

They are multi-wire proportional chambers with two graphite cathode plates, with a gas mixture of CO_2 : n-C_5H_{12} (55 : 45 %). The wires have a diameter of $\sim$ 50 μm and are placed between the two graphite cathode planes, each plane equipped on the external surface by strips placed either parallel or orthogonally with respect to the wires direction. The wires arranged in the ϕ direction provide the trigger signal for the r coordinate, while the strips orthogonal to these wires provide the ϕ coordinate.

A voltage of 2.9 kV is applied on the anode wires. Including the variation of the propagation time on the wires and the strips, the signals arrive with 99 % probability inside a time window of 25 ns. There are four layers of TGC at each end-cap region.

Cathode Strip Chambers

The limit for safe operation of MDTs is at counting rates of about 150 Hz/cm^2. This is exceeded in the region $|\eta|>$ 2 in the first layer of the end-cap. In this η region of the first layer, the MDT are replaced by CSCs, which combine high spatial, time and double track resolution with high-rate capability and low neutron sensitivity. Operation is considered safe up to counting rates of about 1000 Hz/cm^2, which is sufficient up to the region of $|\eta|$= 2.7.

They are multi-wire proportional chambers filled with Ar : CO_2 (80 : 20 %) as gas mixture, with an anode pitch of 2.5 mm and a cathode strip read-out with a pitch of $\sim$ 5.308-5.567 mm. The charge interpolation between neighboring strips allows for the precision measurement of the second coordinate ϕ, with a resolution per CSC plane of $\sim$ 60 μm. An illustration of the CSC readout strips can be found in Figures 2.12 and 2.13.

The measurement of the η coordinate is obtained either from the signal coming from the wires, that present a maximum drift time of $\sim$ 20 ns, or from the strips placed parallel with respect to the wires on the second cathode plane; in this case the spacing of the readout strips is larger than the one in the bending plane ($\sim$ 13-21 mm) leading to a resolution of about 5 mm per plane. The wires are kept at 1800 V.

Monitored Drift Tubes

The MDT system extends in both barrel and end-cap regions. Each chamber hosts layers made of pressurized drift tube with a diameter of 29.970 mm made of aluminum, operating with Ar : CO_2 (93 : 7 %) gas at 3 bar (see Figure 2.14).

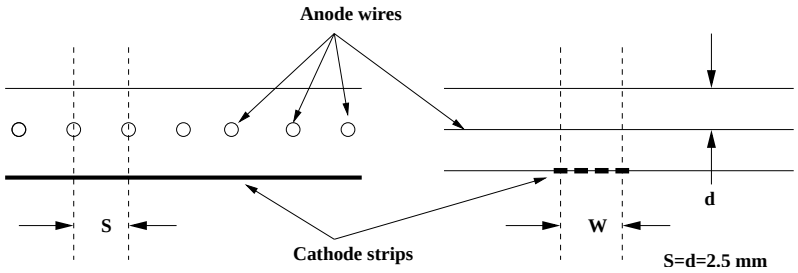

Figure 2.12: The structure of the CSC cells looking down the wires. The wire pitch, s, is equal to the anode-cathode spacing, d=2.5 mm. The view in the perpendicular direction (bending plane), down the readout and intermediate strips is shown side by side. The induction of the avalanche is spread out over 3–5 readout strips.

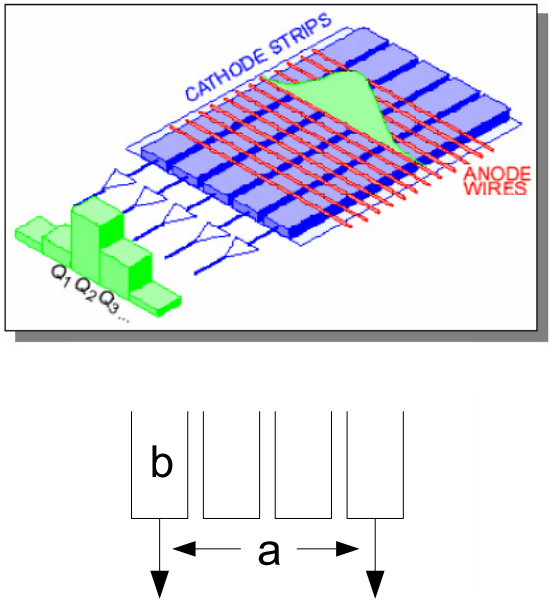

Figure 2.13: Segmentation of the CSC cathodes. The individual strip widths for the large and small chambers are b=1.519 mm and 1.602 mm, respectively. The inter-strip gap is 0.25 mm, resulting in readout pitches of a=5.308 mm and 5.567 mm. The intermediate strips contribute an additional charge interpolation, improving the linearity of the reconstructed position.

The electrons coming from the ionization are collected at the central tungsten–rhenium (W–Re) wire with a diameter of 50 μm, at a potential of 3080 V. The wire is held in position at the tube ends by a cylindrical end-plug (Figure 2.15) which guarantees the concentrality of the wire with respect to the tube with an accuracy of $\sigma < 10\mu m$. The central conductor holding the wire also serves for the gas transfer in and out of the tube. Signal transmission to the electronics and connection to the high voltage supply system are at opposite ends.

Each MDT chamber consists of 2 multilayers (except for all ‘BIS8’, ‘BEE’ and

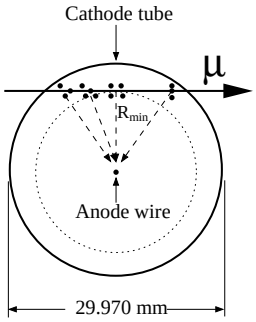

Figure 2.14: The cross-section of a MDT tube.

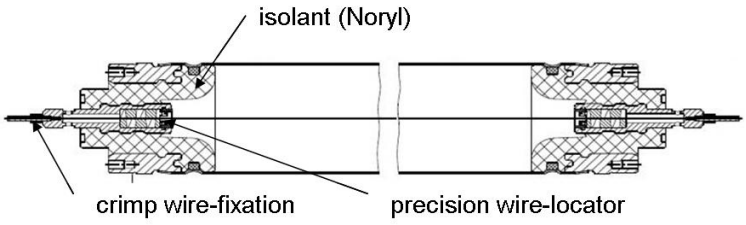

Figure 2.15: The longitudinal cut through a MDT tube.

'EE' chambers that contain only one) while each multilayer consists of either three or four layers of tubes[1]. The length of the tubes vary from 0.7 m to 6.3 m depending on the position inside the MS.

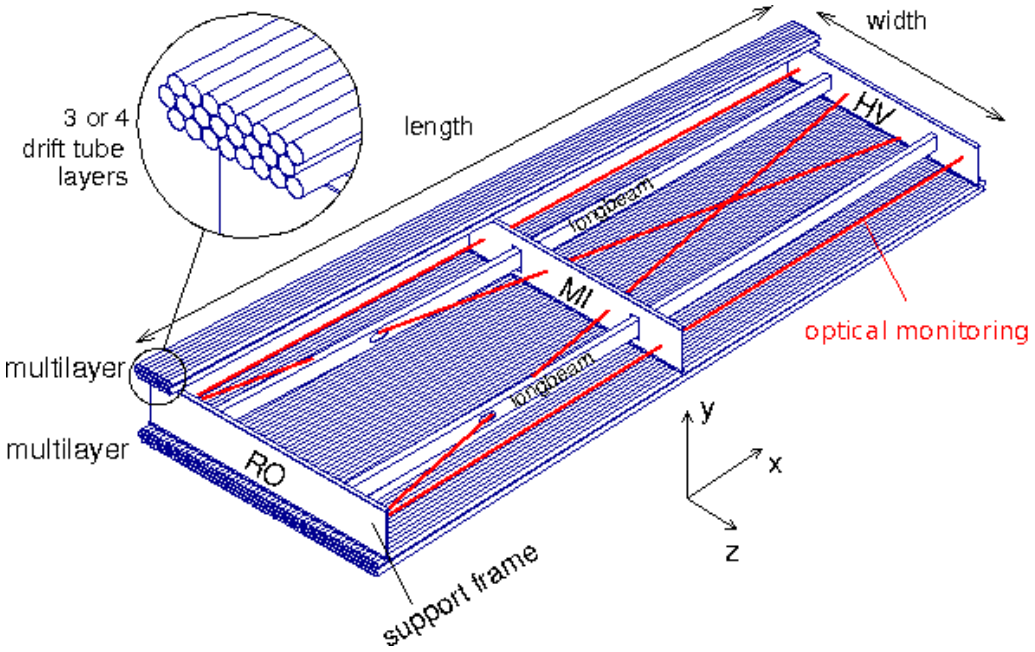

Figure 2.16: The MDT chambers form two multilayers with two or three layers of tubes, glued on a support frame and monitored from the internal alignment point of view through an optical system.

In order to maintain the inherent resolution of the drift tubes a mechanical spacer is responsible for the fixed position of the layers which are mounted on an aluminum support frame as shown in Figure 2.16.

[1]It had been decided to use four rows of tubes in each multilayer for the innermost chambers and three rows for the rest of the chambers.

Since deformations are expected to occur in the various mounting positions in ATLAS and may change in time when thermal gradients are present, an internal chamber optical alignment system, RASNIK [41], has been implemented. The alignment system, which continuously monitors potential deformations of the frame, consists of a set of four optical alignment rays, two running parallel to the tube direction and two in the diagonal direction as shown in Figure 2.16. The relative position of the chambers in the consecutive layers are also monitored by a projective alignment system while the chambers within a layer are referenced to each other by chamber-to-chamber alignment sensors.

The MDT detector system consists of 1150 chambers containing a total of 354000 drift tubes. Out of them, 592 are in barrel and the rest 558 at the end-cap regions. MDTs form three layers[2]: Inner, Middle and Outer according to their distance from the IP. In the barrel they form layers of co-axial cylindrical shells whereas in the end-cap regions, consecutive concentric disks: the Small Wheel (Inner), the Big Wheel (Middle) and the Outer Wheel (Outer). The MDT chambers coverage[3] extends up to $|\eta| = 2.7$.

Each layer is divided in a number of stations. For the barrel, the stations indicate the position of the chambers with respect to the IP in the direction parallel to the beam axis, being numbered from 0 to 7, while for the end-cap regions, the stations indicate the position of the chamber with respect to the radial coordinate, being numbered from 1 to 6. According to the azimuthal coordinate, the chambers form 16 sectors of which the odd sectors contain the "Large" chambers and the even sectors the "Small" ones which have a difference in size for better azimuthal coverage.

All the above information is encrypted in the name of the chamber using a simple naming convention. For example BOL1A12 is at barrel region ("B") in the outer layer ("O"), a large ("L") chamber in station 1 ("1") of side A ("A") and sector 12 ("12").

2.2.6 Data Acquisition and Trigger System

The ATLAS Trigger and Data AcQuisition (collectively TDAQ) system is an important component of the experiment that is necessary to allow the efficient and effective performance of the detector given the (externally imposed) limited readout rates and data storage capabilities. Given the current available technologies, the nominal LHC proton-proton bunch crossing rate of 40 MHz is too high for every event to be read out fully and recorded. The trigger system has the role of reducing the rate of events that will be written out without losing interesting physics events [42].

The trigger system has three distinct levels: Level-1 (L1), Level-2 (L2), and the Event Filter (EF) as schematically described in Figure 2.17. Each trigger level sequentially reduces the data rate, using more information and increasingly precise measurements at each level to gradually make more refined decisions.

[2] In the Endcaps a fourth layer (EE) is used in the Power Supplies Detector Control System for better granularity.

[3] In the small wheel, the chambers cover up to $|\eta| = 2.0$

It is designed to use a limited amount of coarse granularity detector hit information from the calorimeters and the muon detectors (which can be read out quickly) to characterize the gross features of each event. The system then makes a fast decision, based on pre-defined criteria, on whether to record the event or not, the overall data-taking rate is reduced to an acceptable level of around 400 Hz with an event size of approximately 1.3 Mbyte.

The first trigger level (L1), which is hardware based, uses information from the calorimeters and the muon trigger chambers only to draw a decision in less than 2.5 μs, reducing the rate to about 75 kHz. It is also responsible for the so-called Region of Interest (RoI), information which is then passed on to the next level (L2) in order to continue the chain.

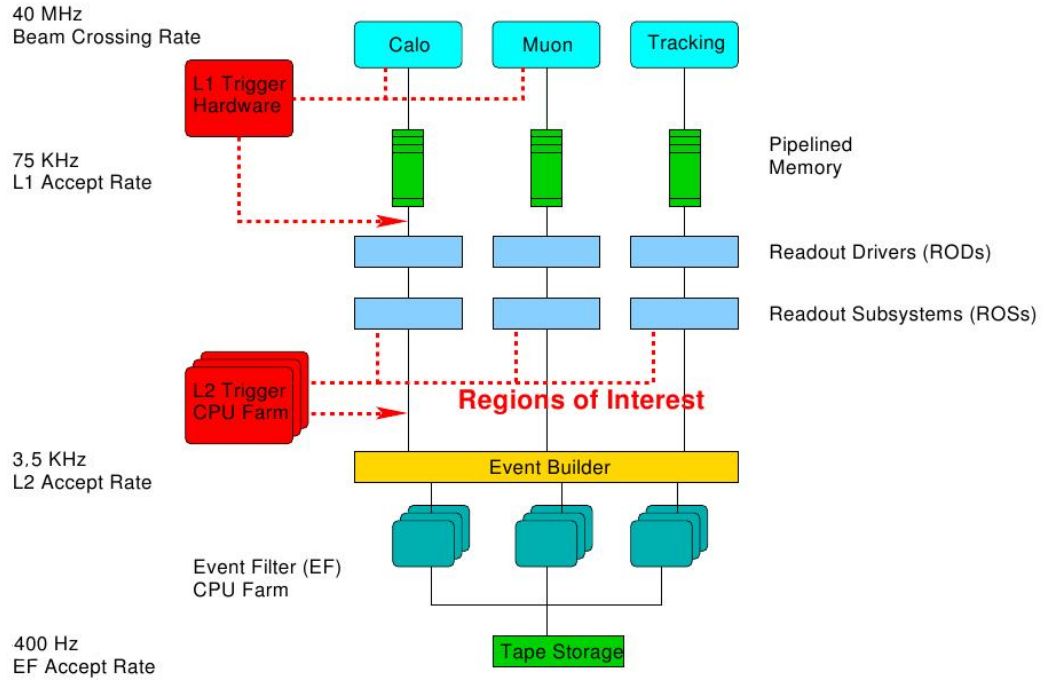

Figure 2.17: The ATLAS three-level trigger schema. ATLAS trigger achieved a final rate of about 400 Hz from the 40 MHz proton-proton collision rate.

The next level of trigger (L2) is software-based and uses the full granularity of the RoI seeded by the L1 (approximately 2% of the total event data) and the Inner Detector to refine the trigger selection. It is designed to reduce the rate down to approximately 3.5 kHz with an average event processing time of 40 ms, depending on the complexity of the event. If an event passes the L2 requirements, all the information of the event is then passed to the Event Filter.

The final level of the trigger chain is the Event Filter. Event Filter is also software based and has access to the event information in full granularity using offline analysis procedures within an average event processing time of the order of four seconds. The events passing the EF are then recorded for further analysis.

Being both software-based, L2 and EF usually are usually denoted as High Level

Trigger (HLT).

Every analysis performed in ATLAS relies on the Trigger capabilities to select events of interest; in particular, for the resonances involving two muons in the final states some sets of di-muon algorithms operating the HLT stage have been provided. This choice is dictated by the limited bandwidth that does not allow to use always single-object triggers.

For the B-Physics studies [43] two different approaches have been implemented: in the first the L2 algorithm is seeded by a di-muon trigger at L1, which produced 2 RoIs, while in the second approach the L2 algorithm starts from a single RoI.

The first approach is denoted as "topological" di-muon trigger: each L1 RoI is separately confirmed at L2, then the two muon candidates are combined into a resonance and a mass cut is applied; finally this chain is confirmed by the EF.

In the second approach the L1 RoI is enlarged and in this "Extended RoI" a second muon is searched starting from a Inner Detector track and extrapolating it to the Muon Spectrometer. This second method is particularly useful in the case in which one of the two muons of the resonance is a low-p_{T} one that may not cross the entire spectrometer or fire the trigger, and in the case in which the angular distance between the tracks of the two muons emitted is smaller than the cone opening angle.

The first approach, instead, can be more useful in the case in which the two muons have similar energies and the angular distance between the tracks of the two muons emitted is larger than the cone opening angle, as for the B mesons.

Both categories of triggers apply extra requirements in invariant mass, opposite charge and vertex χ^2 match in order to reduce the rate and yet keep interesting J/ψ Υ and B meson data.

An illustration for both approaches can be found in Figure 2.18.

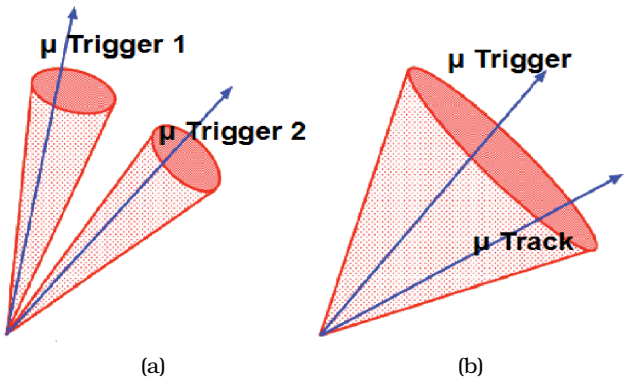

Figure 2.18: A diagram showing how the two different B-physics trigger algorithms are configured. The diagram a shows (a) generic topological trigger, and (b) shows the Di-Muon trigger.

Chapter 3

The ATLAS Detector Control System (DCS)

Various hardware and software systems are required to monitor, control and operate the ATLAS experiment. The interaction of the detector experts and the shifters with the detector hardware is also done with the help of a Detector Control System (DCS).

The experiments at LHC need a coherent and safe operation of their detectors along with ways to make common developments and avoid duplication. The solution to that was provided at the beginning of 1998, when a Joint COntrols Project (JCOP) [44] was set up, aiming to provide common solutions for the control system for all LHC experiments.

The main goal of the JCOP Framework is to develop, provide and support the components and tools which are going to be used widely for the control system of the detectors. To do this a common basis was needed.

An evaluation of various SCADA (Supervision Control And Data Acquisition) products performed at CERN [45] in the frame of the JCOP which ended up with the selection of the Austrian company ETM [46] (recently absorbed by SIEMENS) and its product PVSS–II for SCADA system and the State Management Interface (SMI++) [47] for the Finite State Machine (FSM) hierarchy.

3.1 The SCADA system - PVSS–II

PVSS–II, is a software package designed for the field of automation engineering. Its main application is in the operation and supervision of technical installations with full-graphics capability. In addition to the visualization of the current process states, this application can transfer input values and commands to the process and its control devices. The software includes alerting the user when critical states occur or predefined limits are exceeded, plus archiving of data for later display and analysis.

One of the key features of the PVSS–II is its modularity which enables any project of PVSS–II to be distributed across different machines even with different operating systems. The modular design of PVSS–II is illustrated in Figure 3.1. Each functional

module is specifically created for different tasks with specific roles and constitute separate processes in software. These modules are called managers.

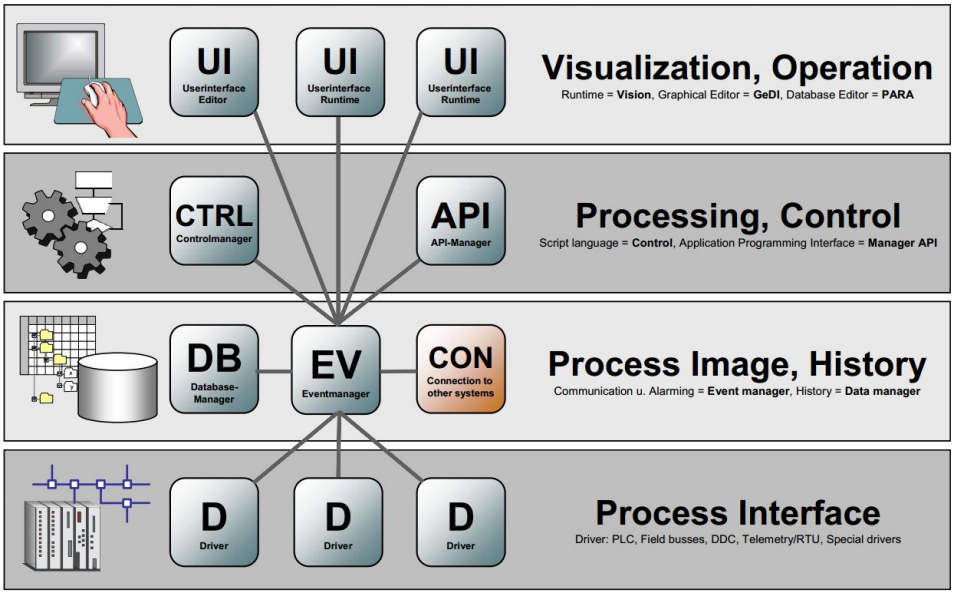

Figure 3.1: An example of a fully configured PVSS–II system showing the core managers among with their cooperation in a hierarchical illustration.

The main manager of PVSS–II is the *Event Manager (EV)*. The EV is managing all communications; it is responsible of receiving data from the Drivers, send them to the *DataBase Manager (DB)* – a manager which provides information to the (run time) database – and ensures the distribution of the information and data to all managers which have subscribed to it in the case of a distributed project.

At the lower level of hierarchy one can find the *Drivers (D)* which are modules materializing the connection of PVSS–II to the external hardware. Commonly used drivers provided with PVSS–II are OPC, ProfiBus, CANbus, Modbus and TCP/IP.

The developer is able to customize and implement algorithms and routines using a C-like language via the graphical editor, the database editor and the general user interface of the application. These custom functions can be transformed and treated as self-contained managers via two methods: *Application Programming Interface (API)* and *Control Manager (CTRL)*.

At the higher level of the organization lie the *User Interface (UI)* managers. Those managers establish the communication with the user.

Simplifying things, a PVSS–II project is an application containing one DB manager, one EV manager and any number of drivers and user interfaces with the ability to be distributed over different platforms.

3.1.1 Datapoints

Real devices within the control system are represented via datapoints (DPs). The DPs are structured device-oriented data object containing all the available infor-

mation (values, states) in an organized way. A DP contains one or more datapoint element (DPE). Every DPE corresponds to a value or state of the device that the DP is representing. In addition to storing the value, the DPE includes attributes, giving the time stamp, quality information and the originator/parent.

While most of the SCADA systems assign a separate datapoint to every individual process variable, PVSS–II takes a more modern approach: nearly all information in the process belongs logically to an entity of varying complexity like a device is organized in a single datapoint.

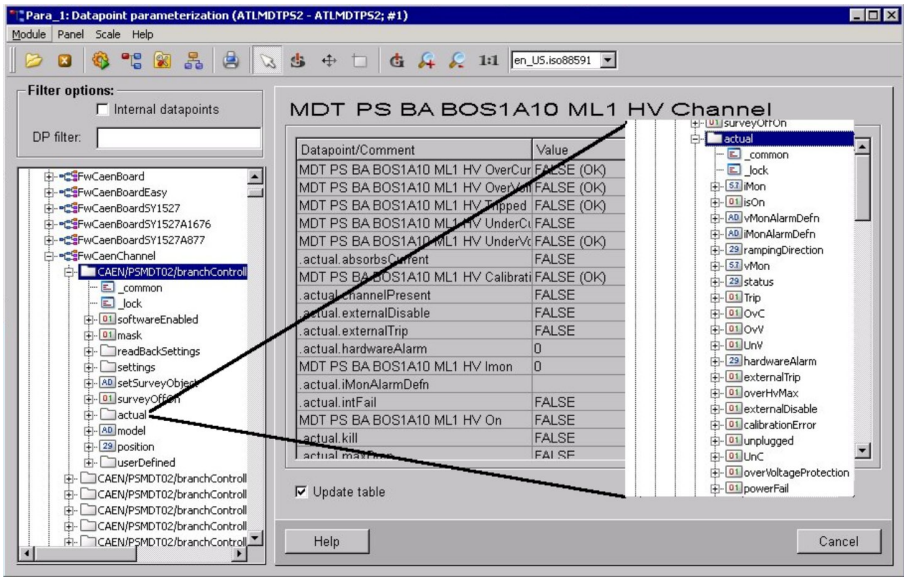

Figure 3.2: An example of a datapoint along with its datapoint elements. The values and states are organized internally (readBackSettings, settings, actual) in logical groups, while each one of these groups accommodates the corresponding values and states.

An example of datapoints and its datapoint elements is given in Figure 3.2. The datapoint of type “FwCaenChannel” contains all the information of a high voltage channel of CAEN. The values and states are organized internally (readBackSettings, settings, actual) in logical groups, while each one of these groups accommodates the corresponding values and states.

3.2 The ATLAS MDT DCS Architecture

Such compound detectors, like ATLAS, needs a well designed and organized back-end architecture for their control and monitoring. The ATLAS experiment is mainly operated by two collaborating systems: the DCS and the Trigger and Data-Acquisition (TDAQ) system.

The DCS system is constantly supervising and controlling the hardware of the experiment and its infrastructure while the TDAQ performs the read out of the detector data generated by the collisions and directs the data streams from the

digitizers to the mass storage units. Dictated by its role, TDAQ operates only during physics data taking periods while the DCS is responsible for continuous monitoring and control of the detector equipment and is supervised by a human operator in the control room.

The DCS has the task to provide coherent and safe operation of ATLAS and to serve as an homogeneous interface to all sub-detectors and to the technical infrastructure of the experiment.

The ATLAS DCS system is categorized in four abstract groups: LHC Overview, Systems, Services and Infrastructure.

LHC Overview: provides access to commonly useful information about the accelerating complex along with the information provided by the other experiments of LHC.

Systems: contains the systems required for the data acquisition (i.e. DAQ, Data Quality) all the sub-detectors (i.e. Inner Detector, Calorimeters, Muon Spectrometer) that ATLAS consists of.

Services: groups services commonly used for the technical operation of the detector like the cooling, gas systems, cryogenics and electrical network.

Infrastructure: contains the safety system, radiation monitors, magnets, counting rooms & cavern, environment, computers & network and database servers.

3.2.1 Power Supply of MDT

For the MDT chambers (one of the four technologies of Muon Spectrometer), one of the main systems to be monitored and controlled is the Power Supply (PS) system.

As described in Section 2.2.5 each MDT chamber consists of tubes where each tube requires a High Voltage (HV) supply of 3080 V in order to operate. Besides the HV, each chamber requires also a voltage supply for the electronics which perform the measurement. For this a Low Voltage (LV) supply of approximately 5 V (depending on the chamber) is used.

For the needs of HV and LV power supplies CAEN A3025B, A3540P and A3016B boards are used. These boards are hosted in easy-creates (module CAEN EASY 3000S) in racks located inside the experimental cavern. Each crate can accommodate up to 21 single-slot cards while one slot of them (the first one) is used for the control of the crate. The crates are organized in groups of five in a chain belonging to one 'Branch Controller' board (A1676A). All Branch Controllers are housed in and controlled by the 'Mainframe' (SY1527) located outside of, but close to, the experimental cavern.

This hardware hierarchy along with the connection schema is illustrated in Figure 3.3.

For the whole MDT system two mainframes are used with total 14 branch controllers. Eight of them are used for the barrel and six for the end-cap region. Totally

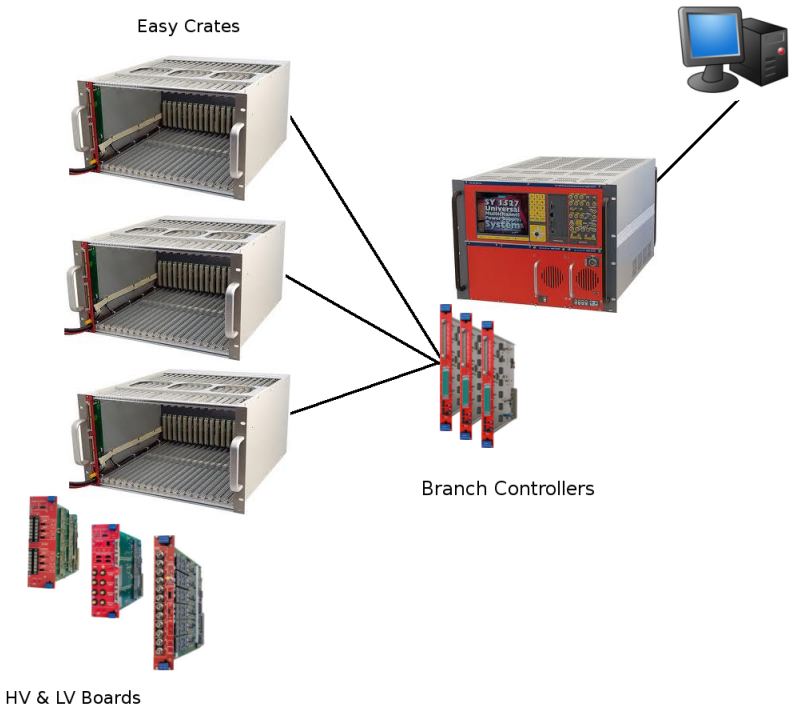

Figure 3.3: The hierarchy of the Power Supply hardware for the MDT chambers.

68 crates are used with 339 HV and LV boards (162 for the end-caps and 177 for the barrel) providing 2820 channels.

3.2.2 Datapoints for the PS

An example of the modern approach of PVSS–II regarding the datapoints organization and grouping can be illustrated via the datapoints of the power supply system. Instead of having an enormous number of datapoints corresponding to all possible processes for all the needs of each of the MDT chambers, datapoints corresponding to the chambers are used.

These datapoints contain the minimum information in order to assess the full working condition of the chamber. They provide the connection mapping, which includes the three channels connected to the chamber: the LV channel for the electronics and the HV for the two multilayers of the chamber. Also some additional information for every channel concerning trip handling and flags are available. Those flags provide information about the safe usage of the channels. A channel may be on various error states (i.e. raise of the temperature of the electronics used for the readout, gas system misbehavior affecting this chamber, etc) where the powering may be dangerous for the chamber itself.

As described above, a connection schema including the SY1527 mainframe, the Branch Controllers, the Easy Crates and the Boards is adapted. For each of the aforementioned hardware units a corresponding datapoint exists containing

general and overall information like the 'coordinates' (position) in the connection chain, serial number, firmware version and module temperature, fan working state respectively.

Datapoints that are mostly used in the PS projects are those corresponding to the channels of the HV and LV boards. As mentioned previously, since the datapoint in PVSS–II represent complex logical units, they have an internal organization. Besides some general information, like the power status and the clock synchronization of the module, each channel datapoint has the elements grouped in 3 main categories:

'actual' This group corresponds to the current (online) values of the channels like the voltage ('vMon'), the current ('iMon') and the power state of the channel ('onOff').

'settings' This group includes all the elements that must be set for proper operation (i.e. the voltage of the channel 'v0', the trip limit 'i0' and the spead in which voltage ramps up or down per second 'rUp'-'rDwn').

'readBackSettings' This group contains the values of settings that the hardware has internally stored and is using at that specific moment.

For each datapoint element, apart from the online value a number of available configurations are available. These configurations ('configs') provide additional functionality to the datapoint elements. Some of them are:

Alerts For each critical parameter PVSS–II provides a built-in alarm mechanism which can be used to point out any incident in which a value moves into a non-nominal area. In this case an alert, which is stored in the '_alert_hdl' configuration, contains the predefined limits along with the definitions of the severity levels of the alarm. Besides the available severity levels ('Warning', 'Error' and 'Fatal') and their corresponding limits the configuration provides the possibility to require acknowledgement (by the shifter or the expert of the system) and also to mask (hide intentionally) known alarms in order to avoid the accumulation of a large number of alarms on the user interface. The responsible user interface for the display of all active and triggered alarms is called Alert Screen (see Figure 3.4) and comprises one of the two main tools for the shifter. The Alert screen has one line per activated alarm providing technical information about the alarm and a short description. If an acknowledgement is required or masking is available, those can be done via the Alert screen.

Archive To make an efficient monitoring of the system, along with the ability of tracing back during troubleshooting, PVSS–II can archive values of the datapoint and alerts. Those values are stored either by the RAIMA DB or Oracle archiving, allowing to diagnose the detector conditions used for physics data reconstruction. In either case an '_archive' configuration accommodates all the needed information about the archiving, i.e. where the value will be archived, if smoothing is going to be used along with the parameters of the smoothing (see section 3.5.1)

Function In order to reduce the amount of the data transmitted the information is organized in bits. A typical example is the status value of a channel. The status is a 16-bit word encrypting all information about the state of the channel and all boolean errors like current status of the channel (ON/OFF, ramping up or down) OverCurrent, OverVoltage, Trip etc. Besides the cases of 'compact' information there are cases where the full picture is scattered in more than one datapoints and the combination of these values is required with the help of mathematical, statistical or logical functions. In order to perform the proper manipulation the '_dp_fct' configuration can be used. Through this the user can built complete automated responses based on more than one datapoints (the function will be triggered when the datapoint containing the 'config' change value) using a custom function from arithmetical, statistical or logical components. The outcome of a datapoint function can be a new value on a predefined datapoint or a signal event (which can trigger an other action).

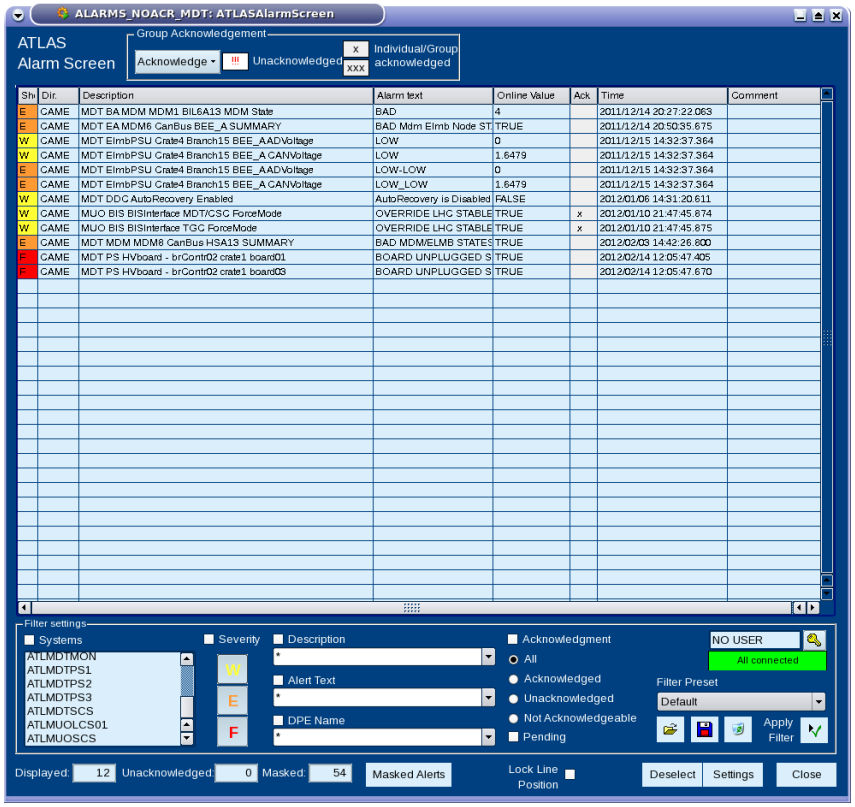

Figure 3.4: The Alert Screen contains all the errors of the system along with a lot of information to track them down and how to react to them. It is one of the main shifter tools.

3.3 Finite State Machine (FSM)

PVSS–II creates a set of concrete entities such as hardware devices or software tasks that needs to be monitored and handled in a specific manner depending on the situation. Due to the enormous size and complexity of the detector and the large amount of data to be monitored, these entities needs to be well organized. Through the SMI++ framework this set is described as a collection of objects behaving as Finite State Machines (FSM). In the context of the DCS, FSM is a model of the detector "objects" (sub-detectors, devices or parts) where each "object" can have a finite number of states where it can be found, transition between these states and actions for each individual state.

The information is abstract, comprehensive or detailed, along with high level control which is available to the users by the FSM software running in the control room. This provides a very human-friendly description and manipulation of the detector for the shifters. The SMI++ framework provides tools to build a FSM and an Expert System which is vital for controlling and recovering in complicated systems as the ATLAS detector is.

During the periods of the ATLAS detector operation, different subsystems, sub-detectors and processes have to collaborate in the most efficient way possible. In order to accomplish this, FSM provides a strict hierarchical tree-like structure with children-parent relations, where the information concerning the states propagates from the children to parent (i.e. if the LV channel of chamber BOL1A08 is in warning state then the sector having the chamber BOL1A08 will be in warning state) while the commands are given to parents and propagate towards the children (i.e. if the user wants to turn off the HV of the barrel part of ATLAS, a "turn off HV" command to the node corresponding to ATLAS Barrel is going to be transmitted to all sectors of the barrel, then to all the chambers for each sector and finally to all the HV channels of these chambers).

Each functional part is represented in the FSM by a node, attributing a "State" of operation and a "Status" reflecting an anomaly. The nodes can be of one of the following types:

Device Unit (DU) The Device Unit typically models a specific piece of equipment (i.e. HV channel) and provides a proper interface for the PVSS II to this device. They derive their states from hardware "translated" values, read by PVSS II and convert commands received from their parents to the hardware settings or commands. A Device Unit node cannot contain any children.

Logical Unit (LU) The Logical Unit nodes cannot interface devices like DUs do, but can contain DUs as children and control them.

Control Unit (CU) The Control Units can model and control the sub-tree below them and typically model abstract or logical items. That gives them the ability to be detached from the rest of the system and function independently. They can have children of all three types but its parent -if any- can only be a Control Unit too. They derive their states from the states of their children. An FSM tree should contain at least one such node.

As mentioned earlier all the information of any node propagates from the children to the parent (from bottom to top). This includes the state and the status.

State defines the operational mode of the system (i.e. the chamber BOL1A08 is in state READY)

Status gives extra detail on how well is the system working in that particular state (i.e. the chamber can be in state READY, but the status can be a WARNING and reflect an temperature over one mezzanine card).

3.4 Operation Interfaces

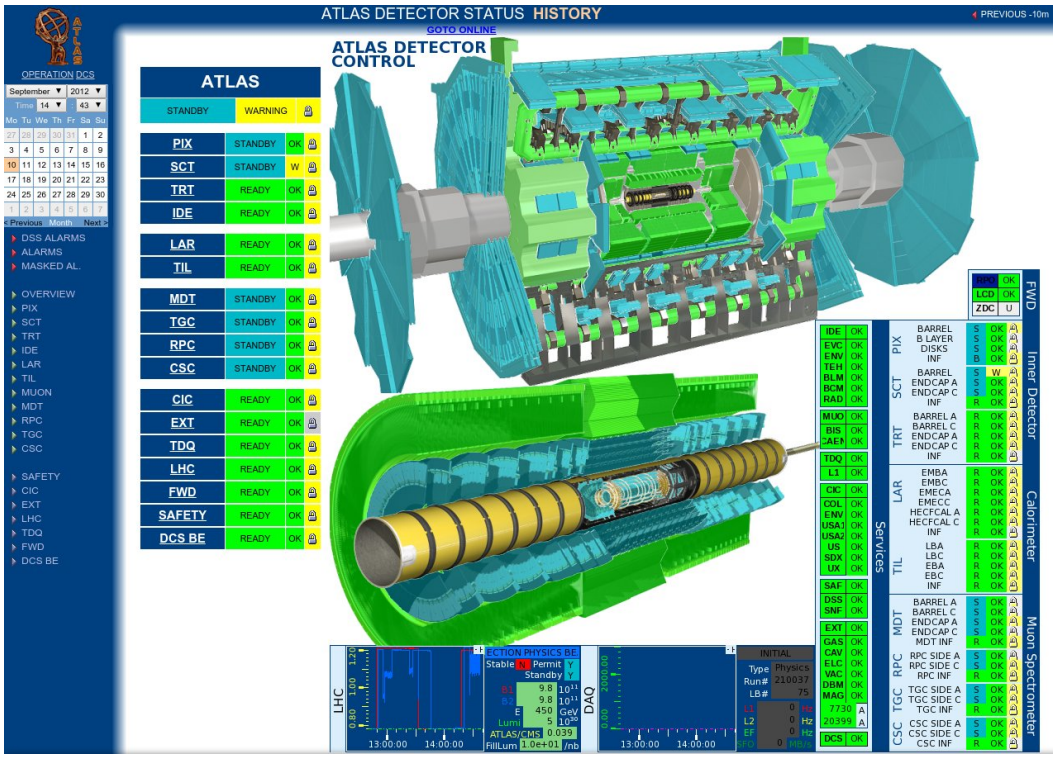

Figure 3.5: A static status monitoring is provided by web pages on a dedicated web server allowing to quickly visualize all high level FSM user interface panels world-wide and without additional load of the detector control stations. The server provides also the ability to browse on a history status of the detector.

The DCS is operated from two primary remotely accessible user interfaces: the Alarm Screen for alarm recognition and acknowledgment (see Figure 3.4). and the FSM Screen for operation of the detector Finite State Machine hierarchy (see Figure 3.6). Static status monitoring is provided by web pages on a dedicated web server allowing to quickly visualize all high-level FSM user interface panels world-wide and without additional load on the detector control stations, see Figure 3.5. These two

User Interfaces (UI) compose the shifter's tools for the complete monitor and control of the detector.

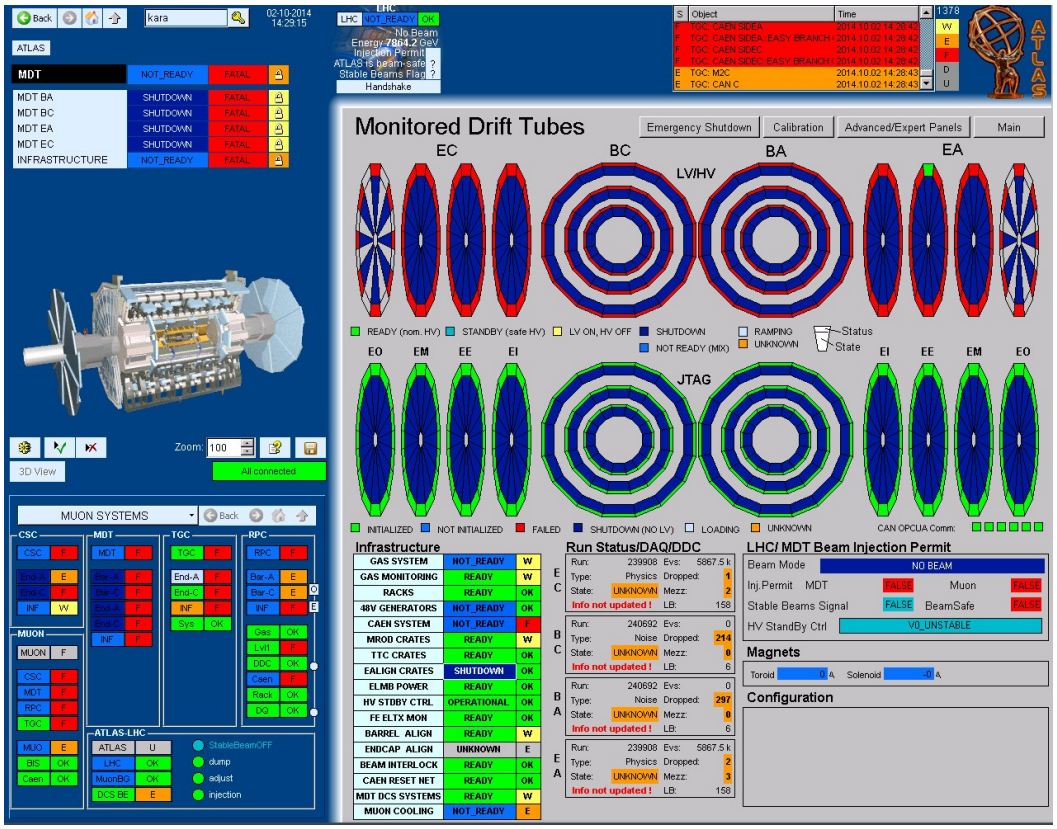

Figure 3.6: One of the shifter's main tool for controlling and monitoring the detector is the FSM panels. Each node of the FSM tree has dedicated panels that grant access to all the necessary information and available actions.

The FSM UI is divided into five different parts providing all the time the maximum available information and notifications for a variety of situations. At the right top part (see Figure 3.6) a summary of the alarm screen is located while on left top, the log-in, navigation and FSM module are located. At the center top a brief snapshot of the LHC is provided. At the bottom left part the "Secondary" module is placed and on the center-right part of the panel -occupying the largest space- the "Main" module is located.

Summary Alarm Screen In this part latest arrived alarms are displayed.

Atlas DCS log-in, navigation and FSM Here, the user can sign in and the proper role along with access rights will be granted depending on the user (shifter, expert etc). All the panels and the actions are protected via the Access Control which enables or disables usage of the FSM panel features for the users depending on the role and privileges assigned.

The navigation buttons (back, forward, home and go one level up) provide an easy way to navigate through the FSM tree.

The FSM module shows the current node in the hierarchy that the main FSM panel is represented with black box. The rest of the FSM tree is also accessible through this point. The parents of the displayed node are located on the top of the table with their corresponding structure indicating the above hierarchy, while the children are displayed in the table. For each child three information displayed here, "state", "status" and "control". The control provides information for the specific node (if it is enabled in the system and if it can be controlled by the specific panel).

LHC In this part basic information are for the LHC available. These information include collision energy, presence of beams inside LHC, stable beams and state and status of the LHC.

The Atlas DCS Main Module For each FSM node an FSM panel is displayed here where all the related information are provided concerning either the node itself or information on the children belonging to that specific node. In Figure 3.6 the main module holds the main panel for the MDT system.

The Atlas DCS Secondary module Similar to the main module, a summary of the information shown on the node's Main module. In Figure 3.6 the secondary module holds the information for the whole Muon system.

3.5 Expert tools

In order to provide an easy and fast way to massively interfere with the system, several expert tools have been created in order to control, configure and maintain the DCS. With these tools one can manipulate values of the datapoint elements, add, configure and remove "config's" or even check the integrity of the full configuration of required datapoints.

3.5.1 Archive Handling

Using the panel illustrated in Figure 3.7 various values of the system can be recorded. This is done via the archive "config". In order to enable the archiving a valid configuration must exist. This panel is divided in three parts, depending on the "level" of the archiving, grading manipulation to chambers/channels, boards and branch controllers. Corresponding options as to which elements to archive as well as smoothing configuration exists for each part. The smoothing process provides an essential way of reducing the amount of stored data without losing information since it can be applied on the value and/or the time interval of the archiving. Through that a dead-band can be defined inside of which any changes in the value will be ignored (very useful in order to include the device reading accuracy).

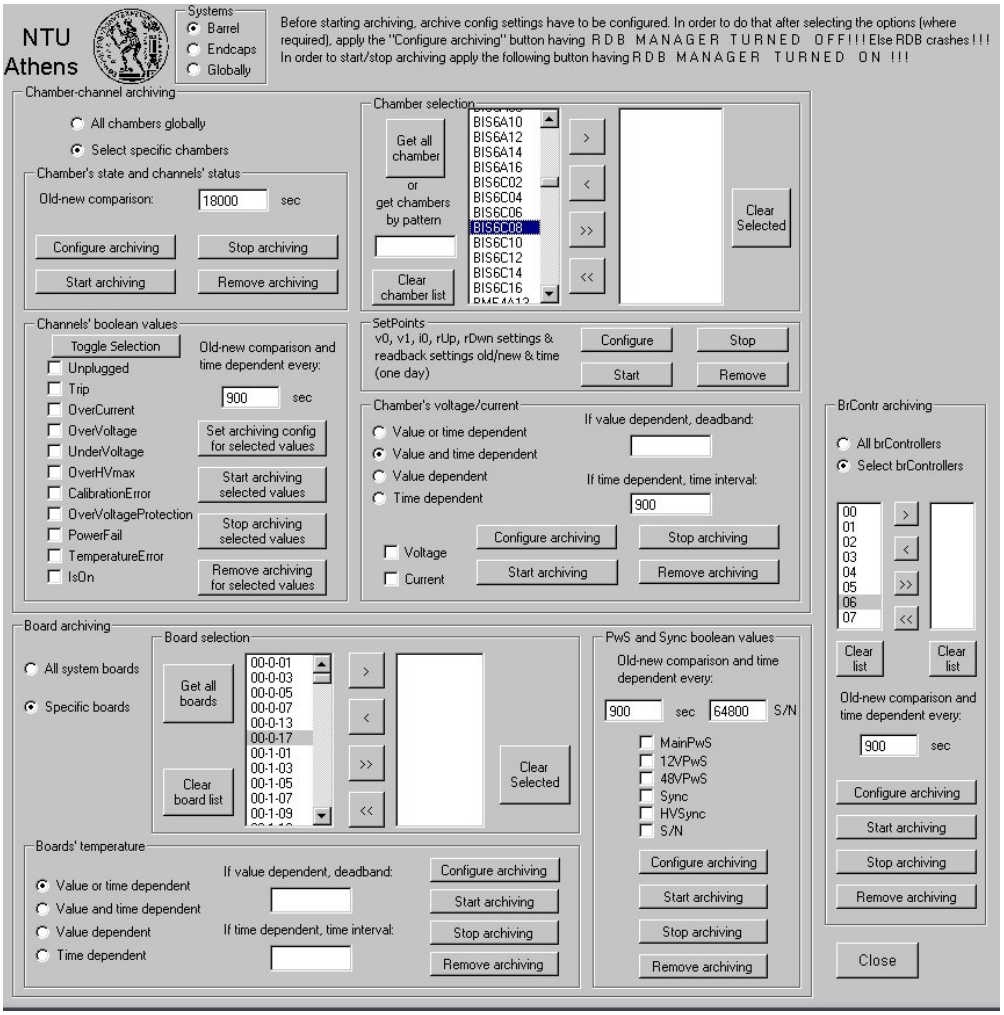

Figure 3.7: The archiving handling panel is the tool used for the configuration of the archiving of elements of the system.

3.5.2 Alarm Handling

The panel in Figure 3.8 is used to configure, activate, deactivate or delete the alarms for the PS system. At first, the part of the system under consideration is chosen from the radio button (barrel and/or end-cap regions) on the left of the panel and after this different elements (channels/chambers, boards, branch controllers, main-frames etc) can be selected. Besides the alarms set for the final power supply of the chambers there are other crucial elements to be monitored and therefore alarmed like the database connection and the overall hardware communication. Via the alarm handling panel the possibility to create summary alerts for various elements of the system is provided.

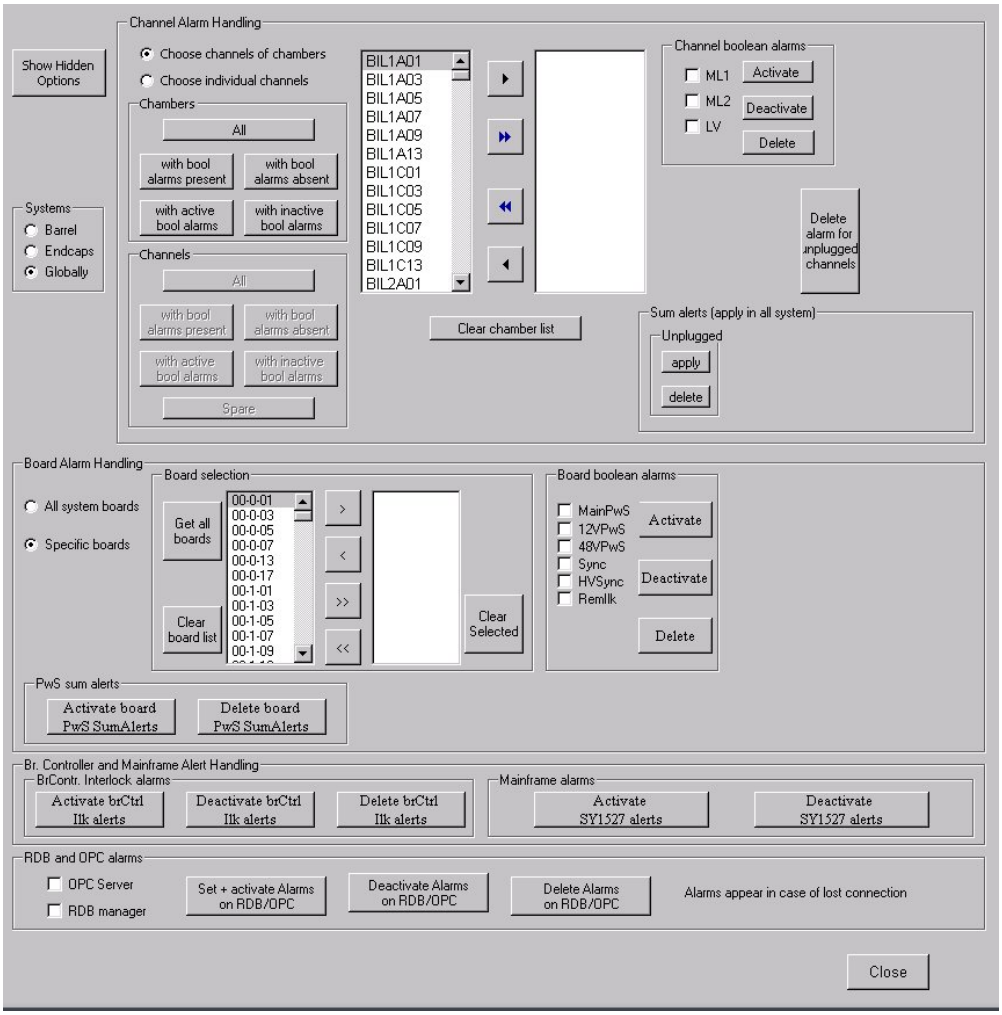

Figure 3.8: The alarm handling panel is the tool to be used for the configuration, activation and deactivation of the alarms of the PS system.

3.5.3 LV Scan (Vcc Optimum)

The LV channels are shared among pairs (most of the times) of chambers. Given the different distances of the chambers to the LV board that supplies their on board electronics, one of them (the closest) may be supplied with more voltage than required (but sure less than harmful). The extra power is transformed into heat on the electronics which in long term can be harmful. The main goal of the panel, illustrated in Figure 3.9, is to find the optimum LV v0 for each chamber.

The definition used in the concept of this panel as optimum is the lowest possible LV that is putting both chambers (that they share this channel) in a working condition. For the moment the Vcc is checked for each chamber and the scanning of one LV channel is consider as successful if all chambers sharing this channel have a Vcc value greater than the target one (by default the panel has a target value for Vcc at 3.6 V but it can be changed by the user).

Figure 3.9: The LV scan panel is the tool to be used in order to find the optimum value for the LV of the electronics of the chambers.

The LV v0 step is 0.1 V. The user can select from the top part of the panel the desired chambers that wants to be scanned. The panel will append also the chambers sharing the LV channel (noted on the table on the panel with a "+" in front of their name). The scanning procedure starts when the user pushes the "Scan Selected" button. For each step the panel has to wait almost 2.5 minutes in order to be assure that all the values for all the chambers regarding Vcc have been read and stored. This means that the whole scanning procedure can take long (up to 3 hours).

The results of the scan that displayed on the main part of the panel are:

Chamber the chamber name

LV (exist) the LV for that chamber before the scanning

Vcc (exist) the Vcc for that chamber before the scanning

Scan LV the optimum LV that the panel has found

Scan Vcc the corresponding Vcc for the optimum LV

Diff absolute value of v0 difference before and after the scan

Scan Status OK, Fail (no v0 gave Vcc > target Vcc), Off (channel is Off)

Selected check-box to select the desired chambers that have to be updated to the new optimum v0 value found by the scan

After the scan has been completed the "Set Selected" button gets enabled which will change the LV v0 setting value for all the chambers selected in the table. Additionally with the "Display Selected" button the table is populated with the already applied setting of the selected chambers without any scan performed. Moreover with the button "Save v0 txt" a text file is created in the log folder of the system and all the existing settings of the chambers selected are saved there for debug reasons. Finally a log file (.txt) with the results of the scan is created in the log folder of the system.

3.5.4 Validation Tool

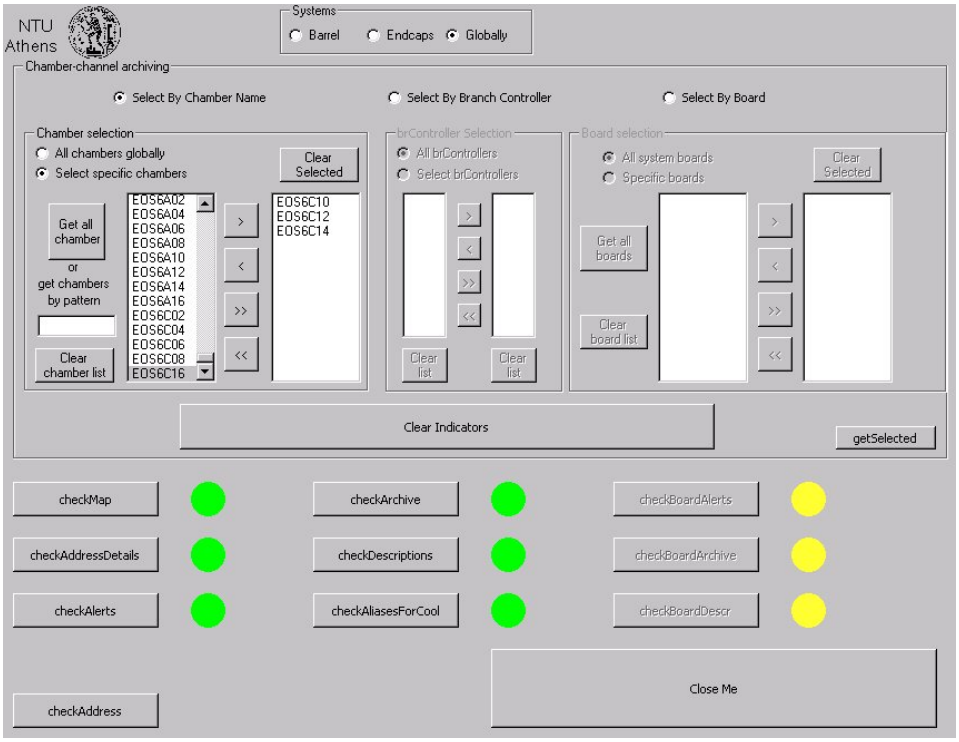

Figure 3.10: The validation panel is the tool to be used to verify that all required information for the smooth operation of the PS system on the datapoint level exists and is correct.

The panel in Figure 3.10 is used in order to verify that all required information for the smooth operation of the PS system on datapoint level exists and is correct. It can be ran either on a subgroup of elements or on a global scale (selecting all elements).

The tool checks the existence and the integrity of the following information:

Map (for chambers only) if the information about the channels (HV and LV) providing the power supply to the chamber exists.

Address details if the address details are correct and enabled, which will allow the communication and the readout of the values.

Alerts if the alarm configurations exist, if they are correct and if they are enabled.

Archive if the archive configurations exist, if they are correct and if they are enabled.

Descriptions in case of an alarm, the descriptions which will displayed in the alarm screen.

Aliases unique aliases for elements (used by via the database communication).

Chapter 4

Measurement of the J/ψ and $\psi(2S)$ Production Cross-Sections

The decay of J/ψ and $\psi(2S)$ mesons into two muons provides a striking signature for measuring these mesons in particle collider events. The production of heavy quarkonia, like J/ψ and $\psi(2S)$, at hadron colliders provides particular challenges and opportunities for insight into the theory of Quantum Chromodynamics (QCD) as its mechanisms of production operate at the boundary of the perturbative and non-perturbative regimes. Despite being among the most studied of the bound-quark systems, there is still no clear understanding of the production mechanism of quarkonium states like the J/ψ and $\psi(2S)$ that can consistently explain the production cross-section.

The data obtained by the LHC provide an unexplored test-bench for the existing theoretical models of quarkonium production in a new energy regime, at higher transverse momenta and in wider rapidity ranges than have previously been studied. The J/ψ is among the decay products of heavier particle states (such as particles containing b-quarks) and serves as a good signature for studying B-physics related processes.

This chapter presents the analysis performed to measure the production cross sections of the J/ψ and $\psi(2S)$ mesons, the J/ψ and $\psi(2S)$ non-prompt fractions, and the ratio of $\psi(2S)$ to J/ψ in prompt and non-prompt production. The definition prompt refers to the J/ψ or ψ(2S) states — hereafter called ψ to refer to either — produced from short-lived QCD sources, including feed-down from other charmonium states as long as they are also produced from short-lived sources; if the decay chain producing a ψ state includes long-lived particles such as b-hadrons, then such ψ mesons are labeled as non-prompt.

For the measurement presented here data corresponding to 11.4 fb^{-1} of pp collisions at $\sqrt{s} = 8$ TeV recorded by the ATLAS detector during 2012 data taking period were used.

4.1 Data selection

The data for this analysis were taken during LHC proton-proton collisions at a centre-of-mass energy of 8 TeV, collected between July 2012 and December 2012. The events were collected using a trigger requiring two oppositely-charged muon candidates that satisfy a fit constraining the muons to originate from a common vertex while taking into account track parameter uncertainties and applying a loose selection on the vertex fit quality, which is fully efficient for signal candidates. This trigger was unprescaled for the majority of the data taking periods. This data selection resulted to a total integrated luminosity of $11.4 \pm 0.3\text{fb}^{-1}$. It is derived, following the same methodology described in Ref. [48], from a preliminary calibration of the luminosity scale derived from beam-separation scans performed in November 2012.

Events with at least two muons, identified by the muon spectrometer and tracks reconstructed in the inner detector [4] were selected. For the momenta of interest in this analysis, measurements of the muons are degraded by multiple scattering within the ATLAS detector and so only the inner detector tracking information is considered. To ensure accurate inner detector measurements, each muon track must contain at least five silicon microstrip detector hits and at least one pixel detector hit.

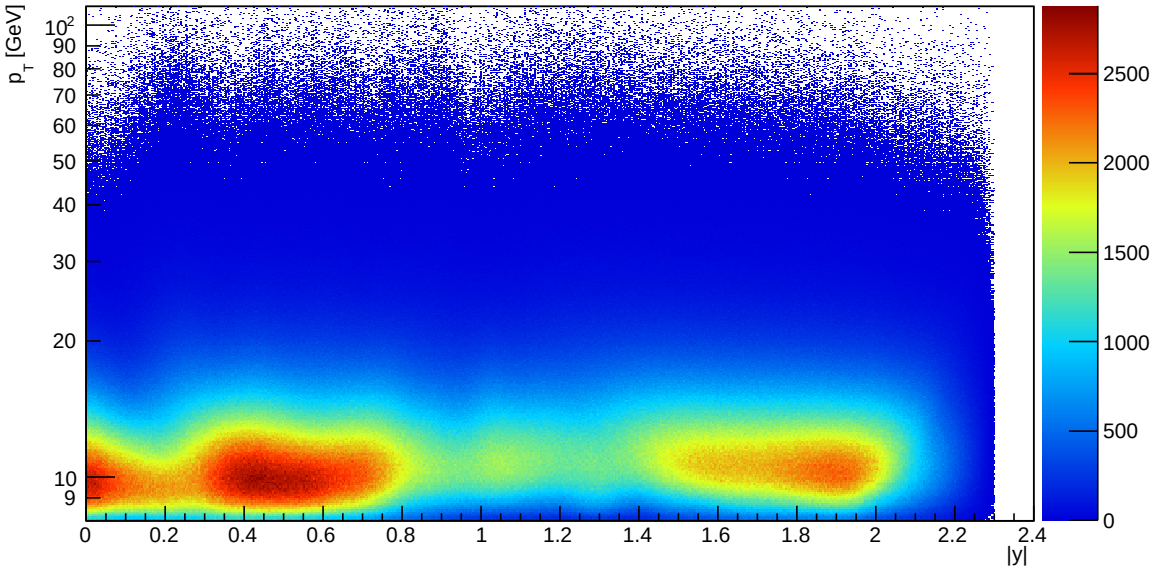

Figure 4.1: The distribution of the selected di-muon candidates, within the invariant mass range $2.6 < M(\mu\mu) < 4.0$ GeV as a function of the di-muon absolute rapidity $|y|$ versus transverse momentum p_T.

Muon pairs passing these criteria are required to have opposite-sign, with $p_T > 4$ GeV and $|\eta| < 2.3$ and a successful fit to a common vertex. Good spatial matching

$\Delta R = \sqrt{(\Delta\eta)^2 + (\Delta\phi)^2} < 0.01$ between each reconstructed muon candidate and the trigger identified candidates is required to accurately correct for trigger inefficiencies. All di-muon candidates with an invariant mass, as determined from the fit to the common vertex, within $2.6 < M(\mu\mu) < 4.0$ GeV are retained for the analysis. The dataset containers along with further details on the criteria for the data and the event selection can be found in in Appendix A, in which the muons have already passed the ATLAS Muon Combined Performance (MCP) requirements, as given in Table 4.1.

Number of pixel hits+number of crossed dead pixel sensors > 0
Number of SCT hits+number of crossed dead SCT sensors > 4
Number of pixel holes + number of SCT holes < 3
A successful TRT extension where expected (i.e. in the eta acceptance of the TRT)
An unsuccessful extension corresponds to either no TRT hit associated, or a
set of TRT hits associated as outliers. The technical recommendation is therefore:
Case 1: Let nTRThits denote the number of TRT hits on the muon track,
nTRToutliers the number of TRT outliers on the muon track
and n = nTRThits + nTRToutliers
Case 2: $0.1 < \|\eta\| < 1.9$. Require n > 5 and nTRToutliers < 0.9 n

Table 4.1: The Muon Combined Performance (MCP) requirements applied to the muon candidates

The distribution of the selected di-muon candidates is shown in Figure 4.1 as a function of the absolute rapidity and the transverse momentum.

4.1.1 The Bin Labeling

This analysis is performed in bins of the absolute rapidity and transverse momentum of the di-muon system. To facilitate the descriptions and presentation of the results, each slice of p_T and $|y|$ is assigned an index number, in the order of increasing values. Tables 4.2 and 4.3 define the correspondence between each index value and the transverse momentum and the absolute rapidity range, respectively.

Index	0	1	2	3	4	5
Range [GeV]	8.0-8.5	8.5-9.0	9.0-9.5	9.5-10.0	10.0-10.5	10.5-11.0
	6	7	8	9	10	11
	11.0-11.5	11.5-12.0	12.0-12.5	12.5-13.0	13.0-14.0	14.0-15.0
	12	13	14	15	16	17
	15.0-16.0	16.0-17.0	17.0-18.0	18.0-20.0	20.0-22.0	22.0-24.0
	18	19	20	21	22	23
	24.0-26.0	26.0-30.0	30.0-35.0	35.0-40.0	40.0-60.0	60.0-110.0

Table 4.2: The p_T bin labeling and their corresponding p_T ranges in GeV.

Index	0	1	2	3	4	5	6	7
Range	0.0-0.25	0.25-0.5	0.5-0.75	0.75-1.0	1.0-1.25	1.25-1.5	1.5-1.75	1.75-2.0

Table 4.3: The rapidity bin labeling and their corresponding ranges in absolute rapidity.

4.2 Determination of the measured quantities

The label "prompt" refers to J/ψ or $\psi(2S)$ states produced from short-lived QCD sources, including feed-down from other charmonium states as long as they are also produced from short-lived sources. If the decay chain producing a J/ψ or $\psi(2S)$ state includes long-lived particles such as b-hadrons, then such J/ψ or $\psi(2S)$ mesons are labeled as "non-prompt".

To distinguish between these prompt and non-prompt processes, the signed projection of a di-muon flight distance, $\vec{L}$, onto its transverse momentum, $\vec{p}_T^{(\mu\mu)}$, is constructed, according to the following formula:

$$L_{xy} \equiv \vec{L} \cdot \vec{p}_T^{\mu\mu} / |p_T^{(\mu\mu)}| \tag{4.1}$$

where $\vec{L}$ is the vector from the primary vertex to the di-muon decay vertex and $\vec{p}_T^{(\mu\mu)}$ is the transverse momentum vector of the di-muon.

The probability for the decay of a b-hadron as a function of proper decay time t follows an exponential distribution

$$P(t) = \frac{1}{\tau_B} exp(-t/\tau_B) \tag{4.2}$$

where τ_B is the lifetime of the b-hadron. For each decay the proper decay time can be calculated as

$$t = \frac{L}{\beta\gamma} \tag{4.3}$$

where L is the distance between the b-hadron production and decay point and $\beta\gamma$ is the Lorentz factor. Taking the projection of the decay length and momentum on the transverse plane for b-hadrons, one obtains:

$$t = \frac{L_{xy} m_B}{p_T^B} \tag{4.4}$$

In this case, L_{xy} is measured between the position of the reconstructed secondary vertex and the primary vertex of the event. The primary vertex is refitted with the two muon tracks excluded, to avoid any bias. The uncertainty on L_{xy} is calculated from the covariance matrices of the primary and the secondary vertices. The majority of the events contain only a single primary vertex. In the few that contain multiple vertices, the di-muon is assigned to a primary vertex based on the use of the tracks by the ATLAS reconstruction software. If at least one muon contributes to the construction of the primary vertex, these tracks are removed and the vertex is refitted. Since the b-hadron is not fully reconstructed, one does not know its transverse momentum. Instead the di-muon momentum is used to construct a variable called the "pseudo-proper time"

$$\tau = \frac{L_{xy} m_{(\mu\mu)}}{p_T^{(\mu\mu)}}. \tag{4.5}$$

4.2.1 Differential cross section determination

The differential di-muon prompt and non-prompt cross sections for the production of J/ψ or $\psi(2S)$ mesons are measured according to the relations:

$$\frac{d^2\sigma^p}{dp_T dy} \times Br(pp \to \psi \to \mu^+\mu^-) = \frac{N_\psi^p}{\Delta p_T \times \Delta y \times \int \mathcal{L} dt} \tag{4.6}$$

$$\frac{d^2\sigma^{np}}{dp_T dy} \times Br(bb \to \psi \to \mu^+\mu^-) = \frac{N_\psi^{np}}{\Delta p_T \times \Delta y \times \int \mathcal{L} dt} \tag{4.7}$$

where $\int \mathcal{L} dt$ is the integrated luminosity, Δp_T and Δy are the bins sizes in terms of di-muon transverse momentum and rapidity, respectively and $N_\psi^{p,np}$ is the number of observed prompt or non-prompt J/ψ or $\psi(2S)$ mesons in the bin under study, corrected for acceptance, trigger and reconstruction efficiencies. These differential cross-sections are determined separately for the J/ψ and the $\psi(2S)$ states.

Determination of the cross sections proceeds in several steps. First, a weight is determined for each selected di-muon candidate equals to the inverse of the total efficiency for each candidate. Second, a fit is performed to the distribution of weighted events using an unbinned maximum likelihood fit in the observables of di-muon invariant mass, $M(\mu\mu)$, and pseudo-proper lifetime, τ, to determine the yields of the J/ψ and ψ(2S) mesons produced in each $(p_T(\mu\mu),\ y(\mu\mu))$ bin. These yields are determined separately for prompt and non-prompt processes. Finally, the differential cross section times $\mathcal{B}(\psi \to \mu^+\mu^-)$ branching ratio is calculated for each state using the integrated luminosity and the p_T and rapidity bin widths using equations 4.6 and 4.7.

The weight, w_{tot}, for each ψ candidate includes the fraction of produced $\psi \to \mu^+\mu^-$ decays with both muons falling into the the kinematic region $p_T(\mu) > 4$ GeV

and $|\eta(\mu)| < 2.3$, the probability that a candidate falling within the acceptance passes the offline reconstruction cuts (the reconstruction efficiency, ϵ_{reco}), and the probability that a reconstructed event passes the trigger selection (the trigger efficiency, ϵ_{trig}). The weights assigned to a given candidate when calculating the cross sections are then given by:

$$w_{tot} = (\mathcal{A} \cdot \epsilon_{reco} \cdot \epsilon_{trig})^{-1} \tag{4.8}$$

4.2.2 Non-prompt fraction

The non-prompt fraction is defined to be the number (after all corrections) of non-prompt di-muon (produced via the decay of a b-hadron) relative to the number of inclusively produced di-muon:

$$f_B^{\psi} \equiv \frac{pp \to B + X \to \psi + X'}{pp \xrightarrow{Inclusive} \psi + X'} = \frac{N_{\psi}^{np}}{N_{\psi}^{np} + N_{\psi}^{p}} \tag{4.9}$$

where this fraction is determined for both J/ψ and $\psi(2S)$ mesons. The fraction has the advantage that acceptances and efficiencies are then similar for the numerator and denominator, and therefore systematic effects are reduced.

4.2.3 The ratio of $\psi(2S)$ to J/ψ production in prompt and non-prompt production

For the ratio measurements, similarly to the non-prompt fraction, the acceptance and efficiency corrections largely cancel between the numerator and denominator, thus allowing a more precise measurement. Theoretically, such ratios are also predicted with fewer uncertainties, as several dependencies, such as parton pdfs and/or b meson production spectra, also largely cancel in the ratio. The ratio is defined as:

$$R^{p,np} = \left\{ \frac{N_{\psi(2S)}}{N_{J/\psi}} \right\}^{p,np} \tag{4.10}$$

where $N_{\psi}^{p,np}$ is the number of prompt or non-prompt J/ψ , or $\psi(2S)$ mesons in a bin corrected for selection efficiencies and acceptance.

4.2.4 Muon Reconstruction Efficiency Determination

For the muon reconstruction efficiency, the corresponding maps acquired from the muon reconstruction efficiency measurement in ATLAS 2012 pp collision data [49] were used.

The map for the central values of the single muon reconstruction efficiency that was used for this analysis can be found in Figure 4.2.

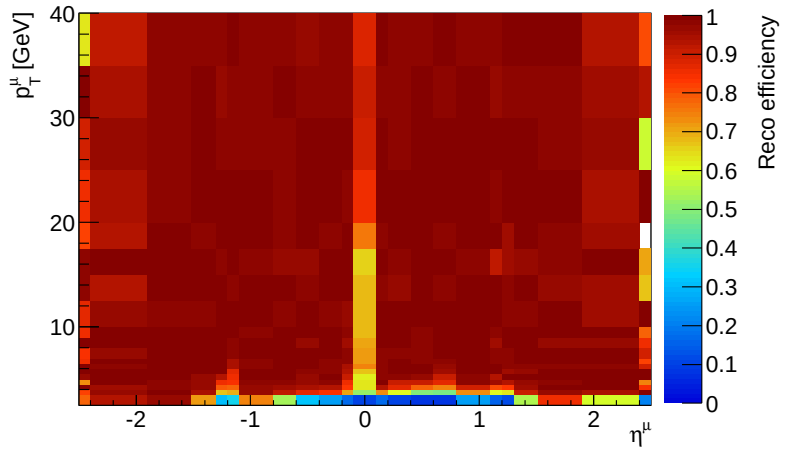

Figure 4.2: Single muon efficiency map in bins of $p_T(\mu)$ vs $q \times \eta(\mu)$.

4.2.5 Acceptance

The kinematic acceptance $\mathcal{A}(p_T, y)$ is the probability that the muons from a di-muon with transverse momentum p_T and rapidity y fall into the fiducial volume of the detector. This is calculated using generator-level simulations, applying selection criteria on the momenta and pseudo-rapidities of the simulated muons to emulate the detector geometry.

Unfortunately, the spin-alignment (and therefore the angular distribution) of the di-muon system may vary depending on the mechanism of production. As the acceptance itself depends on angular distributions of the muons from the di-muon decay, a complete measurement of the cross section without any uncertainty due to this angular dependence cannot take place. In this analysis, the measurement is performed under the assumption of a nominal spin alignment scenario, and these results are then considered under various additional spin-alignment hypotheses. Theoretical predictions for the inclusive cross-sections generally come with their own specific prediction of the spin-alignment of J/ψ and $\psi(2S)$ mesons. The experimental results here can be recast in terms of these specific spin-alignment assumptions, given the central result and the variation under different hypotheses presented in this chapter.

The acceptance $\mathcal{A}$ depends on five independent variables (the two muon momenta constrained by the $M(\mu\mu)$ mass condition), chosen as p_T , $|y|$, azimuthal angle ϕ of di-muon in the lab frame, and two angles characterising the di-muon decay into two muons in its decay frame, $\theta^\star$ and $\phi^\star$. The $\theta^\star$ is the angle between the direction of the positive muon momentum in the di-muon decay frame, and the momentum of di-muon itself in the lab frame, while $\phi^\star$ is defined as the angle between the di-muon production and decay planes in the lab frame. The distributions in $\theta^\star$ and $\phi^\star$ are different for various possible spin alignment scenarios of di-muon The coefficients $\lambda_\theta, \lambda_\phi, \lambda_{\theta\phi}$ in

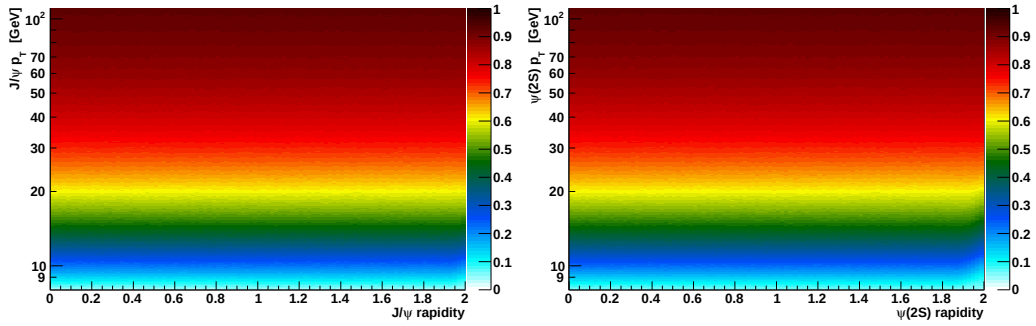

(a) (b)

Figure 4.3: The acceptance maps for the J/ψ (a) and $\psi(2S)$ (b) mesons, produced as a function of the di-muon p_T and rapidity assuming the central ("FLAT") spin-alignment hypothesis, using the muon selection criteria: $p_T(\mu) > 4$ GeV and $|\eta(\mu)| < 2.3$.

$$\frac{d^2N}{d\cos\theta^\star d\phi^\star} \propto 1 + \lambda_\theta \cos^2\theta^\star + \lambda_\phi \sin^2\theta^\star \cos 2\phi^\star + \lambda_{\theta\phi} \sin 2\theta^\star \cos\phi^\star \tag{4.11}$$

are related to the spin density matrix elements of the di-muon spin wave function. The same technique has been used also in other measurements like [50–52].

A large number of possible combinations of the coefficients $\lambda_\theta, \lambda_\phi, \lambda_{\theta\phi}$ have been studied, and seven extreme cases have been identified, using which one can recalculate the cross section for any combination of the three λ parameters in equation 4.11. These are:

1. Isotropic distribution, independent of $\theta^\star$ and $\phi^\star$ i.e. $\lambda_\theta = \lambda_\phi = \lambda_{\theta\phi} = 0$ labeled as "FLAT". This is used as the main (central) hypothesis.

2. Longitudinally aligned di-muon decays, yielding $\lambda_\theta = -1$ $\lambda_\phi = \lambda_{\theta\phi} = 0$ labeled as "LONG".

3. Transversely aligned di-muon decays, yielding $\lambda_\theta = +1$ $\lambda_\phi = \lambda_{\theta\phi} = 0$ labeled as "trp0".

4. Transversely aligned di-muon decays, yielding $\lambda_\theta = +1$ $\lambda_\phi = +1$ $\lambda_{\theta\phi} = 0$ labeled as "trpP".

5. Transversely aligned di-muon decays, yielding $\lambda_\theta = +1$ $\lambda_\phi = -1$ $\lambda_{\theta\phi} = 0$ labeled as "trpM".

6. Positive off-plane term, $\lambda_\theta = 0$ $\lambda_\phi = 0$ $\lambda_{\theta\phi} = +0.5$ labeled as "OffP".

7. Negative off-plane term, $\lambda_\theta = 0$ $\lambda_\phi = 0$ $\lambda_{\theta\phi} = -0.5$ labeled as "OffN".

For each of the two mass-points (corresponding to the J/ψ and $\psi(2S)$ masses) 2D maps are produced as a function of di-muon p_T and $|y|$ for all the spin-alignment hypotheses.

The acceptance maps are defined within the range $8 < p_T(\mu\mu) < 110$ GeV and $0 < |y(\mu\mu)| < 2.0$, corresponding to the data considered in the analysis. As the reconstructed candidates in the data will cover a range of masses, corresponding to the detector resolution of the signal mesons and non-signal background contributions, the acceptance for a given candidate is interpolated linearly as a function of the reconstructed mass $M(\mu\mu)$ using the J/ψ and $\psi(2S)$ known masses and acceptance maps to define the linear interpolation.

Figure 4.3 shows the acceptance maps for the "FLAT" hypothesis for the J/ψ and $\psi(2S)$ mesons. Each map is defined by 100 slices in absolute rapidity and 4400 in p_T, using 200k trials for each point. The uncertainty in the statistical precision of each point is negligible. The alternate hypotheses for J/ψ and $\psi(2S)$ are shown in Figures 4.4 and 4.5 respectively.

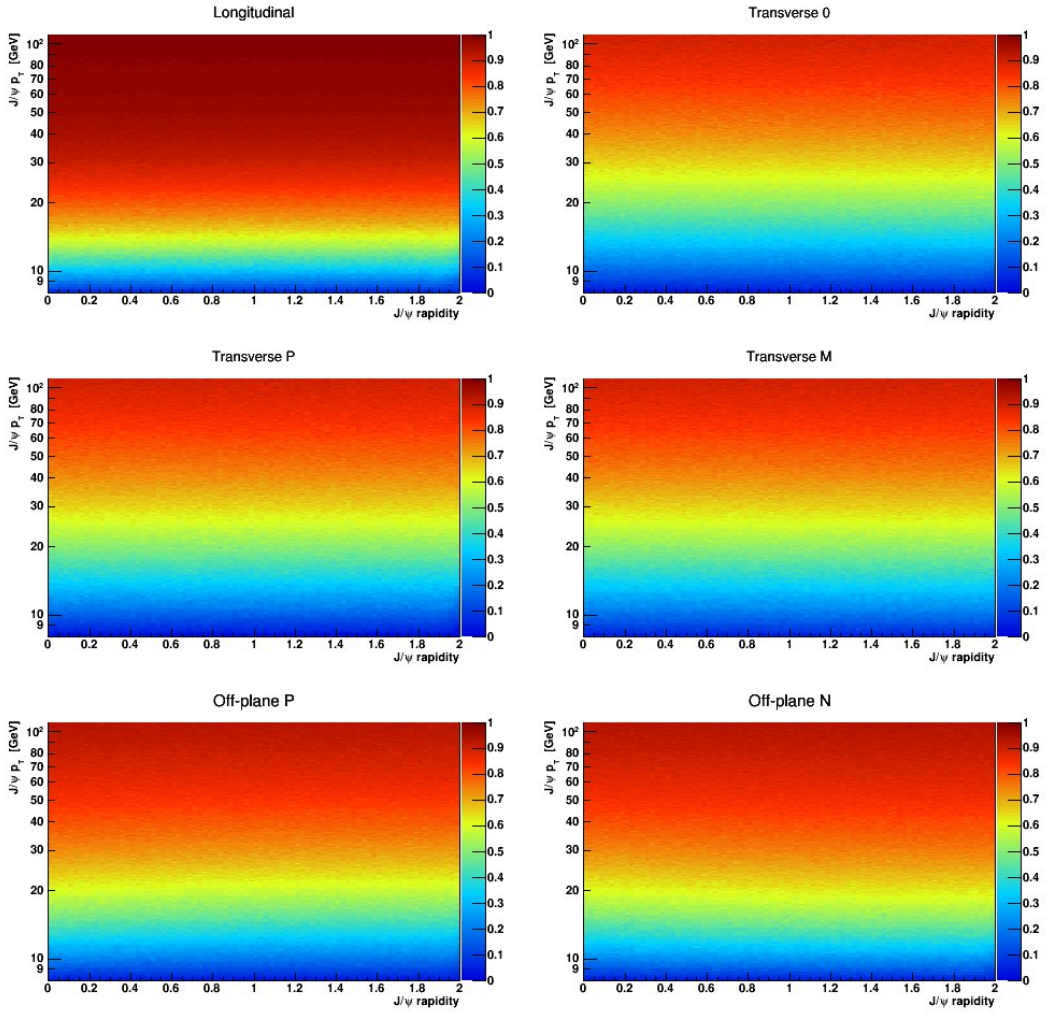

Figure 4.4: Alternative spin-alignment hypotheses for J/ψ : Longitudinally, transverse 0, transverse P, transverse M, off-plane P, off-plane N, from left to right, top to bottom, respectively.

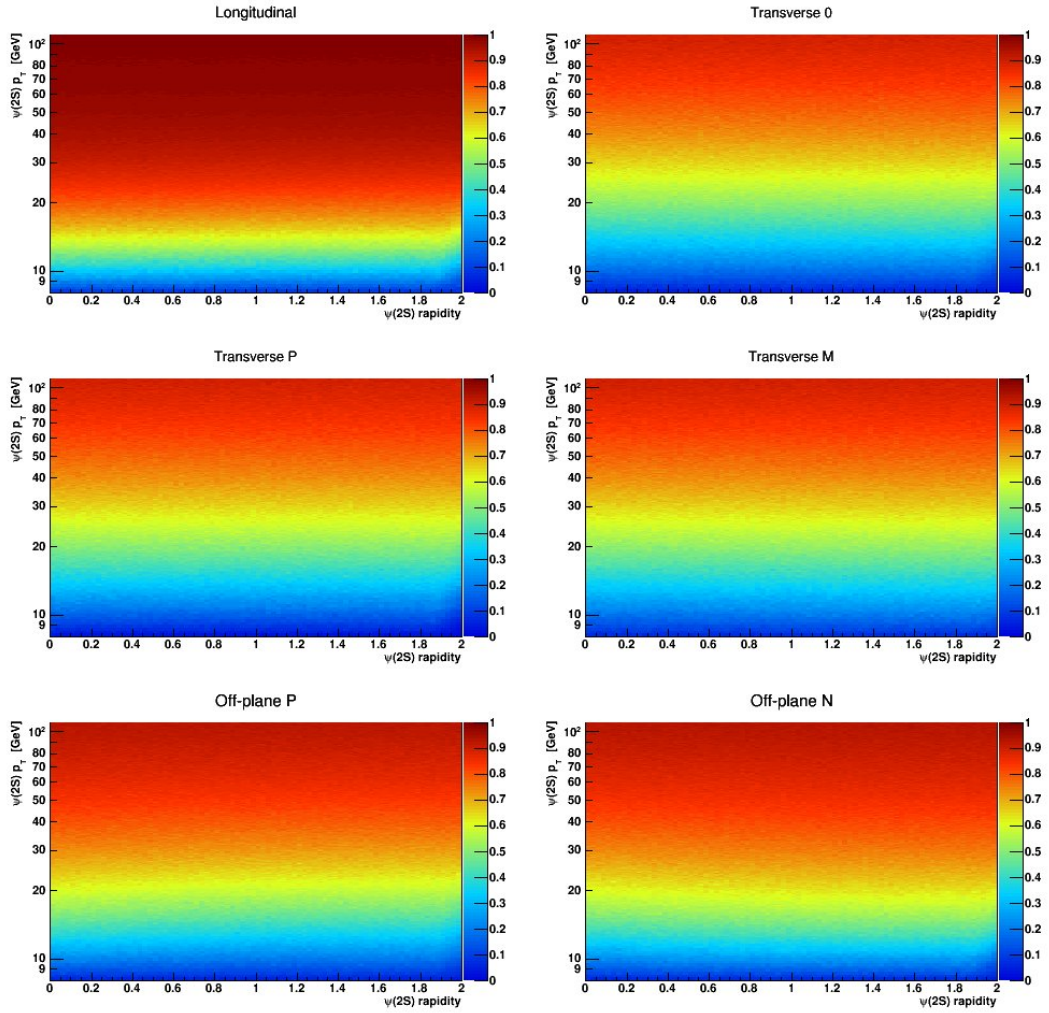

Figure 4.5: Alternative spin-alignment hypotheses for $\psi(2S)$: Longitudinally, transverse 0, transverse P, transverse M, off-plane P, off-plane N, from left to right, top to bottom, respectively.

4.2.6 Trigger Efficiency

The trigger efficiency was measured for Runs C6 through Runs L of the 2012 data for analyses using the EF_2mu4T_L2StarB dimuon triggers.

There are two parts to these correction maps. The first part represents the trigger efficiency for a single muon in bins of $p_T(\mu)$ vs $q \times \eta(\mu)$. For the di-muon systems there is a second correction, to account for efficiency losses due to: overlapping RoIs, vertex quality cuts, and opposite sign requirements. This correction is performed in three rapidity bins. The correction is a function of $\Delta R(\mu\mu)$ in the first two rapidity bins and function of $\Delta R(\mu\mu)$ and $|y(J/\psi)|$ in the last bin.

The map for the central values of the single muon trigger efficiency that was used for this analysis can be found in Figure 4.6.

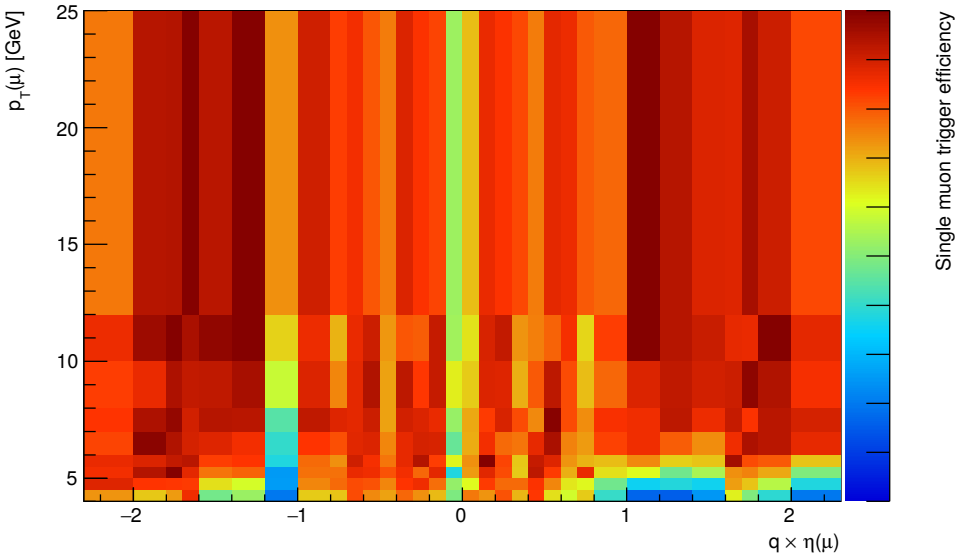

Figure 4.6: The trigger efficiency map for a single muon with $p_T > 4$ GeV in bins of $p_T(\mu)$ vs $q \times \eta(\mu)$.

4.2.7 Weight distributions

The preceding sections describe the correction terms that are applied to each candidate in the selected sample. In this section, the effects of these weights are described in terms of the analysis bins, which are shown as a function of the ψ p_T and $|y|$. A summary of the mean weight and its RMS as a function p_T and $|y|$ is presented in figures 4.7, 4.8 and 4.9, for acceptance, muon reconstruction, and trigger weight distributions, respectively. These figures are for illustrative purposes only, as each candidate had individual weights applied, not an average weight as shown here. The definition of the ranges defined by each bin is given in section 4.1.1.

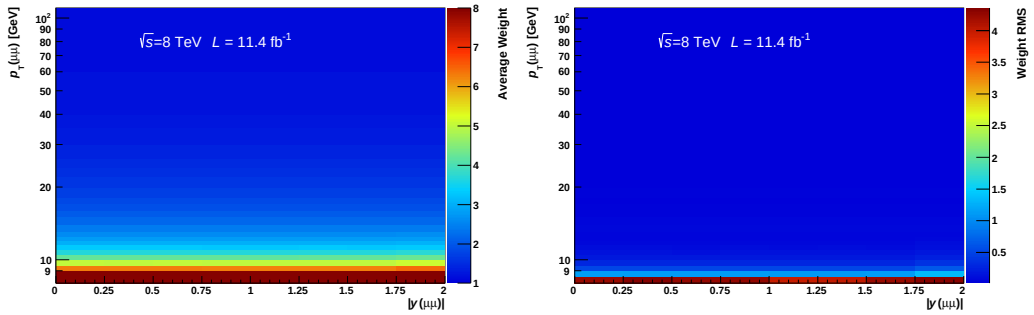

(a) (b)

Figure 4.7: (a) the mean weight as a function of p_T and $|y|$ from the acceptance correction. The mean is calculated using the weight distribution for all candidates that pass the selections and fall into a particular bin. (b) the value of the RMS for the corresponding distributions.

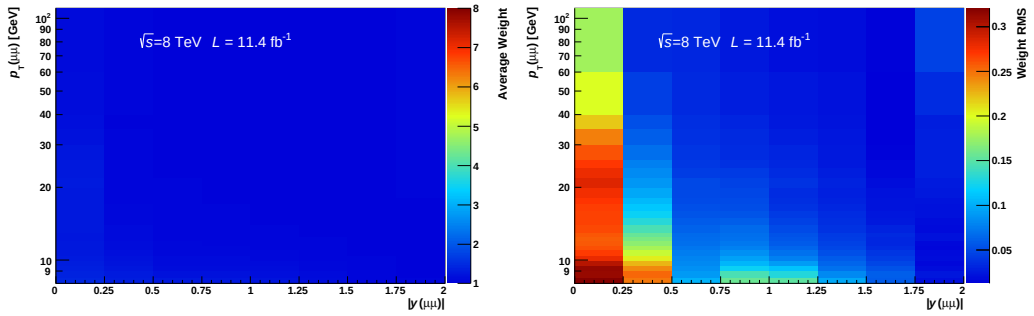

(a) (b)

Figure 4.8: (a) the mean weight as a function of p_T and $|y|$ from the muon reconstruction correction. The mean is calculated using the weight distribution for all candidates that pass the selections and fall into a particular bin. (b) the value of the RMS for the corresponding distributions.

Finally, the yields of all candidates in each analysis bin, before and after applying the combination of all mentioned above weight corrections are summarized in Figure 4.10. Again, this is only for illustration purposes since each candidate had individual weights applied in for the fitting procedure.

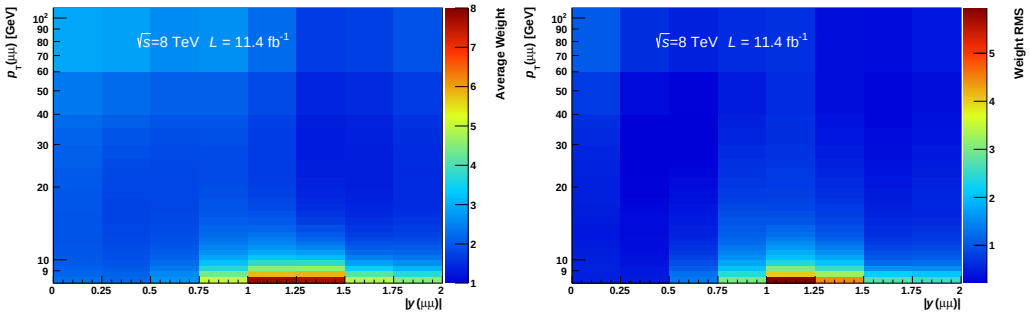

(a) (b)

Figure 4.9: (a) the mean weight as a function of p_T and $|y|$ from the trigger reconstruction correction. The mean is calculated using the weight distribution for all candidates that pass the selections and fall into a particular bin. (b) the value of the RMS for the corresponding distributions.

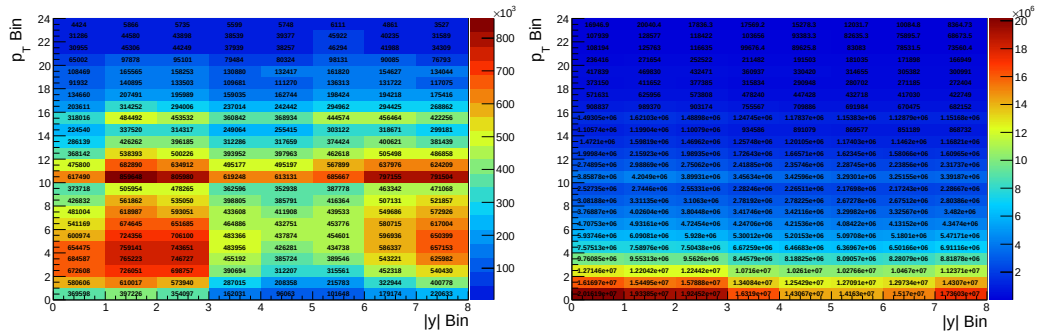

(a) (b)

Figure 4.10: (a) the number of di-muon candidates without any weight applied. (b) the corrected yield after the weights have been applied.

4.3 Fitting Procedure

For each p_T and $|y|$ bin a 2-dimensional weighted unbinned maximum likelihood fit (henceforth referred to as the "fit"), is performed in the dimensions of di-muon invariant mass and pseudo-proper lifetime. Di-muon candidates must be within the ranges: $2.6 < M(\mu\mu) < 4.0$ GeV and -4 $< \tau(\mu\mu) <$ 14 ps^{-1}. From the fitted parameters, the quantities of interest, such as yields, non-prompt fractions and ratios of $\psi(2S)$ to J/ψ production are calculated. The fit is performed using the ROOT framework and RooFit (version 3.60).

The weighted events (as described in the previous sections) are fitted using the Probability Density Function (PDF):

$$PDF(m,\tau) = \sum_{i=1}^{7} \oplus f_i(m) \ \cdot h_i(\tau) \otimes g_i(\tau) \tag{4.12}$$

where $\otimes$ implies a convolution and the individual components are given in table 4.4

i	Sig / Bkg	Source	$f_i(m)$	$h_i(\tau)$
1	J/ψ	Prompt	$CB_1(m) \oplus G_1(m)$	$\delta(\tau)$
2	J/ψ	Non-Prompt	$CB_1(m) \oplus G_1(m)$	$E_1(\tau)$
3	$\psi(2S)$	Prompt	$CB_2(m) \oplus G_2(m)$	$\delta(\tau)$
4	$\psi(2S)$	Non-Prompt	$CB_2(m) \oplus G_2(m)$	$E_2(\tau)$
5	Bkg	Prompt	$F(m)$	$\delta(\tau)$
6	Bkg	Non-Prompt	$P1(m)$	$E_3(\tau)$
7	Bkg	Non-Prompt	$E_4(m)$	$E_5(\|\tau\|)$

Table 4.4: Fit model PDF. The definition of each term in described in the text. The symbols $\oplus$ and $\otimes$ are used to define a normalized weighted average and convolution, respectively. The subscripts on each term refer to different PDF terms, which may or may not share some common parameters with other terms.

The component PDF terms are defined below:

- **CB** Crystal Ball (Implemented as a RooCBShape)
- **G** Gauss (RooGaussian)
- **F** Flat
- **P1** First order polynomial
- **E** Exponential
- δ delta function
- Resolution function $g(\tau)$ is a double Gaussian

In order to make the fitting procedure robust and stabilize the fit model, a reduction of the free parameters was needed. To reduce the number of free parameters, a number of component terms share common parameters, or use a scaling (free) parameter. The details of the fit model are described below.

The signal mass shapes are described by the sum of a Crystal Ball shape (CB) [53] and Gaussian. For each of the J/ψ and $\psi(2S)$ the CB and Gaussian share a common mean. The width term in the CB function is equal to the Gaussian sigma times a free scaling term. This scaling term is common between the J/ψ and $\psi(2S)$. The CB α and n parameters are fixed and variations are considered as part of the fit model systematic uncertainties. The width of the Guassian of the $\psi(2S)$ is set to the width of the J/ψ multiplied by a free parameter scaling term. The relative fraction of CB and Gaussian is free, but common between the J/ψ and $\psi(2S)$.

The signal lifetime shapes are described by an exponential (for positive τ only) convoluted with a double Gaussian (describing the lifetime resolution) for the non-prompt component and the same Gaussians to describe the prompt contributions. The resolution Gaussians has fixed means at τ = 0 and free widths. The lifetime of the J/ψ is free and the $\psi(2S)$ lifetime is scaled by a free parameter from the J/ψ lifetime.

The background contributions are described by prompt, non-prompt and a double-sided exponential (convoluted with Gaussian) describing candidates of mis-reconstructed or non-coherent di-muon pairs. The same resolution Gaussian is used to describe also the background, as for the signal. For the non-resonant mass parameterizations, the non-prompt contribution is modeled by a first order polynomial. The prompt mass contribution follows a flat distribution and the double-sided background uses an exponential. Variations of this fit model are considered within the systematics uncertainties.

The important quantities extracted from the fit are: the fraction of the signal; the fraction of the signal that is prompt; the fraction of the prompt signal that is $\psi(2S)$; and the fraction of the non-prompt signal that is $\psi(2S)$. From these parameters (and their covariance matrix) and the weighted sum of entries, all measured values are extracted. In total there are 22 free parameters in the fit.

4.4 Fitting Results

In total, 172 fits are performed across the range of p_T (from 8 up to 110 GeV) and absolute rapidity (from 0 up to 2) excluding the area where p_T is less than 10 GeV and simultaneously absolute rapidity is greater than 0.75. This exclusion is done due to a steeply changing low trigger efficiency and correlation effects at that area, which lead to artificial fluctuations across rapidity of the measured cross sections.

From each set of fitted parameters, the measured quantities are extracted and their results presented in the sections 4.5, 4.6 and 4.7. To visualize the results, the data can be projected into each of the mass and pseudo-proper lifetime dimensions and the fitted curves projected onto the single dimensions. Three randomly selected bins can be seen in Figure 4.11.

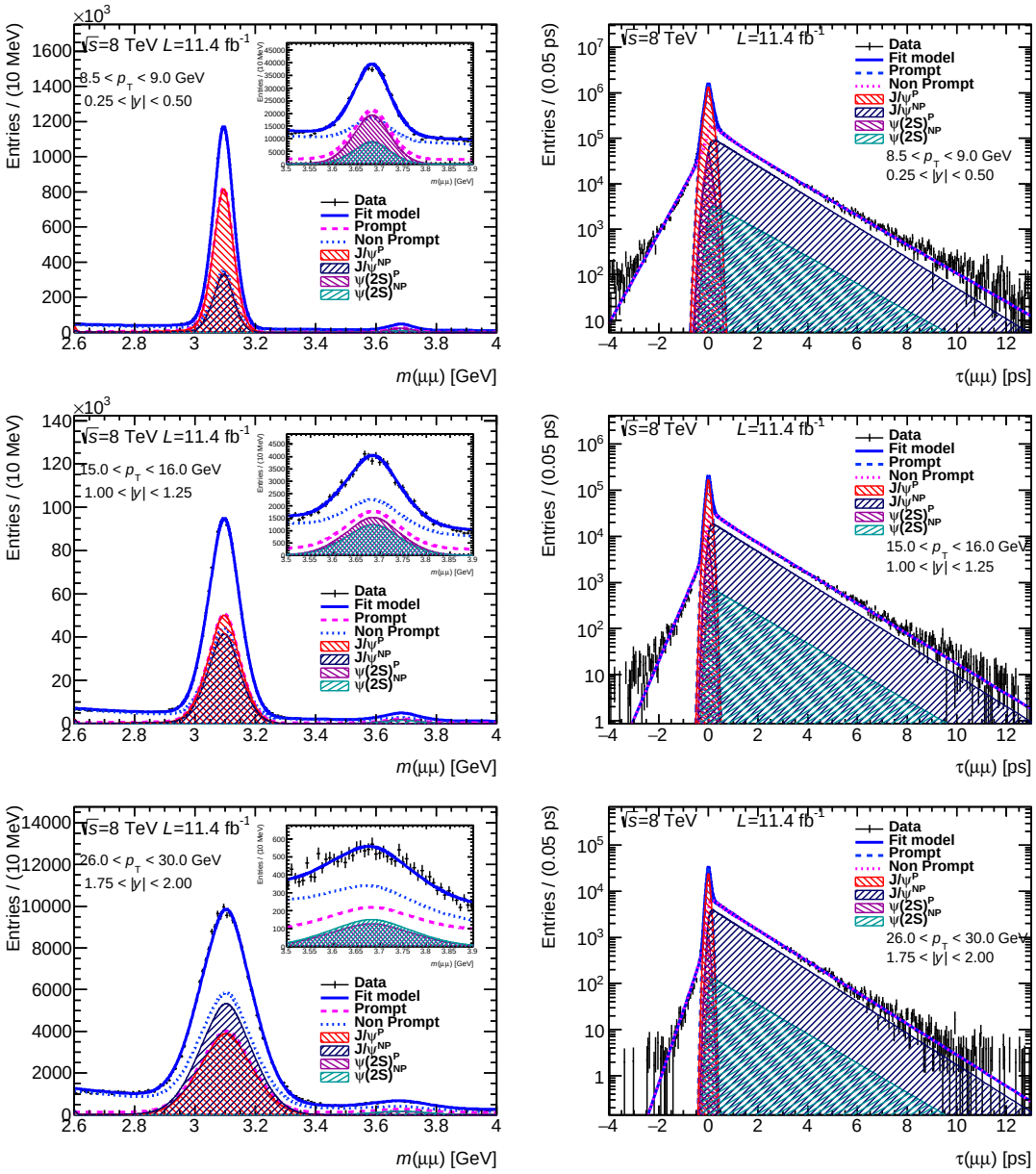

Figure 4.11: The fit results can be seen from the projection of the likelihood on the p_T and τ dimensions for low p_T and low absolute rapidity in the first row, middle p_T and middle absolute rapidity in the second row and high p_T and high absolute rapidity in the last row. The corresponding p_T and absolute rapidity ranges are specified on the plots. The projection of the data and fit results for the invariant mass is shown on the left column and the projection as a function of the pseudo-proper lifetime is shown on the right column.

4.5 Differential Cross Section Results

The prompt and non-prompt differential J/ψ and $\psi(2S)$ cross sections are determined in bins of p_T and $|y|$, as described in section 4.1.1 and the results are presented in figures 4.12, 4.13, 4.14 and 4.15 for different rapidities as a function of p_T.Additionally, results are also presented for different slices of p_T, as a function of rapidity, as shown in figures 4.16 – 4.19. Full tables of all the respective cross section values are given in appendix B.1.3.

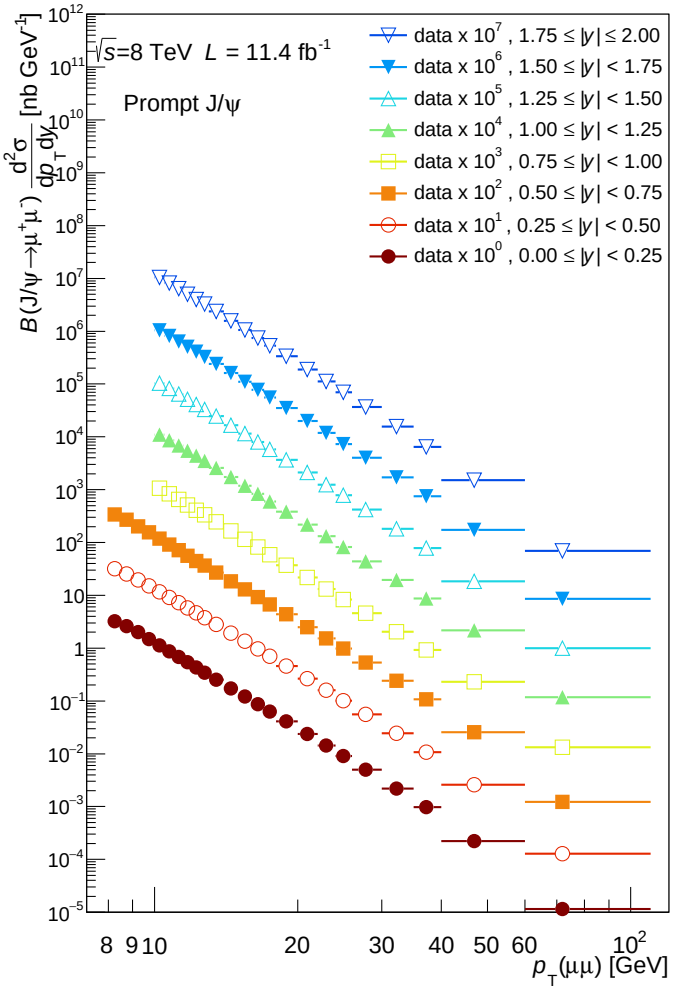

Figure 4.12: The differential J/ψ prompt cross-section as a function of $p_T(\mu\mu)$ for each of the slices of rapidity . For each increasing rapidity slice, a scaling factor of $\times$ 10 is applied to the plotted points. The center of each bin on the horizontal axis represents the mean of the weighted p_T distribution. The horizontal error-bars represent the range of p_T for the bin and the vertical error-bar covers the statistical and the systematic uncertainty (with the same multiplicative scaling applied).

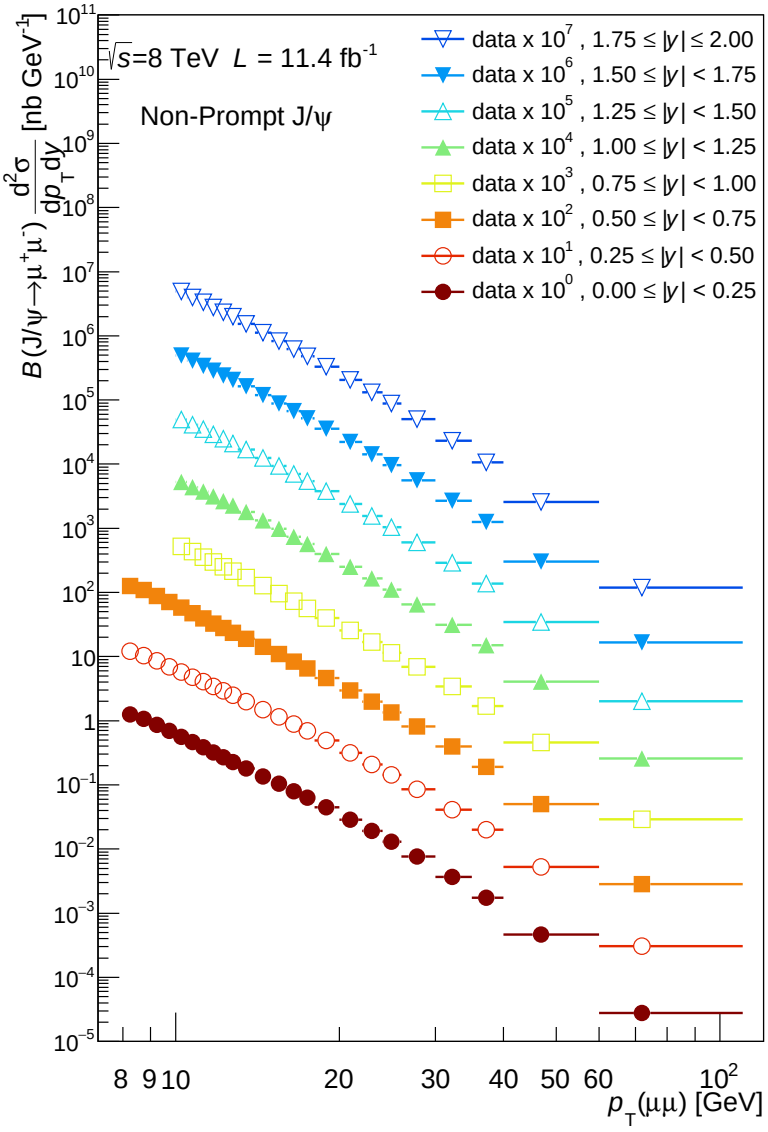

Figure 4.13: The differential J/ψ non-prompt cross-section as a function of $p_T(\mu\mu)$ for each of the slices of rapidity along with the relevant FONLL prediction. For each increasing rapidity slice, a scaling factor of $\times$ 10 is applied to the plotted points. The center of each bin on the horizontal axis represents the mean of the weighted p_T distribution. The horizontal error-bars represent the range of p_T for the bin and the vertical error-bar covers the statistical and the systematic uncertainty (with the same multiplicative scaling applied).

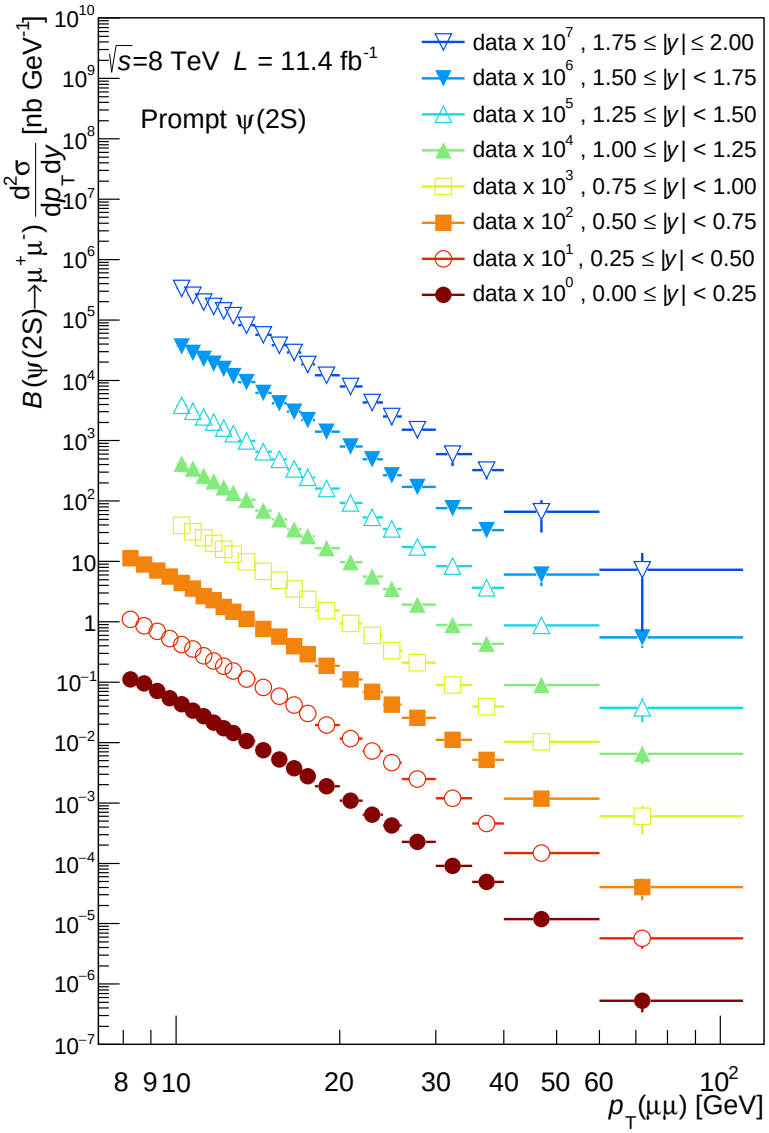

Figure 4.14: The differential $\psi(2S)$ prompt cross-section as a function of $p_T(\mu\mu)$ for each of the slices of rapidity . For each increasing rapidity slice, a scaling factor of $\times$ 10 is applied to the plotted points. The center of each bin on the horizontal axis represents the mean of the weighted p_T distribution. The horizontal error-bars represent the range of p_T for the bin and the vertical error-bar covers the statistical and the systematic uncertainty (with the same multiplicative scaling applied).

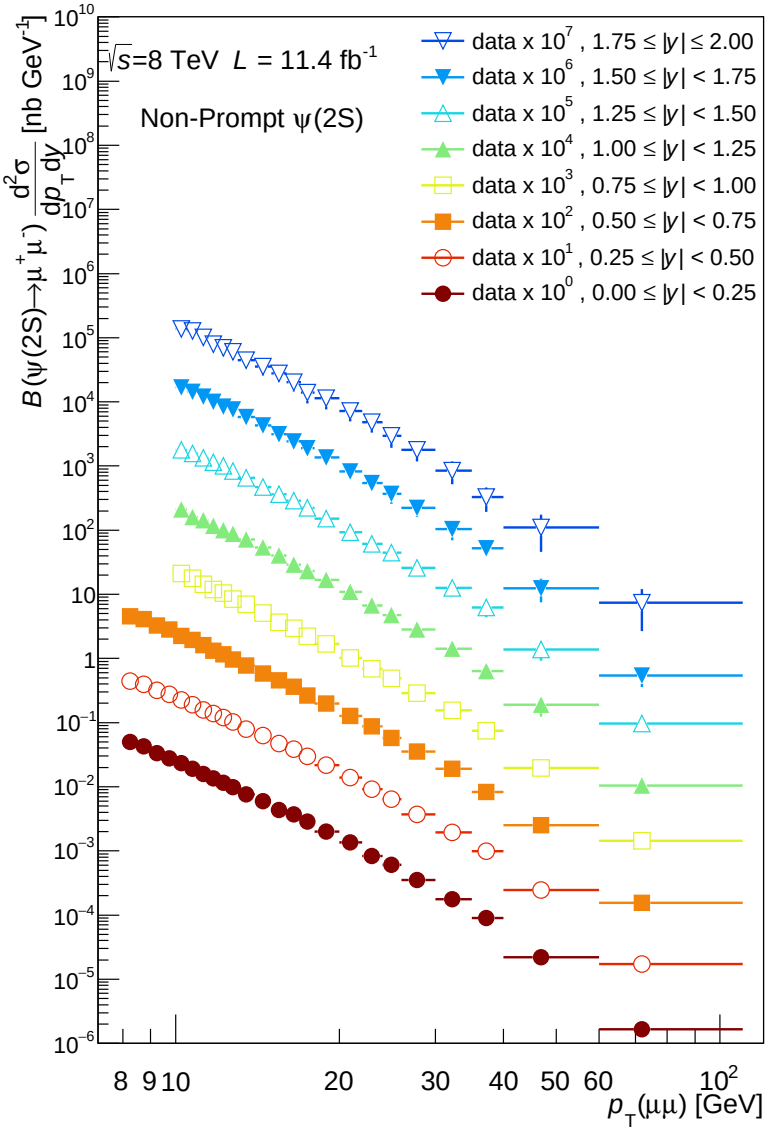

Figure 4.15: The differential $\psi(2S)$ non-prompt cross-section as a function of $p_T(\mu\mu)$ for each of the slices of rapidity . For each increasing rapidity slice, a scaling factor of $\times$ 10 is applied to the plotted points. The center of each bin on the horizontal axis represents the mean of the weighted p_T distribution. The horizontal error-bars represent the range of p_T for the bin and the vertical error-bar covers the statistical and the systematic uncertainty (with the same multiplicative scaling applied).

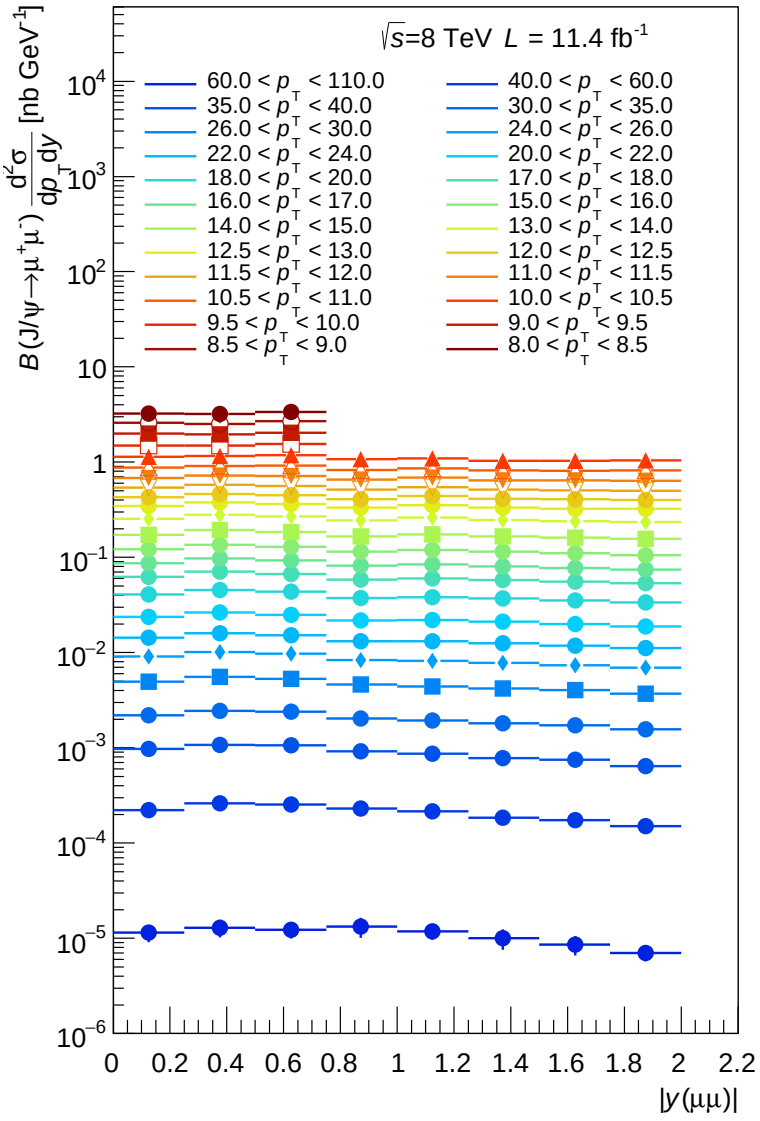

Figure 4.16: The differential J/ψ prompt cross-section as a function of $|y(\mu\mu)|$ for each of the slices of p_T. The center of each bin on the horizontal axis represents the mean of the weighted $|y|$ distribution. The horizontal error-bars represent the range of $|y|$ for the bin and the vertical error-bar covers the statistical and the systematic uncertainty (with the same multiplicative scaling applied).

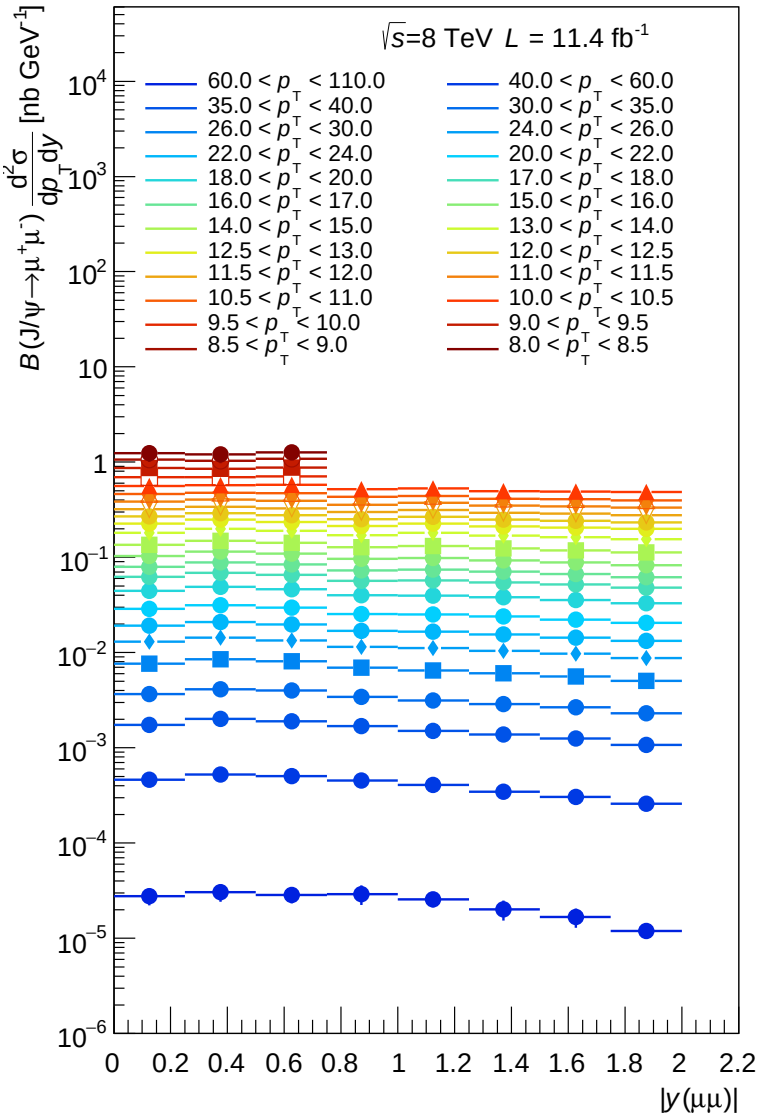

Figure 4.17: The differential J/ψ non-prompt cross-section as a function of $|y(\mu\mu)|$ for each of the slices of p_T. The center of each bin on the horizontal axis represents the mean of the weighted $|y|$ distribution. The horizontal error-bars represent the range of $|y|$ for the bin and the vertical error-bar covers the statistical and the systematic uncertainty (with the same multiplicative scaling applied).

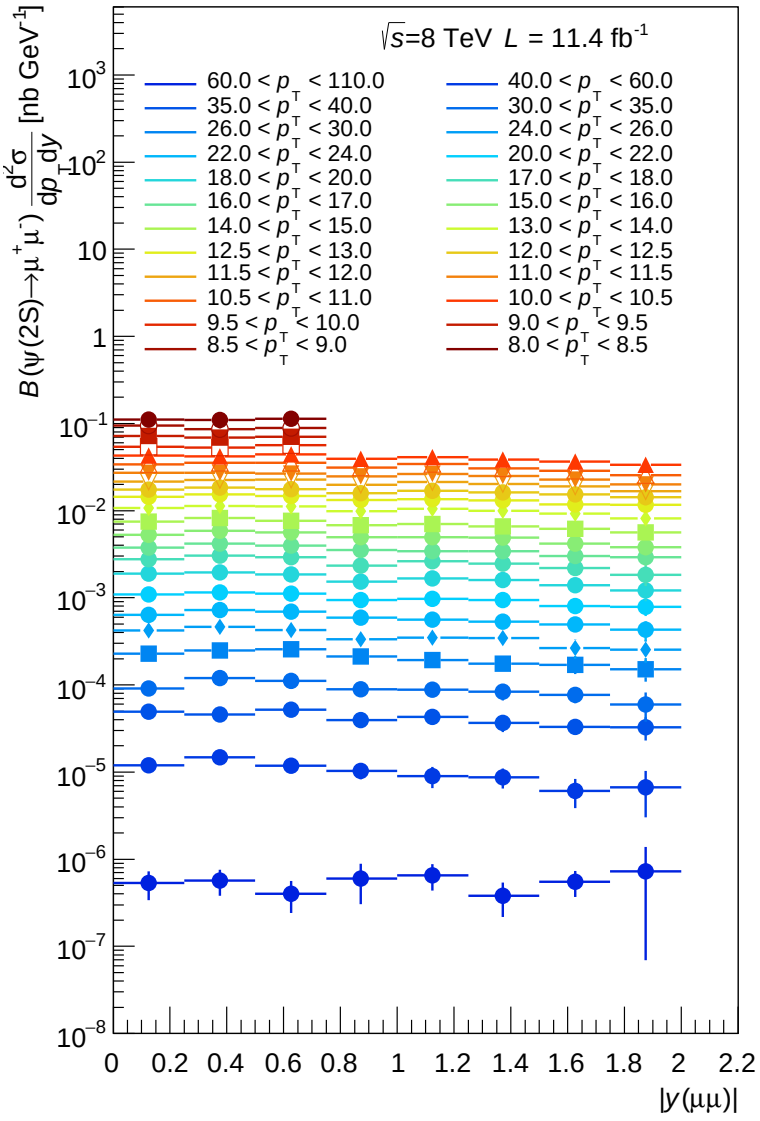

Figure 4.18: The differential $\psi(2S)$ prompt cross-section as a function of $|y(\mu\mu)|$ for each of the slices of p_T. The center of each bin on the horizontal axis represents the mean of the weighted $|y|$ distribution. The horizontal error-bars represent the range of $|y|$ for the bin and the vertical error-bar covers the statistical and the systematic uncertainty (with the same multiplicative scaling applied).

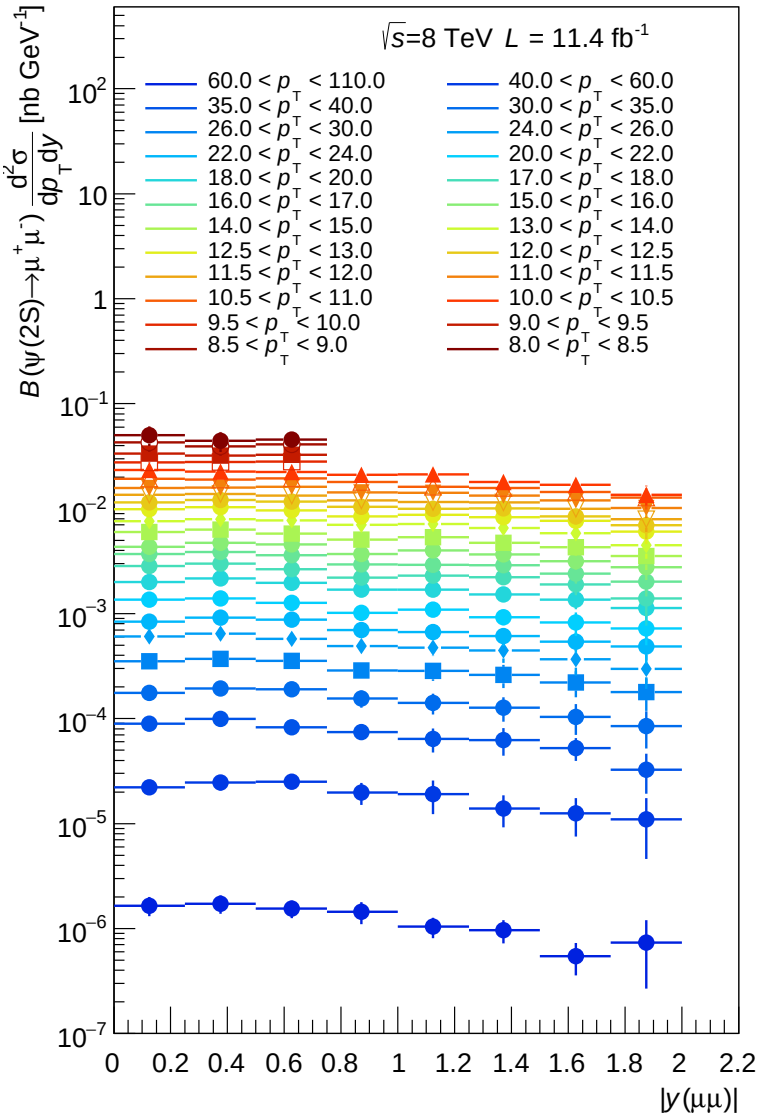

Figure 4.19: The differential $\psi(2S)$ non-prompt cross-section as a function of $|y(\mu\mu)|$ for each of the slices of p_T. The center of each bin on the horizontal axis represents the mean of the weighted $|y|$ distribution. The horizontal error-bars represent the range of $|y|$ for the bin and the vertical error-bar covers the statistical and the systematic uncertainty (with the same multiplicative scaling applied).

4.6 Non-Prompt Fraction Results

The results of the fits for the non-prompt fractions of J/ψ and $\psi(2S)$), are presented as a function of p_T for slices of rapidity in figures 4.20 and 4.21, respectively, whereas in figures 4.22 and 4.23 the results are presented as a function of $|y|$ for slices of p_T. Full tables of all the respective measured values are given in appendix B.1.3.

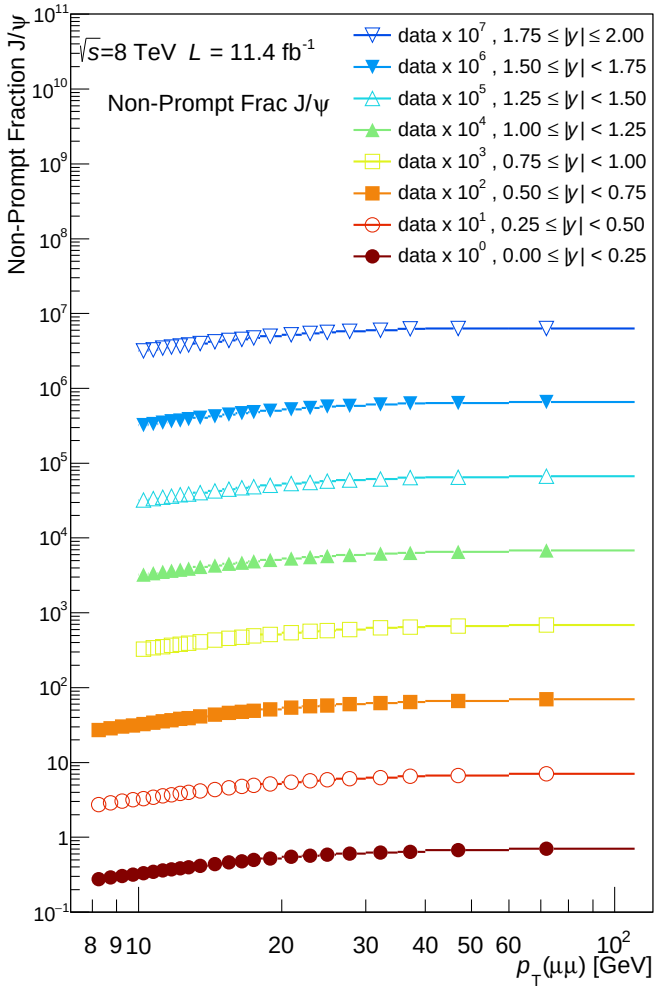

Figure 4.20: The non-prompt J/ψ fraction as a function of $p_T(\mu\mu)$ for each of the slices of rapidity. For each increasing rapidity slice, a scaling factor of x 10 is applied to the plotted points. The centre of each bin on the horizontal axis represents the mean of the weighted p_T distribution. The horizontal error-bars represent the range of p_T for the bin, and the vertical error-bar covers the statistical and the systematic uncertainty (with the same multiplicative scaling applied).

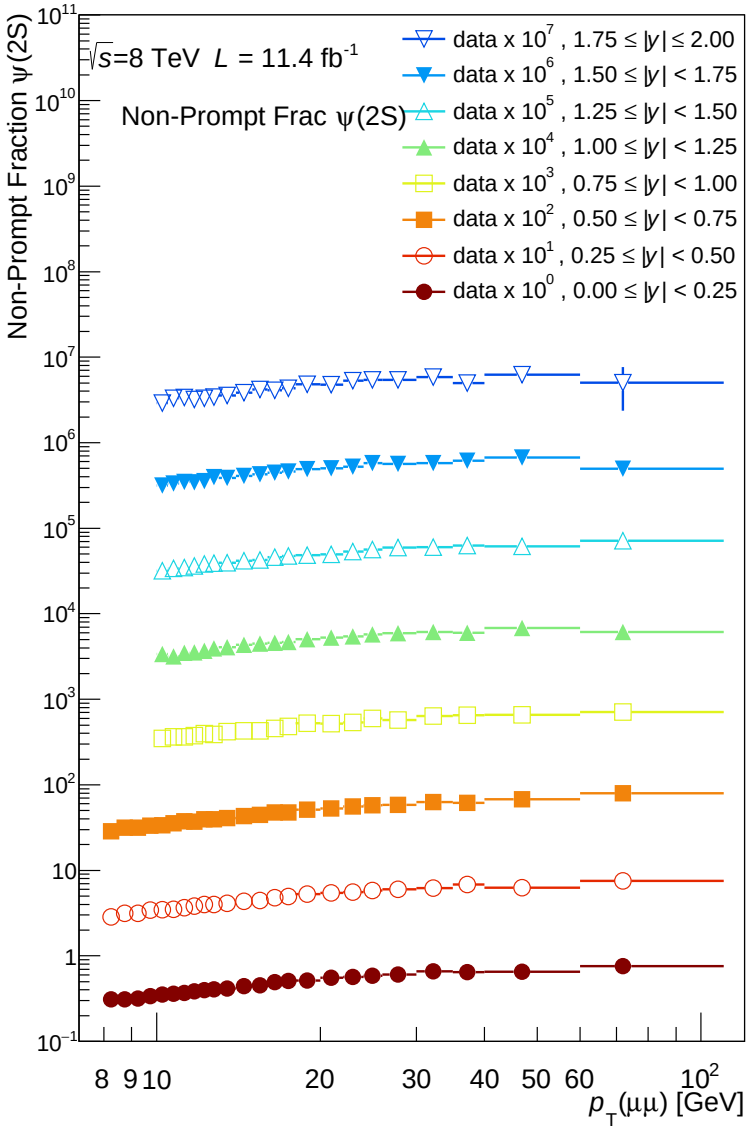

Figure 4.21: The non-prompt $\psi(2S)$ fraction as a function of $p_T(\mu\mu)$ for each of the slices of rapidity. For each increasing rapidity slice, a scaling factor of x 10 is applied to the plotted points. The centre of each bin on the horizontal axis represents the mean of the weighted p_T distribution. The horizontal error-bars represent the range of p_T for the bin, and the vertical error-bar covers the statistical and the systematic uncertainty (with the same multiplicative scaling applied).

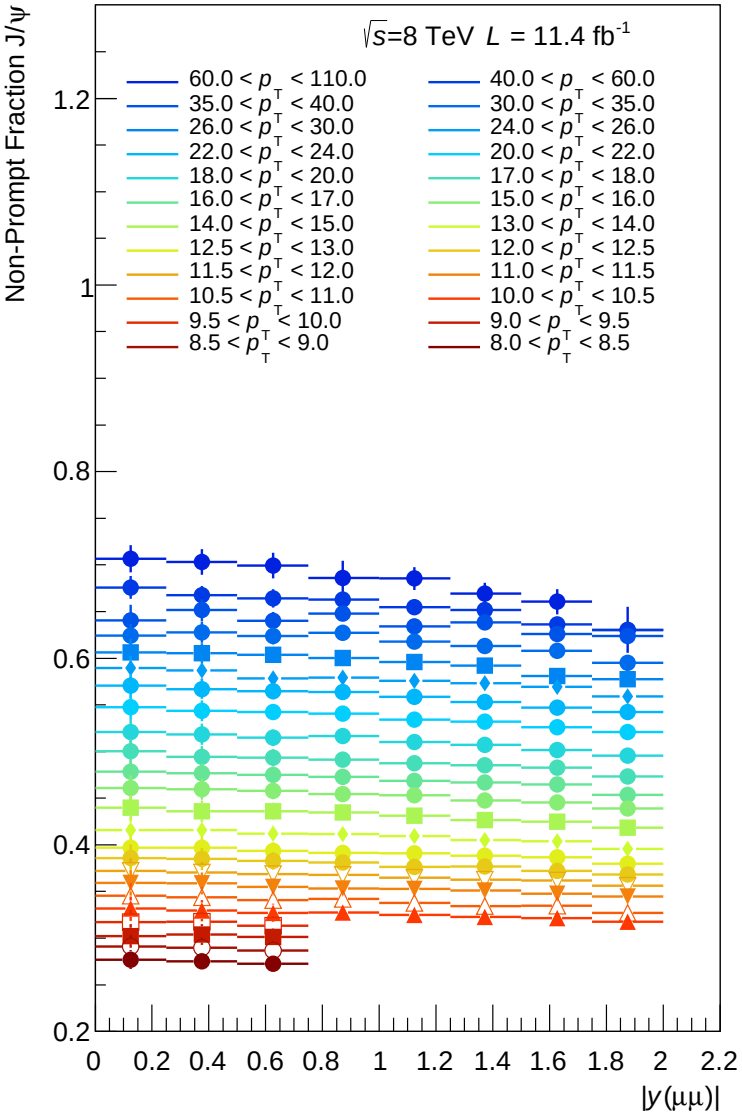

Figure 4.22: The non-prompt J/ψ fraction as a function of $|y(\mu\mu)|$ for each of the slices of p_T. For each increasing p_T slice, a scaling factor of x 10 is applied to the plotted points. The centre of each bin on the horizontal axis represents the mean of the weighted $|y|$ distribution. The horizontal error-bars represent the range of $|y|$ for the bin, and the vertical error-bar covers the statistical and the systematic uncertainty (with the same multiplicative scaling applied).

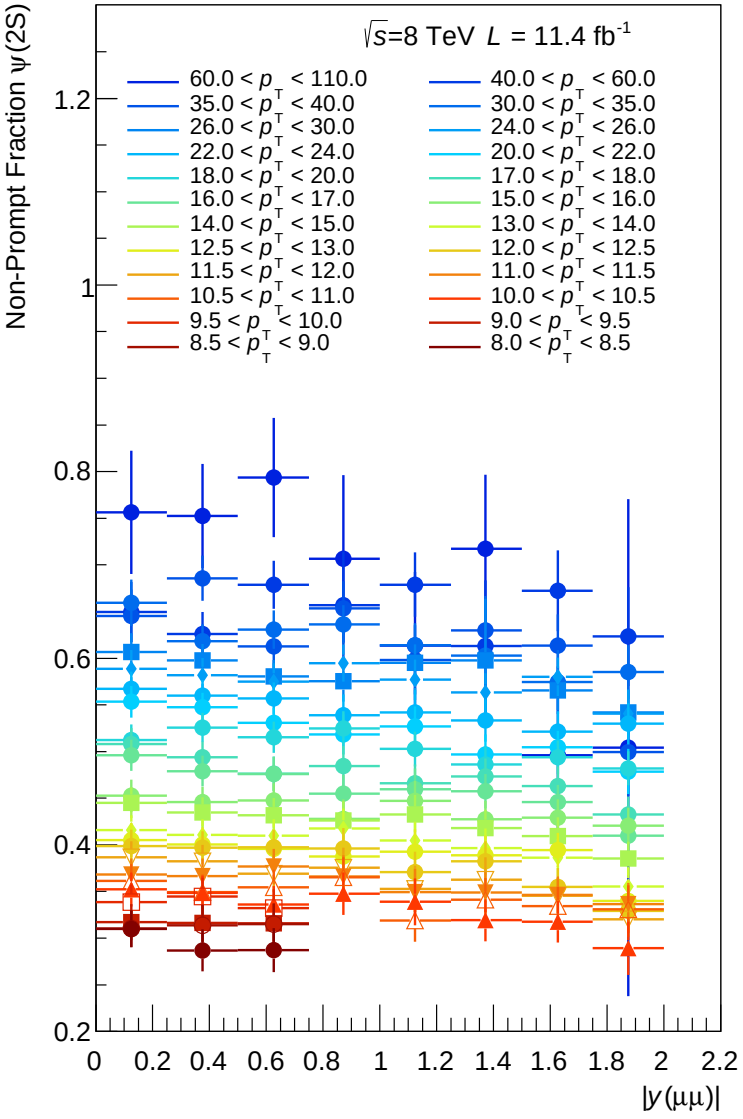

Figure 4.23: The non-prompt $\psi(2S)$ fraction as a function of $|y(\mu\mu)|$ for each of the slices of p_T. For each increasing p_T slice, a scaling factor of x 10 is applied to the plotted points. The centre of each bin on the horizontal axis represents the mean of the weighted $|y|$ distribution. The horizontal error-bars represent the range of $|y|$ for the bin, and the vertical error-bar covers the statistical and the systematic uncertainty (with the same multiplicative scaling applied).

4.7 Ratio Results

The results of the fits for the ratio of $\psi(2S)$ to J/ψ production in prompt and non-prompt processes, are presented here as a function of p_T for slices of rapidity in figures 4.24 and 4.25, respectively, whereas in figures 4.26 and 4.27 the results are presented as a function of $|y|$ for slices of p_T. Full tables of all the respective measured values are given in appendix B.1.3.

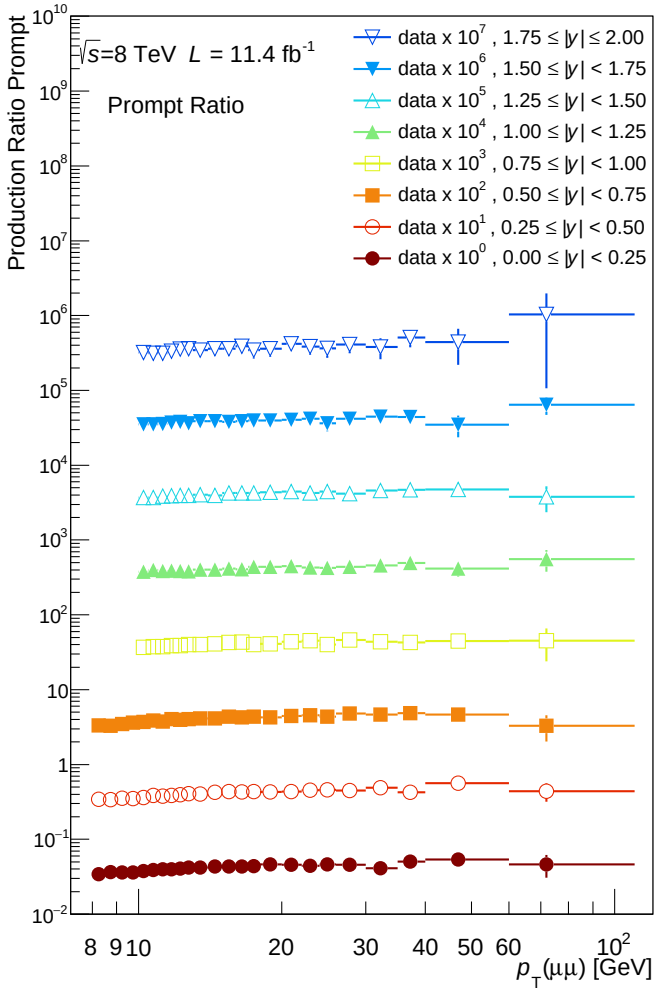

Figure 4.24: The ratio of $\psi(2S)$ to J/ψ prompt production as a function of $p_T(\mu\mu)$ for each of the slices of rapidity. The center of each bin on the horizontal axis represents the mean of the weighted p_T distribution. The horizontal error-bars represent the range of p_T for the bin, and the vertical error-bar covers the statistical and the systematic uncertainty.

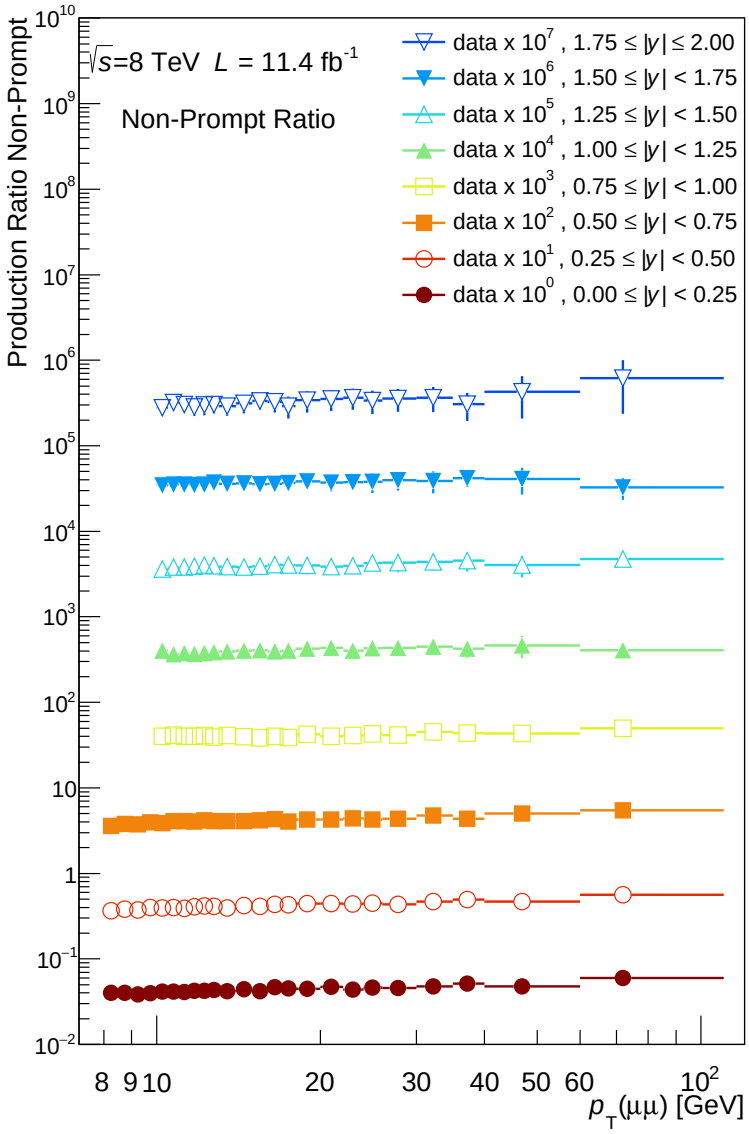

Figure 4.25: The ratio of $\psi(2S)$ to J/ψ non-prompt production as a function of $p_T(\mu\mu)$ for each of the slices of rapidity. The center of each bin on the horizontal axis represents the mean of the weighted p_T distribution. The horizontal error-bars represent the range of p_T for the bin, and the vertical error-bar covers the statistical and the systematic uncertainty.

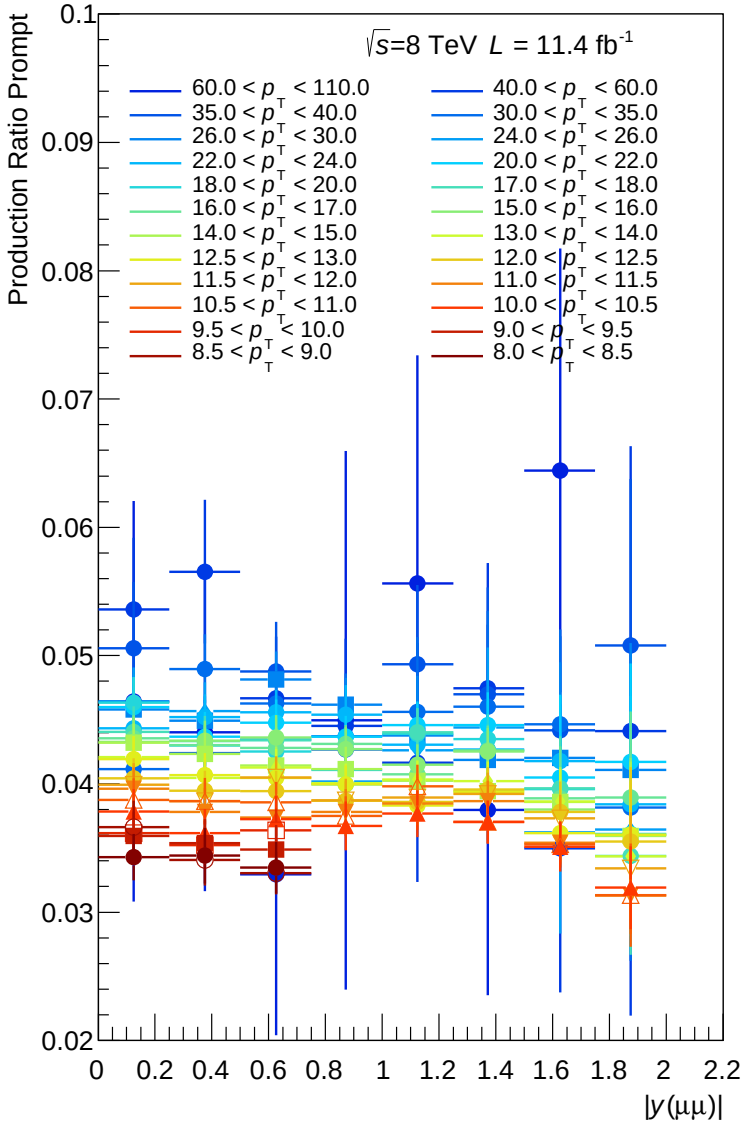

Figure 4.26: The ratio of $\psi(2S)$ to J/ψ prompt production as a function of $|y(\mu\mu)|$ for each of the slices of p_T. The center of each bin on the horizontal axis represents the mean of the weighted $|y|$ distribution. The horizontal error-bars represent the range of $|y|$ for the bin, and the vertical error-bar covers the statistical and the systematic uncertainty.

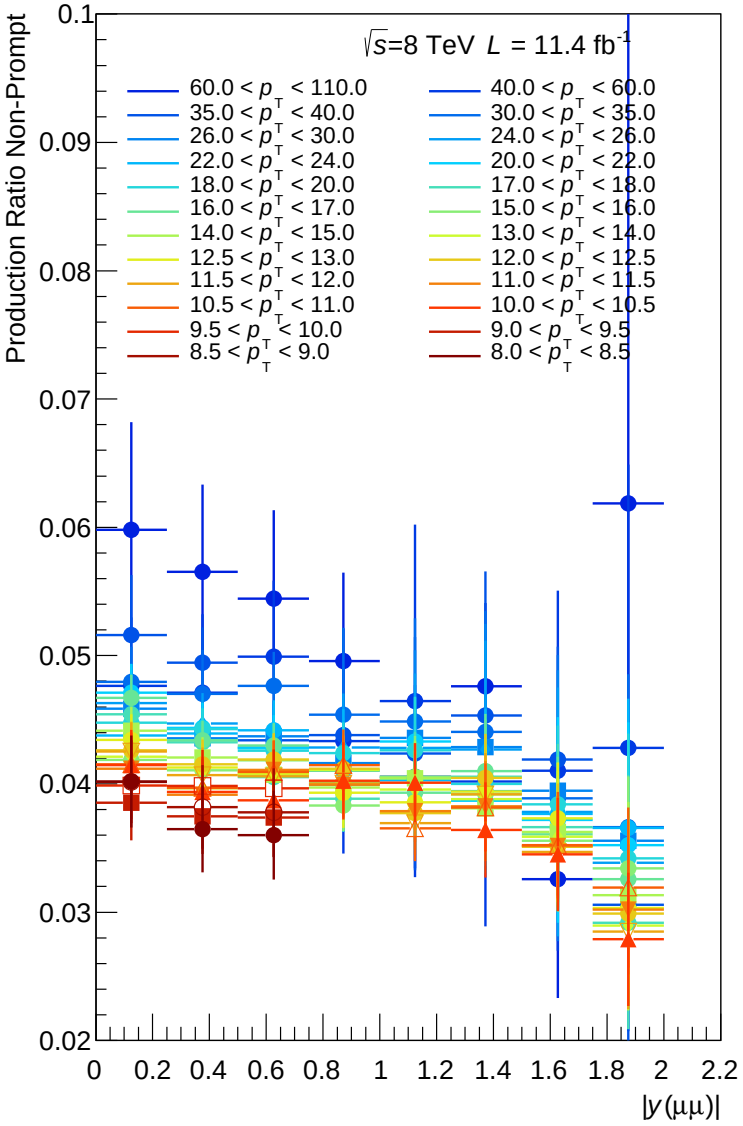

Figure 4.27: The ratio of $\psi(2S)$ to J/ψ non-prompt production as a function of $|y(\mu\mu)|$ for each of the slices of p_T. The center of each bin on the horizontal axis represents the mean of the weighted $|y|$ distribution. The horizontal error-bars represent the range of $|y|$ for the bin, and the vertical error-bar covers the statistical and the systematic uncertainty.

4.8 Comparison to the Theoretical Predictions

For the prompt ψ production, comparison is made to NLO NRQCD calculations [54], as shown in Figures 4.28 and 4.29 where the corresponding theoretical calculations are represented with all their uncertainties with the red band. In Figure 4.30 the comparisons between the theory and data, plotted as a ratio, are provided for J/ψ and $\psi 2s$ at both 8 TeV centre-of-mass energy can be found. The uncertainties in the theory prediction originate from the choice of scale, charm quark mass and long distance matrix elements and is discussed further in Ref. [55]. Reasonable agreement is seen between theory and data at all transverse momenta. There is no observed dependence on the behavior between data and the theory predictions as a function of the rapidity of the ψ meson.

For the prompt ψ production, comparison is also made to fixed-order next-to-leading-logarithm (FONLL) theoretical predictions [56, 57], as shown in Figures 4.31 and 4.32 where the corresponding theoretical calculations are represented with all their uncertainties with the red band. Figure 4.33 shows a comparison for J/ψ and $\psi(2\mathrm{S})$ of FONLL predictions to the data as a function of p_{T} in slices of rapidity for 8 TeV energy plotted as a ratio of theory to data. For J/ψ, the agreement is generally good, however the theory has a softer p_{T} spectra than observed in the data. For $\psi(2\mathrm{S})$, the shape between data and theory appears to be in reasonable agreement, however the normalisation has a tendency for the theory to predict higher yield than the data suggests. There is no observed dependence across rapidity in the comparisons between theory and data for the non-prompt ψ production.

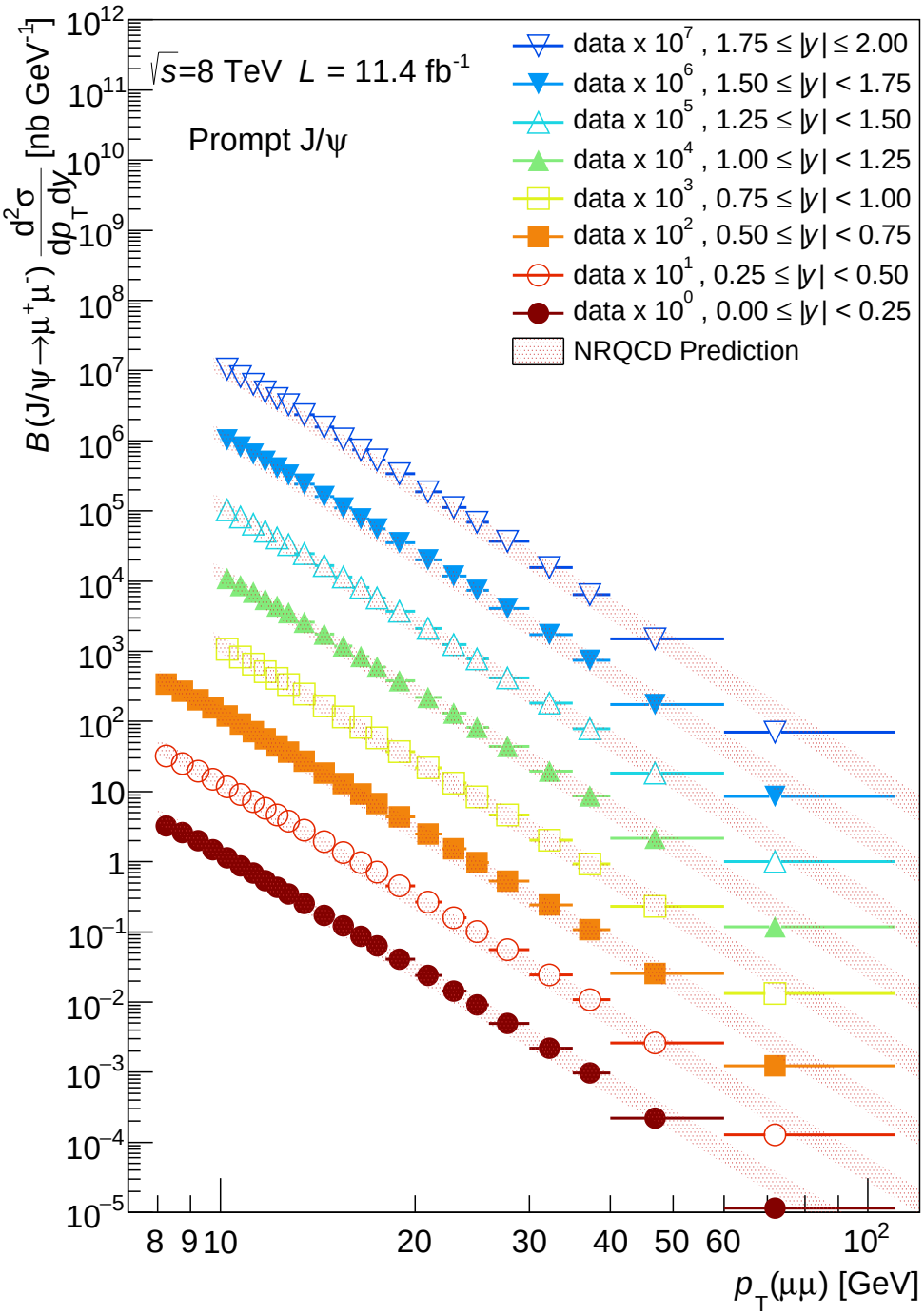

Figure 4.28: The differential J/ψ prompt cross-section as a function of $p_T(J/\psi)$ for each of the slices of rapidity along with the relevant NLO prediction. For each increasing rapidity slice, a scaling factor of $\times$ 10 is applied to the plotted points. The center of each bin on the horizontal axis represents the mean of the weighted p_T distribution. The horizontal error-bars represent the range of p_T for the bin and the vertical error-bar covers the statistical and the systematic uncertainty (with the same multiplicative scaling applied).

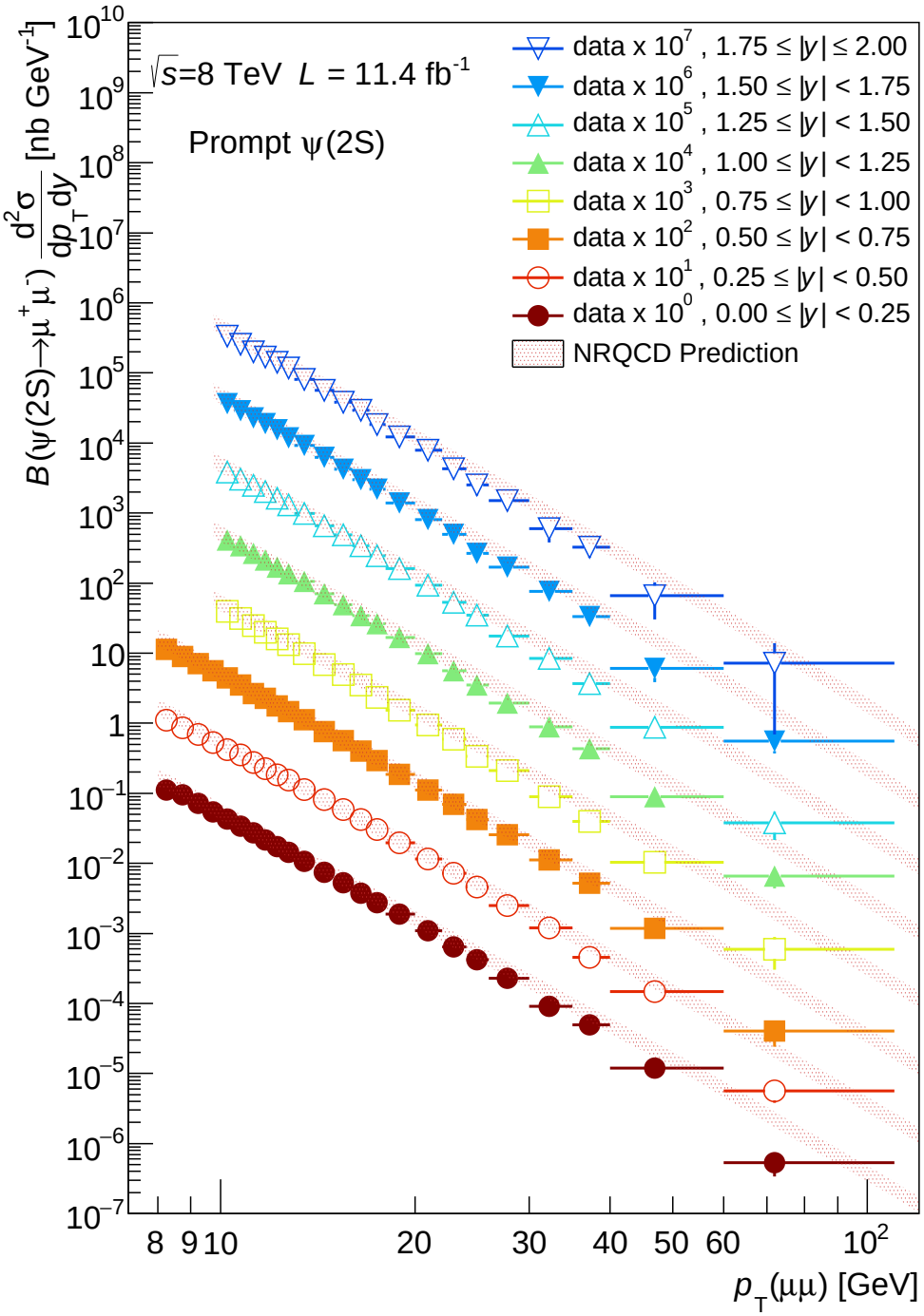

Figure 4.29: The differential $\psi(2S)$ prompt cross-section as a function of $p_T(\psi(2S)$) for each of the slices of rapidity along with the relevant NLO prediction. For each increasing rapidity slice, a scaling factor of $\times$ 10 is applied to the plotted points. The center of each bin on the horizontal axis represents the mean of the weighted p_T distribution. The horizontal error-bars represent the range of p_T for the bin and the vertical error-bar covers the statistical and the systematic uncertainty (with the same multiplicative scaling applied).

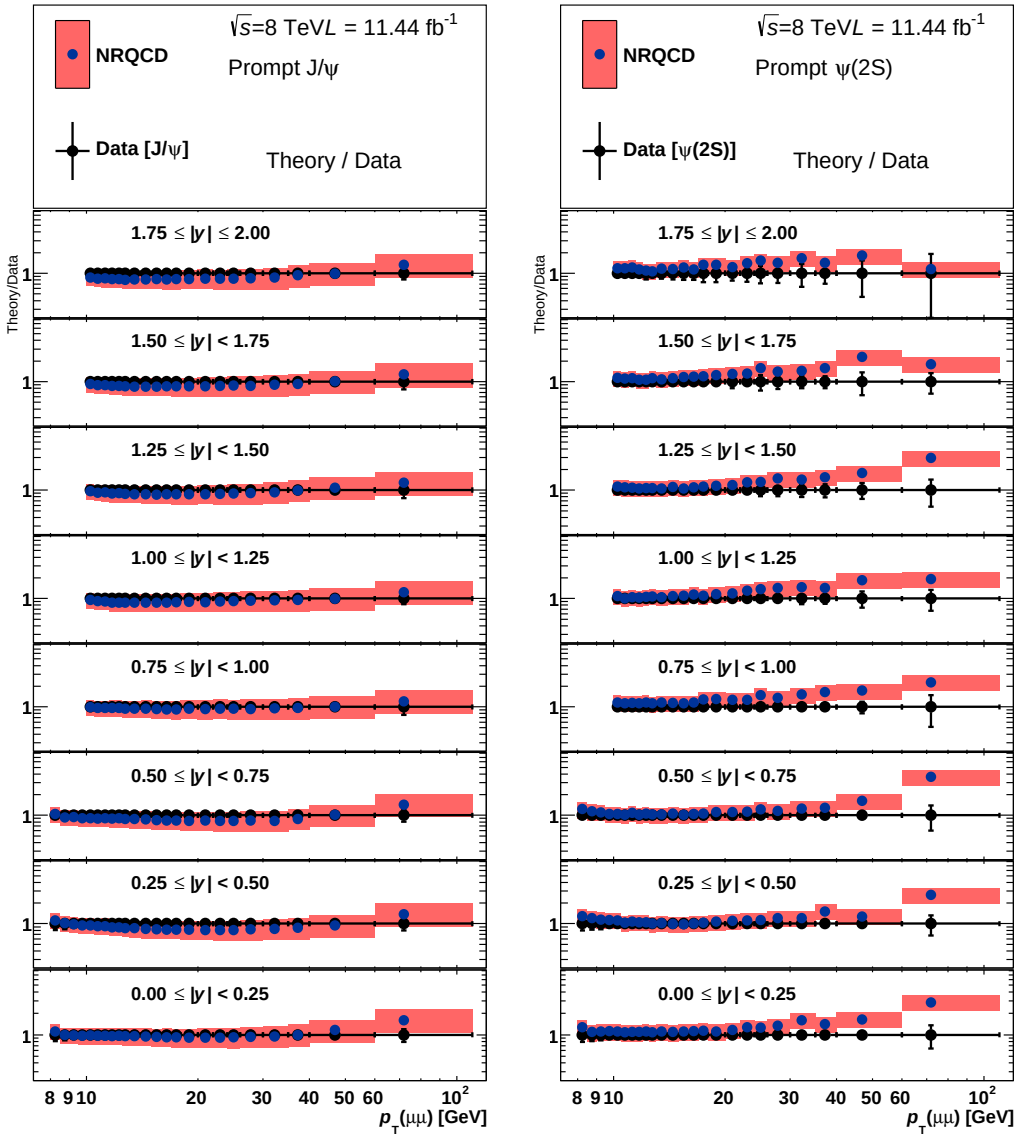

Figure 4.30: The ratios of the NRQCD theoretical prediction to data are presented for the differential prompt cross-section of J/ψ at the left and $\psi(2S)$ at the right as a function of $p_T(J/\psi)$ for each of the slices of rapidity. The error on the data is the relative error of each data point while the error bars on the theory prediction is the relative error of each theory point.

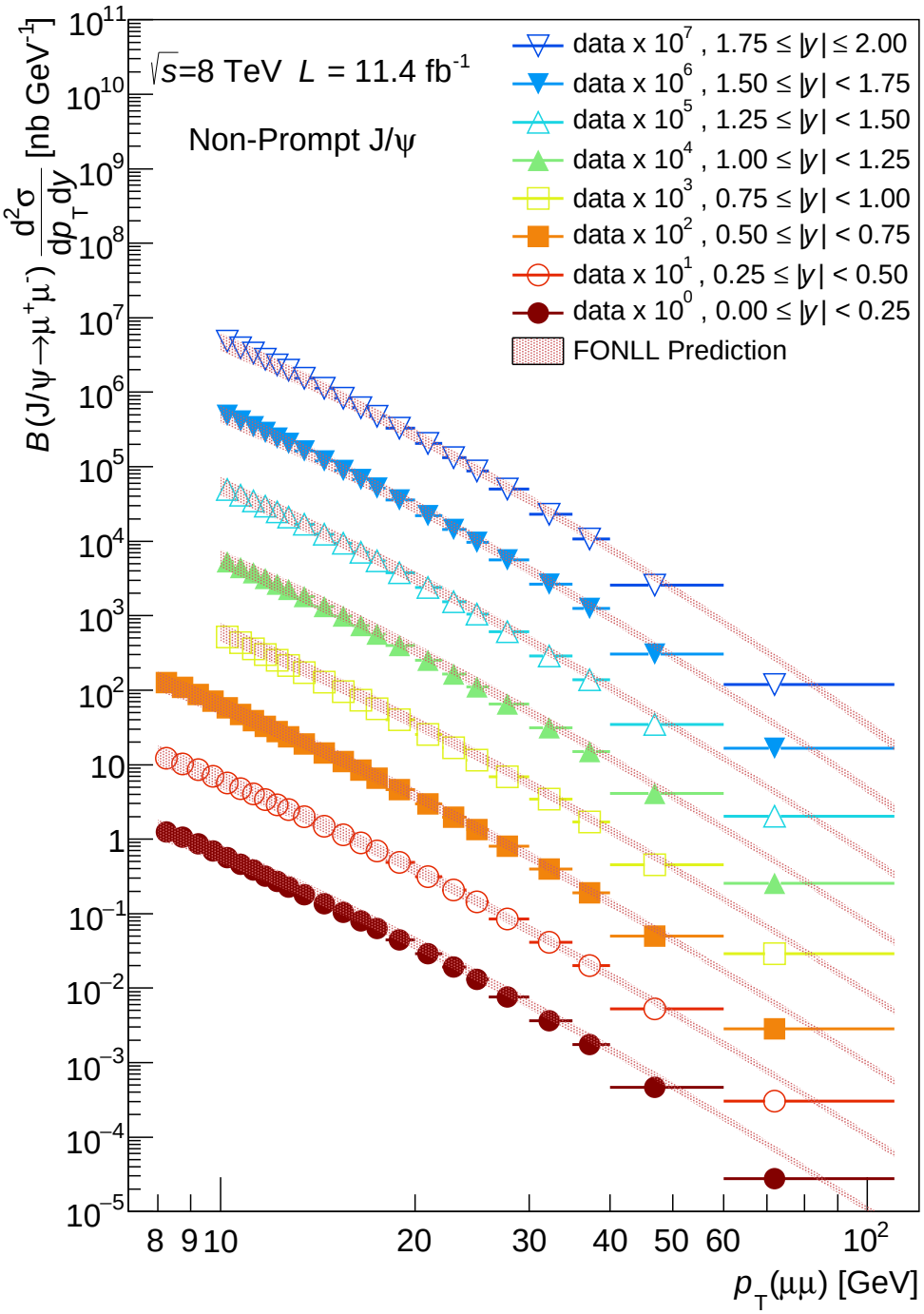

Figure 4.31: The differential J/ψ non-prompt cross-section as a function of $p_T(J/\psi)$ for each of the slices of rapidity along with the relevant FONLL prediction. For each increasing rapidity slice, a scaling factor of $\times$ 10 is applied to the plotted points. The center of each bin on the horizontal axis represents the mean of the weighted p_T distribution. The horizontal error-bars represent the range of p_T for the bin and the vertical error-bar covers the statistical and the systematic uncertainty (with the same multiplicative scaling applied).

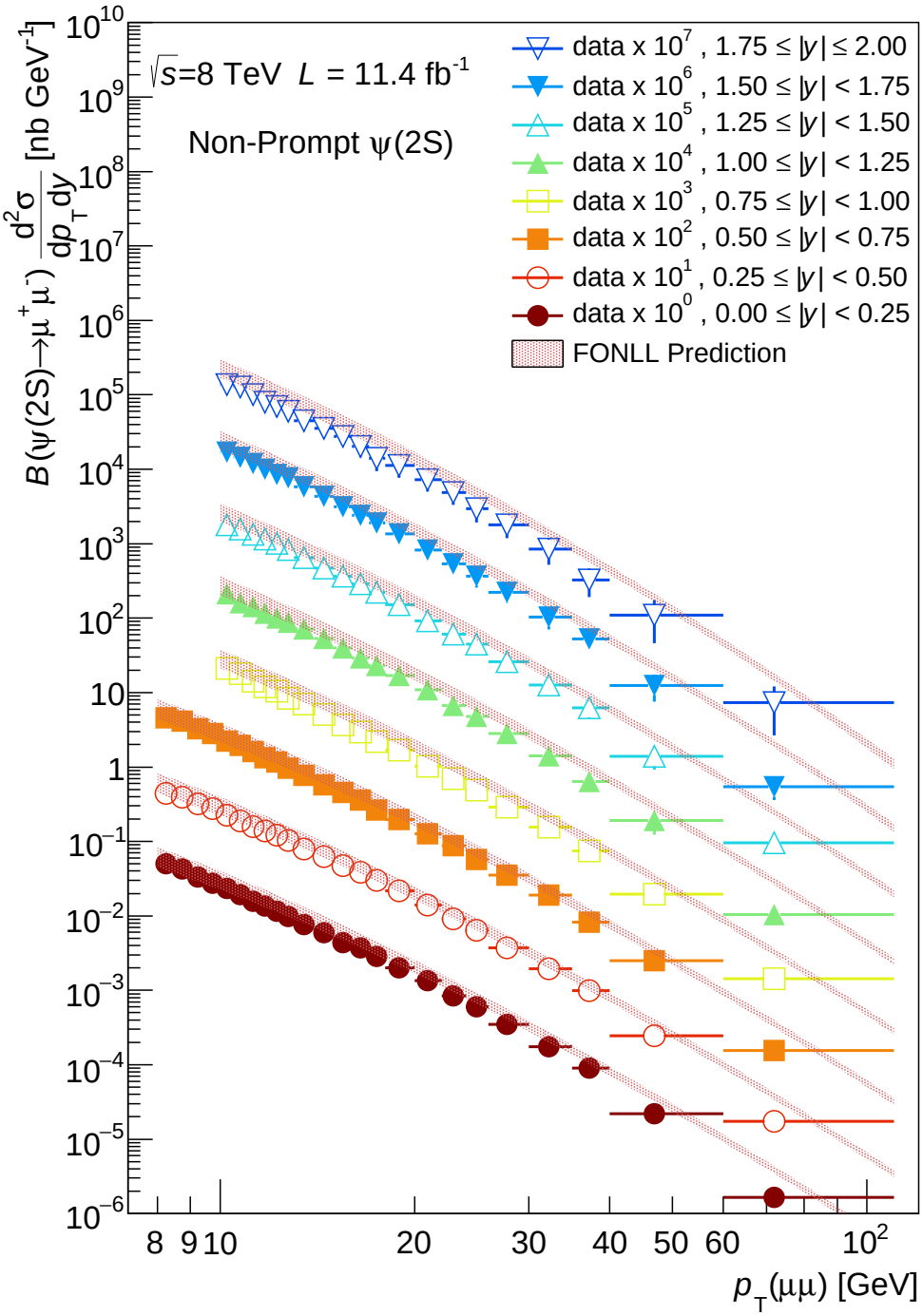

Figure 4.32: The differential $\psi(2S)$ non-prompt cross-section as a function of $p_T(\psi(2S))$ for each of the slices of rapidity along with the relevant FONLL prediction. For each increasing rapidity slice, a scaling factor of $\times$ 10 is applied to the plotted points. The center of each bin on the horizontal axis represents the mean of the weighted p_T distribution. The horizontal error-bars represent the range of p_T for the bin and the vertical error-bar covers the statistical and the systematic uncertainty (with the same multiplicative scaling applied).

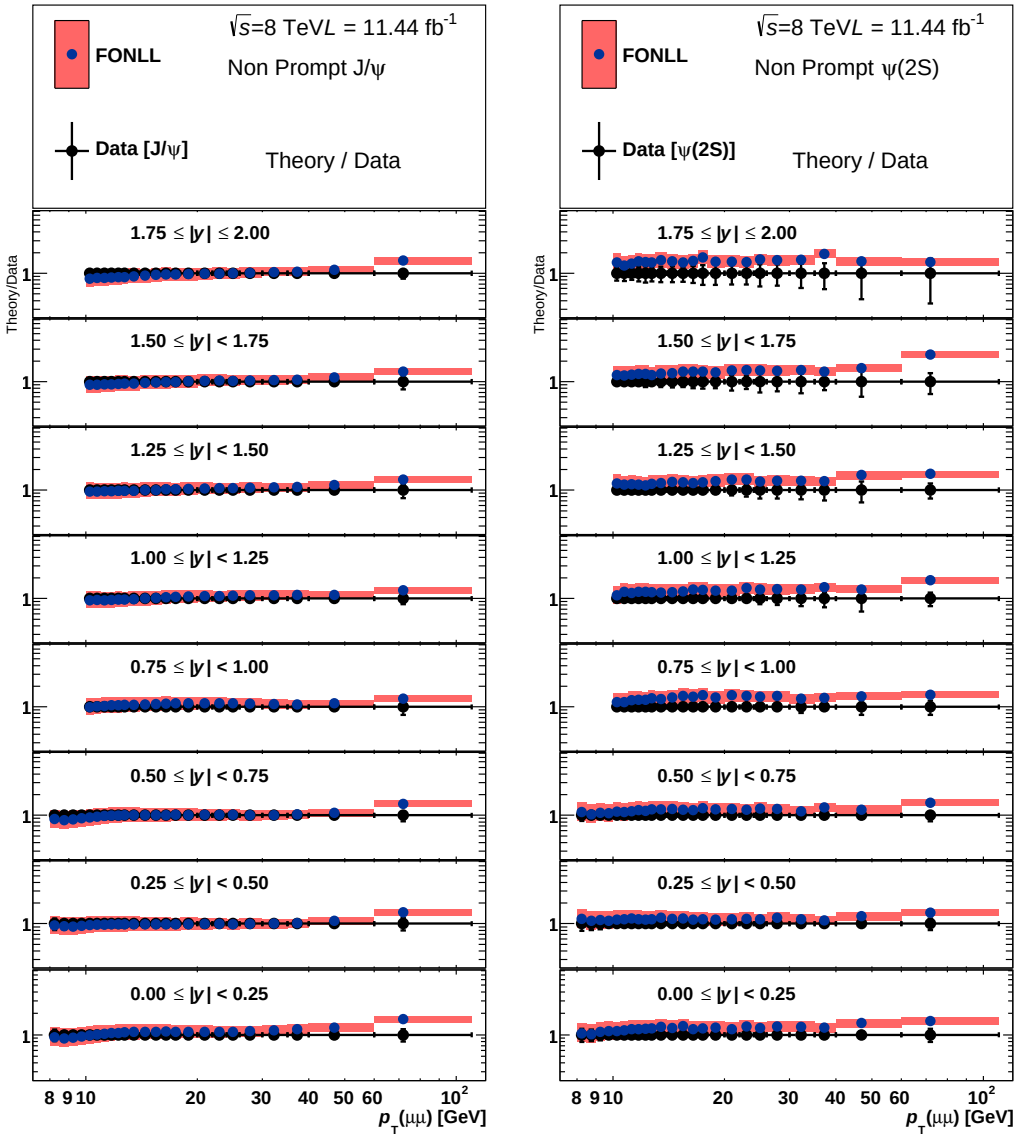

Figure 4.33: The ratio of the FONLL theoretical prediction to data are presented for the differential non-prompt cross-section of J/ψ at the left and $\psi(2S)$ at the right as a function of $p_{\mathrm{T}}(J/\psi)$ for each of the slices of rapidity. The error on the data is the relevant error of each data point while the error bars on the theory prediction is the relevant error of each theory point.

4.9 Systematic Uncertainties

The considered sources of systematic uncertainties are:

- the luminosity determination,
- the inner Detector tracking efficiency,
- the muon reconstruction efficiency,
- the muon trigger efficiency,
- the acceptance corrections
- the migration between $p_T(\mu\mu)$ and $|y(\mu\mu)|$ bins due to resolution,
- the background and signal fit models used.

The relative luminosity uncertainty is 2.8% and it is taken from Ref. [48]. A 1% uncertainty is applied to account for the inner detector reconstruction efficiency for each muon (0.5% per muon). This uncertainty is applied to the differential cross-sections and non-prompt fraction measurements, however, it is assumed to cancel in the ratio measurements.

As the statistical component of the uncertainties associated to the determination of ϵ_{reco} and ϵ_{trig} is dominant, the uncertainties on the cross sections are derived from the statistics of the control samples used to extract them using a series of 100 pseudo-experiments. The goal for each pseudo-experiment is: by varying the weights (reconstruction and trigger) used for each di-muon candidate, according to the uncertainties on the efficiency maps, to estimate the distribution of the weighed candidates. For each pseudo-experiment a new map was created with efficiencies smeared with a gaussian distribution with mean value the original efficiency and sigma the provided error. Using the new map for each event the new total weight was calculated and four maps - accumulators (J/ψ – Prompt, J/ψ – Non-Prompt, $\psi(2S)$ – Prompt, $\psi(2S)$ – Non-Prompt) that follow the analysis binning labeling (described in section 4.1.1) filled. Each event that has absolute value of pseudo-proper time smaller than 0.6 is treated as Prompt otherwise as Non-Prompt and for the J/ψ and $\psi(2S)$ characterization the rough limits that were used are [2.876, 3.316] and [3.450, 3.910] respectively.

The systematic contributions arising from the non-cancellation observed between the efficiencies of prompt and non-prompt J/ψ and $\psi(2S)$ are found to be at the 0.1% level and are neglected.

The systematic uncertainties associated to the fit model used to extract the measured quantities from the di-muon data sample are quantified by taking the largest deviation between each of the measured quantities found in the variations of model combinations and the main values used for the final result.

4.9.1 Fit Model Systematics

The following figures 4.34 to 4.41 are used to show the relative uncertainty of variations of the fit model compared to the central fit result for the measured parameters. Variations to the central model fit were considered as:

- The signal model mass shape: by using a double Gaussian in place of the Crystal Ball (CB) plus Gaussian model; and varying the α and n parameters of the CB model, which are originally fixed.
- The background mass shapes: by varying the model, using exponentials, quadratic polynomial to describe the prompt, non-prompt and double-sided background mass terms.
- The background lifetime shape: For the non-prompt component, single exponential was considered.
- The lifetime resolution: Using a single Gaussian in place of the double Gaussian to model the lifetime resolution (also prompt lifetime shape); and varying the mixing terms for the two Gaussians for the measurement.

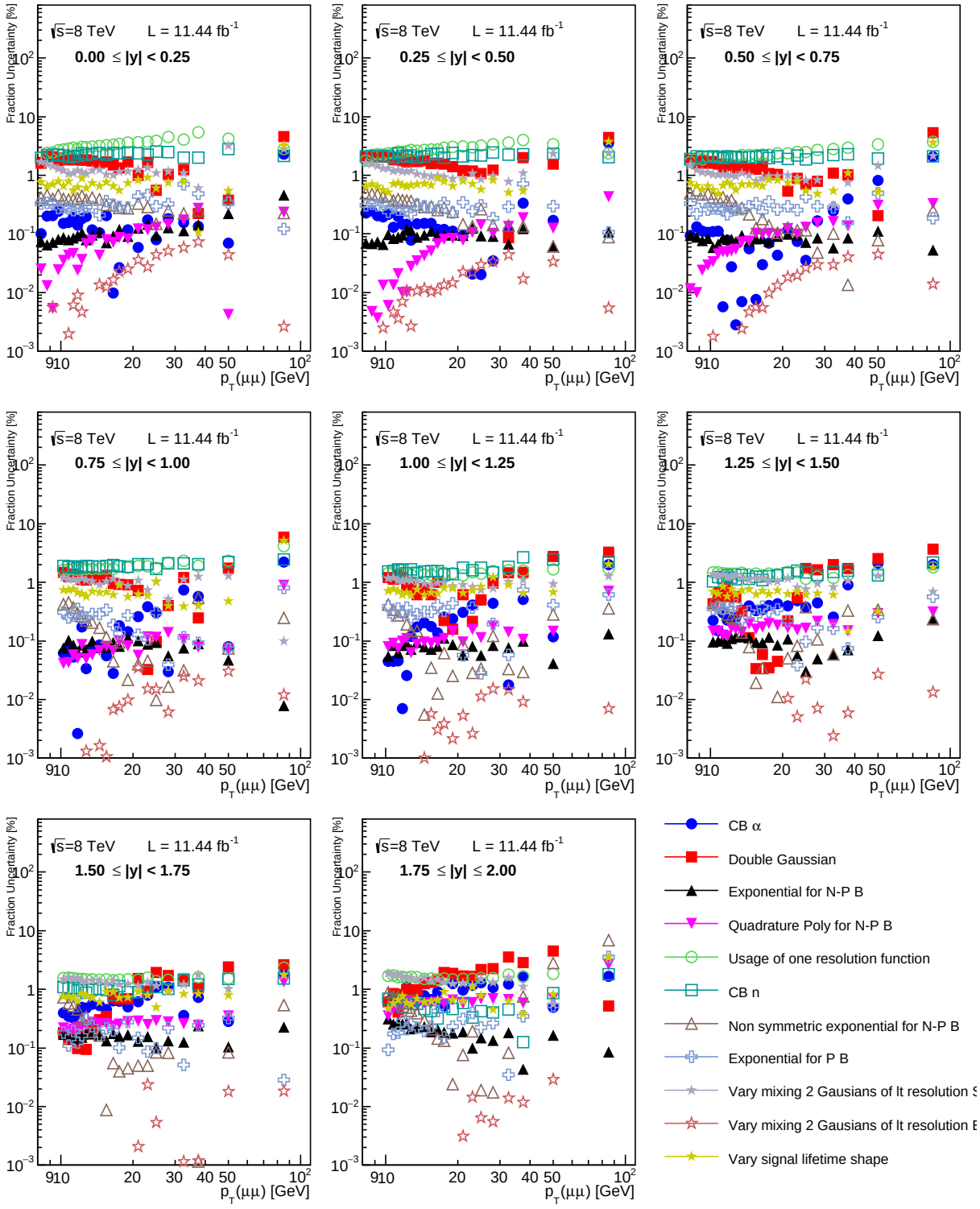

Figure 4.34: Effect of the various fit model variations on the prompt J/ψ cross-section, shown as a function of p_T in bins of increasing rapidity.

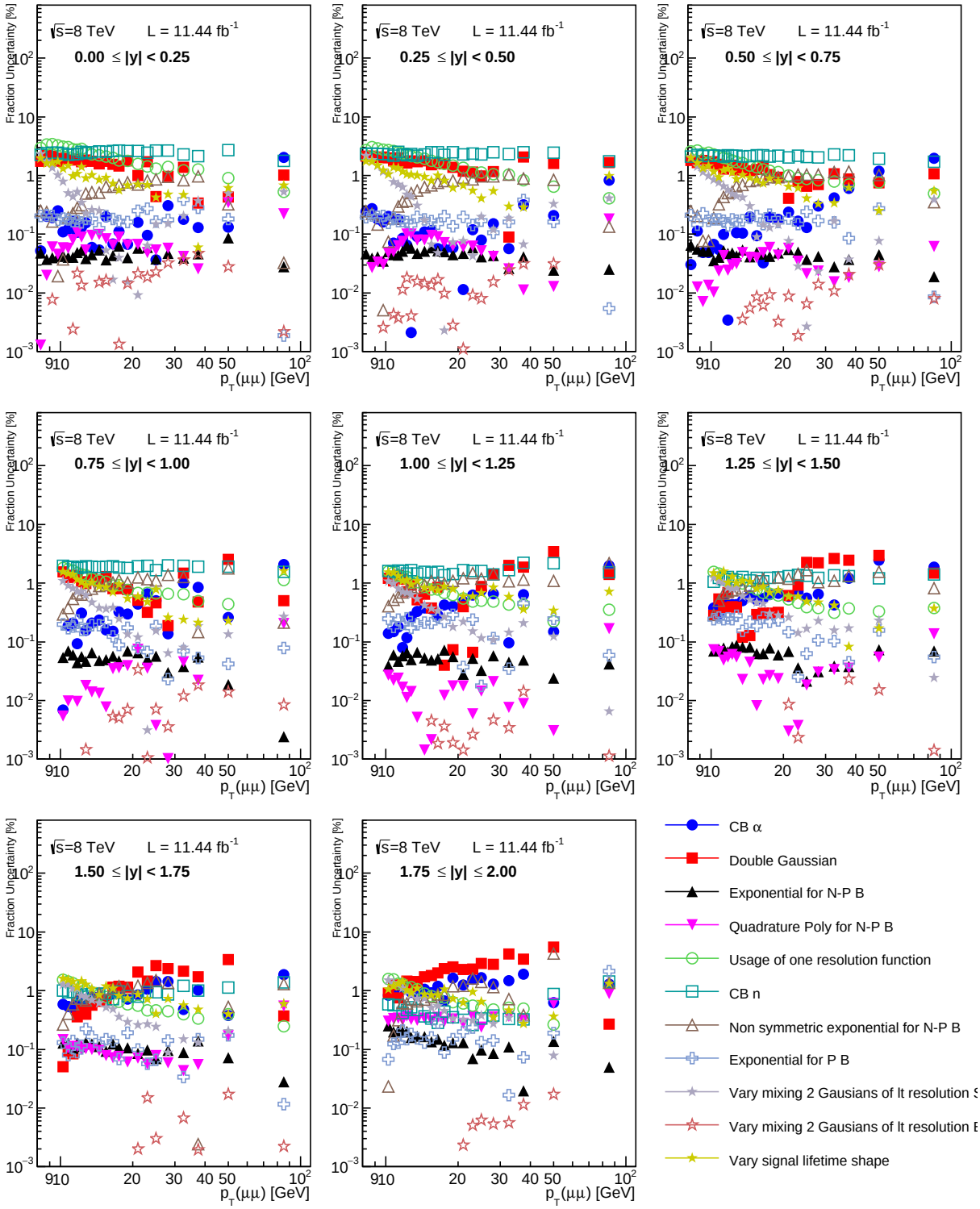

Figure 4.35: Effect of the various fit model variations on the non-prompt J/ψ cross-section, shown as a function of p_T in bins of increasing rapidity.

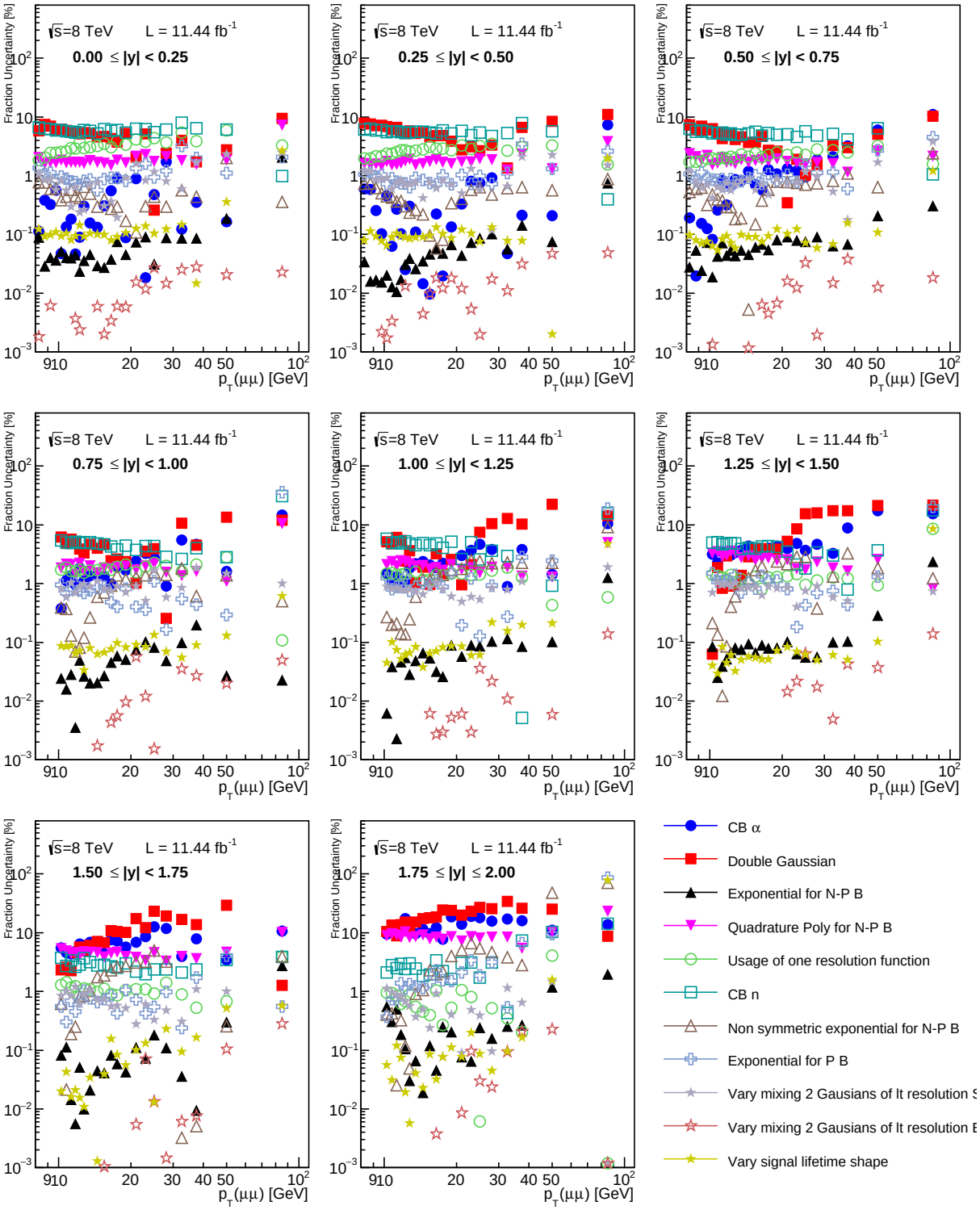

Figure 4.36: Effect of the various fit model variations on the prompt $\psi(2S)$ cross-section, shown as a function of p_T in bins of increasing rapidity.

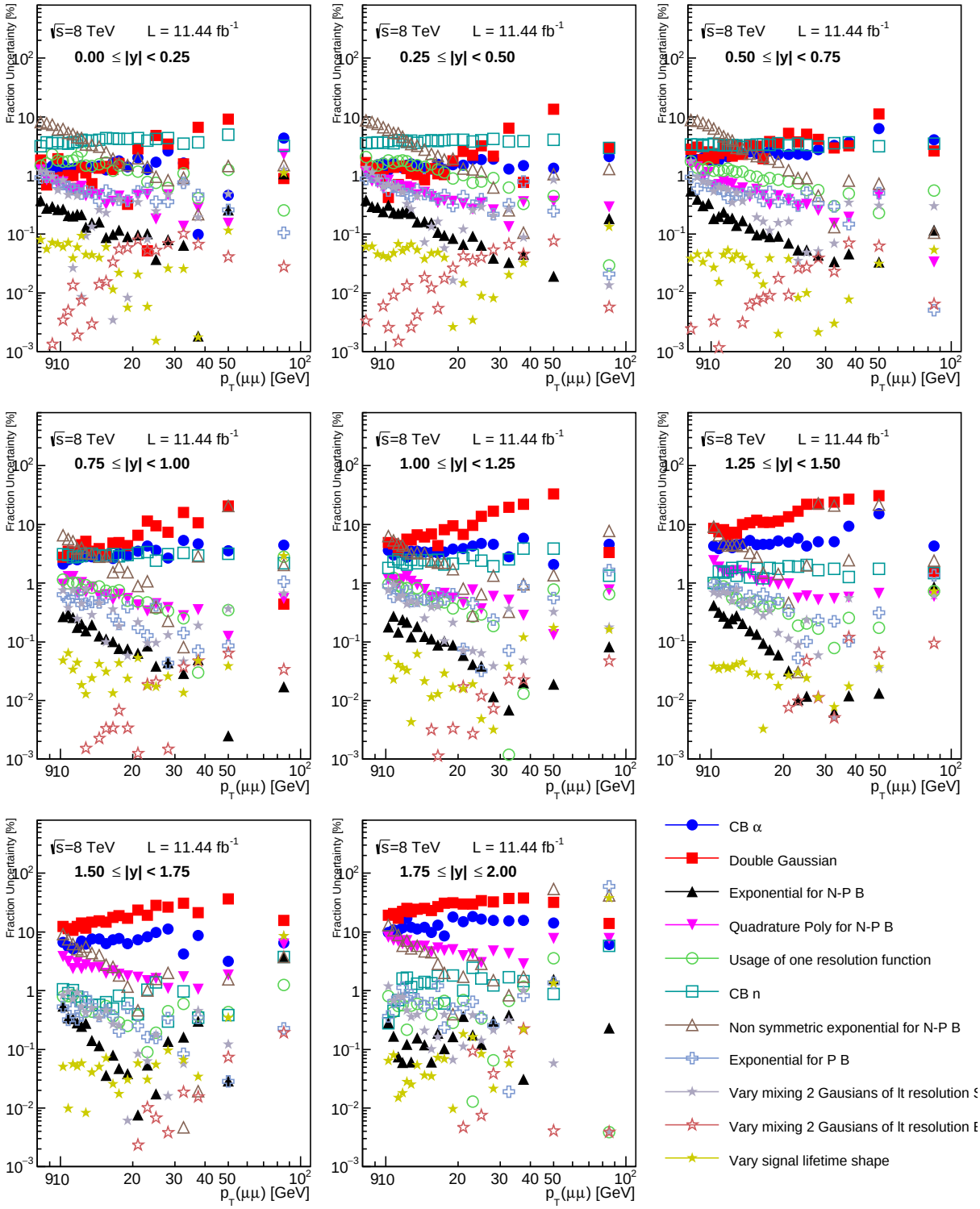

Figure 4.37: Effect of the various fit model variations on the non-prompt $\psi(2S)$ cross-section, shown as a function of p_T in bins of increasing rapidity.

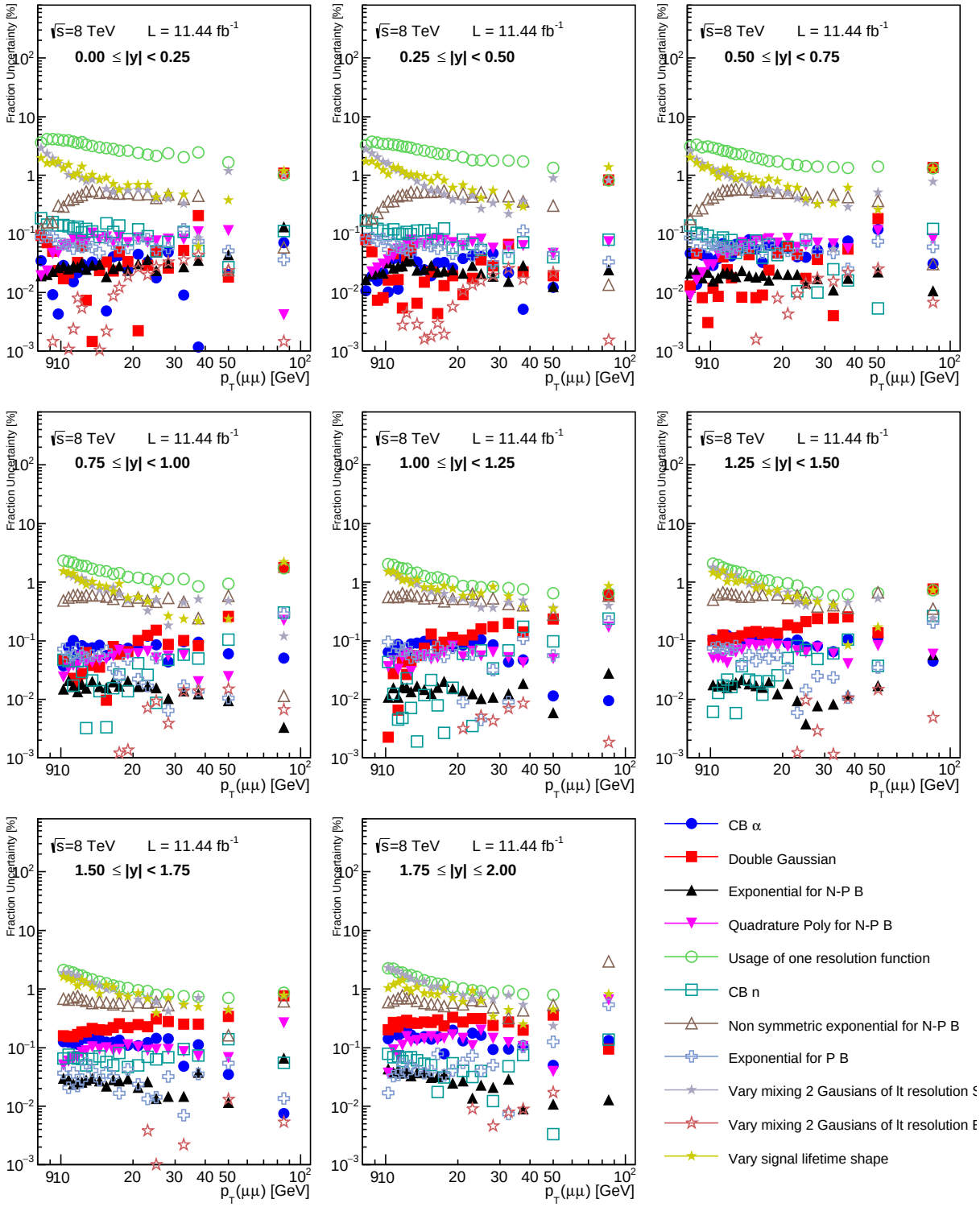

Figure 4.38: Effect of the various fit model variations on the non-prompt fraction of J/ψ, shown as a function of p_T in bins of increasing rapidity.

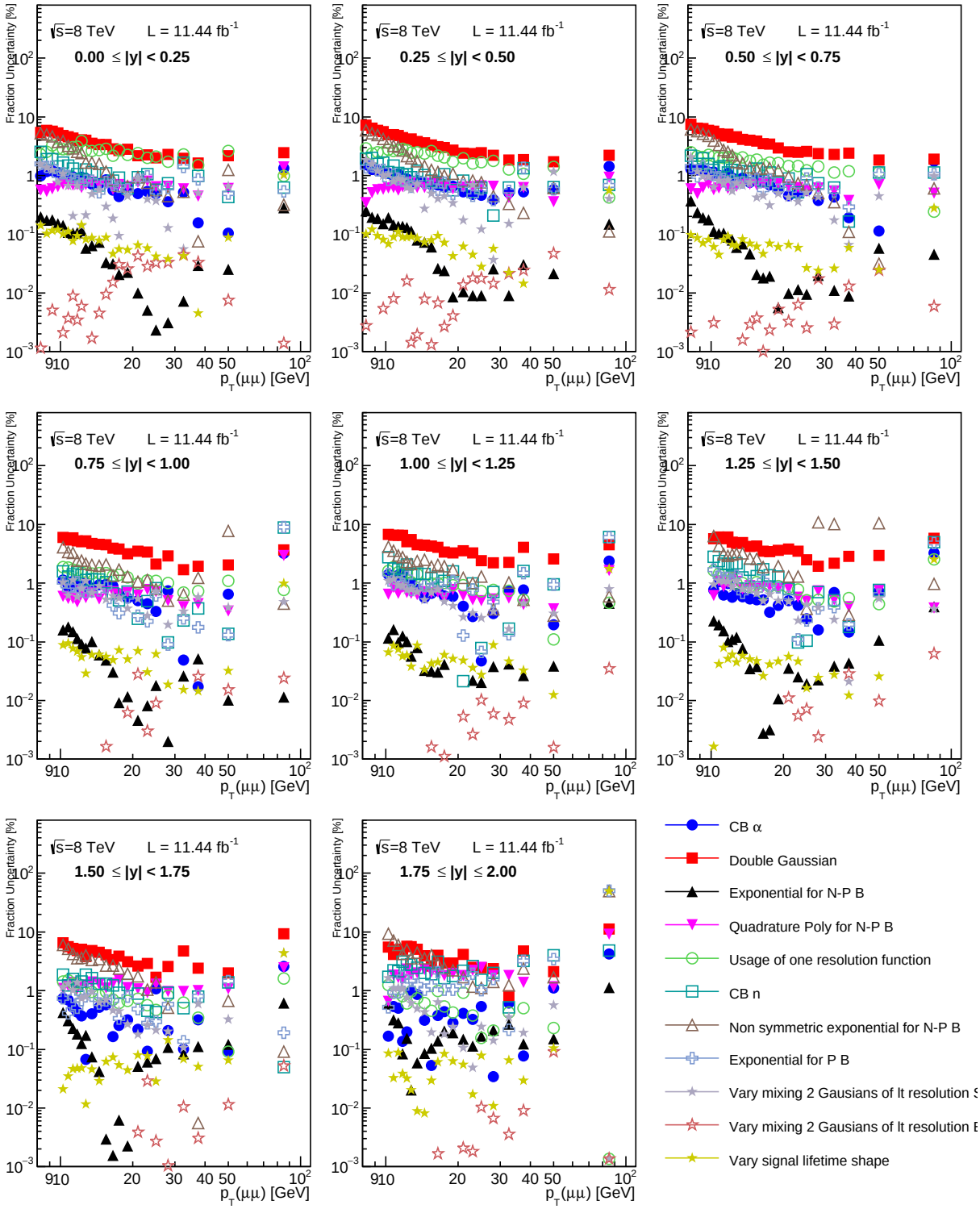

Figure 4.39: Effect of the various fit model variations on the non-prompt fraction of $\psi(2S)$, shown as a function of p_T in bins of increasing rapidity.

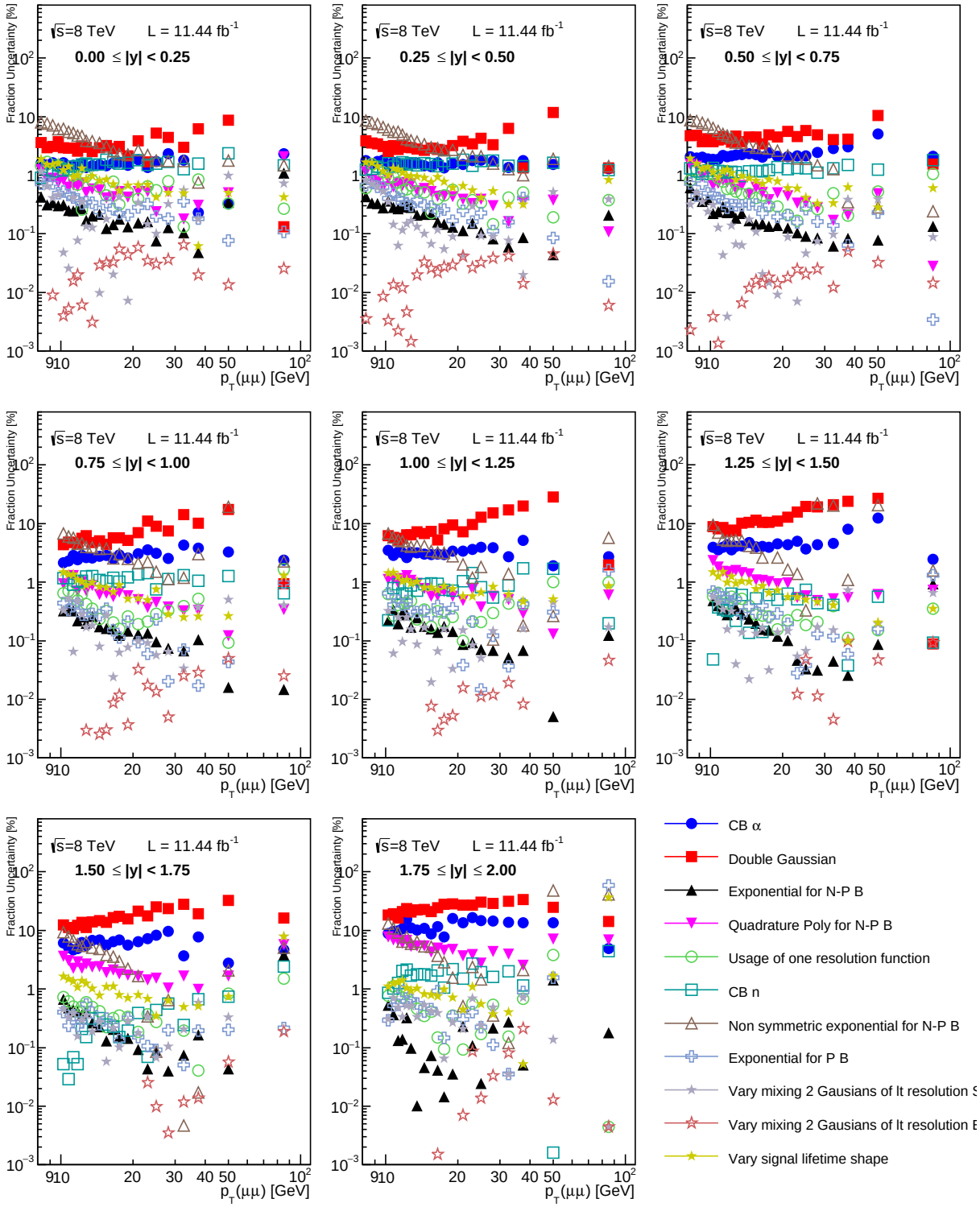

Figure 4.40: Effect of the various fit model variations on the prompt ratio, shown as a function of p_T in bins of increasing rapidity.

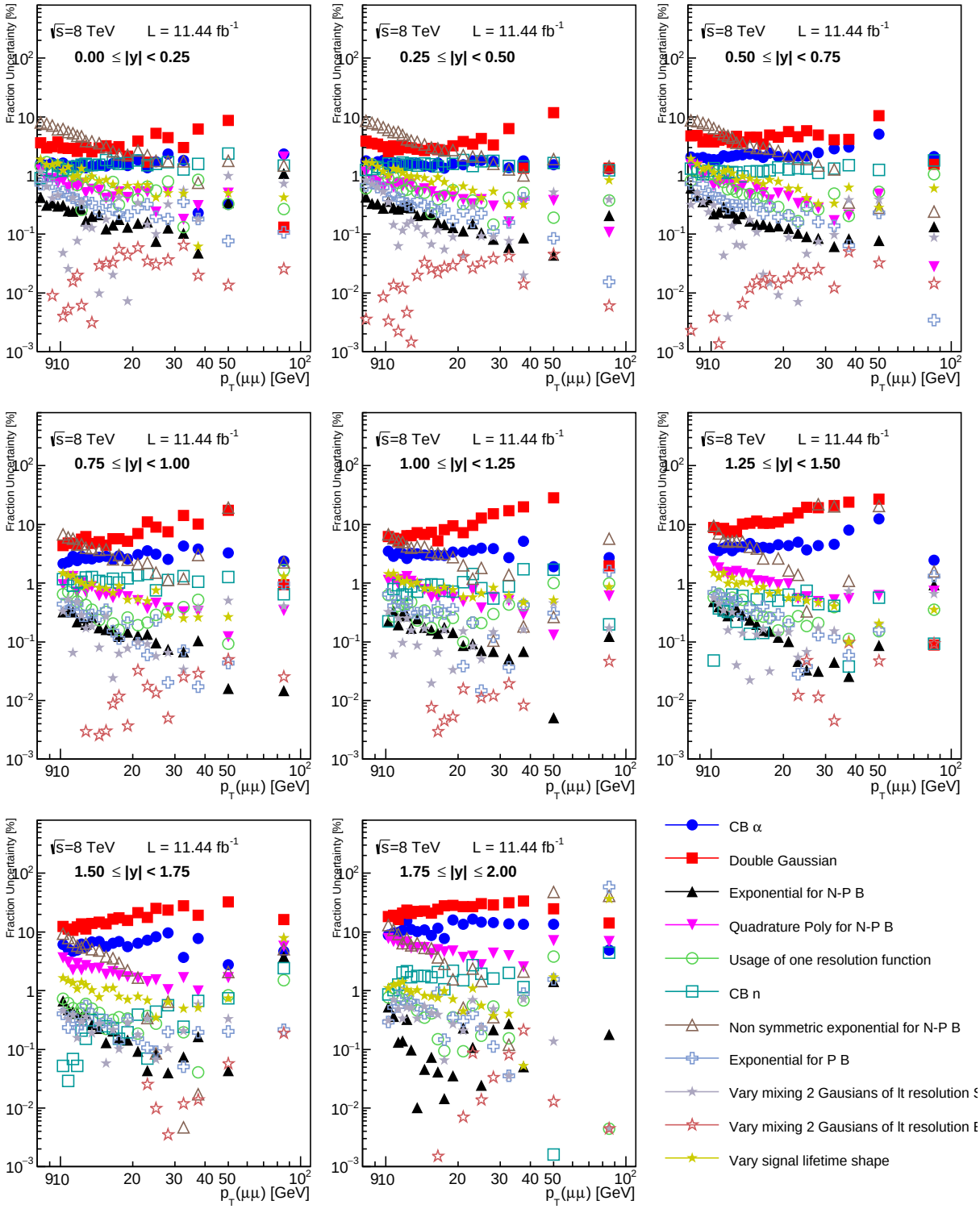

Figure 4.41: Effect of the various fit model variations on the non-prompt ratio, shown as a function of p_T in bins of increasing rapidity.

4.9.2 Total Systematics

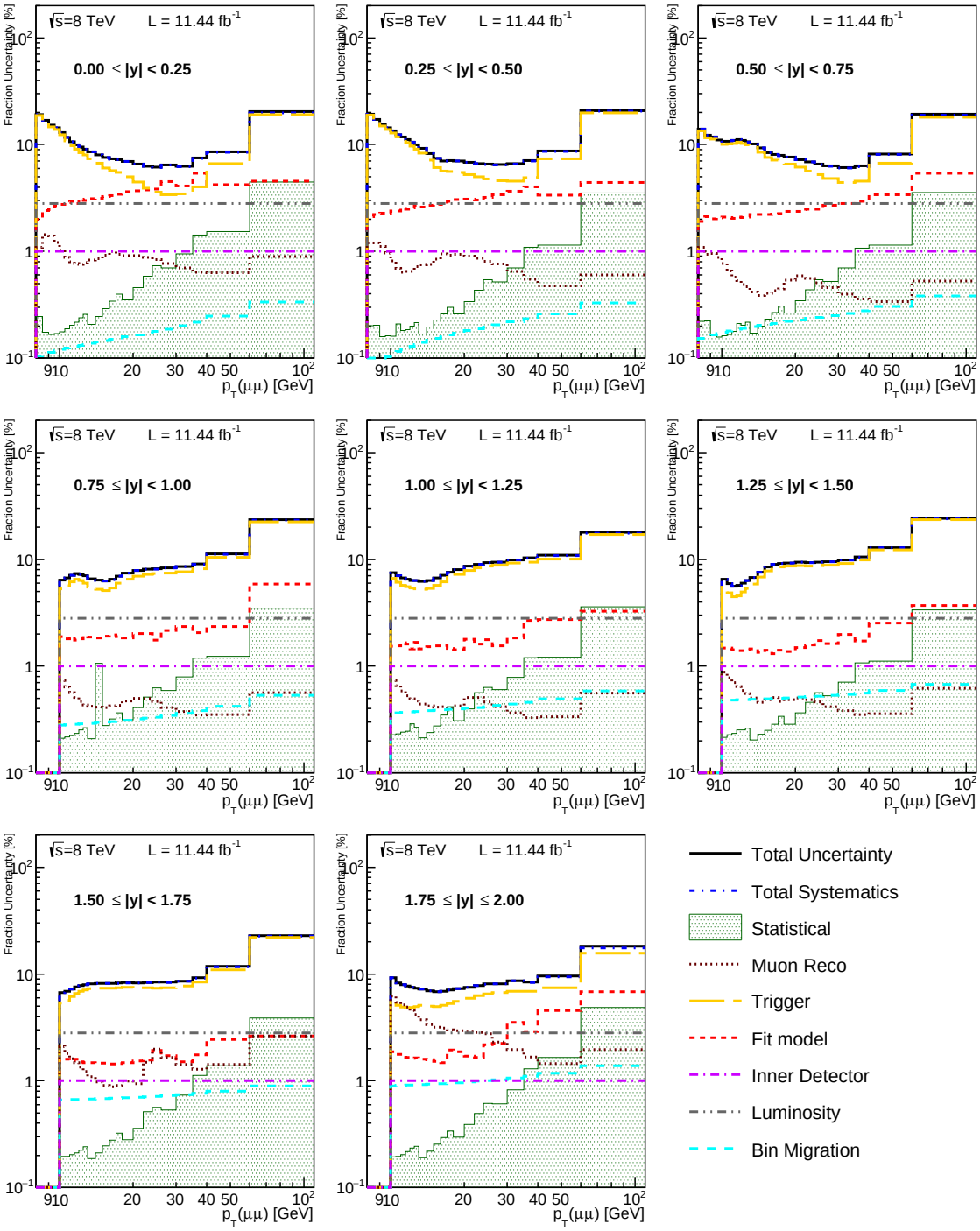

Figure 4.42: The fractional uncertainty contributions of the the prompt J/ψ differential cross-section, shown as a function of p_T in bins of increasing rapidity.

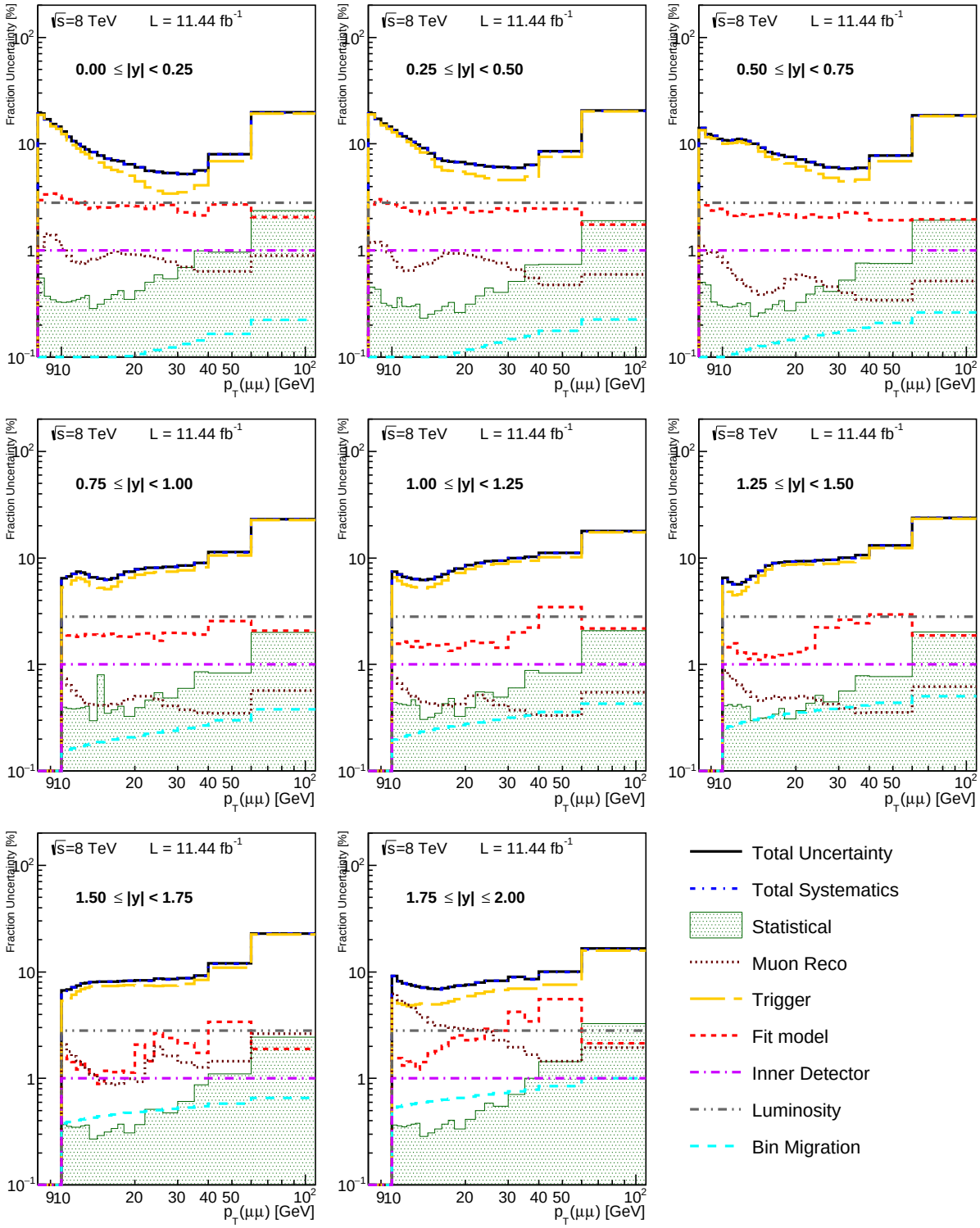

Figure 4.43: The fractional uncertainty contributions of the the non-prompt J/ψ differential cross-section, shown as a function of p_T in bins of increasing rapidity.

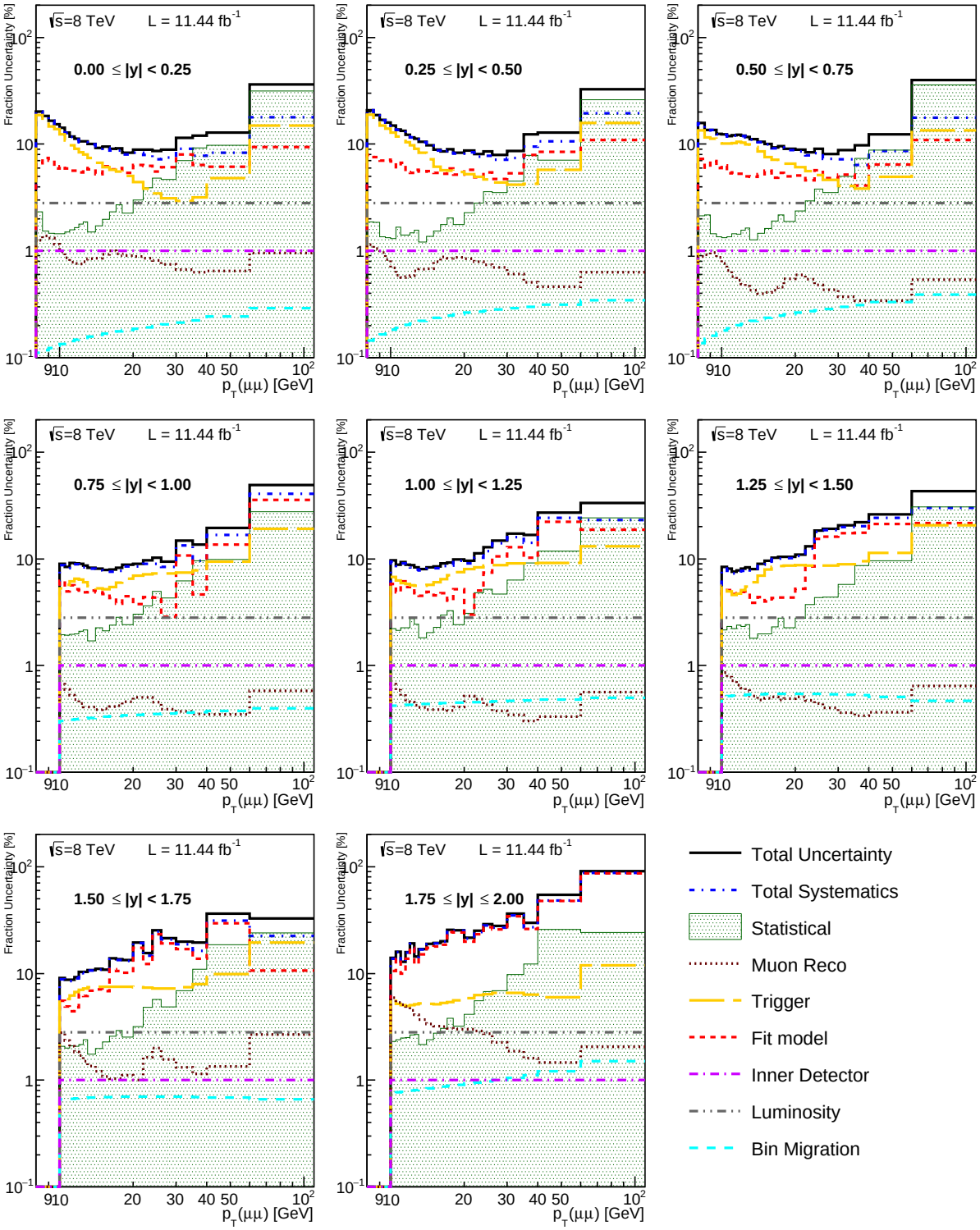

Figure 4.44: The fractional uncertainty contributions of the the prompt $\psi(2S)$ differential cross-section, shown as a function of p_T in bins of increasing rapidity.

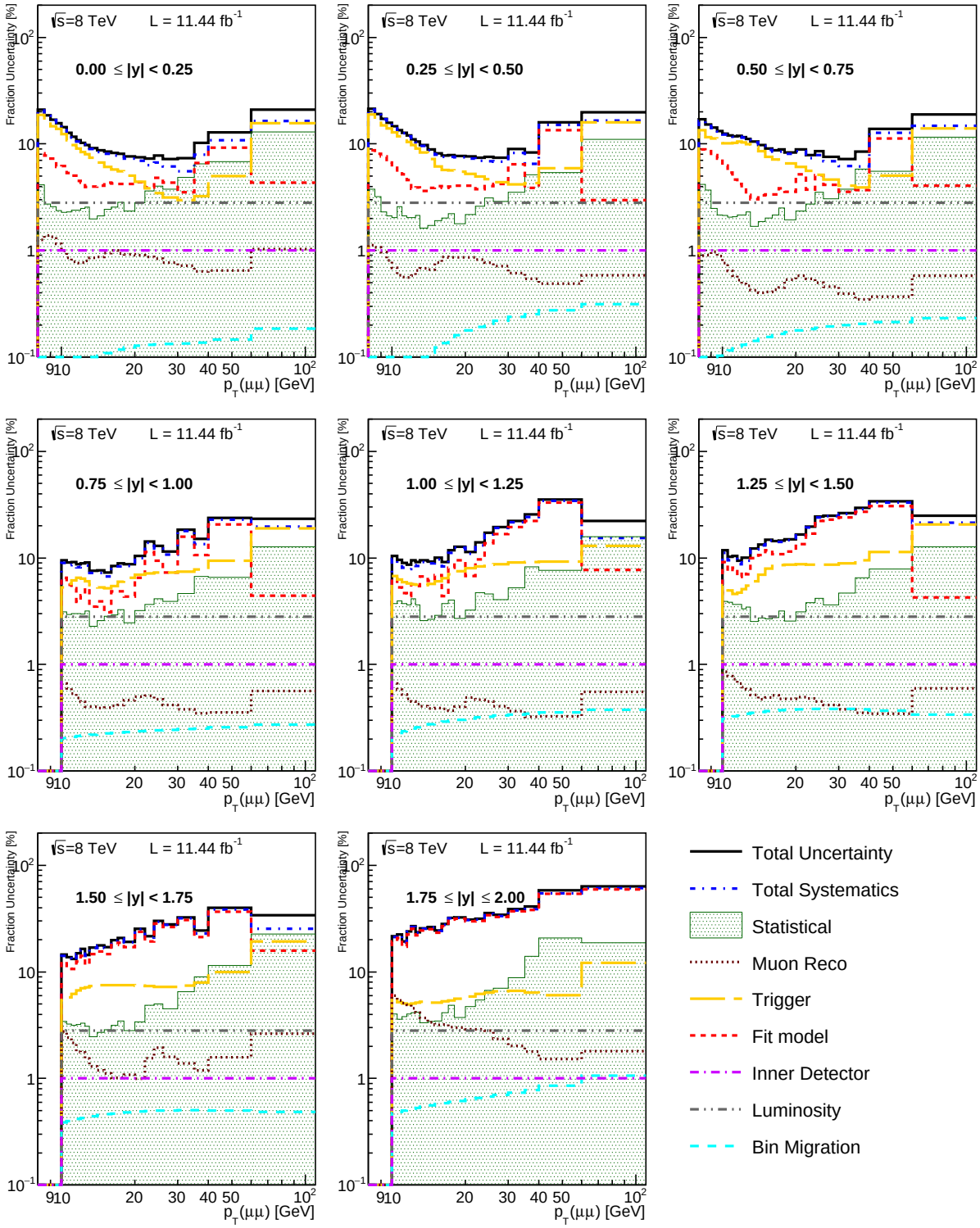

Figure 4.45: The fractional uncertainty contributions of the the non-prompt $\psi(2S)$ differential cross-section, shown as a function of p_T in bins of increasing rapidity.

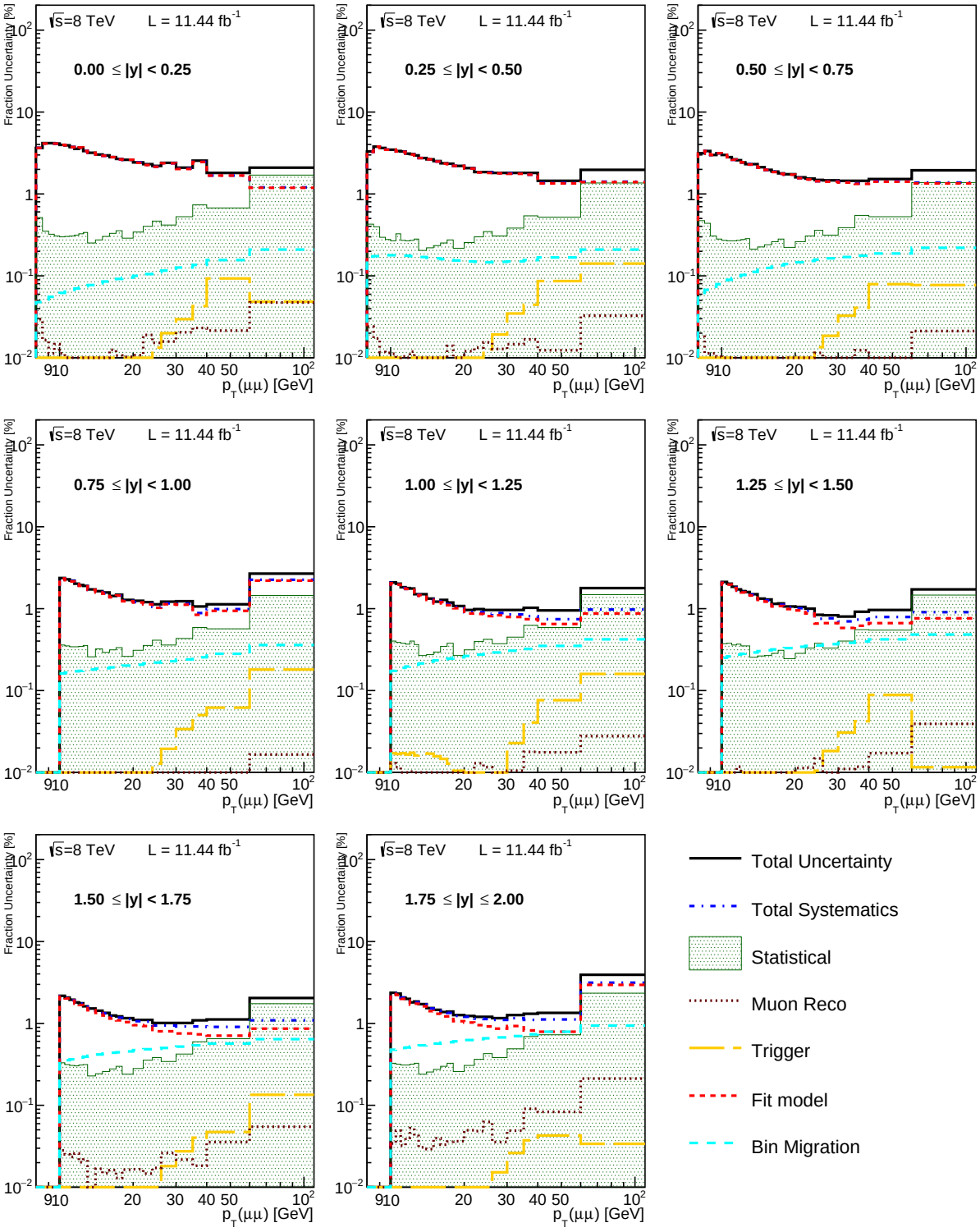

Figure 4.46: The fractional uncertainty contributions of the the J/ψ non-prompt fraction, shown as a function of p_T in bins of increasing rapidity.

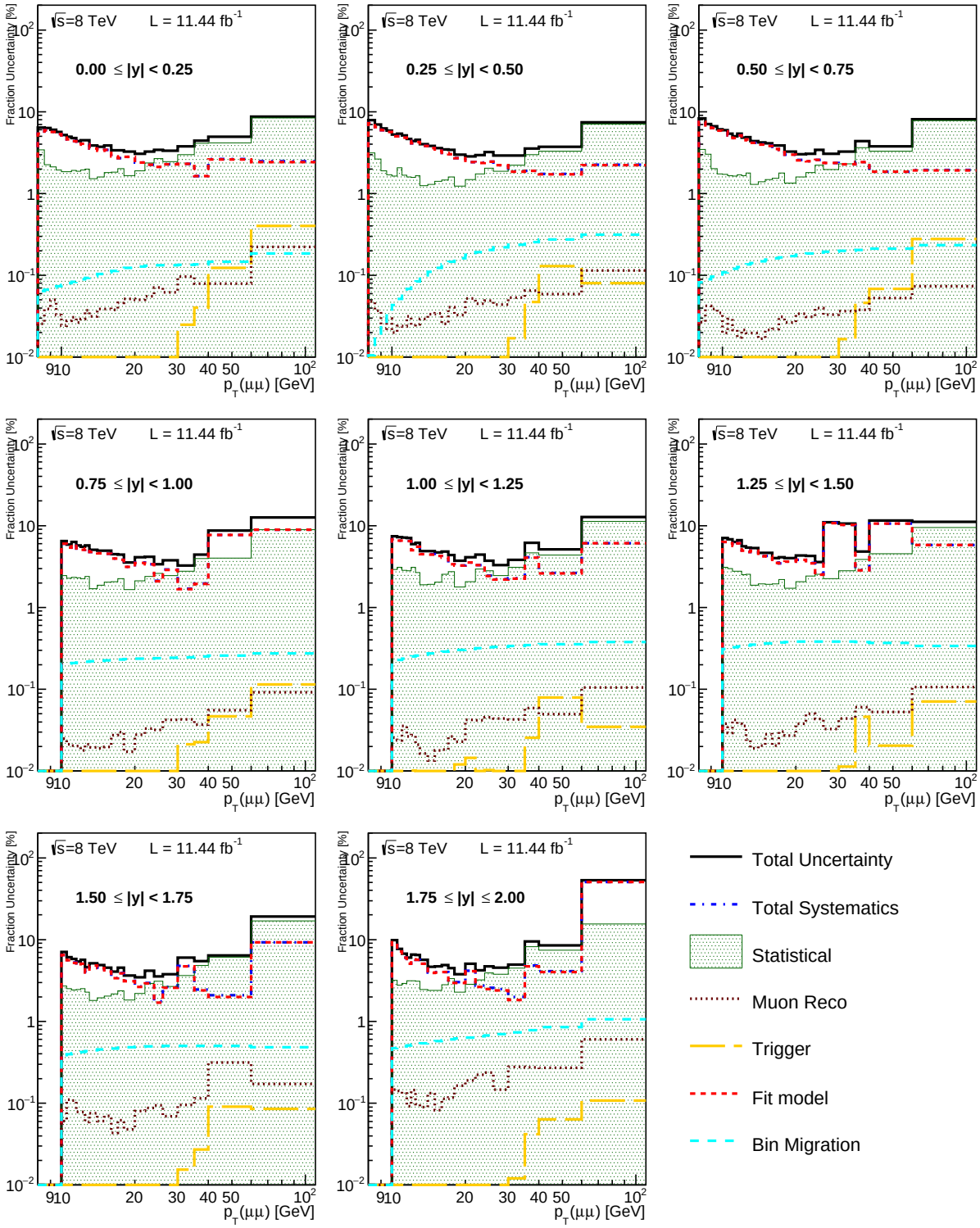

Figure 4.47: The fractional uncertainty contributions of the the $\psi(2S)$ non-prompt fraction, shown as a function of p_T in bins of increasing rapidity.

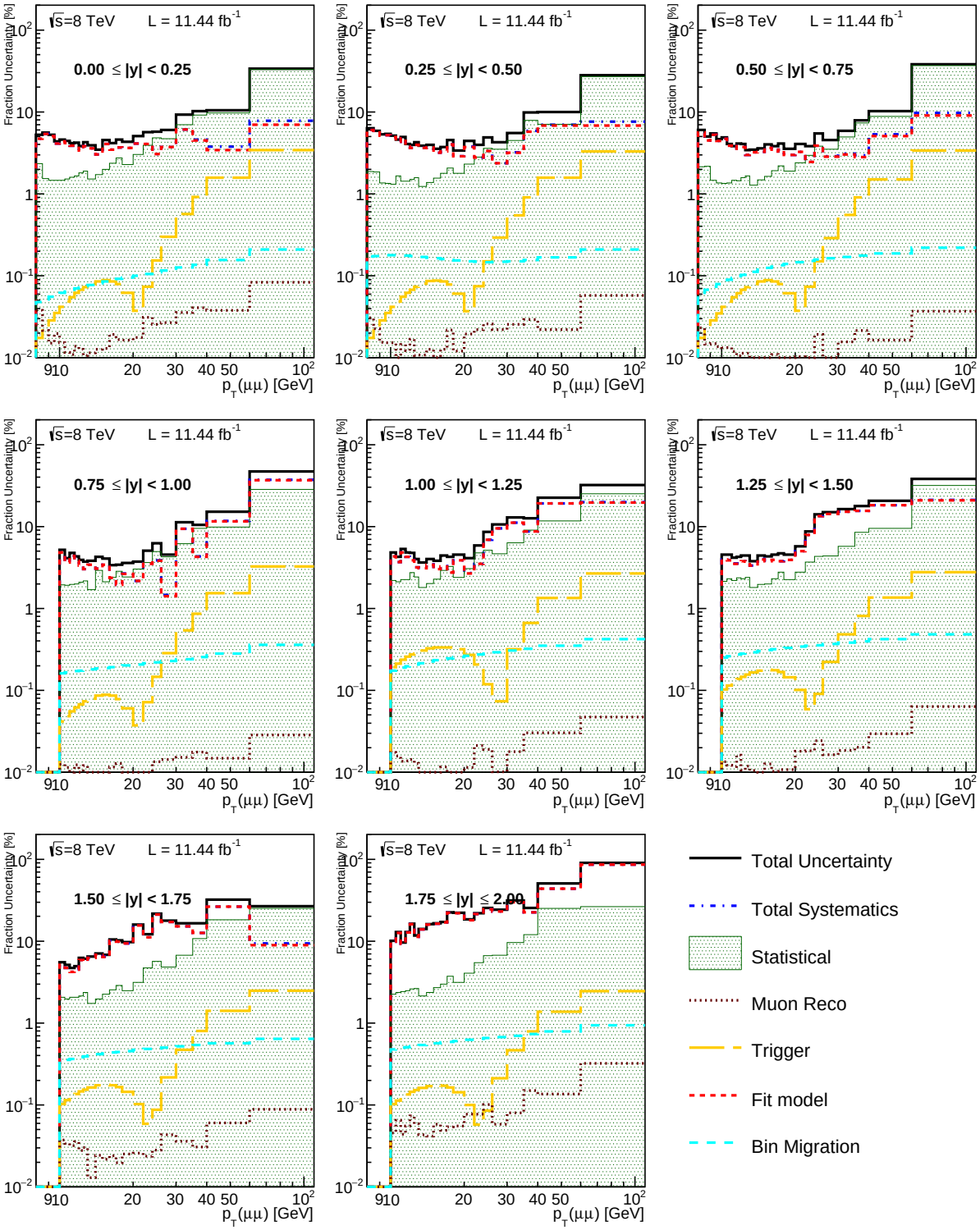

Figure 4.48: The fractional uncertainty contributions of the the prompt ratio, shown as a function of p_T in bins of increasing rapidity.

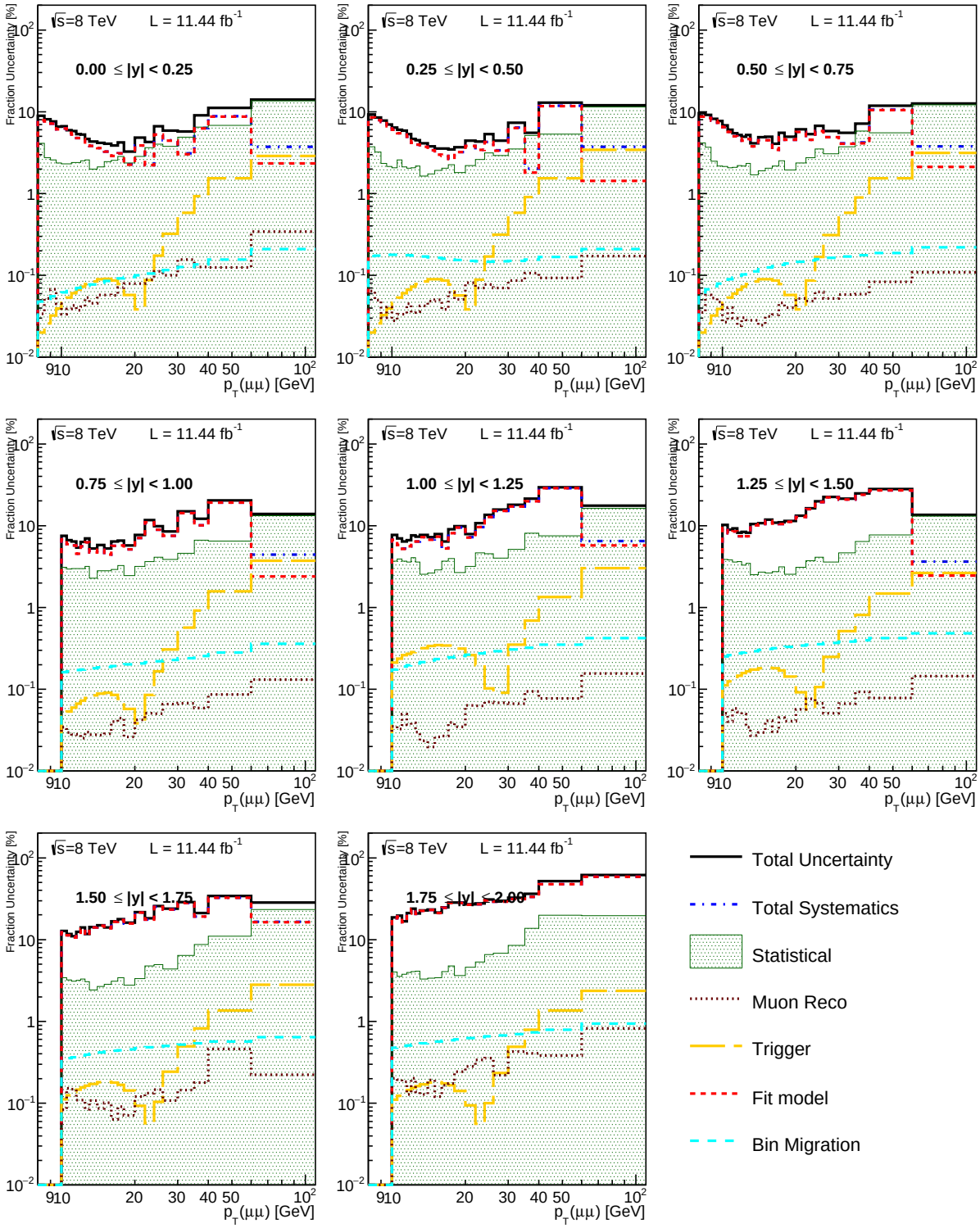

Figure 4.49: The fractional uncertainty contributions of the the non-prompt ratio, shown as a function of p_T in bins of increasing rapidity.

4.10 Spin-Alignment Correction Factors

The measurements presented here assume an unpolarised spin-alignment hypothesis for determining the correction factors. In principle, the J/ψ or $\psi(2S)$ will not be unpolarised and their polarisation may vary with p_T. In order to correct these measurements when well-measured J/ψ and $\psi(2S)$ polarisations are available, a set of correction factors are provided in tables 4.5 – 4.16 . These tables are created by altering the spin alignment hypothesis for either the J/ψ or $\psi(2S)$ meson and determining the ratio of the mean weights of new hypotheses to the original flat hypothesis. The mean weight is calculated from all the events in each di-muon p_T and rapidity analysis bin, selecting those di-muons within $\pm 2\sigma$ of the ψ mean mass position.

The effect of varying both ψ hypotheses, compared to keeping one fixed, is observed to have a small effect (less than 1%) on the final numbers, and is not considered further. For illustration purposes an example where both hypotheses have been altered to long and the results are compared to the case where one is fixed can be found on table 4.17.

4.10.1 J/ψ correction factors

	Absolute Rapidity Range							
p_T [GeV]	0.00–0.25	0.25–0.50	0.50–0.75	0.75–1.00	1.00–1.25	1.25–1.50	1.50–1.75	1.75–2.00
8.00 – 8.50	0.672	0.674	0.678	–	–	–	–	–
8.50 – 9.00	0.670	0.673	0.678	–	–	–	–	–
9.00 – 9.50	0.671	0.674	0.679	–	–	–	–	–
9.50 – 10.00	0.674	0.676	0.681	–	–	–	–	–
10.00 – 10.50	0.676	0.678	0.683	0.686	0.691	0.694	0.695	0.696
10.50 – 11.00	0.680	0.681	0.686	0.689	0.693	0.696	0.697	0.698
11.00 – 11.50	0.684	0.685	0.690	0.692	0.695	0.698	0.700	0.701
11.50 – 12.00	0.688	0.688	0.693	0.695	0.698	0.701	0.702	0.704
12.00 – 12.50	0.692	0.692	0.696	0.698	0.702	0.704	0.705	0.706
12.50 – 13.00	0.696	0.696	0.700	0.702	0.705	0.707	0.708	0.710
13.00 – 14.00	0.702	0.703	0.705	0.707	0.710	0.712	0.713	0.715
14.00 – 15.00	0.710	0.711	0.713	0.714	0.717	0.719	0.720	0.722
15.00 – 16.00	0.719	0.719	0.721	0.722	0.724	0.725	0.727	0.729
16.00 – 17.00	0.726	0.727	0.729	0.729	0.732	0.733	0.734	0.735
17.00 – 18.00	0.734	0.735	0.736	0.737	0.738	0.740	0.740	0.743
18.00 – 20.00	0.744	0.745	0.746	0.746	0.748	0.750	0.750	0.752
20.00 – 22.00	0.758	0.759	0.760	0.759	0.761	0.762	0.763	0.764
22.00 – 24.00	0.771	0.771	0.772	0.771	0.773	0.774	0.774	0.776
24.00 – 26.00	0.783	0.783	0.783	0.783	0.784	0.786	0.786	0.787
26.00 – 30.00	0.797	0.798	0.798	0.797	0.798	0.799	0.800	0.800
30.00 – 35.00	0.817	0.817	0.817	0.816	0.817	0.818	0.818	0.820
35.00 – 40.00	0.836	0.836	0.836	0.835	0.835	0.836	0.836	0.840
40.00 – 60.00	0.862	0.862	0.861	0.861	0.861	0.862	0.862	0.863
60.00 – 110.00	0.904	0.902	0.903	0.902	0.903	0.904	0.905	0.906

Table 4.5: The mean weight correction factor for J/ψ under the spin-alignment longitudinally hypothesis.

	Absolute Rapidity Range							
p_T [GeV]	0.00–0.25	0.25–0.50	0.50–0.75	0.75–1.00	1.00–1.25	1.25–1.50	1.50–1.75	1.75–2.00
8.00 – 8.50	1.326	1.321	1.311	–	–	–	–	–
8.50 – 9.00	1.326	1.320	1.309	–	–	–	–	–
9.00 – 9.50	1.322	1.316	1.306	–	–	–	–	–
9.50 – 10.00	1.317	1.312	1.302	–	–	–	–	–
10.00 – 10.50	1.311	1.306	1.297	1.291	1.283	1.278	1.275	1.273
10.50 – 11.00	1.304	1.300	1.292	1.286	1.279	1.274	1.272	1.269
11.00 – 11.50	1.297	1.293	1.286	1.280	1.275	1.270	1.268	1.265
11.50 – 12.00	1.290	1.287	1.280	1.275	1.270	1.266	1.263	1.261
12.00 – 12.50	1.283	1.280	1.274	1.270	1.264	1.261	1.259	1.257
12.50 – 13.00	1.276	1.273	1.268	1.264	1.260	1.256	1.254	1.252
13.00 – 14.00	1.265	1.264	1.259	1.256	1.252	1.249	1.247	1.245
14.00 – 15.00	1.253	1.251	1.247	1.245	1.241	1.238	1.237	1.235
15.00 – 16.00	1.240	1.239	1.236	1.234	1.231	1.229	1.227	1.225
16.00 – 17.00	1.228	1.227	1.225	1.223	1.220	1.218	1.218	1.216
17.00 – 18.00	1.218	1.217	1.215	1.213	1.211	1.209	1.209	1.206
18.00 – 20.00	1.204	1.203	1.201	1.201	1.199	1.197	1.196	1.195
20.00 – 22.00	1.186	1.186	1.185	1.185	1.183	1.182	1.181	1.180
22.00 – 24.00	1.172	1.171	1.171	1.171	1.169	1.168	1.168	1.167
24.00 – 26.00	1.159	1.159	1.158	1.158	1.157	1.156	1.156	1.154
26.00 – 30.00	1.144	1.144	1.143	1.144	1.143	1.142	1.141	1.141
30.00 – 35.00	1.125	1.125	1.125	1.125	1.124	1.124	1.124	1.122
35.00 – 40.00	1.108	1.108	1.108	1.108	1.108	1.108	1.107	1.105
40.00 – 60.00	1.087	1.086	1.087	1.087	1.087	1.087	1.087	1.086
60.00 – 110.00	1.056	1.057	1.057	1.057	1.057	1.056	1.055	1.055

Table 4.6: The mean weight correction factor for J/ψ under the spin-alignment transverse 0 hypothesis.

	Absolute Rapidity Range							
p_T [GeV]	0.00–0.25	0.25–0.50	0.50–0.75	0.75–1.00	1.00–1.25	1.25–1.50	1.50–1.75	1.75–2.00
8.00 – 8.50	1.926	1.933	1.930	–	–	–	–	–
8.50 – 9.00	1.555	1.558	1.559	–	–	–	–	–
9.00 – 9.50	1.463	1.464	1.465	–	–	–	–	–
9.50 – 10.00	1.416	1.418	1.418	–	–	–	–	–
10.00 – 10.50	1.386	1.388	1.387	1.390	1.390	1.390	1.391	1.411
10.50 – 11.00	1.363	1.365	1.365	1.367	1.367	1.366	1.368	1.382
11.00 – 11.50	1.345	1.347	1.346	1.348	1.348	1.348	1.349	1.358
11.50 – 12.00	1.330	1.331	1.331	1.333	1.333	1.332	1.333	1.340
12.00 – 12.50	1.316	1.318	1.317	1.319	1.318	1.319	1.319	1.325
12.50 – 13.00	1.304	1.305	1.305	1.307	1.307	1.307	1.306	1.311
13.00 – 14.00	1.288	1.290	1.290	1.291	1.291	1.291	1.291	1.293
14.00 – 15.00	1.270	1.271	1.271	1.272	1.272	1.271	1.272	1.272
15.00 – 16.00	1.253	1.254	1.254	1.255	1.255	1.255	1.254	1.255
16.00 – 17.00	1.239	1.240	1.240	1.241	1.240	1.240	1.241	1.240
17.00 – 18.00	1.227	1.227	1.227	1.228	1.228	1.227	1.228	1.226
18.00 – 20.00	1.211	1.211	1.211	1.212	1.212	1.211	1.211	1.210
20.00 – 22.00	1.191	1.192	1.192	1.193	1.193	1.192	1.192	1.192
22.00 – 24.00	1.175	1.176	1.176	1.177	1.176	1.176	1.176	1.175
24.00 – 26.00	1.162	1.162	1.162	1.163	1.162	1.162	1.162	1.161
26.00 – 30.00	1.146	1.146	1.146	1.147	1.146	1.146	1.146	1.146
30.00 – 35.00	1.126	1.126	1.126	1.127	1.127	1.126	1.126	1.125
35.00 – 40.00	1.109	1.109	1.109	1.110	1.110	1.109	1.109	1.107
40.00 – 60.00	1.087	1.087	1.088	1.088	1.088	1.087	1.087	1.087
60.00 – 110.00	1.056	1.057	1.057	1.057	1.057	1.056	1.056	1.055

Table 4.7: The mean weight correction factor for J/ψ under the spin-alignment transverse P hypothesis.

	Absolute Rapidity Range							
p_T [GeV]	0.00–0.25	0.25–0.50	0.50–0.75	0.75–1.00	1.00–1.25	1.25–1.50	1.50–1.75	1.75–2.00
8.00 – 8.50	1.026	1.017	1.005	–	–	–	–	–
8.50 – 9.00	1.157	1.145	1.129	–	–	–	–	–
9.00 – 9.50	1.207	1.196	1.178	–	–	–	–	–
9.50 – 10.00	1.231	1.220	1.203	–	–	–	–	–
10.00 – 10.50	1.244	1.234	1.218	1.204	1.192	1.182	1.177	1.161
10.50 – 11.00	1.250	1.241	1.227	1.214	1.202	1.193	1.188	1.175
11.00 – 11.50	1.252	1.244	1.231	1.220	1.209	1.200	1.195	1.184
11.50 – 12.00	1.253	1.246	1.234	1.223	1.213	1.206	1.201	1.191
12.00 – 12.50	1.251	1.245	1.234	1.224	1.215	1.208	1.204	1.196
12.50 – 13.00	1.248	1.243	1.233	1.224	1.216	1.210	1.206	1.199
13.00 – 14.00	1.243	1.239	1.230	1.222	1.215	1.210	1.206	1.200
14.00 – 15.00	1.236	1.231	1.224	1.218	1.212	1.207	1.204	1.200
15.00 – 16.00	1.226	1.223	1.217	1.212	1.207	1.203	1.200	1.197
16.00 – 17.00	1.218	1.215	1.210	1.206	1.201	1.197	1.195	1.193
17.00 – 18.00	1.209	1.206	1.202	1.199	1.195	1.192	1.190	1.187
18.00 – 20.00	1.197	1.195	1.192	1.189	1.186	1.183	1.182	1.180
20.00 – 22.00	1.182	1.181	1.178	1.177	1.174	1.172	1.170	1.170
22.00 – 24.00	1.168	1.167	1.166	1.165	1.162	1.161	1.160	1.159
24.00 – 26.00	1.156	1.156	1.154	1.153	1.152	1.150	1.150	1.148
26.00 – 30.00	1.142	1.141	1.140	1.140	1.139	1.137	1.137	1.136
30.00 – 35.00	1.124	1.123	1.123	1.123	1.122	1.121	1.121	1.119
35.00 – 40.00	1.107	1.107	1.107	1.107	1.107	1.106	1.106	1.103
40.00 – 60.00	1.087	1.086	1.087	1.086	1.087	1.086	1.086	1.085
60.00 – 110.00	1.056	1.057	1.057	1.057	1.056	1.056	1.055	1.055

Table 4.8: The mean weight correction factor for J/ψ under the spin-alignment transverse M hypothesis.

	Absolute Rapidity Range							
p_T [GeV]	0.00–0.25	0.25–0.50	0.50–0.75	0.75–1.00	1.00–1.25	1.25–1.50	1.50–1.75	1.75–2.00
8.00 – 8.50	1.016	1.048	1.074	–	–	–	–	–
8.50 – 9.00	1.019	1.056	1.087	–	–	–	–	–
9.00 – 9.50	1.019	1.055	1.086	–	–	–	–	–
9.50 – 10.00	1.018	1.053	1.083	–	–	–	–	–
10.00 – 10.50	1.017	1.051	1.079	1.101	1.117	1.127	1.134	1.138
10.50 – 11.00	1.016	1.048	1.075	1.096	1.110	1.120	1.126	1.131
11.00 – 11.50	1.015	1.045	1.071	1.090	1.104	1.113	1.119	1.124
11.50 – 12.00	1.014	1.043	1.067	1.085	1.098	1.107	1.113	1.117
12.00 – 12.50	1.014	1.040	1.063	1.080	1.093	1.101	1.106	1.111
12.50 – 13.00	1.013	1.038	1.059	1.076	1.087	1.095	1.100	1.104
13.00 – 14.00	1.012	1.035	1.055	1.070	1.080	1.088	1.092	1.096
14.00 – 15.00	1.011	1.031	1.049	1.062	1.072	1.078	1.082	1.085
15.00 – 16.00	1.010	1.028	1.044	1.056	1.065	1.070	1.074	1.076
16.00 – 17.00	1.009	1.025	1.040	1.050	1.058	1.063	1.067	1.069
17.00 – 18.00	1.008	1.023	1.036	1.046	1.053	1.057	1.060	1.062
18.00 – 20.00	1.007	1.020	1.031	1.040	1.046	1.050	1.053	1.054
20.00 – 22.00	1.006	1.017	1.026	1.033	1.039	1.042	1.044	1.045
22.00 – 24.00	1.005	1.014	1.022	1.028	1.033	1.036	1.038	1.039
24.00 – 26.00	1.004	1.012	1.019	1.024	1.028	1.030	1.032	1.033
26.00 – 30.00	1.004	1.010	1.016	1.020	1.023	1.025	1.026	1.027
30.00 – 35.00	1.003	1.008	1.012	1.015	1.018	1.019	1.020	1.021
35.00 – 40.00	1.002	1.006	1.009	1.012	1.013	1.015	1.015	1.015
40.00 – 60.00	1.001	1.004	1.006	1.008	1.009	1.010	1.010	1.010
60.00 – 110.00	1.001	1.002	1.003	1.003	1.004	1.004	1.004	1.005

Table 4.9: The mean weight correction factor for J/ψ under the spin-alignment off-plane P hypothesis.

	Absolute Rapidity Range							
p_T [GeV]	0.00–0.25	0.25–0.50	0.50–0.75	0.75–1.00	1.00–1.25	1.25–1.50	1.50–1.75	1.75–2.00
8.00 – 8.50	0.985	0.957	0.936	–	–	–	–	–
8.50 – 9.00	0.982	0.950	0.926	–	–	–	–	–
9.00 – 9.50	0.982	0.950	0.926	–	–	–	–	–
9.50 – 10.00	0.983	0.952	0.929	–	–	–	–	–
10.00 – 10.50	0.984	0.954	0.932	0.916	0.905	0.898	0.894	0.891
10.50 – 11.00	0.985	0.956	0.935	0.919	0.909	0.903	0.899	0.895
11.00 – 11.50	0.985	0.959	0.938	0.923	0.913	0.907	0.903	0.900
11.50 – 12.00	0.986	0.961	0.941	0.927	0.918	0.911	0.908	0.905
12.00 – 12.50	0.987	0.963	0.944	0.931	0.922	0.916	0.912	0.909
12.50 – 13.00	0.988	0.965	0.947	0.934	0.925	0.920	0.916	0.913
13.00 – 14.00	0.988	0.967	0.951	0.939	0.930	0.925	0.922	0.919
14.00 – 15.00	0.990	0.971	0.955	0.944	0.937	0.932	0.929	0.927
15.00 – 16.00	0.991	0.974	0.960	0.950	0.943	0.938	0.936	0.934
16.00 – 17.00	0.991	0.976	0.963	0.954	0.948	0.944	0.941	0.939
17.00 – 18.00	0.992	0.978	0.967	0.958	0.952	0.949	0.946	0.945
18.00 – 20.00	0.993	0.981	0.971	0.963	0.958	0.954	0.952	0.951
20.00 – 22.00	0.994	0.984	0.975	0.969	0.964	0.961	0.959	0.958
22.00 – 24.00	0.995	0.986	0.979	0.973	0.969	0.967	0.965	0.964
24.00 – 26.00	0.996	0.988	0.982	0.977	0.973	0.971	0.970	0.969
26.00 – 30.00	0.996	0.990	0.985	0.981	0.978	0.976	0.975	0.974
30.00 – 35.00	0.997	0.992	0.988	0.985	0.983	0.982	0.981	0.980
35.00 – 40.00	0.998	0.994	0.991	0.989	0.987	0.986	0.985	0.985
40.00 – 60.00	0.999	0.996	0.994	0.992	0.991	0.991	0.990	0.990
60.00 – 110.00	0.999	0.998	0.997	0.997	0.996	0.996	0.996	0.996

Table 4.10: The mean weight correction factor for J/ψ under the spin-alignment off-plane N hypothesis.

4.10.2 $\psi(2S)$ correction factors

	Absolute Rapidity Range							
p_T [GeV]	0.00–0.25	0.25–0.50	0.50–0.75	0.75–1.00	1.00–1.25	1.25–1.50	1.50–1.75	1.75–2.00
8.00 – 8.50	0.672	0.677	0.686	–	–	–	–	–
8.50 – 9.00	0.674	0.680	0.689	–	–	–	–	–
9.00 – 9.50	0.677	0.682	0.691	–	–	–	–	–
9.50 – 10.00	0.680	0.684	0.692	–	–	–	–	–
10.00 – 10.50	0.683	0.688	0.695	0.702	0.709	0.713	0.717	0.721
10.50 – 11.00	0.687	0.692	0.698	0.705	0.710	0.715	0.718	0.722
11.00 – 11.50	0.692	0.695	0.701	0.708	0.714	0.716	0.718	0.725
11.50 – 12.00	0.695	0.698	0.704	0.710	0.715	0.718	0.721	0.725
12.00 – 12.50	0.700	0.703	0.708	0.713	0.718	0.721	0.723	0.728
12.50 – 13.00	0.704	0.706	0.711	0.716	0.721	0.722	0.726	0.730
13.00 – 14.00	0.710	0.713	0.717	0.722	0.725	0.727	0.730	0.733
14.00 – 15.00	0.719	0.721	0.724	0.728	0.731	0.733	0.736	0.738
15.00 – 16.00	0.727	0.728	0.732	0.735	0.737	0.740	0.741	0.743
16.00 – 17.00	0.735	0.737	0.739	0.742	0.743	0.746	0.748	0.750
17.00 – 18.00	0.742	0.744	0.746	0.750	0.750	0.753	0.755	0.755
18.00 – 20.00	0.753	0.754	0.756	0.759	0.760	0.761	0.762	0.765
20.00 – 22.00	0.767	0.768	0.769	0.771	0.773	0.773	0.775	0.775
22.00 – 24.00	0.779	0.779	0.782	0.783	0.784	0.785	0.785	0.788
24.00 – 26.00	0.791	0.791	0.793	0.794	0.793	0.795	0.795	0.795
26.00 – 30.00	0.805	0.804	0.806	0.807	0.808	0.809	0.809	0.811
30.00 – 35.00	0.823	0.823	0.824	0.824	0.826	0.826	0.828	0.828
35.00 – 40.00	0.841	0.841	0.840	0.842	0.843	0.842	0.843	0.843
40.00 – 60.00	0.866	0.867	0.866	0.868	0.868	0.866	0.868	0.870
60.00 – 110.00	0.905	0.906	0.906	0.909	0.907	0.903	0.906	0.905

Table 4.11: The mean weight correction factor for $\psi(2S)$ under the spin-alignment longitudinally hypothesis.

	Absolute Rapidity Range							
p_T [GeV]	0.00–0.25	0.25–0.50	0.50–0.75	0.75–1.00	1.00–1.25	1.25–1.50	1.50–1.75	1.75–2.00
8.00 – 8.50	1.325	1.316	1.301	–	–	–	–	–
8.50 – 9.00	1.321	1.311	1.295	–	–	–	–	–
9.00 – 9.50	1.316	1.307	1.291	–	–	–	–	–
9.50 – 10.00	1.310	1.301	1.288	–	–	–	–	–
10.00 – 10.50	1.303	1.295	1.283	1.272	1.261	1.254	1.249	1.244
10.50 – 11.00	1.296	1.289	1.278	1.267	1.259	1.252	1.247	1.241
11.00 – 11.50	1.289	1.283	1.273	1.262	1.254	1.250	1.246	1.238
11.50 – 12.00	1.282	1.276	1.267	1.258	1.251	1.246	1.242	1.236
12.00 – 12.50	1.274	1.270	1.261	1.253	1.247	1.242	1.239	1.233
12.50 – 13.00	1.267	1.263	1.256	1.248	1.242	1.239	1.235	1.230
13.00 – 14.00	1.257	1.254	1.247	1.241	1.236	1.232	1.229	1.225
14.00 – 15.00	1.244	1.241	1.236	1.230	1.227	1.223	1.220	1.217
15.00 – 16.00	1.232	1.230	1.225	1.221	1.217	1.215	1.213	1.211
16.00 – 17.00	1.221	1.218	1.215	1.211	1.209	1.206	1.204	1.202
17.00 – 18.00	1.210	1.208	1.206	1.202	1.200	1.197	1.195	1.195
18.00 – 20.00	1.197	1.195	1.193	1.190	1.188	1.187	1.186	1.184
20.00 – 22.00	1.180	1.179	1.177	1.175	1.173	1.172	1.171	1.171
22.00 – 24.00	1.165	1.165	1.163	1.162	1.161	1.159	1.159	1.157
24.00 – 26.00	1.153	1.153	1.151	1.150	1.150	1.149	1.149	1.149
26.00 – 30.00	1.138	1.139	1.138	1.136	1.136	1.135	1.135	1.133
30.00 – 35.00	1.121	1.121	1.120	1.119	1.119	1.118	1.117	1.117
35.00 – 40.00	1.105	1.104	1.105	1.104	1.103	1.104	1.103	1.103
40.00 – 60.00	1.084	1.083	1.084	1.083	1.083	1.084	1.083	1.081
60.00 – 110.00	1.056	1.055	1.055	1.053	1.054	1.057	1.055	1.056

Table 4.12: The mean weight correction factor for $\psi(2S)$ under the spin-alignment transverse 0 hypothesis.

	Absolute Rapidity Range							
p_T [GeV]	0.00–0.25	0.25–0.50	0.50–0.75	0.75–1.00	1.00–1.25	1.25–1.50	1.50–1.75	1.75–2.00
8.00 – 8.50	2.029	2.023	2.022	–	–	–	–	–
8.50 – 9.00	1.620	1.620	1.618	–	–	–	–	–
9.00 – 9.50	1.504	1.504	1.502	–	–	–	–	–
9.50 – 10.00	1.444	1.444	1.443	–	–	–	–	–
10.00 – 10.50	1.405	1.405	1.404	1.404	1.402	1.401	1.400	1.500
10.50 – 11.00	1.377	1.377	1.376	1.375	1.375	1.373	1.373	1.443
11.00 – 11.50	1.354	1.354	1.354	1.352	1.351	1.353	1.353	1.403
11.50 – 12.00	1.336	1.336	1.335	1.334	1.335	1.334	1.333	1.375
12.00 – 12.50	1.320	1.320	1.320	1.319	1.319	1.319	1.318	1.351
12.50 – 13.00	1.306	1.307	1.306	1.305	1.304	1.306	1.304	1.331
13.00 – 14.00	1.289	1.289	1.289	1.288	1.288	1.288	1.287	1.308
14.00 – 15.00	1.268	1.269	1.268	1.267	1.268	1.267	1.266	1.281
15.00 – 16.00	1.251	1.251	1.250	1.251	1.251	1.250	1.250	1.261
16.00 – 17.00	1.236	1.236	1.236	1.236	1.236	1.235	1.235	1.242
17.00 – 18.00	1.223	1.222	1.223	1.222	1.223	1.221	1.221	1.227
18.00 – 20.00	1.206	1.206	1.206	1.205	1.206	1.206	1.206	1.208
20.00 – 22.00	1.186	1.186	1.186	1.186	1.186	1.186	1.185	1.187
22.00 – 24.00	1.170	1.171	1.170	1.170	1.170	1.170	1.170	1.169
24.00 – 26.00	1.157	1.157	1.156	1.156	1.157	1.157	1.157	1.158
26.00 – 30.00	1.141	1.142	1.141	1.141	1.141	1.140	1.141	1.140
30.00 – 35.00	1.122	1.122	1.122	1.122	1.122	1.122	1.121	1.121
35.00 – 40.00	1.106	1.105	1.106	1.106	1.105	1.106	1.105	1.105
40.00 – 60.00	1.085	1.084	1.085	1.084	1.084	1.085	1.084	1.083
60.00 – 110.00	1.056	1.055	1.055	1.054	1.054	1.057	1.055	1.056

Table 4.13: The mean weight correction factor for $\psi(2S)$ under the spin-alignment transverse P hypothesis.

	Absolute Rapidity Range							
p_T [GeV]	0.00–0.25	0.25–0.50	0.50–0.75	0.75–1.00	1.00–1.25	1.25–1.50	1.50–1.75	1.75–2.00
8.00 – 8.50	0.995	0.986	0.970	–	–	–	–	–
8.50 – 9.00	1.116	1.102	1.081	–	–	–	–	–
9.00 – 9.50	1.170	1.156	1.133	–	–	–	–	–
9.50 – 10.00	1.199	1.185	1.163	–	–	–	–	–
10.00 – 10.50	1.215	1.202	1.182	1.163	1.146	1.135	1.127	1.075
10.50 – 11.00	1.225	1.212	1.194	1.175	1.161	1.150	1.142	1.098
11.00 – 11.50	1.230	1.218	1.201	1.184	1.170	1.161	1.155	1.114
11.50 – 12.00	1.232	1.222	1.206	1.190	1.178	1.169	1.162	1.127
12.00 – 12.50	1.232	1.223	1.208	1.194	1.182	1.174	1.168	1.137
12.50 – 13.00	1.231	1.223	1.210	1.196	1.185	1.178	1.172	1.146
13.00 – 14.00	1.228	1.220	1.209	1.197	1.188	1.181	1.176	1.154
14.00 – 15.00	1.221	1.215	1.206	1.196	1.188	1.182	1.177	1.161
15.00 – 16.00	1.214	1.209	1.200	1.193	1.186	1.181	1.177	1.165
16.00 – 17.00	1.206	1.202	1.195	1.188	1.183	1.178	1.175	1.166
17.00 – 18.00	1.198	1.195	1.189	1.183	1.179	1.174	1.171	1.165
18.00 – 20.00	1.188	1.184	1.180	1.175	1.171	1.168	1.166	1.161
20.00 – 22.00	1.173	1.171	1.168	1.164	1.161	1.159	1.157	1.154
22.00 – 24.00	1.161	1.160	1.156	1.154	1.151	1.149	1.149	1.145
24.00 – 26.00	1.150	1.149	1.146	1.144	1.143	1.141	1.141	1.140
26.00 – 30.00	1.136	1.136	1.134	1.132	1.131	1.129	1.129	1.127
30.00 – 35.00	1.119	1.119	1.117	1.117	1.115	1.115	1.113	1.113
35.00 – 40.00	1.104	1.103	1.103	1.102	1.101	1.101	1.100	1.100
40.00 – 60.00	1.084	1.083	1.083	1.082	1.082	1.083	1.082	1.080
60.00 – 110.00	1.056	1.054	1.055	1.053	1.054	1.057	1.055	1.055

Table 4.14: The mean weight correction factor for $\psi(2S)$ under the spin-alignment transverse M hypothesis.

	Absolute Rapidity Range							
p_T [GeV]	0.00–0.25	0.25–0.50	0.50–0.75	0.75–1.00	1.00–1.25	1.25–1.50	1.50–1.75	1.75–2.00
8.00 – 8.50	1.018	1.053	1.081	–	–	–	–	–
8.50 – 9.00	1.021	1.062	1.095	–	–	–	–	–
9.00 – 9.50	1.021	1.062	1.096	–	–	–	–	–
9.50 – 10.00	1.020	1.060	1.094	–	–	–	–	–
10.00 – 10.50	1.020	1.057	1.089	1.114	1.130	1.140	1.146	1.145
10.50 – 11.00	1.018	1.055	1.085	1.108	1.124	1.133	1.139	1.142
11.00 – 11.50	1.017	1.052	1.080	1.102	1.117	1.127	1.133	1.137
11.50 – 12.00	1.017	1.049	1.076	1.096	1.111	1.120	1.126	1.132
12.00 – 12.50	1.016	1.046	1.072	1.091	1.105	1.113	1.119	1.125
12.50 – 13.00	1.015	1.043	1.068	1.086	1.099	1.108	1.112	1.119
13.00 – 14.00	1.013	1.040	1.062	1.079	1.091	1.099	1.104	1.111
14.00 – 15.00	1.012	1.036	1.056	1.071	1.082	1.089	1.093	1.099
15.00 – 16.00	1.011	1.032	1.050	1.064	1.073	1.080	1.084	1.090
16.00 – 17.00	1.010	1.029	1.045	1.057	1.067	1.072	1.076	1.081
17.00 – 18.00	1.009	1.026	1.041	1.052	1.060	1.065	1.068	1.073
18.00 – 20.00	1.008	1.023	1.036	1.045	1.053	1.057	1.060	1.063
20.00 – 22.00	1.007	1.019	1.030	1.038	1.044	1.048	1.050	1.053
22.00 – 24.00	1.006	1.016	1.025	1.032	1.037	1.040	1.043	1.044
24.00 – 26.00	1.005	1.014	1.022	1.028	1.032	1.035	1.037	1.038
26.00 – 30.00	1.004	1.012	1.018	1.023	1.026	1.029	1.030	1.031
30.00 – 35.00	1.003	1.009	1.014	1.017	1.020	1.022	1.023	1.023
35.00 – 40.00	1.002	1.007	1.010	1.013	1.015	1.017	1.017	1.018
40.00 – 60.00	1.002	1.004	1.007	1.009	1.010	1.011	1.012	1.012
60.00 – 110.00	1.001	1.002	1.003	1.004	1.004	1.005	1.005	1.005

Table 4.15: The mean weight correction factor for $\psi(2S)$ under the spin-alignment off-plane P hypothesis.

	Absolute Rapidity Range							
p_T [GeV]	0.00–0.25	0.25–0.50	0.50–0.75	0.75–1.00	1.00–1.25	1.25–1.50	1.50–1.75	1.75–2.00
8.00 – 8.50	0.983	0.952	0.931	–	–	–	–	–
8.50 – 9.00	0.980	0.945	0.920	–	–	–	–	–
9.00 – 9.50	0.980	0.945	0.919	–	–	–	–	–
9.50 – 10.00	0.981	0.946	0.921	–	–	–	–	–
10.00 – 10.50	0.981	0.949	0.924	0.908	0.897	0.891	0.887	0.888
10.50 – 11.00	0.982	0.951	0.928	0.912	0.901	0.895	0.891	0.890
11.00 – 11.50	0.983	0.953	0.931	0.916	0.906	0.899	0.895	0.893
11.50 – 12.00	0.984	0.956	0.934	0.919	0.910	0.903	0.900	0.896
12.00 – 12.50	0.985	0.958	0.937	0.923	0.914	0.908	0.904	0.900
12.50 – 13.00	0.986	0.960	0.940	0.927	0.918	0.911	0.908	0.904
13.00 – 14.00	0.987	0.963	0.945	0.932	0.923	0.917	0.914	0.910
14.00 – 15.00	0.988	0.967	0.950	0.938	0.930	0.925	0.922	0.917
15.00 – 16.00	0.989	0.970	0.955	0.944	0.936	0.931	0.928	0.924
16.00 – 17.00	0.990	0.973	0.959	0.949	0.941	0.937	0.934	0.931
17.00 – 18.00	0.991	0.975	0.962	0.953	0.946	0.943	0.940	0.936
18.00 – 20.00	0.992	0.978	0.967	0.958	0.953	0.949	0.946	0.944
20.00 – 22.00	0.993	0.981	0.972	0.965	0.960	0.956	0.955	0.952
22.00 – 24.00	0.994	0.984	0.976	0.970	0.965	0.963	0.961	0.960
24.00 – 26.00	0.995	0.986	0.979	0.974	0.970	0.967	0.966	0.965
26.00 – 30.00	0.996	0.989	0.983	0.978	0.975	0.973	0.972	0.971
30.00 – 35.00	0.997	0.991	0.987	0.983	0.981	0.979	0.978	0.978
35.00 – 40.00	0.998	0.993	0.990	0.987	0.985	0.984	0.983	0.983
40.00 – 60.00	0.998	0.996	0.993	0.992	0.990	0.989	0.989	0.989
60.00 – 110.00	0.999	0.998	0.997	0.996	0.996	0.995	0.995	0.995

Table 4.16: The mean weight correction factor for $\psi(2S)$ under the spin-alignment off-plane N hypothesis.

4.10.3 Example of altering both hypotheses

Here as a test case, two hypotheses changed at the same time and the correction factors were compared to the case where only one hypothesis was considered. The results from this test are shown in Table 4.17 where the majority of points have a difference less than 1%.

	Absolute Rapidity Range							
p_T [GeV]	0.00–0.25	0.25–0.50	0.50–0.75	0.75–1.00	1.00–1.25	1.25–1.50	1.50–1.75	1.75–2.00
8.00 - 8.50	0.468	0.217	0.100	-	-	-	-	-
8.50 - 9.00	0.049	0.255	0.360	-	-	-	-	-
9.00 - 9.50	0.306	0.475	0.478	-	-	-	-	-
9.50 - 10.00	0.423	0.623	0.622	-	-	-	-	-
10.00 - 10.50	0.567	0.711	0.699	0.976	0.973	0.935	1.065	1.224
10.50 - 11.00	0.586	0.815	0.747	1.005	0.981	0.921	1.055	1.119
11.00 - 11.50	0.649	0.834	0.788	0.999	1.017	0.962	1.021	1.040
11.50 - 12.00	0.750	0.953	0.851	1.041	1.044	1.013	1.043	1.016
12.00 - 12.50	0.763	0.942	0.884	1.076	1.001	1.066	1.088	1.090
12.50 - 13.00	0.823	0.973	0.890	1.089	1.075	1.055	1.027	1.023
13.00 - 14.00	0.809	0.980	0.964	1.129	1.087	1.088	1.073	0.941
14.00 - 15.00	0.932	0.991	0.984	1.151	1.121	0.999	1.084	0.901
15.00 - 16.00	0.868	1.001	0.997	1.154	1.129	1.082	0.954	0.845
16.00 - 17.00	0.908	0.995	0.975	1.120	1.012	0.971	1.043	0.879
17.00 - 18.00	0.908	0.956	0.992	1.069	1.085	0.958	1.036	0.742
18.00 - 20.00	0.931	0.966	0.968	1.113	1.071	0.943	0.974	0.790
20.00 - 22.00	0.892	0.962	0.951	1.120	1.071	0.947	0.919	0.878
22.00 - 24.00	0.879	0.904	0.948	1.083	0.942	0.954	0.949	0.799
24.00 - 26.00	0.802	0.857	0.883	0.968	0.916	0.783	0.820	0.649
26.00 - 30.00	0.838	0.754	0.799	0.960	0.865	0.745	0.750	0.705
30.00 - 35.00	0.685	0.678	0.722	0.903	0.806	0.690	0.724	0.494
35.00 - 40.00	0.505	0.542	0.603	0.706	0.715	0.632	0.594	0.200
40.00 - 60.00	0.428	0.461	0.461	0.479	0.537	0.380	0.394	0.398
60.00 - 110.00	0.158	0.331	0.226	0.326	0.221	0.046	0.094	0.104

Table 4.17: The relative difference in percent between correction factors calculated with one hypothesis fixed and both hypotheses altered. For this example the comparison took place between: J/ψ under the spin-alignment hypothesis long and J/ψ and $\psi(2S)$ under the spin-alignment hypothesis long. The majority of the points have a difference less than 1%.

Chapter 5

Study of the Decay $\chi_b \to J/\psi J/\psi$

As mentioned before, the non-relativistic nature of heavy quark-antiquark bound states, or heavy quarkonia, provides a valid component in order to better understand the nature of Quantum Chromodynamics (QCD) close to the boundary between the perturbative and non-perturbative regimes. During the LHC era, a large amount of such $q\bar{q}$ states could be produced inside the hadron collider. This large number of heavy quarkonium states make the accurate study on this system possible. On the other hand, the large scale of the heavy quark mass allows people to investigate some of its properties within perturbative QCD.

The production rates for P-wave spin-triplet bottomonium states χ_{bJ}, $(J = 0,\ 1,\ 2)$ decays into double charmonium states were calculated only recently using various theoretical models after a first attempt about 30 years ago with a perturbative QCD method [58].

The authors of Ref. [59] calculated $\chi_{\rm b} \to J/\psi J/\psi$ in the framework of the NRQCD factorization formalism, including second-order relativistic corrections in the relative charm-quark velocity u_c, as well as an electromagnetic correction. The branching fraction is predicted to be of the order 10^{-5} for $\chi_{b0} \to J/\psi J/\psi$ and 10^{-11} for $\chi_{b2} \to J/\psi J/\psi$.

A blinded analysis has been performed using ATLAS 2010 data [60] quoting an upper limit for the branching ratio of this decay at 5.7×10^{-3} at 95% confidence level.

Here, a blinded analysis is presented using ATLAS 2012 data for the study of the $\chi_{\rm b} \to J/\psi J/\psi \to \mu^+\mu^-\mu^+\mu^-$ decay.

5.1 Analysis Methodology

The strategy follows a single bin CL_s based on a statistical extraction approach and since the branching fraction is not yet measured a blinded signal region is established. The signal "blinding box" is determined by the cuts described in details in 5.3.2 using the signal Monte Carlo 5.2. All events belonging to the "blinding box" are excluded from any step of the presented analysis till the "box opening".

The data events outside of the signal "blinding box" are characterized as "sidebands". The sidebands are going to be used for the optimization procedure. Since

at the final stage ("box opening") the machinery will be run on data and estimate the number of background events in the signal region via the fit model, there is no need to use half of the sidebands.

For the selection criteria optimization, signal Monte Carlo events are used for the characterization of the signal behavior of each discriminating variable in combination to half of the sidebands for the characterization of the background in each variable. The cuts are optimized with respect to some objective figure of merit [61] like:

$$P = \frac{\epsilon_{sig}}{1 + \sqrt{N_{bck}}} \tag{5.1}$$

where ϵ_{sig} is the efficiency of the signal and N_{bck} is the (expected) number of background events in the signal region. The ϵ_{sig} and N_{bck} are obtained from signal Monte Carlo for signal (efficiency) and from sidebands for background, while the actual signal region remains "blinded".

Two methods are used for the selection criteria optimization. At the beginning the "N-1" technique is tried (described in Section 5.4.2) but oscillations among the optimum cuts on the discriminating variables made this approach unstable. The second method, which established the final set of cuts was a simultaneous multidimensional optimization of the discriminating variables (Section 5.4.2).

The final measurement (observation or limit on signal events or branching fraction) is going to be derived using the following formula:

$$\mathcal{B}\left(\chi_{\mathrm{b}} \to J/\psi J/\psi \to \mu^+\mu^-\mu^+\mu^-\right) = \frac{1}{\epsilon A \cdot \sigma \cdot \mathcal{B}^2\left(J/\psi \to \mu^+\mu^-\right) \cdot \mathcal{L}} \cdot N_{J/\psi J/\psi} \tag{5.2}$$

where $N_{J/\psi J/\psi}$ is the number of observed events, ϵA is the efficiency times acceptance, σ the cross-section, $\mathcal{L}$ the integrated luminosity and $\mathcal{B}\left(J/\psi \to \mu^+\mu^-\right)$ is the decay fraction of $J/\psi \to \mu^+\mu^-$channel.

The final number of signal events can be estimated from the number of observed events in the signal region and the number of expected background events in this region, where the background is acquired from the fit model. A limit on $N_{J/\psi J/\psi}$ automatically reflects into a limit on $\mathcal{B}\left(\chi_{\mathrm{b}} \to J/\psi J/\psi \to \mu^+\mu^-\mu^+\mu^-\right)$ through a multiplicative coefficient, often referred to as Single Event Sensitivity (SES):

$$SES = \frac{1}{\epsilon A \cdot \sigma \cdot \mathcal{B}^2\left(J/\psi \to \mu^+\mu^-\right) \cdot \mathcal{L}_{J/\psi J/\psi}}. \tag{5.3}$$

The total uncertainty of the SES (systematics coming from all sources) is taken into account in the determination of an upper limit on $\mathcal{B}\left(\chi_{\mathrm{b}} \to J/\psi J/\psi \to \mu^+\mu^-\mu^+\mu^-\right)$ treating it as an efficiency correction factor with uncertainty to the signal yield.

The baseline approach for the extraction of the limit will be a CL_s based on a statistical extraction built on a mass classification of the signal and background candidates.

5.2 Simulation of Signal events

The needs of this analysis demand to have a signal Monte Carlo (MC) sample for the cut optimization procedure (Section 5.4.2) where the spectrum of various discriminating variables of the sideband background data are compared to the signal MC.

For the generation process under study ($\chi_{\rm b} \rightarrow J/\psi J/\psi \rightarrow \mu^+\mu^-\mu^+\mu^-$) the Pythia8 [62] generator was used. For this, the following version of the software were used:

Athena version – 17.2.11.8 (EVNT), 17.2.6.2 (HITS), 17.2.1.4 (AOD).

Generator – Pythia 8.170.

Generator PDF tune – CTEQ6L1 with LO α_s.

Simulation – Atlfast II.

In Pythia the available decay modes for the χ_b are only the following:

$\chi_{\rm b} \rightarrow Y\gamma$

$\chi_{\rm b} \rightarrow gg$

The desired mode is not existing in Pythia and therefore a tweak was used in order to include it and create the MC sample.

1. All decay modes of χ_b are turned off.
2. A new decay channel for $\chi_{\rm b} \rightarrow J/\psi J/\psi$ was introduced with probability 100%.
3. The J/ψ mesons decays were all forced to decay to $\mu^+\mu^-$.

In order to assure an efficient production a certain set of cuts had to be introduced into the generation of the χ_b meson and its final stable particles. On the other hand the cuts had to be chosen in order not to bias the production of the MC sample. The available variables for those cuts are the "ptHatMin" (cut on the $p_{\rm T}$ of b quark), $p_{\rm T}$ and η of the muons.

For the choice of optimum ptHatMin value three test samples were generated (only generation and not reconstruction was needed for the purpose of this study):

1. ptHatMin = 4 GeV [Considered as the baseline sample "unbiased"]
2. ptHatMin = 5 GeV [Considered as a test sample "biased"]
3. ptHatMin = 6 GeV [Considered as a test sample "biased"]

From these three samples the one generated with ptHatMin = 4 GeV was considered as the "unbiased" and used as baseline for the comparisons. The $p_{\rm T}$ and η spectrum of the χ_b were compared between samples 1–2 and 1–3 and the sample which was found to be more compatible to the "unbiased" was chosen.

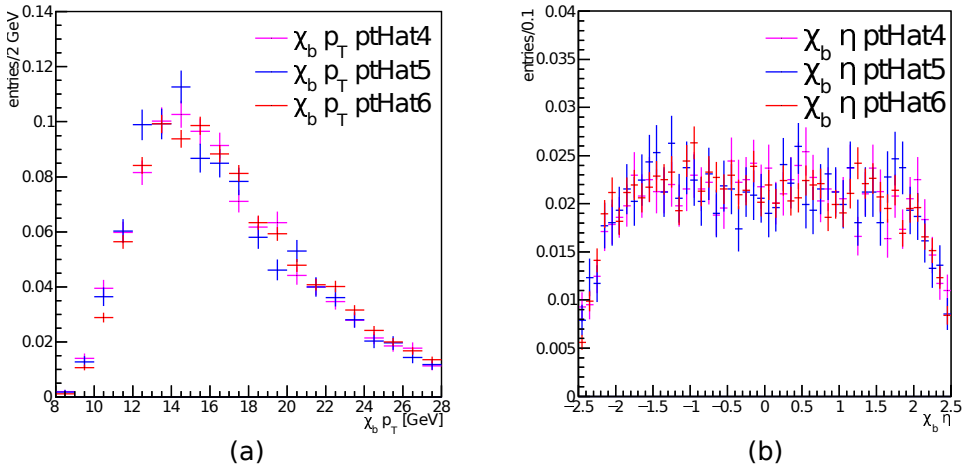

Figure 5.1: Using the "True" information of the three test MC sample (altering the ptHatMin from 4 to 5 and to 6 GeV), (a) the p_{T} spectrum of the χ_b and (b) the η spectrum.

Table 5.1: Summary table for the compatibility test (Kolmogorov and χ^2) between the samples generated with ptHatMin 4 and 5 and ptHatMin 4 and 6.

	ptHatMin = 5		ptHatMin = 6	
	p_{T}	η	p_{T}	η
χ^2	97.7%	10.1%	92.3%	7.3%
Kolmogorov	32.1%	64.7%	3.9%	26.2%
Result	Unbiased		Biased	

In Figure 5.1 the p_{T} and η spectrum of the generated χ_b with ptHatMin = 4, 5 and 6 GeV is shown. For the comparison of the distributions both the Kolmogorov-Smirnov and the χ^2 tests were used. The result of the tests is summarized in Table 5.1, where the sample generated with ptHatMin = 5 GeV found to be more compatible to the "unbiased" and therefore this value was chosen.

For the optimum choice of cuts on the p_{T} and η of the muons various combinations were considered. The summary plots for both p_{T} and η spectrum of the χ_b is shown in Figure 5.2, where the η cut varies from 3.0 down to 2.5, the p_{T} cut on all muons from 2.0 up to 3.5 GeV and the p_{T} cut for at least two muons per event from 2.0 up to 4.0 GeV. This information has been encapsulated on the name of each histogram following the schema: 'eta_XX__pt_Y1_Y2" where XX is the cut on the absolute value of η, Y2 is minimum p_{T} that at least two muons should have and Y1 is the p_{T} cut on all muons. For example eta_2.7__pt_3.5_2.5 has a cut on the

absolute value of η at 2.7, all muons have to have a p_{T}greater than 2.5 GeV and two of them have a harder cut on p_{T} at 3.5 GeV.

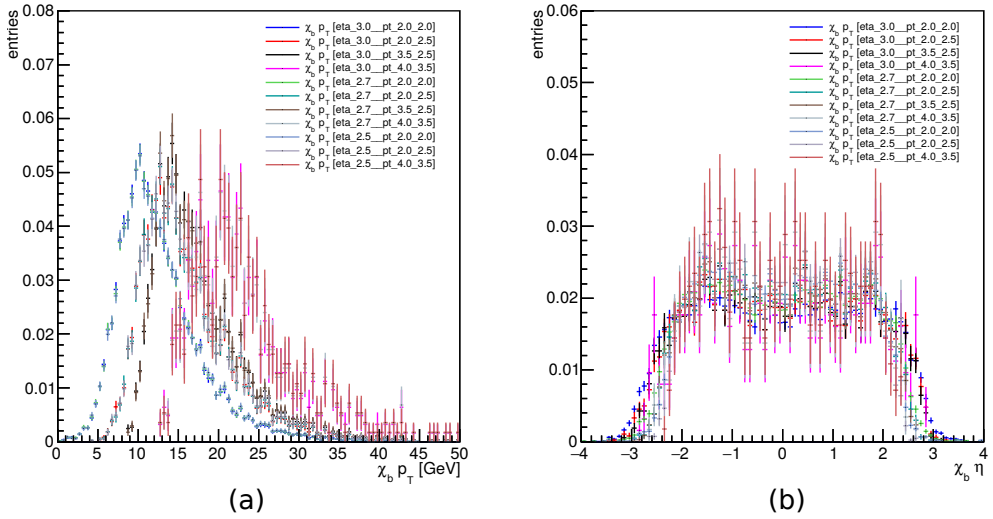

Figure 5.2: Using the "True" information of the test MC sample (generated with ptHatMin = 5) the p_{T} (a) and η (b) spectra of the χ_b for various combinations of η cuts, p_{T} cut on all muons and p_{T} on at least two muons are illustrated here. The abbreviation of the histogram naming is: "eta_XX__pt_Y1_Y2" where XX is the cut on the absolute value of η, Y1 is minimum p_{T} that at least two muons should have and Y2 is the p_{T} cut on all muons.

Concerning the η cut the value that was chosen was $|\eta| < 2.7$ while for the muon p_{T} selection it was required that all muons have $p_{\mathrm{T}} > 2.5$ GeV and at least two muons with $p_{\mathrm{T}} > 3.5$ GeV in order to assure the possibility of firing a dimuon trigger which requires at least $p_{\mathrm{T}} > 4$ GeV.

In order to assure a sufficiently large sample of signal MC 500k events were simulated. Using the "True" information of the signal MC the plots of χ_b mass and J/ψ_1 as a function of J/ψ_2 mass (where J/ψ_1 is considered the J/ψ with the highest p_{T}) can be found on Figure 5.3, χ_b and J/ψ p_{T} on Figure 5.4 and χ_b and J/ψ η on Figure 5.5.

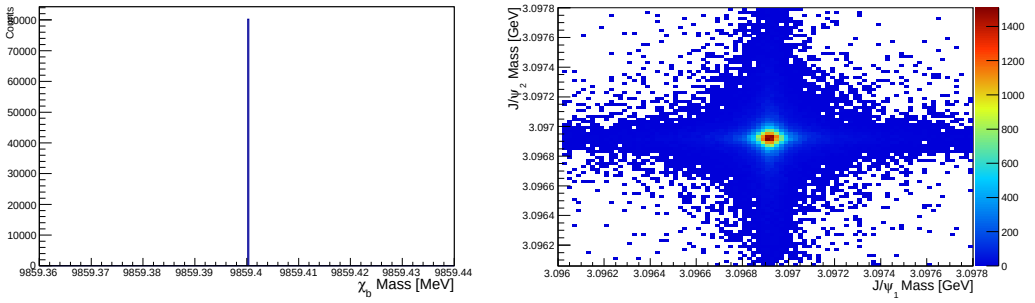

(a) (b)

Figure 5.3: Using the "True" information of the MC sample, (a) the mass of the χ_b (b) the scatter plot of J/ψ_1 mass as a function of J/ψ_2 mass

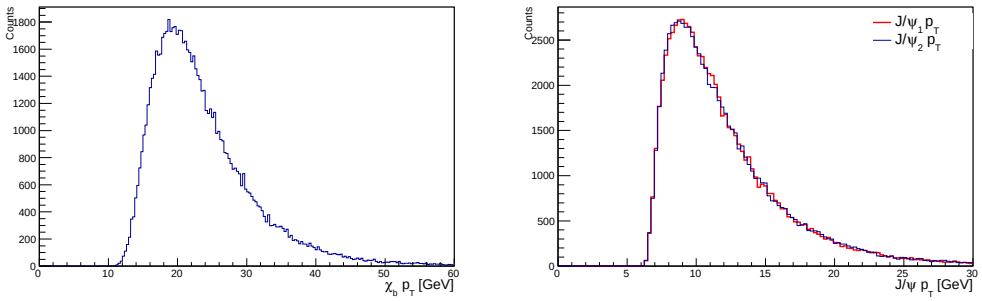

(a) (b)

Figure 5.4: Using the "True" information of the MC sample, (a): the p_{T} spectrum of the χ_b (b): with the red thicker line the p_{T} spectrum of the J/ψ_1 while with the blue thinner line the p_{T} spectrum of the J/ψ_2

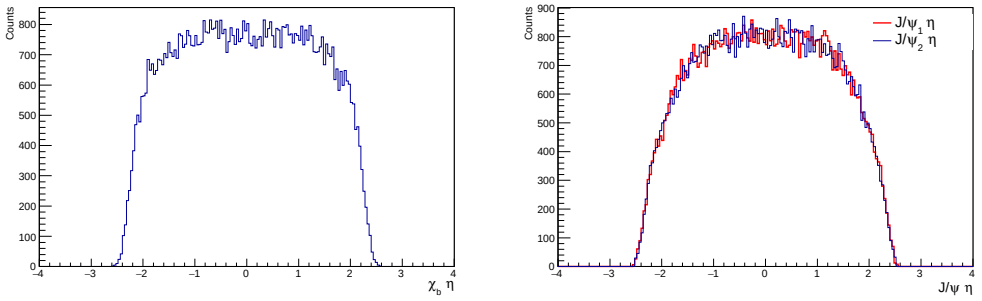

(a) (b)

Figure 5.5: Using the "True" information of the MC sample, (a): the η spectrum of the χ_b (b): with the red thicker line the η spectrum of the J/ψ_1 while with the blue thinner line the η spectrum of the J/ψ_2

5.3 Event Reconstruction and Selection

The data sample (ntuples) prepared for this analysis can be used for other interesting measurements by other groups as well. In order to accommodate all the dynamic and fruitful changing needs in terms of variables, approaches and calculations on the level of the ATLAS reconstruction software (ATHENA), a 3 stage schema was established for the data preparation.

Starting from AODs the final goal is to break down in independent steps the preparation of the DiJpsi flat ntuples (ntuples where for each entry a pair of $J/\psi \rightarrow \mu^+\mu^-$, fully reconstructed, can be fitted to a common vertex). This can be summarized into the following steps:

Create D2AODs

Create BPhysics-style ntuples

Create DiJpsi (flat) ntuples

The first stage is running on AOD files in order to create D2AODs (skimmed by a pattern AOD like pool file datasets). This provides the advantage to have full access to all available information in a skimmed way. Datasets are created with BPhysDAOD-00-00-33 in ATHENA release 17.2.9 requiring at least two J/ψ mesons from the combination of $J/\psi \rightarrow \mu^+\mu^-$(stored in the Onia container) and $J/\psi \rightarrow ee$ (stored in the Z container) candidates, with minimum one $J/\psi \rightarrow \mu^+\mu^-$.

Algorithms used on this stage:

- DiMu: selects di-muons or di-electrons events:
  1. good candidates are required to fall within the mass ranges: $\mu^+\mu^-$ [2.2 GeV, 4.0 GeV], e^+e^- [1.0 GeV, 4.0 GeV]
  2. leptons require to have opposite charge
  3. di-lepton quality of vertex fit $\chi^2 < 10000$
  4. no additional p_{T} cut (besides the forced one coming from the offline reconstruction) is applied
  5. the MCP cuts are not applied,
  6. there is at least one combined muon in the event
- DiOnia: select events with at least 2 di-leptons (onia objects created from the DiMu algorithm) where at least one of them is $\mu^+\mu^-$ ($J/\psi(\mu^+\mu^-)$ + J/ψ $(\mu^+\mu^- \,||\, e^+e^-)$)
- Input dataset used:
  data12_8TeV.period*.physics_Bphysics.PhysCont.AOD.repro14_v01

The second stage is running on D2AODs (algorithm can either be used on D2AODs or directly on AODs). The algorithm created for this stage is the DiJpsi (part of JpsiUpsilonAlgs). The ntuples are created with BPhysDAOD-00-00-33,

BPhysAnalysisTools-00-02-19, BPhysAnalysisObjects-00-00-50, JpsiUpsilonTools-00-00-59, JpsiUpsilonAlgs-00-00-37, PrimaryDPDMaker-00-04-48 in ATHENA release 17.2.10.2. Good candidates are required to be fitted to a common vertex with a χ^2 cut of 10000. The fit in the 4 distinct tracks is performed twice, with and without the J/ψ mass constraint. Typical Good Run List used in order to grand quality data suitable for measurement. The final product of stage 2 is asynchronous ntuples [1] with the relevant trees:

- DiJpsi: DiJpsi without mass constraint
- DiJpsiConst: DiJpsi with mass constraint
- Onia: J/ψ $(\mu^+\mu^-)$
- Trigger information
- Muons
- Primary Vertex
- Tracks

Additional variables are included in this stage to the final ntuples (i.e. χ_b isolation, pointing angle) for DiJpsi (both trees) and Jpsi. The additional variables used are the same as the Rare B-Decays group uses.

The third stage is running on DiJpsi ntuples (where the trees are asynchronous) and produces flat ntuples. A custom ntuple reader, synchronizes the trees of the DiJpsi ntuples and saves on a flat ntuple [2] all events passing the basic cuts (i.e. ATLAS Muon Combined Performance (MCP) cuts, $|\eta(\mu)| < 2.5$). Finally, one tree per mode (with / without fit constraint) is created with the option of blinding a region for searches (needed in $\chi_\mathrm{b} \to J/\psi J/\psi$ analysis) while one entry gives one DiJpsi candidate with all relevant information in one dimension.

- Input: data12_8TeV.period*.physics_Bphysics.PhysCont.AOD.repro14_v01/
- Out [D2AOD] : user.kara.D2AOD.period*.BphysicsAOD.repo1.v1/
- Out [ntuples] : user.kara.data12_8TeV.period*_r1v1.DiJpsi.repo1.v1/

Finally, the events chosen, contain at least four muons (two pairs) and out of them, at least one pair of muons coming from the same J/ψ to be identified by the muon spectrometer with tracks reconstructed in the inner detector [63].

Each pair of muons must have a successful fit to a common vertex with mass around the J/ψ mass, opposite-sign, with $p_T > 2.5$ GeV for all muons and $p_T > 4$ GeV for at least two of the muons and $|\eta| < 2.3$. All four muons must have a

[1] An asynchronous ntuple has more than one trees which they have have varying length and the matching of the corresponding variables per tree is done with the help of indexes.

[2] The flat ntuple has one or more trees which they have one to one correspondence among all variables.

Number of pixel hits+number of crossed dead pixel sensors > 0
Number of SCT hits+number of crossed dead SCT sensors > 4
Number of pixel holes + number of SCT holes < 3
A successful TRT extension where expected (i.e. in the eta acceptance of the TRT) An unsuccessful extension corresponds to either no TRT hit associated or a set of TRT hits associated as outliers. The technical recommendation is therefore:
Case 1: Let nTRThits denote the number of TRT hits on the muon track, nTRToutliers the number of TRT outliers on the muon track and n = nTRThits + nTRToutliers
Case 2: $0.1 < \|\eta\| < 1.9$. Require n > 5 and nTRToutliers < 0.9 n

Table 5.2: The Muon Combined Performance (MCP) requirements applied to the muon candidates

successful fit to a common vertex. For the case of the constrained variables the latter fit has the constrain that each pair of muon coming from a J/ψ must have the J/ψ mass as given in Ref. [9]. Good spatial matching $\Delta R = \sqrt{(\Delta\eta)^2 + (\Delta\phi)^2} < 0.05$ between the reconstructed muons of at least one of the J/ψ and the trigger is required. All muons must satisfy the MCP requirements, as given in Table 5.2.

5.3.1 Preselection Cuts

Using the reconstructed MC sample for signal events, a set of baseline selection cuts was established in order to skim the available ntuples. This study performed on the signal MC after matching the reconstructed and the generator level information requiring both J/ψ to originate from the χ_b. The concept for this set of cuts is either to enforce the already existing cuts (like the trigger imposed p_{T} cuts, all objects to be within the fiducial volume of ATLAS with $|\eta| < 2.5$ with a harder cut on muons) or to provide more than 99% efficiency on the signal MC (for the χ_b and J/ψ decay related variables).

On the two muons that fired the trigger an extra cut is applied requiring p_{T} to be greater than 4 GeV (the "EF_2mu4_Jpsimumu_L2StarB" trigger is used). The total p_{T} spectrum of all muons is shown in Figure 5.6 where the first dashed line at 2.5 GeV is the cut point from the fiducial cuts of the ntuple while the second dashed line at 4 GeV is the trigger imposed cut applied to the muons that fired the trigger.

For the second group, the following variables were considered:

1. The quality of the 4-track fit vertex describing the χ_b meson (χ_b vertex χ^2/NDF).
2. The transverse momentum of the χ_b (χ_b p_{T}).
3. The quality of the 2-track fit vertex describing each J/ψ meson (J/ψ vertex χ^2/NDF).
4. The transverse momentum of each J/ψ (J/ψ p_{T}).

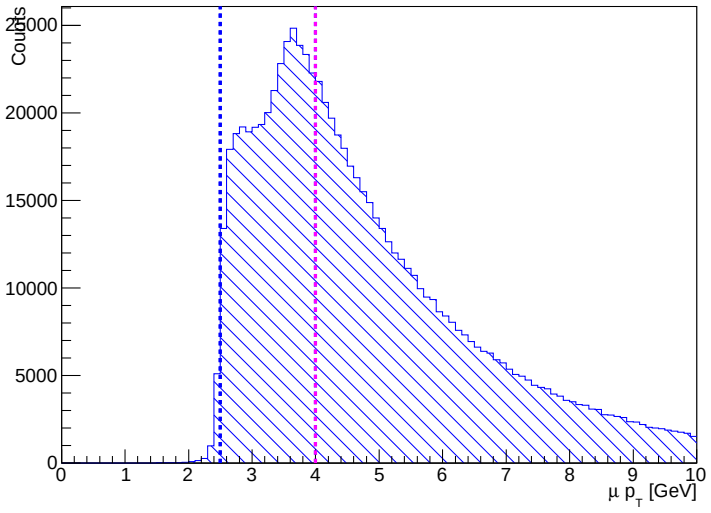

Figure 5.6: The p_{T} spectrum of all four muons from signal MC events. The first dashed line at 2.5 GeV is the cut point from the fiducial cuts of the ntuple while the second dashed line at 4 GeV is the trigger imposed cut applied to the muons that fired the trigger.

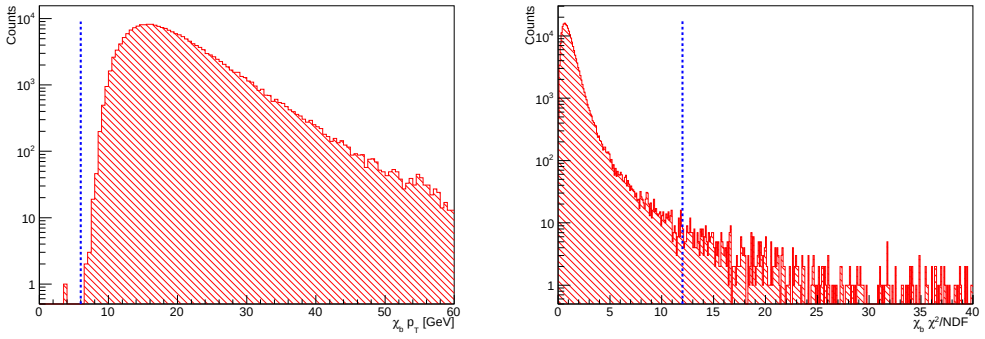

(a) (b)

Figure 5.7: (a) p_{T} spectrum, (b) χ^2/NDF of χ_b from signal MC. The dashed lines illustrate the cut value selected requiring 99% efficiency on signal MC.

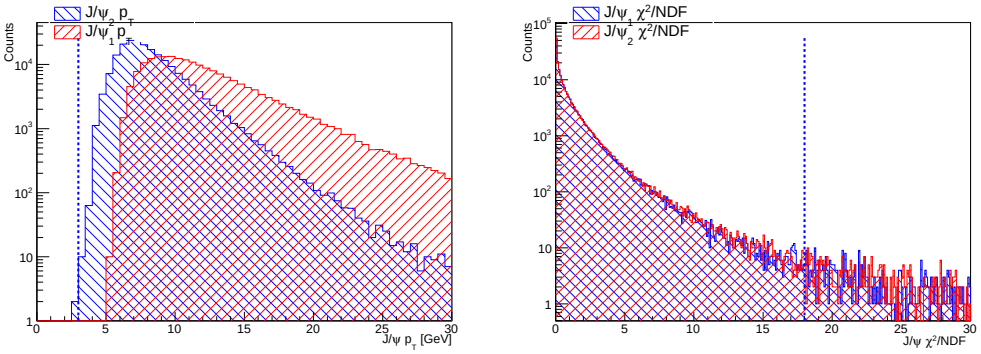

(a) (b)

Figure 5.8: (a) p_{T} spectrum, (b) χ^2/NDF of the two J/ψ from signal MC. The dashed lines illustrate the cut value selected requiring 99% efficiency on signal MC.

The corresponding spectrum for all four variables along with the selected preselection cut values for each variable can be found on Figure 5.7 for the χ_b variables and on Figure 5.8 for the J/ψ related variables.

In Table 5.3 all the preselection cuts that have been established at this stage are summarized.

χ_b	Muons
a. $p_{\mathrm{T}} > 6$ GeV	a. $\lvert\eta\rvert < 2.5$
b. $\lvert\eta\rvert < 2.5$	b. MCP cuts
c. $\chi^2/NDF < 12$	c. all muons $p_{\mathrm{T}} > 2.5$ GeV
	d. trigger muons $p_{\mathrm{T}} > 4$ GeV
	e. at least one combined muon per J/ψ
J/ψ	Event
a. $p_{\mathrm{T}} > 3$ GeV	a. Trigger matching
b. $\lvert\eta\rvert < 2.5$	b. Standard Good Run List
c. $\chi^2/NDF < 18$	

Table 5.3: Summary table with all preselection cuts.

5.3.2 Blinding

The strategy adopted for this analysis (more details in Section 5.1) requires the blinding of the signal region. Instead of proceeding by fully blinding an area around the signal mass value of the χ_b meson which inevitably would also include non-resonant background blinding in 3 dimensions was used.

The very same nature of the channel itself (the χ_b decaying into two J/ψ and each J/ψ decaying into $\mu^+\mu^-$) provides an insight for the expected backgrounds by only observing the J/ψ mass. Based on the mass of each J/ψ the expected backgrounds can be summarized as:

i. J/ψ (resonant) + background

ii. background + background

iii. J/ψ (resonant) + J/ψ (resonant) – continuum background

The background modes (i) and (ii) are distinguishable due to J/ψ masses. Events belonging to the background modes (i) or (ii) can be inside the χ_b signal mass window without being signal events. In order to enhance the data treatment without introducing any bias effect to the analysis itself a data driven characterization with suitable J/ψ mass control regions along with the χ_b mass was used.

The χ_b mass signal window is chosen to be the $\pm 3\sigma$ region around the χ_b invariant mass [9.26 , 10.460] GeV. The corresponding signal MC χ_b mass spectrum and the lines indicating the χ_b mass signal window is shown in Figure 5.9.

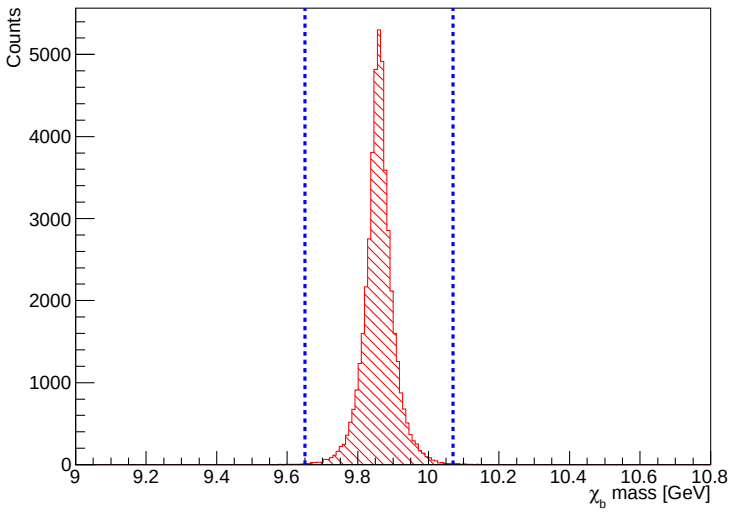

Figure 5.9: The signal MC χ_b mass spectrum. The lines indicate the $\pm 3\sigma$ region around the χ_b invariant mass which are used to define the χ_b mass signal window.

Similarly, the J/ψ mass signal window is chosen to be the $\pm 3\sigma$ region around the $\mu^+\mu^-$ invariant mass [2.9, 3.3] GeV. The corresponding signal MC $\mu^+\mu^-$ mass

spectrum (for both J/ψ) and the lines indicating the J/ψ mass signal window is shown in Figure 5.10.

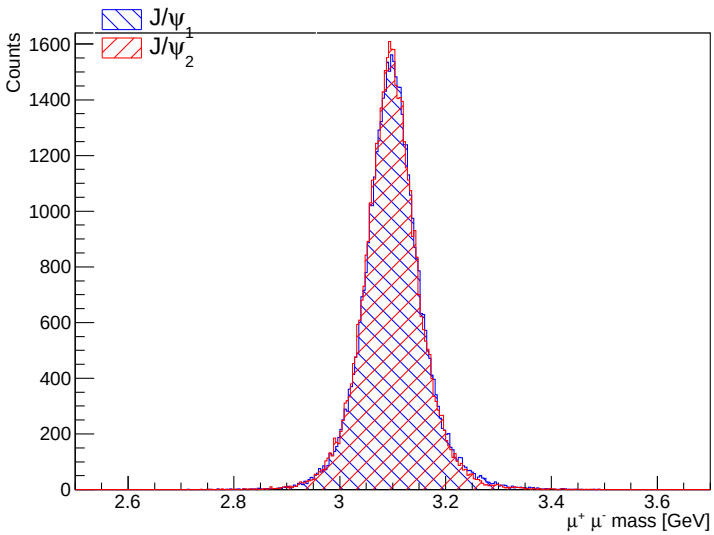

Figure 5.10: The signal MC $\mu^+\mu^-$ mass spectrum. The lines indicate the $\pm 3\sigma$ region around the $\mu^+\mu^-$ invariant mass which are used to define the J/ψ mass signal window.

For the 3D blinding of any event belonging simultaneously at the J/ψ signal mass window (for both J/ψ) and the χ_b mass signal window is treated as signal and not included on any of the studies till the "box opening". Any other event with J/ψ mass [2.5, 3.7] GeV and DiJpsi mass [7.11, 12.61] GeV is treated as background and included in the studies.

5.4 Selection Variables and Optimization

5.4.1 Discriminating Variables Selection

The choice of the discriminating variables made is trying to exploit differences between the the signal and the background events:

- In general the dynamics of the two systems (signal and background) are expected to be quite different. For a signal case any given vector pointing from the primary to the secondary vertex is expected to be very close to the direction of the momentum of the χ_b. On the other hand, for a background case the two directions are expected to be uncorrelated.
- The χ_b particle is produced at the interaction point and it is a heavy particle with a very short lifetime. On the other hand, many DiOnia events have J/ψ which are originated from b-particles and travel long before their decay. Based on that good separation variables should reflect the distance between the primary decay vertex (PV) and the secondary χ_b candidate vertex (SV). Also, discriminating variables should reflect the distance of the J/ψ vertices. Those vertices should coincide, while the others coming from background events are expected to be rather separated.

A complete list of the initial discriminants can be found here:

- The quantity for the quality of the 4-track fit vertex of the χ_b meson (χ_b χ^2/NDF).

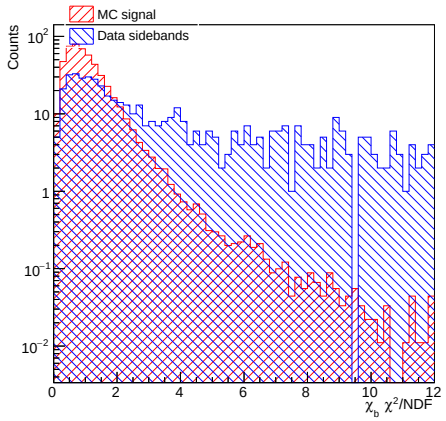

Figure 5.11: The χ^2/NDF for MC signal events (red) and data sidebands (blue). The distributions shown are normalized to the integral of the MC spectrum.

- The L_{xy} and L_{xy} significance ($L_{xy}Sig$) of the χ_b meson

  $L_{xy} = \vec{l}_{xy} \cdot \hat{p}_{\chi_b}$, where $\vec{l}_{xy}$ is the vector from the Primary to the Secondary Vertex and $\hat{p}_{\chi_b}$ is the unitary momentum vector of χ_b. The L_{xy} significance is

defined as $L_{xy}/\sigma L_{xy}$, where the uncertainty σL_{xy} has been calculated using full vertex fit covariance matrix.

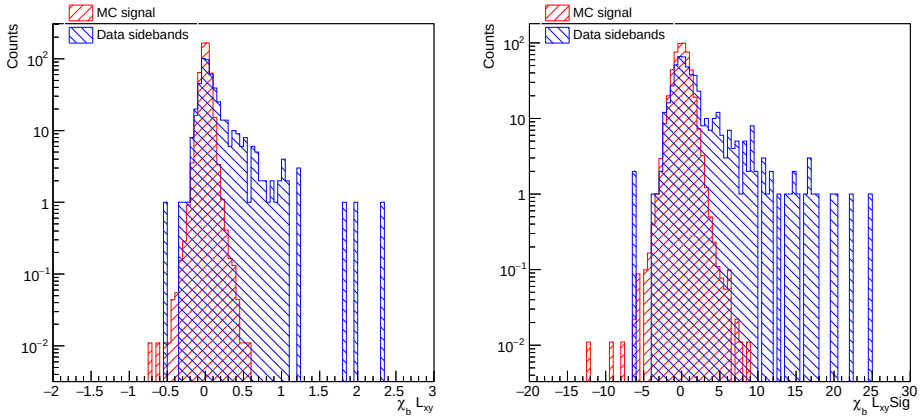

(a) (b)

Figure 5.12: The spectrum of L_{xy} (a) and $L_{xy}Sig$ (b) for MC signal events (red) and data sidebands (blue). The distributions shown are normalized to the integral of the MC plot.

- The χ_b pseudo-proper lifetime (τ) and pseudo-proper lifetime significance (τSig)

  The pseudo-proper lifetime is defined as $\tau = L_{xy}M_{\chi_b}/p_{\mathrm{T}}$, where p_{T} , M_{χ_b} are the transverse momentum and the mass of the DiJpsi meson, respectively, while the pseudo-proper lifetime significance, is defined as τ/σ_τ, with σ_τ the error of the pseudo-proper lifetime.

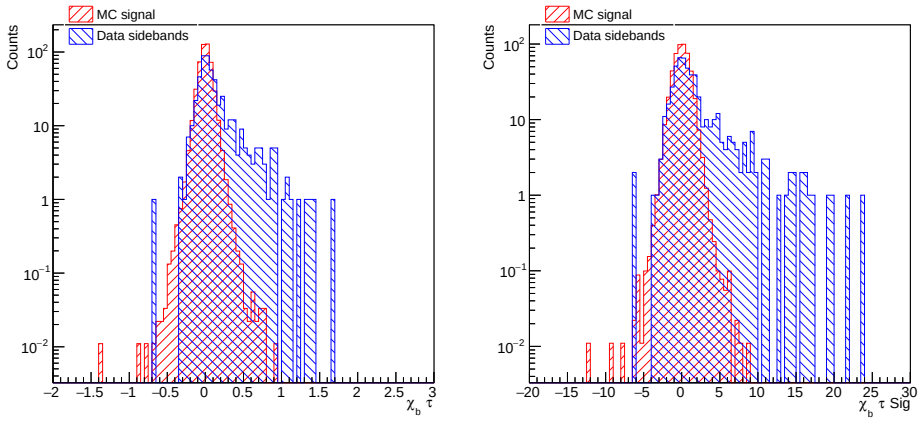

(a) (b)

Figure 5.13: The spectrum of (a) τ and (b) τSig for MC signal events (red) and data sidebands (blue). The distributions shown are normalized to the integral of the MC plot.

- $\chi^2(PV-SV)_{1Dz}$ and $\chi^2(PV-SV)_{2D}$

  These variables are derived from the positions $(\overrightarrow{PV}, \overrightarrow{SV})$ and covariance matrices $(\Sigma_{PV}, \Sigma_{SV})$ of the Primary and Secondary Vertex respectively. Let $\Delta = \overrightarrow{PV} - \overrightarrow{SV}$, and $\chi^2 = \Delta^T \Lambda \Delta$ where $\Lambda = (\Sigma_{PV} + \Sigma_{SV})^{-1}$. These expressions, evaluated for vectors in the xy plane ("2D") or along z ("1D"), are χ^2-like under the hypothesis that primary and b vertex coincide.

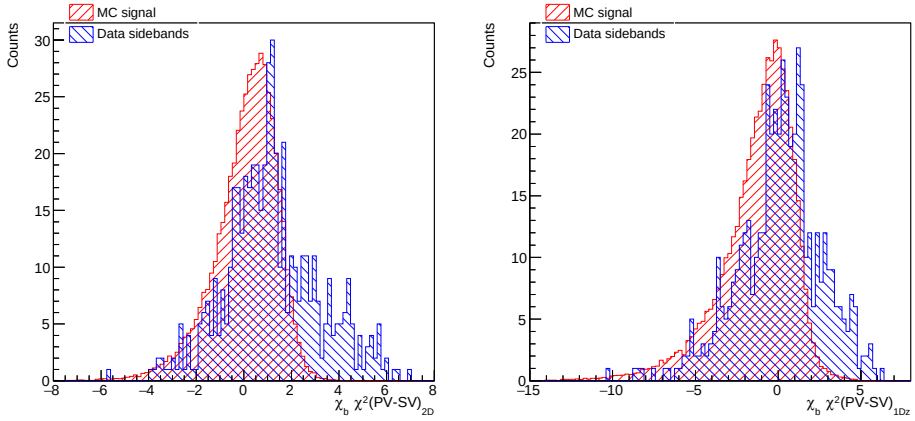

(a) (b)

Figure 5.14: The spectrum of $\chi^2(PV-SV)_{2D}$ (a) and $\chi^2(PV-SV)_{1Dz}$ (b) for MC signal events (red) and data sidebands (blue). The distributions shown are normalized to the integral of the MC plot.

- The transverse momentum of the χ_b meson (χ_b p_{T})

  This is the momentum of the χ_b meson in the x-y plane

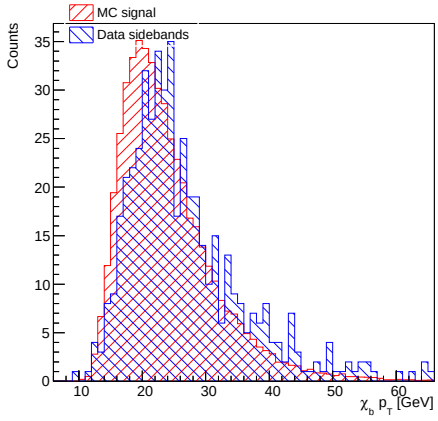

Figure 5.15: The spectrum of χ_b p_{T} for MC signal events (red) and data sidebands (blue). The distributions shown are normalized to the integral of the MC plot.

- The χ_b a_0 and a_0xy; impact parameter of χ_b with respect to the Primary Vertex. The projection of the impact parameter on xy plane, a_0xy is also calculated.

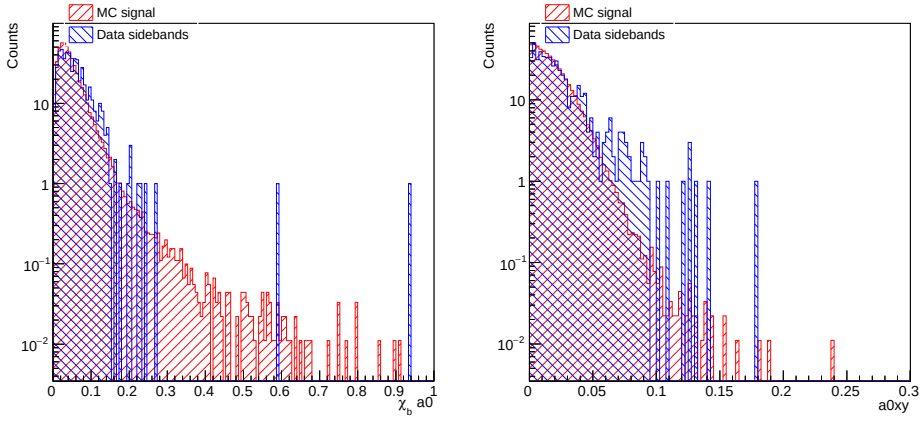

(a) (b)

Figure 5.16: The spectrum of a_0 (a) and a_0xy (b) for MC signal events (red) and data sidebands (blue). The distributions shown are normalized to the integral of the MC plot.

- The χ_b Isolation (8 flavors under test). The isolation is defined by the ratio of the p_{T} of χ_b over the sum of p_{T} of χ_b plus the p_{T} of all tracks that belong to a cone with ΔR, around the p_{T} vector of χ_b. In order to be less sensitive to the pile-up events, the tracks inside the cone are required to be compatible to the χ_b Vertex through a cut at $\chi^2_{VTX-Track} < 6$. See Section 5.4.1 for details.

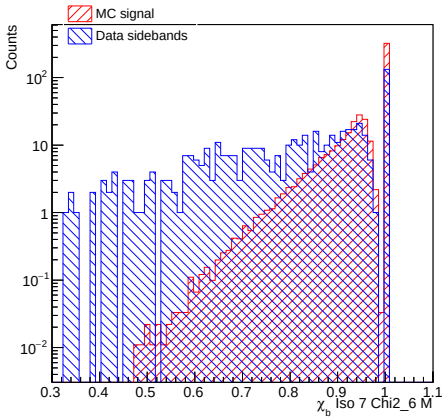

Figure 5.17: The spectrum of the Isolation for MC signal events (red) and data sidebands (blue). The distributions shown are normalized to the integral of the MC plot.

- The χ_b Pointing Angle in 1D (χ_b PAngleT), 2D (χ_b PAngle2D) and 3D (χ_bP̃Angle3D). If $\vec{x}$ is the vector from the Primary Vertex point to the Secondary Vertex point, PAngle2D is the angle of the $\vec{x}$ and the momentum vector of the χ_b. It is calculated in the z direction (1D), in the x-y plane (2D) and in the 3 dimensional space (3D).

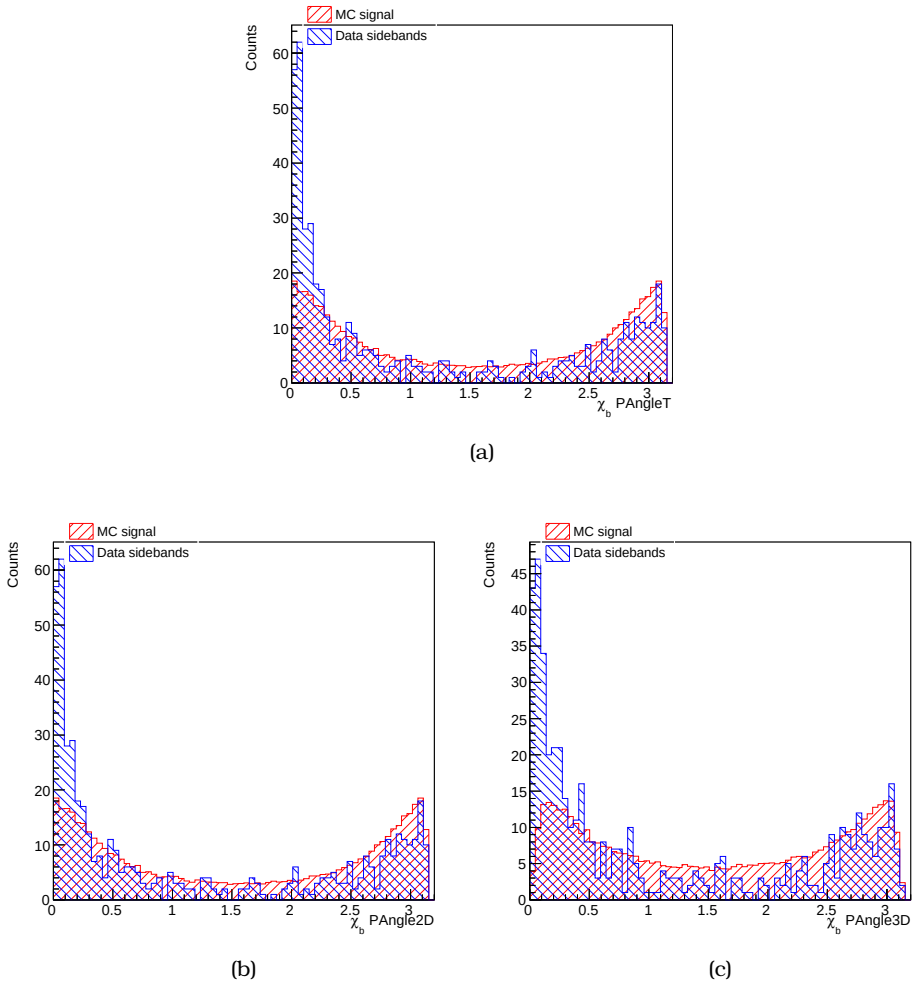

Figure 5.18: The spectra of χ_b PAngleT (a), χ_b PAngleT (b) and χ_b PAngleT (c) for MC signal events (red) and data sidebands (blue). The distributions shown are normalized to the integral of the MC plot.

- The J/ψ pseudo-proper lifetime (τ) and the pseudo-proper lifetime significance (τSig) The pseudo-proper lifetime (τ) and the pseudo-proper lifetime significance (τSig) for each J/ψ.

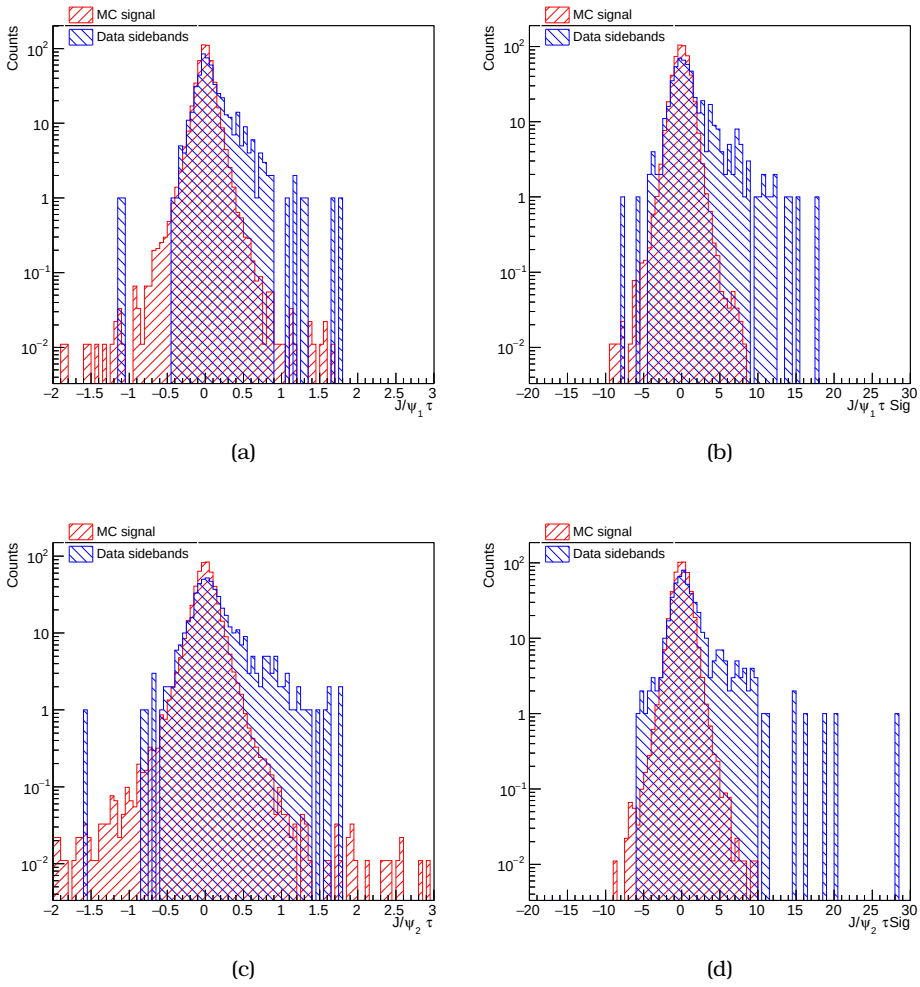

(a) (b)

(c) (d)

Figure 5.19: The spectrum of τ (a,c) and τSig (b,d) for MC signal events (red) and data sidebands (blue). The top row refers to first J/ψ while the lower one to the second. The distributions shown are normalized to the integral of the MC plot.

- The L_{xy} and L_{xy} significance ($L_{xy}Sig$) for each J/ψ meson. Same definition used as in the χ_b meson for the calculation of these variables.

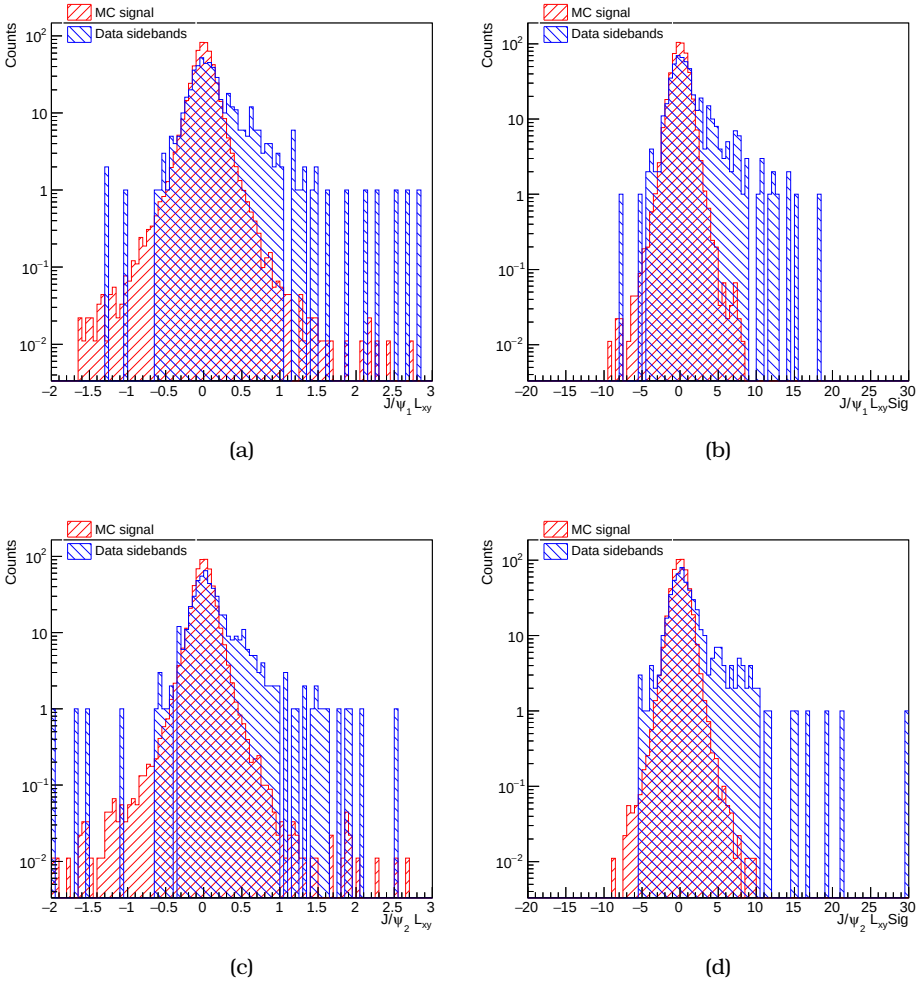

Figure 5.20: The spectrum of L_{xy} (a,c) and $L_{xy}Sig$ (b,d) for MC signal events (red) and data sidebands (blue). The top row refers to first J/ψ while the lower one to the second. The distributions shown are normalized to the integral of the MC plot.

Among the list of variables described above, there are subgroups of discriminating variables describing the same "physics quantity" which can be (and will be) replaced by one representative variable. Those subgroups are the discriminating variables L_{xy}, L_{xy} significance, τ and τ significance for χ_b and J/ψ.

Another group like that is the χ_b isolation where 8 different calculations have been made for this variable. A separate discussion on those groups follow.

Isolation Variables

The decay products of a b-hadron are kinematically isolated from other tracks originating from the same primary vertex as the b-hadron. The *isolation* $(I_{\Delta R})$ of a χ_b meson, defined by a cone of size ΔR is given by:

$$I_{\Delta R} = \frac{p_{T\chi_b}}{p_{T\chi_b} + \sum_{tracks}^{\Delta R} p_{\mathrm{T}}} \tag{5.4}$$

where $p_{T\chi_b}$ is the transverse momentum of the χ_b meson, and $\sum_{tracks}^{\Delta R} p_{\mathrm{T}}$ is the sum of p_{T} of all tracks within a cone ΔR from the direction of χ_b excluding its decay products.

Since the isolation is a possible very good candidate as a discriminating variable and it comes with various flavors (cone ΔR, track properties) in data of ATLAS a detailed study is performed in order to choose the best isolation variable out of 8 different definitions.

The parameters of isolation definition varied are:

- ΔR of the isolation cone
- Track parameters

For the ΔR of the isolation cone two values were considered: $\Delta R < 0.7$ (noted as Iso–7 in the naming of the isolation variables) and $\Delta R < 1.0$ (noted as Iso–10 in the naming of the isolation variables).
For the track parameters, a cut on p_{T} and η of the tracks was considered and some quality criteria like number of hits on the Pixel or Silicon tracker. The variations on the track parameters along with the corresponding name tag can be found in Table 5.4

	Medium (M)	MediumPt05 (MP)	Tight (T)	TightPt05 (TP)
track p_{T} cut [MeV]	1000	500	1500	500
track $\lvert\eta\rvert$ cut	2.5	2.5	2.5	2.5
Pixel hits	1	1	1	1
SCT hits	2	2	6	6

Table 5.4: The definitions of the various isolation variables under study.

In Figures 5.21 and 5.22 the isolation spectrum for the various isolation variables under study can be found, the distributions are normalized to the integral of the corresponding MC spectrum. Based on these one can identify some flavors of the isolation that have a weaker separation power. For the rest of the flavors it is not possible to decide based only on this information. In order to quantify the separation and select the most powerful among them in terms of signal/background separation power the Receiver Operating Characteristic (ROC) curves [64] were used.

In Figure 5.23 the ROC curves of background rejection versus signal efficiency for all the isolation variables under study are shown. Based on the integral of each curve for the region $[0.8, 1.0]$ the "Iso–7 Medium" is found to be the most powerful and will be used from now on as the isolation variable for this study.

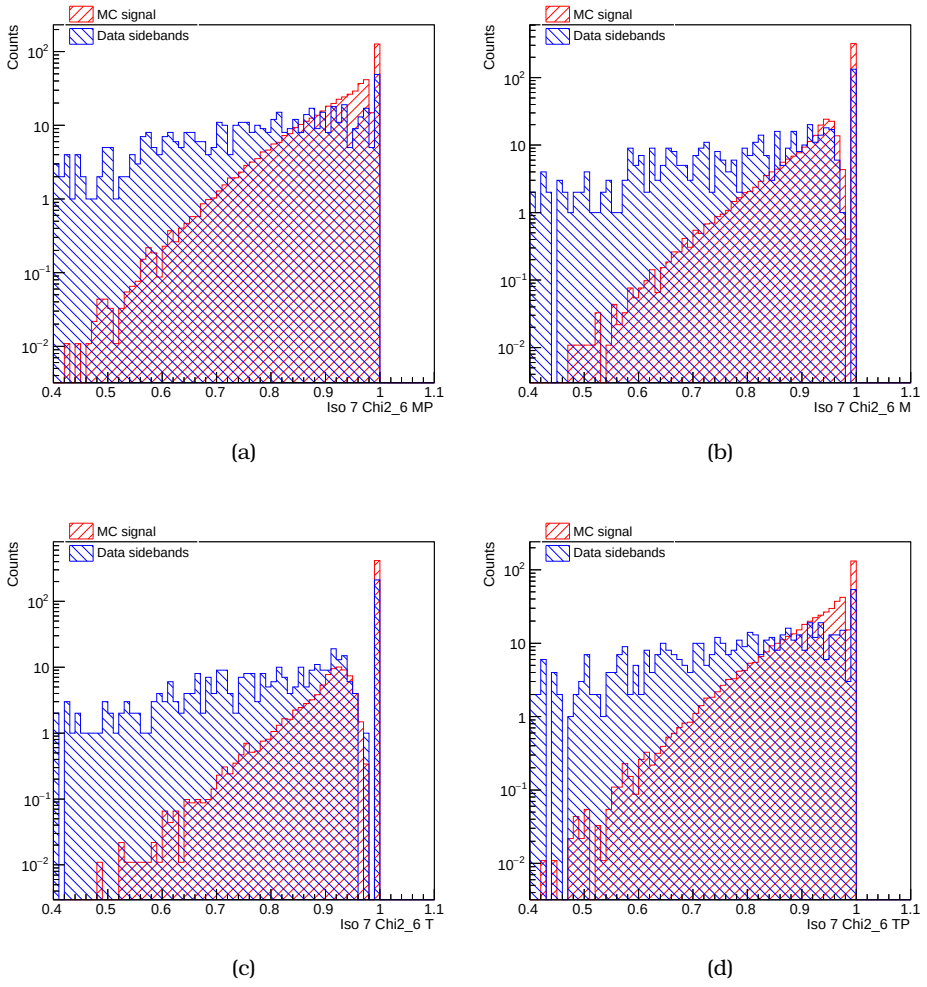

Figure 5.21: The spectrum of the isolation variables for a cone $\Delta R < 0.7$ for MC signal events (red) and data sidebands (blue). (a) MediumPt05, (b) Medium, (c) Tight, (d) TightPt05 track parameters configuration. The distributions are normalized to the integral of MC spectrum.

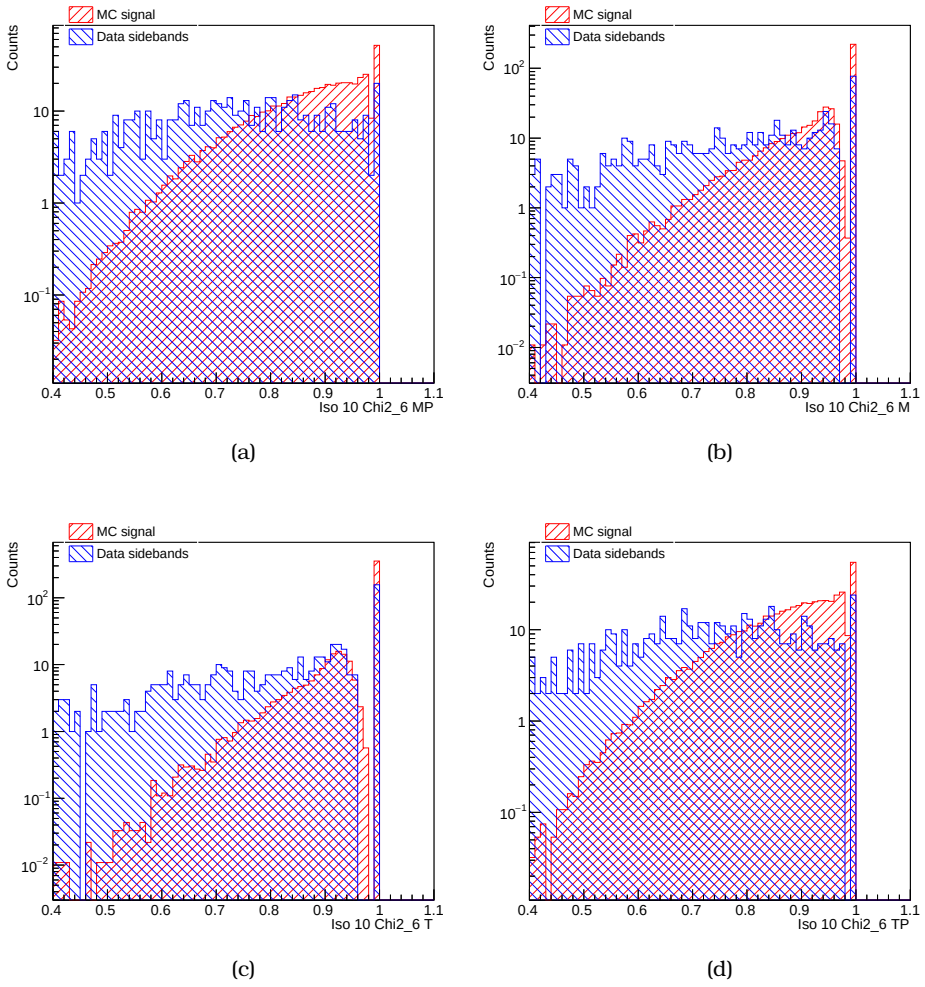

Figure 5.22: The spectrum of the isolation variables for a cone $\Delta R < 1.0$ for MC signal events (red) and data sidebands (blue). (a) MediumPt05, (b) Medium, (c) Tight, (d) TightPt05 track parameters configuration. The distributions are normalized to the integral of MC spectrum.

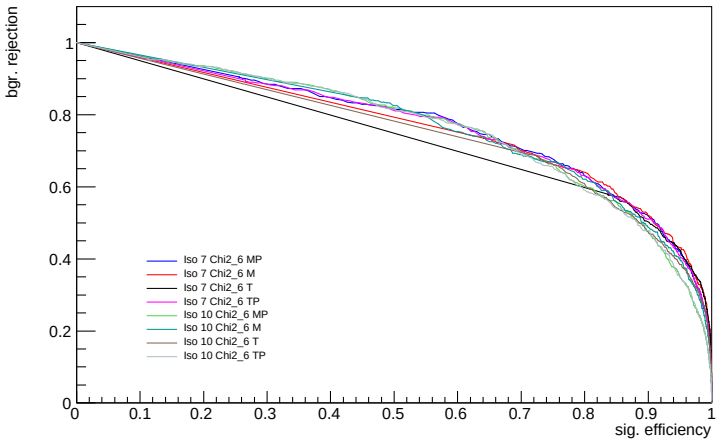

(a)

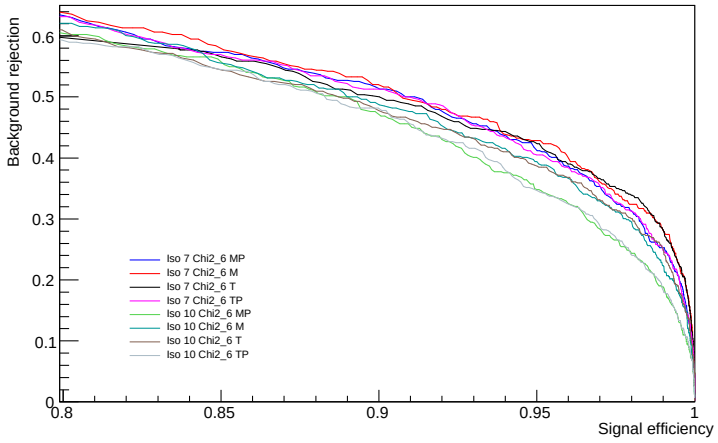

(b)

Figure 5.23: The ROC curves of background rejection as a function of the signal efficiency for all the isolation variables under study. The full range for signal efficiency (a) is shown while on (b) only the range above 0.8 for the signal efficiency are shown.

Lifetime Variables

As mentioned before, the discriminating variables L_{xy}, the L_{xy} significance, the τ and the τ significance describe the same physical quantity and they are fully correlated. Due to this only one will be used for each of the particles (χ_b, J/ψ_1 and J/ψ_2). In order to select the most powerful in terms of signal/background separation power the same procedure as in the isolation study is followed.

In Figure 5.24 the lifetime variable spectrum for χ_b normalized to the integral of the MC spectrum are shown, while using the ROC curves of background rejection as a function of the signal efficiency (shown in Figure 5.25) and calculating the integral for the region $[0.8, 1.0]$ the χ_b L_{xy} found to be the most powerful.

In Figure 5.26 (5.28) the normalized to MC entries distribution for J/ψ_1 (J/ψ_2) can be found, while using the ROC curves of background rejection as a function of the signal efficiency are shown in Figure 5.27 (5.29) and by calculating the integral for the region $[0.8, 1.0]$ the J/ψ pseudo-proper lifetime significance found to be the most powerful.

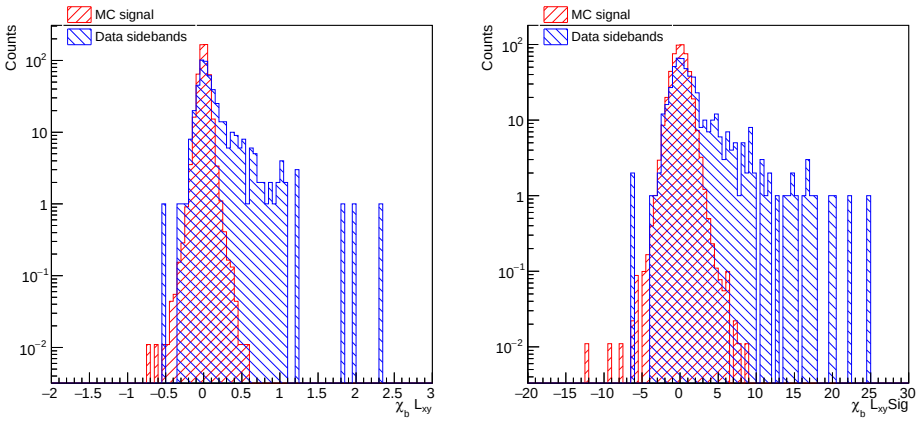

(a) (b)

(c) (d)

Figure 5.24: The χ_b lifetime related variables for MC signal (red) and data sidebands (blue). The distributions shown are normalized to the integral of the MC spectrum. (a) χ_b L_{xy}, (b) χ_b L_{xy} significance, (c) χ_b pseudo-proper lifetime, (d) χ_b pseudo-proper lifetime significance are shown.

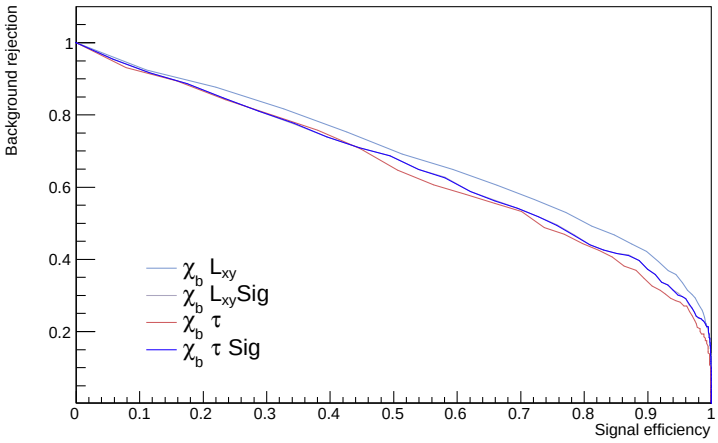

(a)

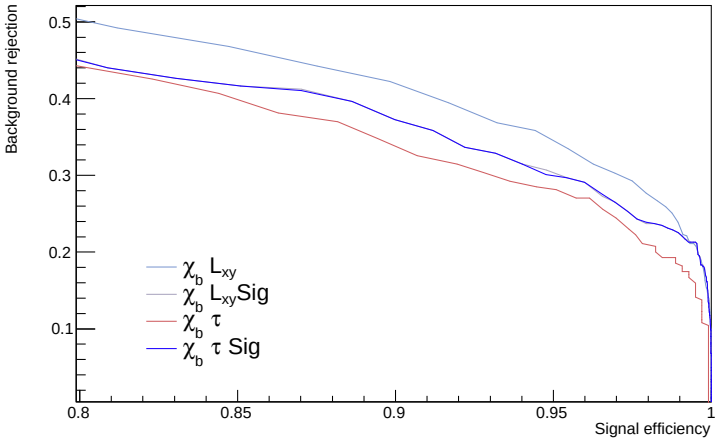

(b)

Figure 5.25: The ROC curves of background rejection as a function of the signal efficiency for χ_b lifetime related variables under study. The full range for signal efficiency (a) is plotted while on (b) only the values above 0.8 are used.

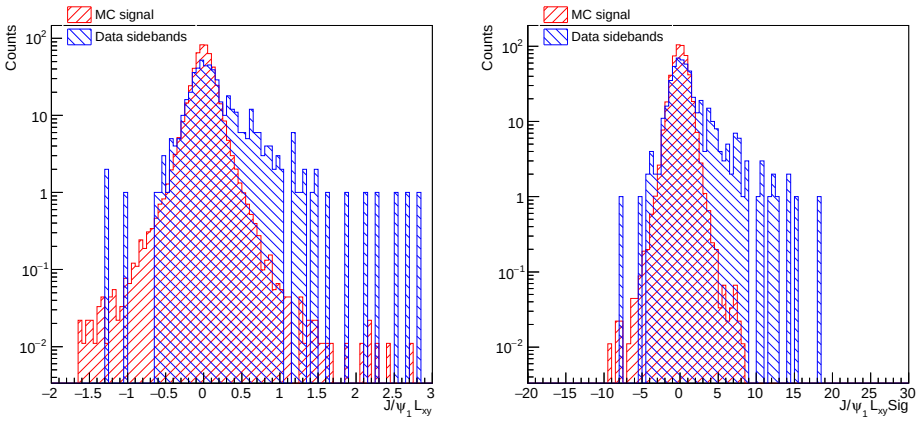

(a) (b)

(c) (d)

Figure 5.26: The spectrum of J/ψ_1 lifetime related variables for MC signal (red) and data sidebands (blue). The distributions shown are normalized to the integral of the MC spectrum. (a) J/ψ_1 L_{xy}, (b) J/ψ_1 L_{xy} significance, (c) J/ψ_1 τ, (d) J/ψ_1 τSig.

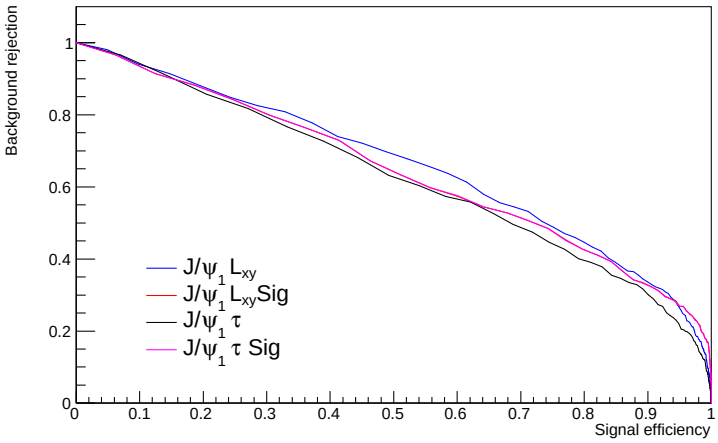

(a)

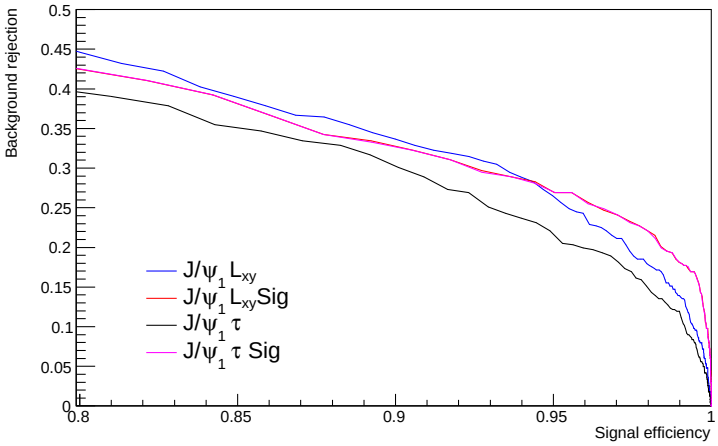

(b)

Figure 5.27: The ROC curves of background rejection as a function of the signal efficiency for J/ψ_1 lifetime related variables under study. The full range for signal efficiency (a) is plotted while on (b) the values above 0.8 are shown.

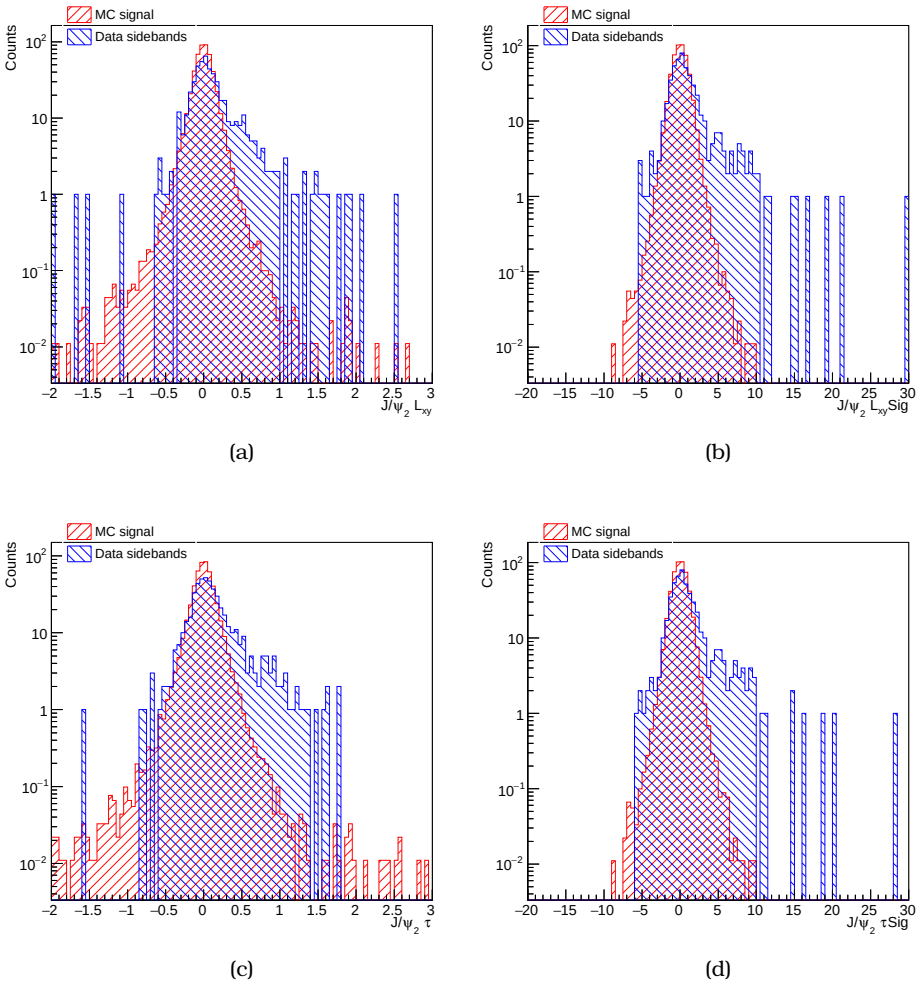

Figure 5.28: The spectrum of J/ψ_2 lifetime related variables for MC signal (red) and data sidebands (blue). The distributions shown are normalized to the integral of the MC spectrum. (a) J/ψ_2 L_{xy}, (b) J/ψ_2 L_{xy} significance, (c) J/ψ_2 τ, (d) J/ψ_2 τSig.

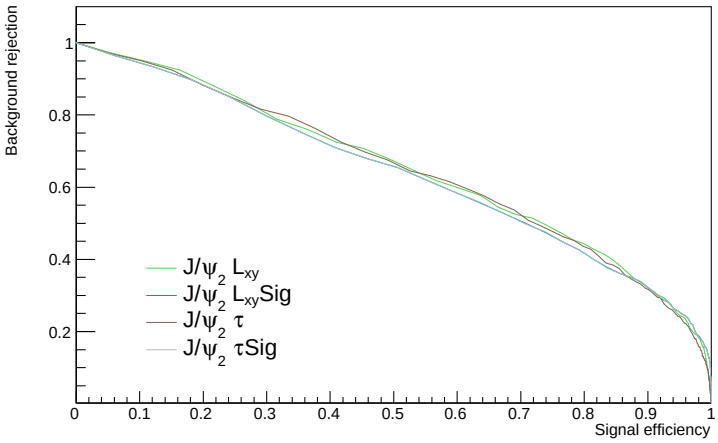

(a)

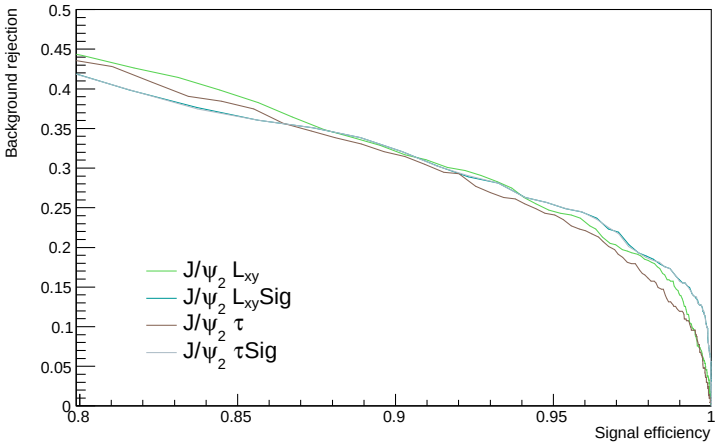

(b)

Figure 5.29: ROC curves of background rejection as a function of the signal efficiency for J/ψ_2 lifetime related variables under study. The full range for signal efficiency (a) is plotted while on (b) values above the values above 0.8 are used.

Correlations of the Variables

A big number of discriminating variables (13 in our case) can potentially cause difficulties and raise instability problems in the optimization procedure. Furthermore, many of these variables are expected to be highly correlated and the simultaneous use of all of them does not contribute further in the signal/background discrimination. After the reduction on the discriminating variables with the isolation and lifetime studies a list of 13 variables is chosen. An effort is done to further reduce the number of these variables with the help of information from the correlations and their discriminating power. The 13 variables are:

1. χ_b χ^2/NDF
2. χ_b L_{xy}
3. J/ψ_1 Pseudo-proper lifetime significance (τSig)
4. J/ψ_2 Pseudo-proper lifetime significance (τSig)
5. χ_b $\chi^2(PV-SV)_{1Dz}$
6. χ_b $\chi^2(PV-SV)_{2D}$
7. χ_b p_{T}
8. χ_b a_0
9. χ_b $a_0 xy$
10. χ_b Pointing Angle in 1D (χ_b PAngleT)
11. χ_b Pointing Angle in 2D (χ_b PAngle2D)
12. χ_b Pointing Angle in 3D (χ_b PAngle3D)
13. χ_b Isolation

The correlations of the discriminating variables hold information about their separation capabilities. In general, a similar correlation behavior indicates that these variables have similar physical meaning and based on this some can be eliminated without loosing any separation power. On the other side, different correlation pattern between background and signal point to variables that have good separation capabilities.

In order to illustrate this information the correlation matrices are used. These matrices group the correlation coefficients of all the possible variable pairs offering an overview of their dependence. In parallel to 13 available discriminating variables, the χ_b mass is also included on the correlation matrices shown in Figure 5.30.

Studying the patterns and the behavior of the variables on the correlation matrices of Figure in 5.30 some helpful deductions are made:

- all variables are substantially uncorrelated with the mass of χ_b

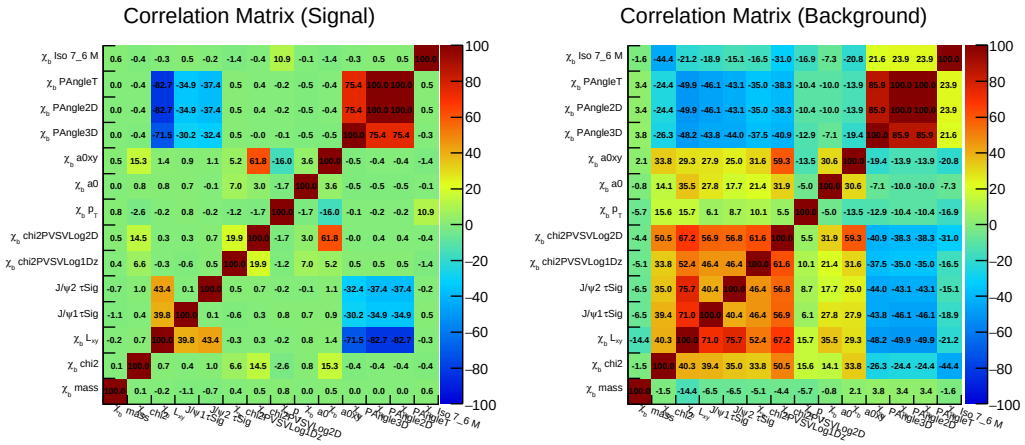

Figure 5.30: The correlation matrix of all discriminating variables under study. On the left for the signal and on the right for the background.

- the variables of pointing angle (χ_b PAngleT, PAngle2D and PAngle3D) are, as expected, highly correlated to each other
- the variables of pointing angle seems to have a secondary correlation with the lifetime variables
- variables with similar behavior simultaneously in signal and background (like pointing angles) can be removed

In order to account also the separation power of the variables the ROC curves are used. In Figure 5.31 all the ROC of 13 variables can be found. Judging by the bottom plot of Figure 5.31 χ_b p_{T} and a_0 has almost no discriminating power and there is no need of keeping them. Similarly the pointing angles were also found to have very small discriminating power and are also removed.

This way we end up with a list of 8 variables where the correlation coefficients both for the signal and the background are shown in Figure 5.32. For illustration purposes the two correlation matrices (signal, background) in the Figure 5.32 have been combined into one. Since any correlation matrix is diagonally symmetric the full information is shown on either the upper or the lower triangle. In this case the upper triangle of the matrix holds the signal correlation coefficients while the lower triangle holds the background correlation coefficients. As one can see, no strong correlation or patterns exists among the final list of the discriminating variables.

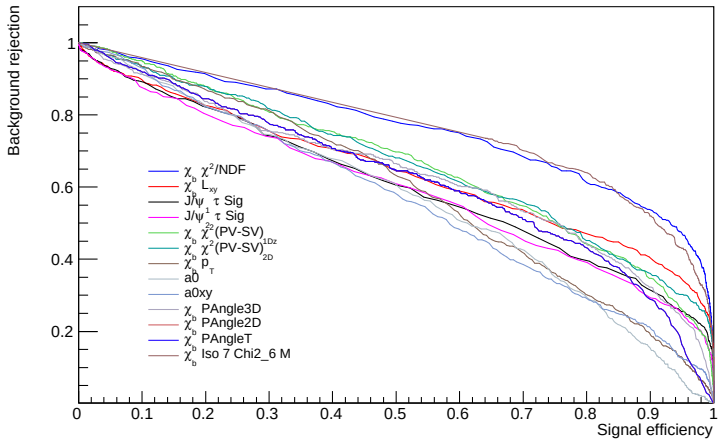

(a)

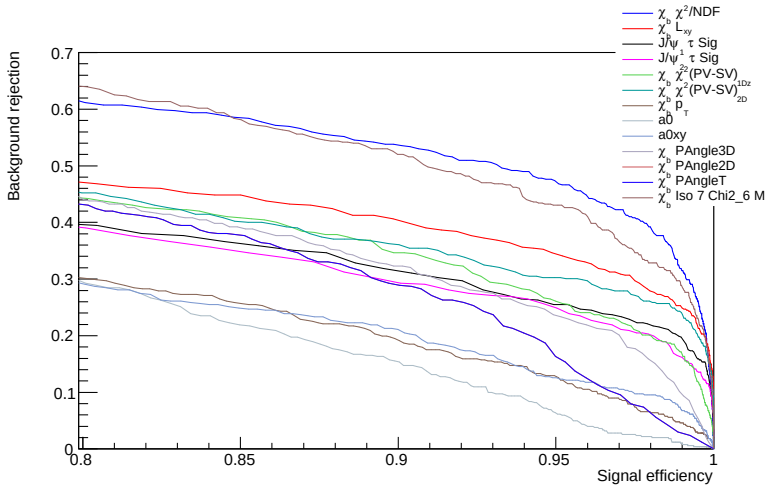

(b)

Figure 5.31: The ROC curves of background rejection as a function of the signal efficiency for the discriminating variables under study. The full range for signal efficiency (a) is plotted while on (b) only the values above 0.8 are shown.

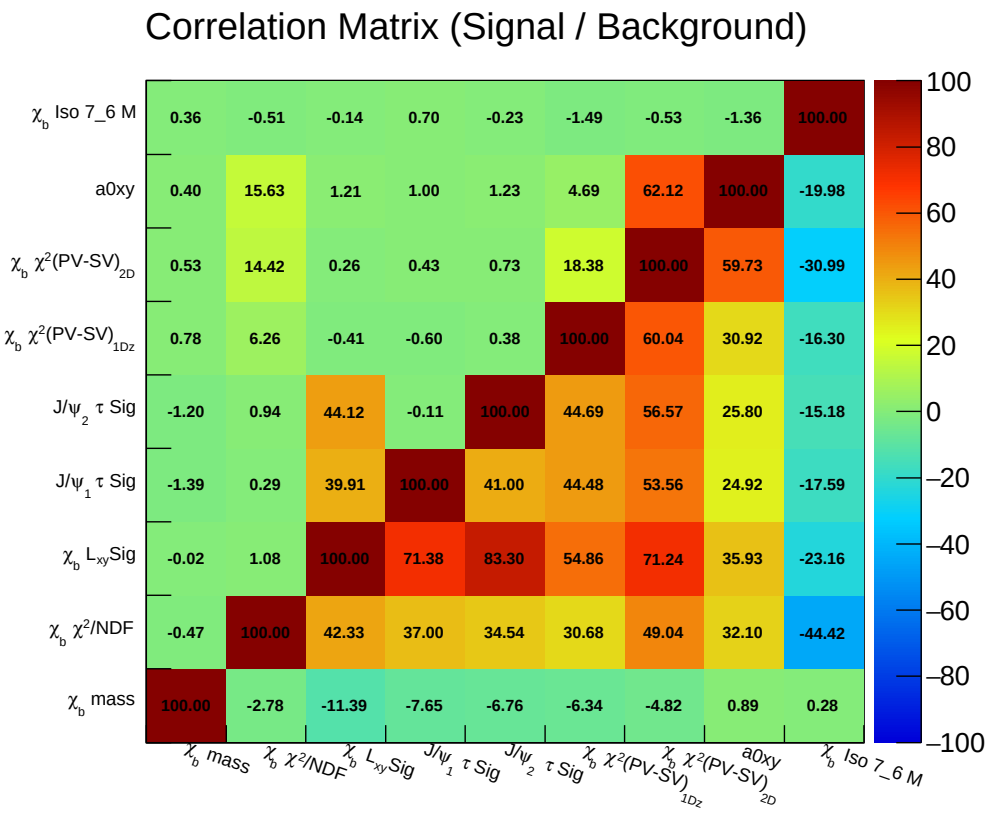

Figure 5.32: The correlation matrix of the final list of discriminating variables. The upper triangle of the matrix holds the signal efficiency correlation coefficients while the lower triangle holds the background rejection correlation coefficients. The mass of χ_b has been included and as expected not correlation found with any discriminating variable.

5.4.2 Selection Criteria Optimization

Using the list with the 8 most powerful discriminating variables selected, the next step is to locate the optimum selection criteria for each one of them. The cut points on the discriminating variables are defined dynamically in order to achieve at the same time the maximum possible signal efficiency while rejecting the maximum background. For any given single discriminating variable a scan is performed on the available cut range. For each scan point the signal efficiency and the background rejection efficiency are estimated while the steps of this scan are defined automatically in order to have enough points across the cut values that can mimic a continuous behavior. Using these quantities acquired for each step an estimator is calculated. The values of the estimator will be used for the definition of the optimal cut point on each variable.

Since the expected background events in the signal region are foreseen to be small the quantity which is used as estimator [61] is:

$$P = \frac{\epsilon_{sig}}{1 + \sqrt{N_{bck}}} \tag{5.5}$$

where ϵ_{sig} is the efficiency of the signal and B is the (expected) number of background events in the signal region. The ϵ_{sig} and N_{bck} are obtained from signal Monte Carlo for signal (efficiency) and from sidebands for background, while the actual signal region remains blinded.

An example of the optimization procedure of the selection criteria for the χ_b χ^2/NDF variable with the use of the estimator is shown in Figure 5.33. The distributions for both MC signal (red) and Data sideband events (blue) can be seen on the 5.33(a). In 5.33(b) the corresponding ROC curve for all the steps of the cut value is shown and in 5.33(c) the estimator's response as a function of the scan points is plotted.

The optimum selection criteria for this variable is found to the maximum of the estimator's response which corresponds at a cut on χ_b $\chi^2/NDF < 2$. This point is highlighted with red in estimator's response and ROC curve and with a dashed line on the MC signal and Data sidebands spectra. The accomplished signal efficiency using that cut is found to be $\sim 90\%$ while at the same time the background rejection to be $\sim 57\%$.

In the simplified scenario with a single variable the optimization procedure would be exactly the one described above and illustrated in Figure 5.33. In the case of more than one variable -like the one faced during this analysis (total 8 variables)- the optimization would require a simultaneous scan of all the variables in the 8-dimensional space since there are correlation behaviors between the variables that can not be expressed analytically in order to be taken into account. This approach is raising performance issues in terms of processing time which disqualifies it. In order to overcome this obstacle, the N-1 optimization technique is used.

N-1 Optimization

The N-1 optimization is an iterative technique where in each step the previously defined set of cuts is used on all variables except the one which is optimized. After

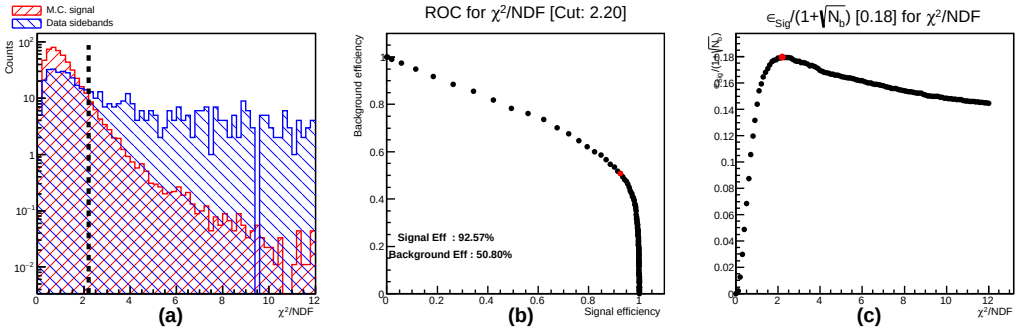

Figure 5.33: The optimization for a single variable (χ_b χ^2/NDF). (a) the distribution of χ_b χ^2/NDF for both MC signal (red) and Data sidebands (blue) is located (spectra are normalized to sideband entries), (b) the ROC curve and the point (red) corresponding to the estimator's position while (c) the estimator's values as a function of the scan cut points. The optimal cut point corresponds to the maximum value of the estimator.

several iterations if the behavior of the variables (in both estimator and optimal selection criteria) is congruent then these selection criteria are the optimal to be used.

In details, on the 0^{th} iteration the optimization is performed on each variable separately. Up to now no cut has been made on any of the variables. At the end of the 0^{th} iteration for each variable the optimum selection criteria has been identified and as foretold, no effects coming from the other variables have been accounted.

On the next iteration, for each variable (variable under study) the optimal selection criteria defined during the previous iteration are applied to all the other variables (except the variable under study) and the single variable selection criteria optimization is performed for this variable. After the optimization has been performed following this logic for all variables the next iteration is performed.

The goal of this technique is to have the cut's values (and correspondingly the estimator's values) to converge to the optimum after several iterations. This was not the case for the N-1 optimization performed for this study. In Figure 5.34 one can see the outcome of the N-1 optimization for the first 6 iterations (on the Figure 5.34(a) the maximum value of the estimator on Figure 5.34(b) the optimum selection criteria).

For most of the discriminating variables the optimization procedure is giving oscillating values for both maximum of the estimator and optimal discriminating variable cut. Based on this, the findings of the N-1 optimization are inconclusive and this technique is not capable to provide the final set of selection criteria.

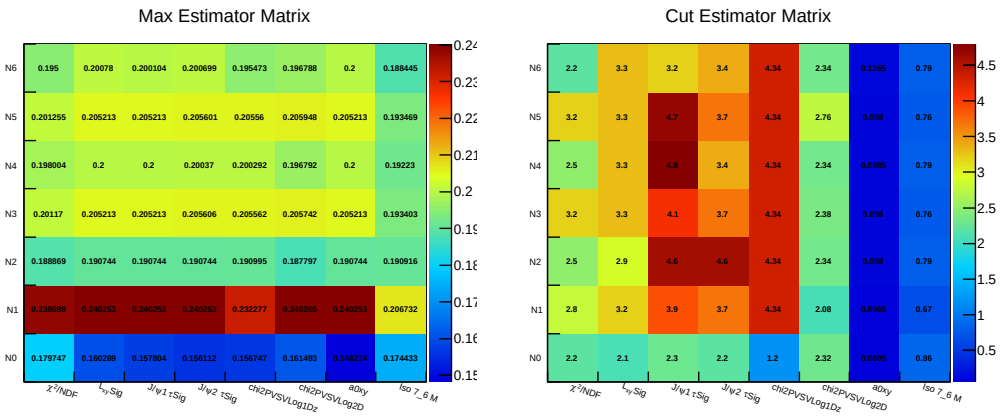

Figure 5.34: The outcome of the N-1 optimization after 6 iteration. (a) the maximum values of the estimator for each iteration versus the 8 discriminating variables is shown while (b) the cut defined from the estimator for each iteration versus the 8 discriminating variables.

Multidimensional Optimization

Since the N-1 optimization technique did not provide solid and usable results concerning the optimal selection criteria for this analysis, a different approach was established. As mentioned before, the point by point scanning of the 8-dimensional space of discriminating variables in order to locate the maximum of the estimator is not a feasible solution. Instead of working in order to locate the maximum of an 8-dimensional function $\mathcal{P}(V_1, V_2, \ldots V_8)$, where the analytical expression is not known one could turn towards a minimization if the final quantity defined as: $-log\mathcal{P}(V_1, V_2, \ldots V_8)$.

Several algorithms exist that can find the minimum of a function. Among them, the most common method used is based on the MIGRAD algorithm inside the MINUIT package. MIGRAD performs the minimization of a function using the variable metric method [65, 66].

Using this approach the optimal selection criteria found after the convergence of the minimizer can be found the Table 5.5.

Variable		Optimal Selection Criteria [MIGRAD]
χ_b χ^2/NDF	<	2.4
χ_b $L_{xy}Sig$	<	3.26
J/ψ_1 τSig	<	4.0
J/ψ_2 τSig	<	4.0
χ_b $\chi^2(PV-SV)_{1Dz}$	<	4.3
χ_b $\chi^2(PV-SV)_{2D}$	<	3.0
χ_b a_0xy	<	0.06
χ_b Isolation	>	0.87

Table 5.5: The optimal cuts for the discriminating variables found after the convergence of the MIGRAD minimizer.

5.4.3 Final Cuts

The final set of cuts has been defined using the technique described in Section 5.4.2 and the corresponding cut for each variable can be found on Table 5.5.

In Figure 5.35 one can see the spectra of MC signal events and Data sidebands before applying any cut on the discriminating variables for all of them and also for the mass, while in Figure 5.36 the corresponding spectra can be found after applying all the cuts. The Figure 5.36 shows that the discriminating variables are strongly correlated for signal and residual background (after applying the optimal cuts).

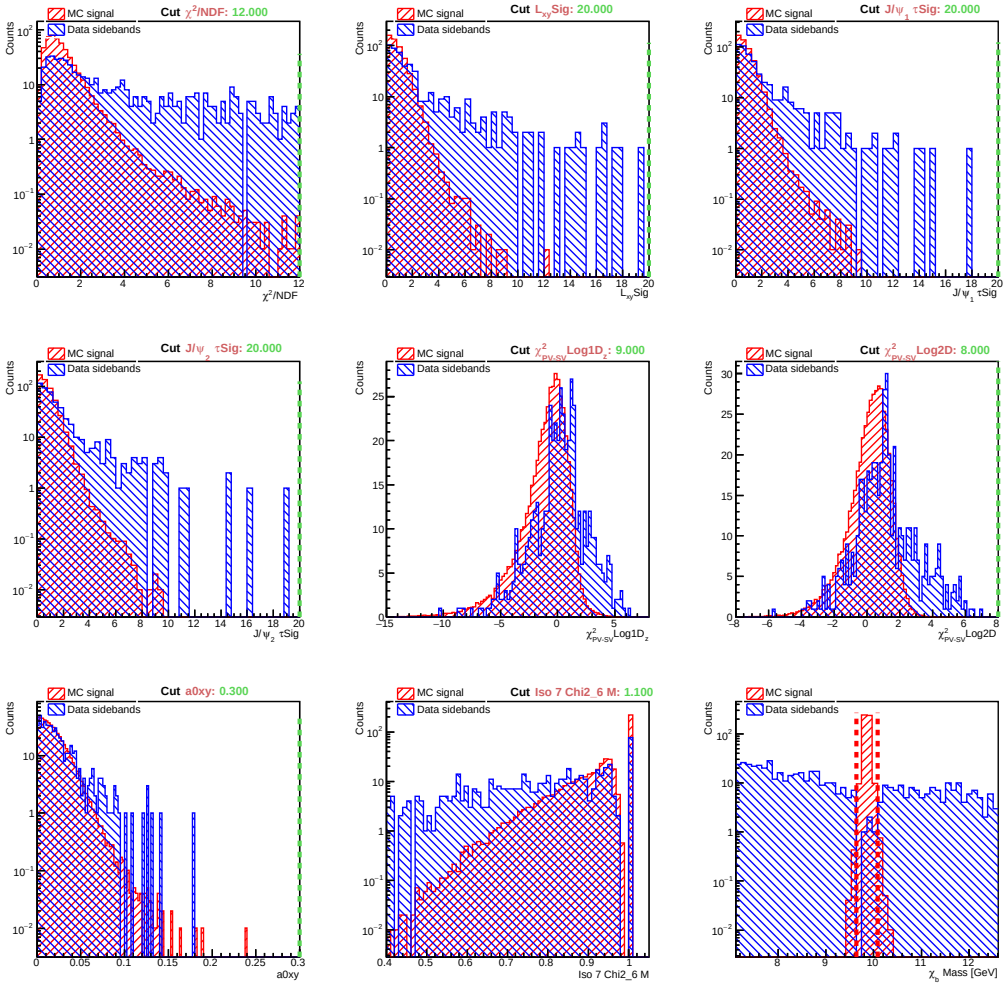

Figure 5.35: Spectra, without applying the optimum cuts, of MC signal events (with red) with Data sidebands (with blue) and cut position (green dotted line) for all discriminating variables (starting from top left: χ_b χ^2/NDF, χ_b $L_{xy}Sig$, J/ψ_1 Pseudo-proper lifetime significance (τSig), J/ψ_2 Pseudo-proper lifetime significance (τSig), χ_b $\chi^2(PV-SV)_{1Dz}$, χ_b $\chi^2(PV-SV)_{2D}$, χ_b a_0xy, χ_b Isolation) and for the mass at the bottom right.

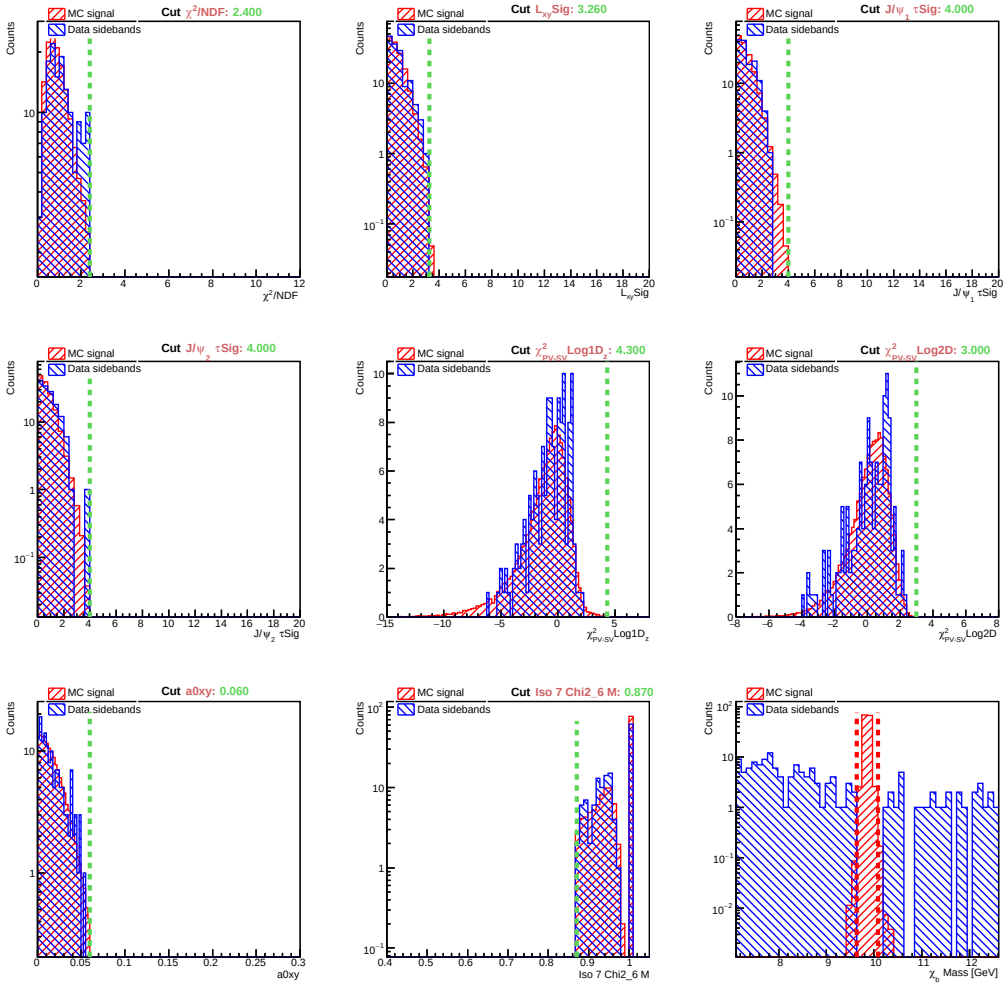

Figure 5.36: Spectra, after applying all the optimum cuts, of MC signal events (with red) with Data sidebands (with blue) and cut position (green dotted line) for all discriminating variables (starting from top left: χ_b χ^2/NDF, χ_b $L_{xy}Sig$, J/ψ_1 Pseudo-proper lifetime significance (τSig), J/ψ_2 Pseudo-proper lifetime significance (τSig), χ_b $\chi^2(PV-SV)_{1Dz}$, χ_b $\chi^2(PV-SV)_{2D}$, χ_b a_0xy, χ_b Isolation) and for the mass at the bottom right.

5.5 Statistical Extraction

Given that the optimal selection cuts have been established (already discussed in section 5.4) the final step before the "box opening" is to create the machinery for the statistical extraction of the result. The $\mathcal{B}\left(\chi_{\mathrm{b}} \to J/\psi J/\psi \to \mu^+\mu^-\mu^+\mu^-\right)$ is obtained by means of the formula 5.2, where substituting the SES (formula 5.3) one gets:

$$\mathcal{B}\left(\chi_{\mathrm{b}} \to J/\psi J/\psi \to \mu^+\mu^-\mu^+\mu^-\right) = SES \cdot N_{J/\psi J/\psi} \tag{5.6}$$

where the SES behaves like a translating factor between the $\mathcal{B}\left(\chi_{\mathrm{b}} \to J/\psi J/\psi \to \mu^+\mu^-\mu^+\mu^-\right)$ and the $N_{J/\psi J/\psi}$ and named like that due to the fact that it reflects the $\mathcal{B}$ if one signal event is found.

All the needed quantities appearing in the SES formula (formula 5.3) are listed in Table 5.6. while a discussion on them is following. The $\mathcal{B}\left(J/\psi \to \mu^+\mu^-\right)$ is used from external sources [67] while the rest of the ingredients collected through the various steps of this analysis.

$\mathcal{B}\left(J/\psi \to \mu^+\mu^-\right)$	World average value of the branching ratio of $J/\psi \to \mu^+\mu^-$
σ	Cross-section acquired from Pythia8B log files
$\mathcal{L}$	Integrated luminosity of pp collisions during 2012 data taking
ϵA	Ratio of the events passing analysis cuts over all generated

Table 5.6: Summary of the ingredients used on the SES formula.

In details:

$\mathcal{B}\left(J/\psi \to \mu^+\mu^-\right)$ with its corresponding uncertainty is retrieved from PDG [67] using the world average value 0.0591 ± 0.0033.

σ

For the cross-section, the Pythia8B log files from the signal generation were used. Based on those, σ is given from the formula $\sigma = PX \cdot N_B/Ac/M_{HAD}$ where PX is the Pythia cross-section, Ac is the number of accepted hard events in generation level, N_B is the number of accepted b-events and M_{HAD} is the repeated hadronizations in each event (equal to 1 for this analysis). The error quoted for this quantity has been estimated from the propagation of the corresponding uncertainties on the quantities used for the calculation. This value taken to be 46.41 ± 2.05 nb.

$\mathcal{L}$

For the purpose of this analysis the data selection resulted in a total integrated luminosity of $11.4 \pm 0.3\mathrm{fb}^{-1}$ for 2012 data taking periods under study, after the effects of prescaling and deadtime of the triggers are taken into account. The uncertainty on the integrated luminosity is 2.8% as further described in Ref. [68].

ϵA

The factor ϵA refers to the detector acceptance and efficiencies in the reconstruction part of the analysis. This number is estimated using the MC signal sample. From the 500000 generated events, only 41099 survived the acceptance of the detector, the preselections, the trigger and optimization cuts. The ϵA is derived by:

$\epsilon A = \frac{N_{recoPassingCutsEvents}}{N_{generated}} = \frac{41099}{500000} = 0.0822.$

For the calculation of the corresponding error, since the two quantities ($N_{recoPassingCutsEvents}$ and $N_{generated}$) are highly correlated (the numerator is a subset of the denominator) binomial error is quoted and found to be $3.88 \cdot 10^{-04}$.

Putting together the four terms, the SES is obtained as:

$SES = (6.56 \pm 0.81) \cdot 10^{-06}$

where, the relative uncertainty is about 12% and it is coming from the contribution of all the ingredients of the formula 5.3.

5.5.1 Expected Signal Events

A valid cross check for the analysis for both signal events and branching ratio, before moving towards the limit extraction, is to use the theoretical predictions in order to estimate the expected signal χ_b events. This can be done with the help of the formula 5.3 where the SES has been evaluated as mentioned above and $\mathcal{B}$ is taken from theoretical predictions. For the purposes of this test two different theoretical approaches were exploited, more details on them can be found on Refs. [69, 70].

Reference	$\mathcal{B}$ Value	Estimated signal χ_b events
[69]	$1.9 \cdot 10^{-5}$	2.9 ± 0.4
[70]	$0.5 \cdot 10^{-5}$	0.8 ± 0.1

Table 5.7: Estimated signal χ_b events using the measured quantities for the SES and $\mathcal{B}$ values coming from Refs. [69, 70]. The quoted error is accounting only uncertainties coming from the SES term.

Based on the ingredients calculated up to now and the box still closed, the two dominant theoretical approaches for the $\mathcal{B}$ of the $\chi_{\rm b} \to J/\psi J/\psi \to \mu^+\mu^-\mu^+\mu^-$ predict no more than 3 signal events.

5.5.2 Expected Limit

To extract an upper limit, the standard prescription set by LHC experiments for the extraction of frequentist limits by means of a standard implementation [71, 72] of the CL_s method [73] with a likelihood is used. The classification of the signal and

the background events is based on the event mass. For this purpose a likelihood of the form:

$$\mathcal{L} = N_{sig} \cdot Signal\,(Mass|\sigma, m) + N_{bkg} \cdot Pol\,(Mass|c_1, c_2) \quad (5.7)$$

can be used, where $Signal\,(Mass|\sigma, m)$ is modeling the signal part of the fit model using a Gaussian while $Pol\,(Mass|c_1, c_2)$ is modeling the background contribution with a second order Chebyshev polynomial. Using likelihood from Equation 5.7 a limit on the observed signal events (N_{sig}) could be set.

Exploiting the relation between N_{sig} and $\mathcal{B}$ provided by the formula 5.6, the likelihood described in Equation 5.7 can be altered in a way to provide directly the $\mathcal{B}$ estimation. This can be achieved by substituting the N_{sig} with $N_{sig} = \mathcal{B}/SES = \mathcal{B} \cdot cF$:

$$\mathcal{L} = ((\mathcal{B}_{est} \cdot cF) \cdot Signal\,(Mass|\sigma, m) + N_{bkg} \cdot Pol\,(Mass|c_1, c_2)) \times Gauss\,(cF|cF_{mean}, cF_{error}) \quad (5.8)$$

where cF is the inverse of SES and the $Gauss\,(cF|cF_{mean}, cF_{error})$ acts like a smearing factor for the uncertainties coming from cF.

Given to the low expected statistics (from expected signal calculation made on subsection 5.5.1 no more than 3 signal events are expected) and in order to make the likelihood robust and stable the width and mean of the Gaussian are going to be fixed to the values acquired from the fitting of the same model to the signal MC events that passed the analysis selection criteria. The result of that fit is shown in Figure 5.37.

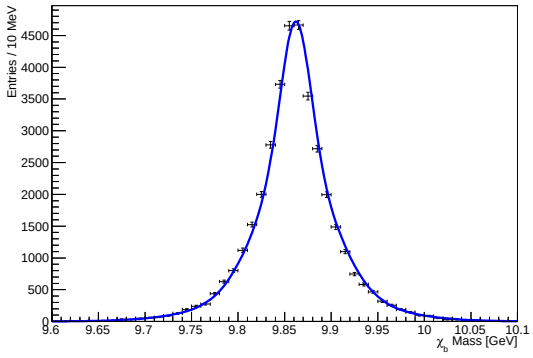

Figure 5.37: Fit of the likelihood on MC signal events that passed all analysis selection criteria in order to establish the parameters of the Gaussian.

Several closure tests were performed in order to validate the good behavior of the likelihood. On each test a dummy dataset was created using the likelihood with a priori known signal and background events. Afterwards the dataset was fitted with the likelihood and the estimated number of signal and background events were compared to the true value. In all cases agreement within the statistical

uncertainty of the fit was found. Two cases are illustrated in Figure 5.38. Toy shown in 5.38a generated with 300 signal events (fit estimated 302) while toy shown in 5.38a generated with 3 signal events (fit estimated 3.9).

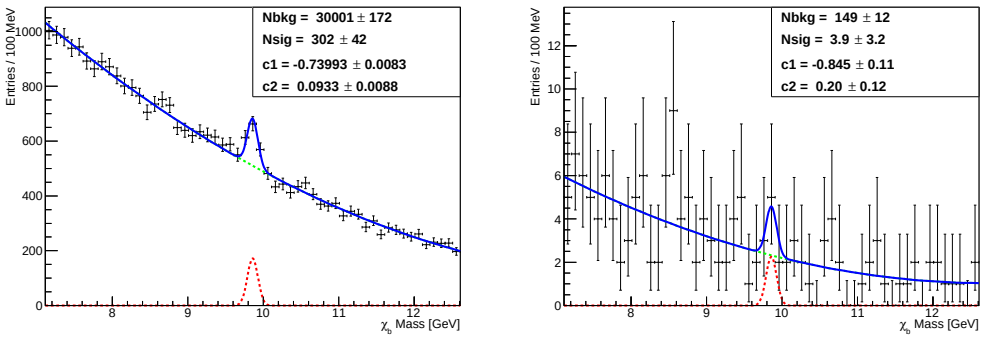

(a) N_{sig} : 300 (b) N_{sig} : 3

Figure 5.38: A toy study for the fit model used in the CL_s machinery. Two extreme cases are shown here, datasets created using the likelihood for the CL_s with 300 signal and 30000 background events (a) and 3 signal and 150 background events (b).

A final test performed using one dummy dataset populated with 3 signal events on the limit extraction machinery. Using the recommended machinery for the limit extraction and as input the outcome of the toy study described above the results for the $\mathcal{B}$ scan can be found in the Figure 5.39 where for 95% confidence level the expected limit is $4.4^{+1.8}_{-2.1} \cdot 10^{-5}$ which is in agreement with the theoretical predictions within the errors.

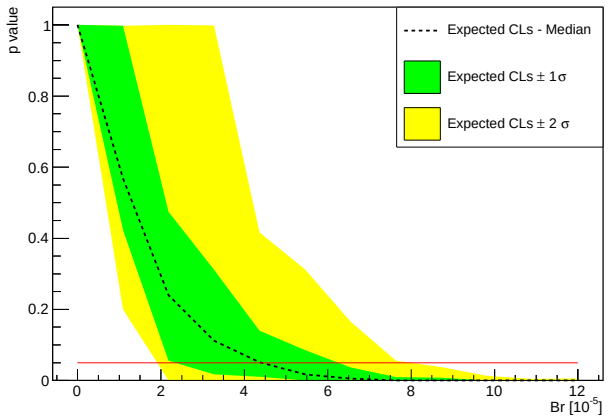

Figure 5.39: The CL_s scan on $\mathcal{B}$ for the toy study. The 95% CL limit is indicated by the horizontal (red) line. The green and yellow bands correspond to $\pm 1\sigma$ and $\pm 2\sigma$ fluctuations on the expectation (dashed line) based on the number of observed events.

5.5.3 Box Opening

Since all analysis components have been settled the revealing of the signal region took place. In total 152 events found in the full mass range under study. The mass distribution, after the "box opening", of candidates in data that passed all analysis selection criteria is shown in Figure 5.40.

From an unbinned fit on the data 1 ± 2.4 signal events were found which is compatible with zero. These events in combination with the likelihood and the SES factor were fed in the the limit extraction machinery yielding the observed CL_s curve reported in Figure 5.41 from which an upper limit $\mathcal{B} < 4.6 \cdot 10^{-5}$ 95% CL_s was set.

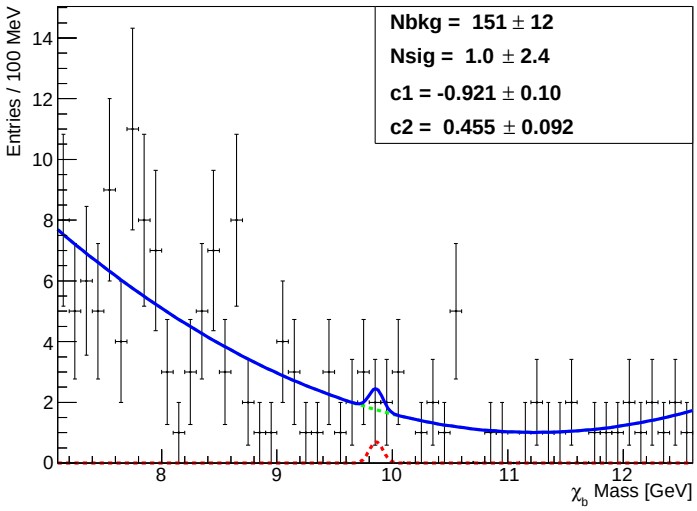

Figure 5.40: Mass distribution of candidates in data that passed all analysis selection criteria after the "box opening". The blue line indicates the total fit model, the green the background component and the red the signal.

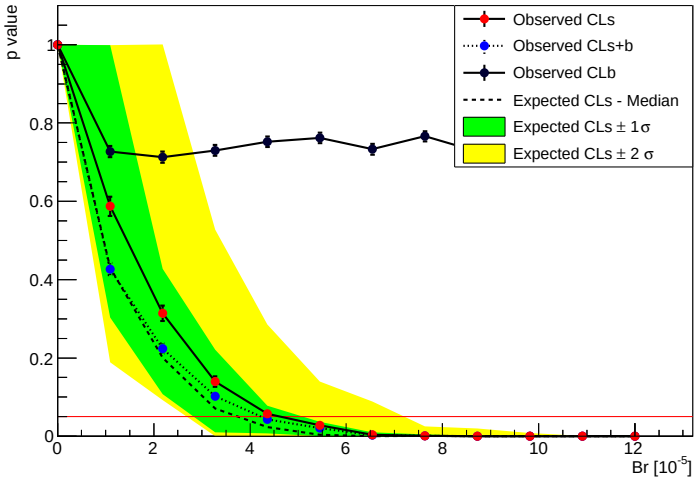

Figure 5.41: Expected CL_s (dashed), CL_{s+b} (blue points), CL_b (black points) as a function of $\mathcal{B}\left(\chi_{\mathrm{b}} \to J/\psi J/\psi \to \mu^+\mu^-\mu^+\mu^-\right)$ for the final analysis input parameters. The 95% CL limit is indicated by the horizontal (red) line. The observed CL_s curve after the box opening is reported with the red points. The green and yellow bands correspond to $\pm 1\sigma$ and $\pm 2\sigma$ fluctuations on the expected CL_s.

Chapter 6

Synopsis

The ATLAS experiment located at the world's largest particle accelerator and collider, LHC at CERN, is providing insights and glances at new and unexplored physics territories. This general purpose detector has a wide physics program starting from Standard Model and extends up to searches for exotic processes. The size and the complexity of a detector of such magnitude requires a powerful and adaptive automated system for the control, supervision and monitor of its various components and subsystems. This has been achieved by using a SCADA system. As shown in this thesis, PVSS II (later on WinCC) was used in order to take over the delicate supervision and alarming of the detector. The fine granularity of the detector itself and of its subsystems enforced the usage of a Finite State Machine inside the SCADA system for a hierarchy-based structure of the detector.

Exploiting the data collected with the ATLAS detector during the RUN-1 phase of the experiment (2011 and 2012 data-taking periods), the author of this thesis performed his work on B-physics area.

His first contribution regarding the B-physics analyses was with the $B_s^0 \to \mu{+}\mu^-$ analysis on the Rare Decays subgroup, a blinded analysis aiming to put a limit on the branching fraction $\mathcal{B}\left(B_s^0 \to \mu + \mu^-\right)$. The decay of $B^\pm \to J/\psi K^\pm$was used as a reference channel for the normalization of the integrated luminosity, acceptance, efficiency and systematics calculations. The main contribution of the author was during the data preparation including several systematic studies for the cuts and triggers that was used in the analysis, preparation and correction at various stages of the reconstructed MC (for both reference and signal channel) and detailed work on the systematics of the analysis.

In the quarkonia territory and more specifically in the charmonium area, a precise measurement held covering a large scale of rapidity and momenta (rapidity $|y| < 2.0$, transverse momenta 8 to 110 GeV) using J/ψ and $\psi(2\mathrm{S})$ decaying into two muons. The prompt and non-prompt production cross-sections, the non-prompt production fraction of the J/ψ and $\psi(2\mathrm{S})$ and the prompt and non-prompt ratios of $\psi(2\mathrm{S})$ to J/ψ production were measured using 11.4 fb^{-1} of pp collision data at a centre-of-mass energy of 8 TeV recorded by the ATLAS experiment at the LHC.

The predictions from the NRQCD model, which includes colour-octet contributions with various matrix elements tuned to earlier collider data, are in a good

agreement with the measured data points. Together with related measurements made by the other LHC collaborations [74–78, 78, 79], these results will help in the improvement of the understanding of the dynamics of the quarkonium production in hadronic collisions, which still has a number of unsolved puzzles.

Exploring further more the quarkonia territory and moving towards the bottomonium field, a blinded study held on $\chi_{b0} \to J/\psi J/\psi$ decay where both J/ψ are decaying into two muons. The first study of its kind on LHC era, putting a limit on both observed signal events and $\mathcal{B}(\chi_{b0} \to J/\psi J/\psi)$, performed using 11.4 fb^{-1} of pp collision data at a centre-of-mass energy of 8 TeV recorded by the ATLAS experiment at the LHC. The data were blinded in three dimensions in order to mine as much as possible information of the background from them while a signal MC was used in order to model the signal behavior needed for the multidimensional cut optimization. After the "box opening" 1 ± 2.4 signal events we found and using the CLs method the upper limit $\mathcal{B}(\chi_{b0} \to J/\psi J/\psi) \ < 4.6 \cdot 10^{-5}$ 95% CL_s was set.

Bibliography

[1] SLAC-SP-017 Collaboration, J. Augustin et al., *Discovery of a Narrow Resonance in e+ e- Annihilation*, Phys.Rev.Lett. **33** (1974) 1406–1408.

[2] E598 Collaboration, J. Aubert et al., *Experimental Observation of a Heavy Particle J*, Phys.Rev.Lett. **33** (1974) 1404–1406.

[3] L. Evans and P. Bryant, *LHC Machine*, Journal of Instrumentation **3** no. 08, (2008) S08001.

[4] ATLAS Collaboration, G. Aad et al., *The ATLAS Experiment at the CERN Large Hadron Collider*, Journal of Instrumentation **3** no. 08, (2008) S08003.

[5] S. Weinberg, *A Model of Leptons*, Phys. Rev. Lett. **19** (1967) 1264–1266, http://link.aps.org/doi/10.1103/PhysRevLett.19.1264.

[6] S. Glashow, *Partial Symmetries of Weak Interactions*, Nucl.Phys. **22** (1961) 579–588.

[7] A. Salam, *Weak and Electromagnetic Interactions*, Conf.Proc. **C680519** (1968) 367–377.

[8] A. Salam and J. C. Ward, *Gauge theory of elementary interactions*, Phys.Rev. **136** (1964) B763–B768.

[9] Particle Data Group Collaboration, K. Olive et al., *Review of Particle Physics*, Chin.Phys. **C38** (2014) 090001.

[10] S. Choudhury, G. C. Joshi, S. Mahajan, and B. H. McKellar, *Probing large distance higher dimensional gravity from lensing data*, Astropart.Phys. **21** (2004) 559–563, arXiv:hep-ph/0204161 [hep-ph].

[11] P. W. Higgs, *Broken Symmetries and the Masses of Gauge Bosons*, Phys.Rev.Lett. **13** (1964) 508–509.

[12] P. W. Higgs, *Spontaneous Symmetry Breakdown without Massless Bosons*, Phys.Rev. **145** (1966) 1156–1163.

[13] F. Englert and R. Brout, *Broken Symmetry and the Mass of Gauge Vector Mesons*, Phys.Rev.Lett. **13** (1964) 321–323.

[14] T. Kibble, *Symmetry breaking in nonAbelian gauge theories*, Phys.Rev. **155** (1967) 1554–1561.

[15] ATLAS Collaboration Collaboration, G. Aad et al., *Observation of a new particle in the search for the Standard Model Higgs boson with the ATLAS detector at the LHC*, Phys.Lett. **B716** (2012) 1–29, arXiv:1207.7214 [hep-ex].

[16] CMS Collaboration Collaboration, T. C. Collaboration, *Observation of a new boson at a mass of 125 GeV with the CMS experiment at the LHC*, Phys.Lett. **B716** (2012) 30–61, arXiv:1207.7235 [hep-ex].

[17] ATLAS, CMS Collaboration, G. Aad et al., *Combined Measurement of the Higgs Boson Mass in pp Collisions at $\sqrt{s} = 7$ and 8 TeV with the ATLAS and CMS Experiments*, Phys.Rev.Lett. **114** (2015) 191803, arXiv:1503.07589 [hep-ex].

[18] M. Gell-Mann and Y. Ne'eman, *The eightfold way New York*. W.A. Benjamin, New York, 1964.

[19] M. Gell-Mann, *A schematic model of baryons and mesons*, Physics Letters **8** no. 3, (1964) 214 - 215, http://www.sciencedirect.com/science/article/pii/S0031916364920013.

[20] G. Zweig, *An SU_3 model for strong interaction symmetry and its breaking; Version 1*, Tech. Rep. CERN-TH-401, CERN, Geneva, Jan, 1964. https://cds.cern.ch/record/352337.

[21] S. W. e. a. Herb, *Observation of a Dimuon Resonance at 9.5 GeV in 400-GeV Proton-Nucleus Collisions*, Phys. Rev. Lett. **39** (1977) 252–255, http://link.aps.org/doi/10.1103/PhysRevLett.39.252.

[22] G. Zweig, *An SU(3) model for strong interaction symmetry and its breaking. Version 1*,.

[23] H. Fritzsch, M. Gell-Mann, and H. Leutwyler, *Advantages of the Color Octet Gluon Picture*, Phys.Lett. **B47** (1973) 365–368.

[24] D. J. Gross and F. Wilczek, *Ultraviolet Behavior of Nonabelian Gauge Theories*, Phys.Rev.Lett. **30** (1973) 1343–1346.

[25] H. D. Politzer, *Reliable Perturbative Results for Strong Interactions?*, Phys.Rev.Lett. **30** (1973) 1346–1349.

[26] E. Eichten, K. Gottfried, T. Kinoshita, K. D. Lane, and T. M. Yan, *Charmonium: The model*, Phys. Rev. D **17** (1978) 3090–3117, http://link.aps.org/doi/10.1103/PhysRevD.17.3090.

[27] H. Fritzsch, *Producing heavy quark flavors in hadronic collisions. A test of quantum chromodynamics*, Physics Letters B **67** no. 2, (1977) 217 - 221, http://www.sciencedirect.com/science/article/pii/0370269377901083.

[28] E. Braaten, S. Fleming, and T. C. Yuan, *Production of heavy quarkonium in high-energy colliders*, Ann.Rev.Nucl.Part.Sci. **46** (1996) 197–235, arXiv:hep-ph/9602374 [hep-ph].

[29] V. Kartvelishvili, A. Likhoded, and S. Slabospitsky, *D meson and ψ meson production in hadronic interactions*, Sov. J. Nucl. Phys. **28** (1978) 678.

[30] J. Owens, E. Reya, and M. Gluck, *Detailed quantum chromodynamic predictions for high-p_{T} processes*, Phys. Rev. **D18** (1978) 1501.

[31] G. T. Bodwin, E. Braaten, and G. P. Lepage, *Rigorous QCD analysis of inclusive annihilation and production of heavy quarkonium*, Phys. Rev. **D51** (1995) 1125–1171, arXiv:hep-ph/9407339 [hep-ph].

[32] M. Butenschoen and B. A. Kniehl, *J/ψ production in NRQCD: A global analysis of yield and polarization*, Nucl. Phys. Proc. Suppl. **222-224** (2012) 151–161, arXiv:1201.3862 [hep-ph].

[33] P. Faccioli, C. Lourenco, J. Seixas, and H. K. Wohri, *Towards the experimental clarification of quarkonium polarization*, Eur.Phys.J. **C69** (2010) 657–673, arXiv:1006.2738 [hep-ph].

[34] O. S. BrG'Oning, P. Collier, P. Lebrun, S. Myers, R. Ostojic, J. Poole, and P. Proudlock, *LHC Design Report*. CERN, Geneva, 2004.

[35] ATLAS Collaboration, G. Aad et al., *Magnet System*. Technical Design Report ATLAS. CERN, Geneva, 1997.

[36] ATLAS Collaboration,, *ATLAS inner detector: Technical design report. Vol. 1*. CERN, 1997.

[37] ATLAS Collaboration, G. Aad et al., *ATLAS inner detector: Technical design report. Vol. 2*. 1997.

[38] The ATLAS Collaboration Collaboration, G. Aad et al., *ATLAS tile calorimeter: Technical design report*. CERN, 1996.

[39] ATLAS Collaboration Collaboration, G. Aad et al., *ATLAS liquid argon calorimeter: Technical design report*. CERN, 1996.

[40] ATLAS Collaboration, G. Aad et al., *ATLAS muon spectrometer: Technical design report*. 1997.

[41] H. L. Groenstege, *The RASNIK/CCD 3D alignment system*, Tech. Rep. ATL-MUON-94-063. ATL-M-PN-63, CERN, Geneva, Dec, 1994.

[42] ATLAS Collaboration, G. Aad et al., *Performance of the ATLAS Trigger System in 2010*, Eur.Phys.J. **C72** (2012) 1849, arXiv:1110.1530 [hep-ex].

[43] E. Piccaro and On Behalf of the ATLAS Collaboration, *Measurement of the ATLAS di-muon trigger efficiency in proton-proton collisions at 7 TeV*, ArXiv e-prints (2011), arXiv:1111.4329 [hep-ex].

[44] M. Gonzalez-Berges, *The Joint COntrols project framework*, eConf **C0303241** (2003) THGT006, arXiv:physics/0305128 [physics].

[45] A. Daneels and W. Salter, *Selection and Evaluation of Commercial SCADA Systems for the Controls of the CERN LHC Experiments*,.

[46] ETM, *ETM website*, 2014. http://www.etm.at/.

[47] B. Franek and C. Gaspar, *SMI++ object oriented framework used for automation and error recovery in the LHC experiments*, J. Phys.: Conf. Ser. **219** (2010) 022031. 10 p.

[48] ATLAS collaboration Collaboration, ATLAS Collaboration, G. Aad et al., *Improved luminosity determination in pp collisions at $\sqrt{(}s) = 7$ TeV using the ATLAS detector at the LHC*, arXiv:1302.4393v2 [hep-ex].

[49] ATLAS Collaboration Collaboration, G. Aad et al., *Measurement of the muon reconstruction performance of the ATLAS detector using 2011 and 2012 LHC proton-proton collision data*, arXiv:1407.3935 [hep-ex].

[50] ATLAS Collaboration,, *Measurement of the production cross-section of $\psi(2S) \to J/\psi\pi^+\pi^-$ in pp collisions at $\sqrt{s} = 7$ TeV at ATLAS*, to appear in JHEP (2014), arXiv:1407.5532 [hep-ex].

[51] ATLAS Collaboration, G. Aad et al., *Measurement of χ_{c1} and χ_{c2} production with $\sqrt{s} = 7$ TeV pp collisions at ATLAS*, JHEP **1407** (2014) 154, arXiv:1404.7035 [hep-ex].

[52] ATLAS Collaboration,, *Measurement of Υ production in $7\,\mathrm{TeV}$ pp collisions at ATLAS*, Phys. Rev. **D 87** (2013) 052004, arXiv:1211.7255 [hep-ex].

[53] M. Oreglia, *A Study of the Reactions $\psi' \to \gamma\gamma\psi$*. PhD thesis, 1980. SLAC-R-0236.

[54] H.-S. Shao, *HELAC-Onia: An automatic matrix element generator for heavy quarkonium physics*, Comput.Phys.Commun. **184** (2013) 2562–2570, arXiv:1212.5293 [hep-ph].

[55] A. Kanaki and C. G. Papadopoulos, *HELAC: A Package to compute electroweak helicity amplitudes*, Comput.Phys.Commun. **132** (2000) 306–315, arXiv:hep-ph/0002082 [hep-ph].

[56] M. Cacciari, S. Frixione, and P. Nason, *The p_{T} spectrum in heavy flavor photoproduction*, JHEP **0103** (2001) 006, arXiv:hep-ph/0102134 [hep-ph].

[57] M. Cacciari, S. Frixione, N. Houdeau, M. L. Mangano, P. Nason, et al., *Theoretical predictions for charm and bottom production at the LHC*, JHEP **1210** (2012) 137, arXiv:1205.6344 [hep-ph].

[58] V. Kartvelishvili and A. Likhoded, *DECAY $\chi_b \to \psi\psi$*, Yad.Fiz. **40** (1984) 1273.

[59] Belle Collaboration, C. Shen, C. Yuan, and T. Iijima, *Search for double charmonium decays of the P-wave spin-triplet bottomonium states*, Phys.Rev. **D85** (2012) 071102, arXiv:1203.0368 [hep-ex].

[60] C. Tsarouchas, T. Alexopoulos, E. Gazis, G. Tsipolitis, and S. Schlenker, *Study of Rare Decays of B Hadrons and Development of a Data Viewer Application of the Detector Control System in the ATLAS Detector*. PhD thesis, Nat. Tech. U. Athens, 2012. https://cds.cern.ch/record/1624086. Presented 2012.

[61] G. Punzi, *Sensitivity of searches for new signals and its optimization*, eConf **C030908** (2003) MODT002, arXiv:physics/0308063 [physics].

[62] T. Sjostrand, S. Mrenna, and P. Z. Skands, *A brief introduction to PYTHIA 8.1*, Comput. Phys. Commun. **178** (2008) 852–867, arXiv:0710.3820 [hep-ph].

[63] ATLAS Collaboration,, *The ATLAS Experiment at the CERN Large Hadron Collider*, JINST **3** (2008) S08003.

[64] T. Fawcett, *An introduction to {ROC} analysis*, Pattern Recognition Letters **27** no. 8, (2006) 861 - 874, {ROC} Analysis in Pattern Recognition, http://www.sciencedirect.com/science/article/pii/S016786550500303X.

[65] F. James and M. Winkler, *MINUIT User's Guide*,.

[66] F. James and M. Roos, *Minuit: A System for Function Minimization and Analysis of the Parameter Errors and Correlations*, Comput.Phys.Commun. **10** (1975) 343–367.

[67] Particle Data Group Collaboration, K. Olive et al., *Review of Particle Physics*, Chin.Phys. **C38** (2014) 090001.

[68] ATLAS Collaboration, G. Aad et al., *Improved luminosity determination in pp collisions at sqrt(s) = 7 TeV using the ATLAS detector at the LHC*, Eur.Phys.J. **C73** no. 8, (2013) 2518, arXiv:1302.4393 [hep-ex].

[69] J. Zhang, H. Dong, and F. Feng, *Exclusive decay of P-wave Bottomonium into double J/ψ*, Phys.Rev. **D84** (2011) 094031, arXiv:1108.0890 [hep-ph].

[70] V. V. Braguta, A. K. Likhoded, and A. V. Luchinsky, *Erratum: Double charmonium production in exclusive bottomonia decays [Phys. Rev. D **80** , 094008 (2009)]*, Phys. Rev. D **85** (2012) 119901, http://link.aps.org/doi/10.1103/PhysRevD.85.119901.

[71] R. Brun, P. Canal, and F. Rademakers, *Design, development and evolution of the ROOT system*, PoS **ACAT2010** (2010) 002.

[72] T. Junk, *Confidence level computation for combining searches with small statistics*, Nucl.Instrum.Meth. **A434** (1999) 435–443, arXiv:hep-ex/9902006 [hep-ex].

[73] A. L. Read, *Presentation of search results: The CL(s) technique*, J.Phys. **G28** (2002) 2693–2704.

[74] CMS Collaboration, CMS Collaboration, *J/ψ and $\psi(2S)$ production in pp collisions at $\sqrt{s} = 7$ TeV*, JHEP **1202** (2012) 011, arXiv:1111.1557 [hep-ex].

[75] CMS Collaboration, CMS Collaboration, *Measurement of the prompt J/ψ and ψ(2S) polarizations in pp collisions at $\sqrt{s} = 7$ TeV*, Phys. Lett. **B727** (2013) 381–402, arXiv:1307.6070 [hep-ex].

[76] LHCb Collaboration, LHCb Collaboration, R Aaij et al., *Measurement of $\psi(2S)$ meson production in pp collisions at $\sqrt{s} = 7$ TeV*, Eur. Phys. J. **C72** (2012) 2100, arXiv:1204.1258 [hep-ex].

[77] LHCb Collaboration, LHCb Collaboration, R Aaij et al., *Exclusive J/ψ and ψ(2S) production in pp collisions at $\sqrt{s} = 7$ TeV*, J.Phys. **G40** (2013) 045001, arXiv:1301.7084 [hep-ex].

[78] ALICE Collaboration, ALICE Collaboration, B. Abelev et al., *Measurement of quarkonium production at forward rapidity in pp collisions at $\sqrt{s} = 7$ TeV*, Eur. Phys. J. **C74** no. 8, (2014) 2974, arXiv:1403.3648 [nucl-ex].

[79] CMS Collaboration, CMS Collaboration, *Measurement of J/ψ and $\psi(2S)$ prompt double-differential cross sections in pp collisions at $\sqrt{(s)} = 7$ TeV*, Phys. Rev. Lett. **114** no. 19, (2015) 191802, arXiv:1502.04155 [hep-ex].

[80] S. Hassani et al., *A muon identification and combined reconstruction procedure for the ATLAS detector at the LHC using the (MUONBOY, STACO, MuTag) reconstruction packages*, Nucl.Instrum.Meth. **A572** (2007) 77–79.

Acknowledgements

I would like to express my gratitude to my professor Georgios Tsipolitis, firstly for trusting me and providing me the opportunity to live this experience and also for consulting me all the way through since the first day we started our collaboration.

I would like to thank my family for the courage and tolerance they had through the tough days and my wife who tried to learn physics in order to help me in the best way she could think of, staying awake through the nights listening to me analyzing a “new approach” I had found for a problem and never stopped believing to me.

My colleagues and friends helped me and supported me with any possible way those years even if that help came in form of disagreement and made me face any given single problem from a different aspect.

This work is partially supported by the European Union (European Social Fund - ESF) and Greek national funds through the Operational Program “Education and Lifelong Learning” of the National Strategic Reference Framework (NSRF) - Research Funding Program: THALES. Investing in knowledge society through the European Social Fund.

Appendix A

$B_s^0 \to \mu^+\mu^-$

In this section the contribution of the author to the analysis performed on the search for the decay $B_s^0 \to \mu^+\mu^-$ will be described. The strategy adopted for this analysis is not to measure directly the $B_s^0 \to \mu^+\mu^-$ branching ratio, but to obtain it from the branching ratio of another well measured B meson decay taken as reference which features similar kinematics as the signal. This choice allows to cancel out the main sources of systematic uncertainties.

The evaluation of the branching ratio can be reduced to the evaluation of the yield of the reference channel and of the relative acceptance and efficiencies. The analysis has been performed with the data collected with the ATLAS detector in 2011 and 2012 corresponding to integrated luminosities of $4.9fb^{-1}$ and $20.3fb^{-1}$ respectively.

A.1 Analysis Method

The number of observed events N_k^{obs} in the detector for a given particle decaying into the channel k is related to the number of events expected by the expression:

$$N_k^{obs} = \alpha_k \cdot \epsilon_k \cdot \sigma^{MC} \cdot Br(k)\mathcal{L} \tag{A.1}$$

where α_k accounts for the geometric and kinematic acceptance, ϵ_k includes the trigger, the reconstruction and the selection efficiency, $\mathcal{L}$ is the integrated luminosity, σ^{MC} is the cross section for the particle's production and $Br(k)$ is the decay branching fraction to the decay channel k. In the case of the rare decays generally the systematic uncertainties dominate the measurement as, apart form the integrated luminosity, all the quantities entering in equation A.1 are evaluated using a Monte Carlo simulation of the process and detector response.

This necessity to reduce as much as possible the systematic uncertainties on the branching ratio measurement of the $B_s^0 \to \mu^+\mu^-$ decay channel leads to the strategy of performing this measurement by normalizing it to the branching ratio of another B meson decay channel taken as reference, so that in the normalization most of the systematics cancel out and no direct measurement of the luminosity and of the cross-section of the process is needed.

In this view, the expression of the branching ratio reads

$$Br(B_s \to \mu^+\mu^-) = \frac{N_{\mu\mu}}{N_{ref}} \times \frac{\epsilon_{ref}\alpha_{ref}}{\epsilon_{\mu\mu}\alpha_{\mu\mu}} \times \frac{f_{ref}}{f_s} \times \frac{\mathcal{L}_{ref}}{\mathcal{L}_{\mu\mu}} \times Br(ref) \quad \text{(A.2)}$$

where the ratio f_{ref}/f_s takes into account the difference in the b-quark fragmentation probabilities, which is directly connected to the ratio of the relative cross sections.

The choice of the reference channel is lead by the similarity of the kinematics between the two decays along with the need of a high branching ratio which can lead to a large enough sample of events to reduce as much as possible the statistical uncertainties entering the measurement.

The reasons mentioned above lead to choose for this analysis as reference channel the $B^\pm \to J/\psi K^\pm$ decay channel, where the J/ψ further decays into two muons having opposite charge; equation A.2 can be so re-expressed as follows:

$$Br(B_s \to \mu^+\mu^-) = \frac{N_{\mu\mu}}{N_{B^\pm}} \times \frac{\epsilon_{B^\pm}\alpha_{B^\pm}}{\epsilon_{\mu\mu}\alpha_{\mu\mu}} \times \frac{f_{B^\pm}}{f_s} \times Br(B \to J/\psi K^\pm) \times Br(J/\psi \to \mu^+\mu^-) \quad \text{(A.3)}$$

where the luminosity factors cancel out since same integrated luminosity is used. Setting $N_{\mu\mu} = 1$ equation A.3 provides the so-called Single Event Sensitivity (SES).

The ATLAS b Physics Rare Decays group has adopted the blind analysis strategy, meaning that all the quantities entering the SES have been evaluated by excluding the signal region from the data sample. The blinding area corresponds to a mass window of $\pm$300MeV around the B_s invariant mass (5.0663 $\pm$ 0.0006 GeV). When the analysis was considered final and approved by the Collaboration the blinding area revealed and the final measurement takes place. For this reason, Monte Carlo samples were used as reference for the signal and the background, while to model the non-resonant background the data belonging in the sidebands of the signal region were used. In reality, the events in the sidebands have been used both for the selection criteria optimization procedure and for the estimation of the number of background events in the signal region.

A.2 Monte Carlo Tuning and Data-MC Comparisons

Discrepancies appear between data and Monte Carlo (MC) simulation due to lack of knowledge of the real B meson kinematics and delicate issues in generating Monte Carlo events (inaccuracy and incompleteness in the detector and simulation and modeling, low statistics, etc). In order to correct these discrepancies at the Generator Level Corrections (GLC) based on real data were calculated. The MC spectra were re-weighted based on real data distributions.

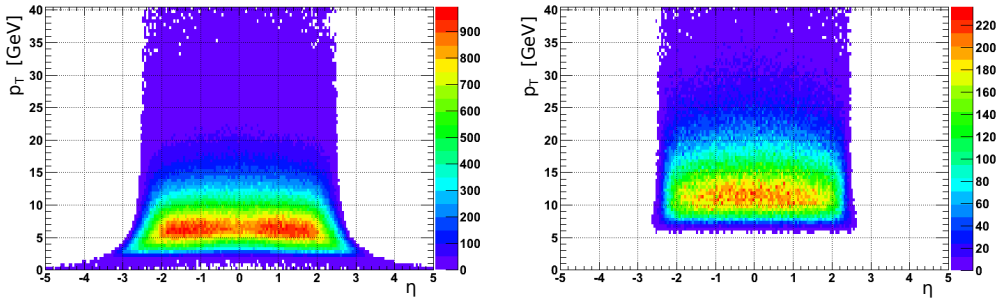

(a) B_s truth biased sample (b) B^+ truth biased sample

Figure A.1: Zoom of the B_s (a) and B^+ (b) truth spectra in the η, p_T plane as in Monte Carlo samples used.

A.2.1 Generator Level bias and correction

All MC samples are generated with PYTHIA in conjunction with PYTHIAB. b quarks generated are selectively forced to the decays of $B_s \to \mu^+\mu^-$, or $B^+ \to J/\psi K^+$ with $J/\psi \to \mu^+\mu^-$. In order to enhance the sample production efficiency, only events with one b quark with $|\eta| < 2.5$ and $p_T > 2.5$ GeV/c have been selected. In particular, in the Monte Carlo samples used, a selection has been applied on the MC true kinematic values: at least one muon with $p_T > 2.5$ GeV/c and $|\eta| < 2.5$ is required. In addition any hadron in the final state should have $p_T > 0.5$ GeV/c and $|\eta| < 2.5$. The MC samples obtained are analyzed with the full ATLAS GEANT4 simulation and the same software tools used for real data.

Additional MC samples for both $B_s \to \mu^+\mu^-$ and $B^+ \to J/\psi K^+$ decays have been privately generated by using PYTHIA in conjunction with PYTHIAB. This time only events with one b quark within $|\eta| < 4$ and $p_T > 2.5$ GeV/c were generated without applying any selection on the final state particles. These samples have been only used in the analysis in order to evaluate the bias introduced by the generator level selections of the final state kinematics and they were not processed via the full ATLAS detector simulation.

The kinematic requirements of the MC samples described above, although they are less stringent than the real analysis selection criteria, bias the b quark spectra of B_s and B^+ differently (since the first is a two body final state while the second a three body one).

Such a bias is shown in Figure A.1, where the B_s and B^+ mesons η and p_T distributions are plotted. The region between 0 and 7 GeV/c is almost empty for the B^+ meson, while B_s spectrum shows a discontinuity in the range of $\eta \in [-0.5, 0.5]$ for $p_T \in [5, 7]$ GeV/c which is not present in the case of the B^+.

To correct for this bias, Monte Carlo events have been generated without any selection on the final state particles. The corresponding η and p_T distributions for both B_s and B^+ mesons are shown in Figure A.2.

It can be seen that the unbiased B_s and B^+ samples have similar distributions. To compare the two distributions in a quantitative manner, a two-dimensional his-

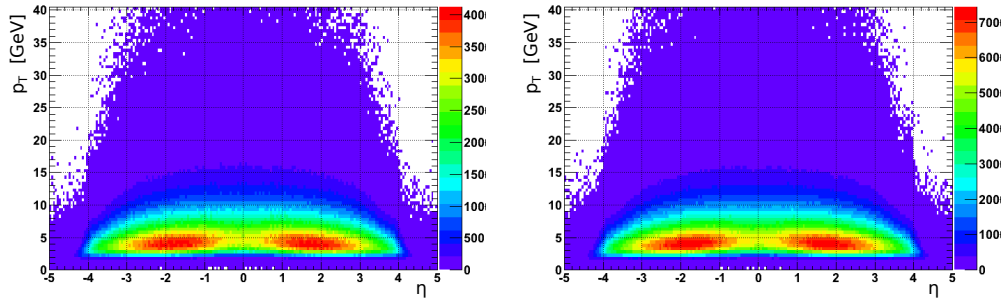

(a) B_s truth unbiased sample (b) B^+ truth unbiased sample

Figure A.2: Zoom of the B_s (a) and B^+ (b) truth spectra in the η, p_T plane generated by removing selection criteria on final state particles.

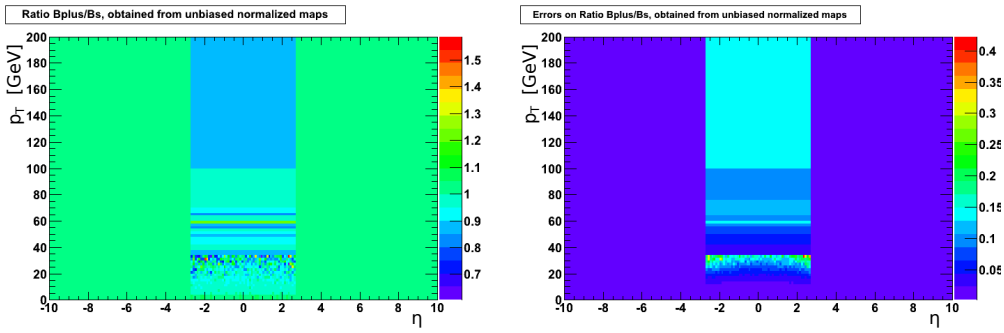

(a) B^+/B_s (b) B^+/B_s relative error

Figure A.3: The ratio of the normalized B^+ and B_s truth spectra (a) and relative errors (b) in the η, p_T plane obtained by using unbiased samples.

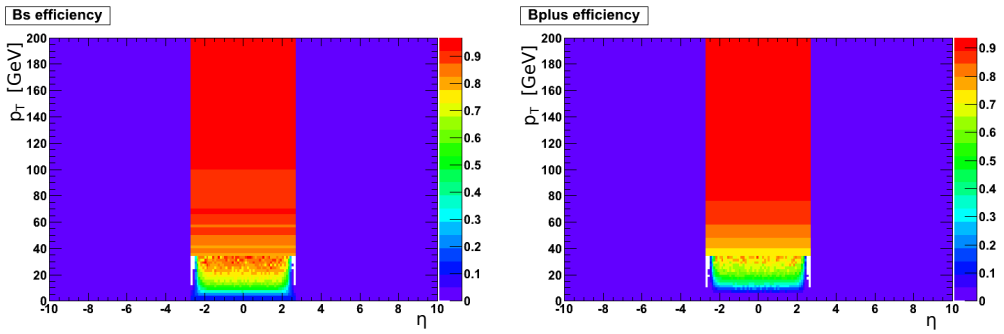

(a) B_s efficiency (b) B^+ efficiency

Figure A.4: The efficie maps of (a) the B_s and (b) B^+ mesons in the η, p_{T} plane. Each plot represents the ratio of the generated events after the selection criteria of the generator level over the full generated sample.

togram with the ratio of the B^+ and the B_s spectra, together with the one containing the relative errors on this ratio are plotted in Figure A.3. These plots confirm that

within the uncertainties the two spectra are compatible.

The generated unbiased samples have been thus used to build two-dimensional histograms to correct the MC generator bias. These histograms are the ratios between the two-dimensional histograms as a function of η and p_T. For the ratio, the numerator contains the number of events after the final selection selection criteria (FS) (at the generator level) and the denominator the total number of generated events. Such a histogram is effectively describing the event selection at the generator level. A separate histogram is generated per each decay mode. These efficiencies can be seen in Figure A.4.
Each event in a (η, p_T) bin is weighted by:

$$W^{GL}(\eta, p_T) = 1/\nu_{ij} \tag{A.4}$$

where ν_{ij} is the above mentioned efficiency for that bin. This weighting procedure is applied for events within the range of the efficiency histogram ($|\eta| < 2.5$).

To verify the procedure the calculated weights have been used to rectify biased MC samples. The effect of the weighting procedure can be seen in Figure A.5. The unbiased MC, the biased one and the re-weighted biased MC for B_s (left) and B^+ is shown. In the re-weighted distributions the mean is shifted to the left towards the mean value of the unbiased distribution. However given the limited range of validity of the weighting procedure, the two distributions do not completely overlap.

The binning of the histograms has been chosen such that it:

- is compatible to the histograms used for the data-driven re-weighting method as described in the following section. This is important as the two corrections will be used simultaneously;
- minimizes any distortion on the shapes of the corrected variables due to the finite bin width.

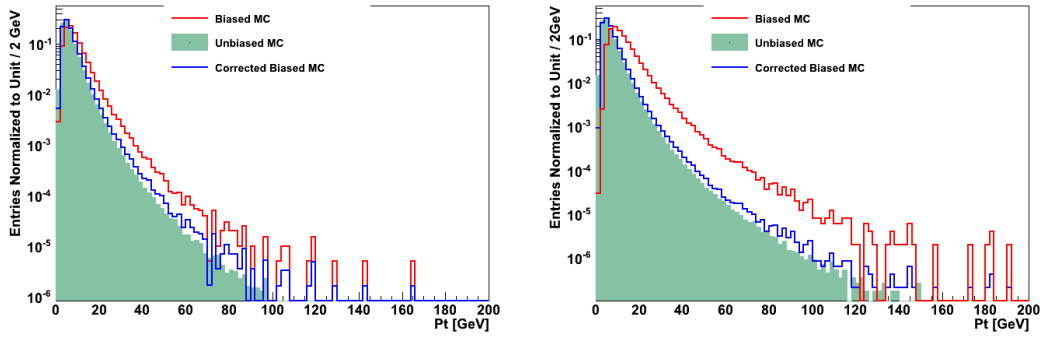

(a) B_s comparison (b) B^+ comparison

Figure A.5: The comparison between unbiased Monte Carlo, biased Monte Carlo and the re-weighted biased Monte Carlo for B_s (a) and B^+ (b).

Effects due to the binning used can be seen in Figure A.6. In Figure A.6a the black line shows the corrected η distribution of the B_s meson by using non-optimized binning for the weight maps: two peaks can be seen at approximately $\eta = \pm 2.5$. The optimized binning (filled violet) shows no such effect. The binning optimization improved as well the shape of the corrected p_T distribution shown in Figure A.6b.

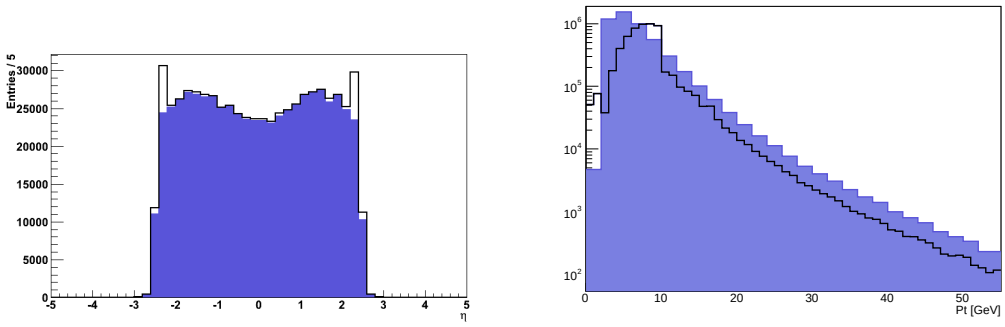

(a) (b)

Figure A.6: a) : the B_s η corrected distributions by using a non optimized (black line) and an optimized (filled violet) binning. (b): a "step-like" behavior of the corrected B^+ p_T can be seen if a non-optimized binning is used.

A.2.2 Data–MC Comparisons

For the calculation of the weights for B^+ mentioned in the previous section real data were used. The invariant mass distribution [5182.96 to 5382.96 MeV], the left sideband (L–S) [5082.96 to 5182.96 MeV] and the right sideband (R–S) [5382.96 to 5482.96 MeV]. For the current study (data driven weight calculation) only odd events from data were used.

Background level estimation

In order to minimize effects due to background events being considered as signal, an estimation of their number was performed based on the sidebands regions as defined in A.2.2. A binned fit is performed in the invariant mass of the $B^{\pm}$ using an exponential and a complementary error function for the background with a double gaussian for the signal.

The estimation of the number of signal and background events in the signal region (N_B) and in the sidebands (N_S) is based on the integral of the background function in these regions. Events in the sidebands will be assigned a weight $W_{SB} = -N_B/N_S$, where for the N_S both sideband regions were included, $\mathrm{N_S} = \mathrm{N_{R--S}} + \mathrm{N_{L--S}}$ while events in the signal region are assigned a weight $W_{SB} = 1$.

The two plots in Figure A.7 show the sideband subtracted distributions from η and p_T for the two muon reconstruction algorithms used for the early 2011 data, staco and muid [80] $\left(D_{\eta,p_T} = D^{signal}_{\eta,p_T} + W_{SB} \cdot D^{SB}_{\eta,p_T}\right)$.

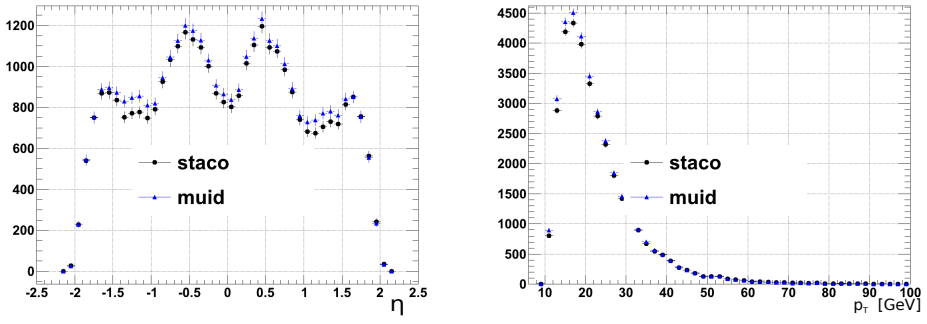

(a) (b)

Figure A.7: The sideband subtracted distributions of η and p_T. Projection of the data in η and p_T after removing the background contribution in the signal region by subtracting the events from sideband regions using a scaling factor acquired from a mass fit.

A.2.3 Data Driven Weight Estimation

Monte Carlo weights based on real data have been estimated using an iterative method. Monte Carlo events have been re-weighted as described in the previous section using the Generator Level Corrections. The data used for this purpose were the sideband-subtracted $B^{\pm} \to J/\psi K^{\pm}$ events (where the subtraction is performed as described in section A.2.2). The limited number of real data events forces the use of two one dimensional efficiency distributions (for η and p_T) instead of the full two dimensional one for the calculation of Data Driven Weights (DDW). This way the corresponding weight per (η, p_T) bin is factorized as a product of two independent weights:

$$W\left(Pt, \eta\right) = W_{Pt} \cdot W_{\eta} \tag{A.5}$$

where $W = \nu^{data}/\nu^{MC}$ and ν is the data (or MC) efficiency as a function of p_T or η. These weights are then used to re-weight the MC and the procedure is iterated until the weights converge.

In order to study the behavior of this iterative procedure, a study based entirely on Monte Carlo data was performed. The whole MC sample was divided in three different samples:

- sample A was artificially modified, to serve as an example of incorrect Monte Carlo simulation
- sample B was used as 'real data' for generating the appropriate weights
- and sample C was used as the reference sample for comparison.

The distributions from sample A before and after re-weighting are compared with these from sample C in Figures A.8 (for the pseudo-rapidity in the first two rows and p_T in the next two rows). In both cases the re-weighted distribution is closer to the one of the reference sample.

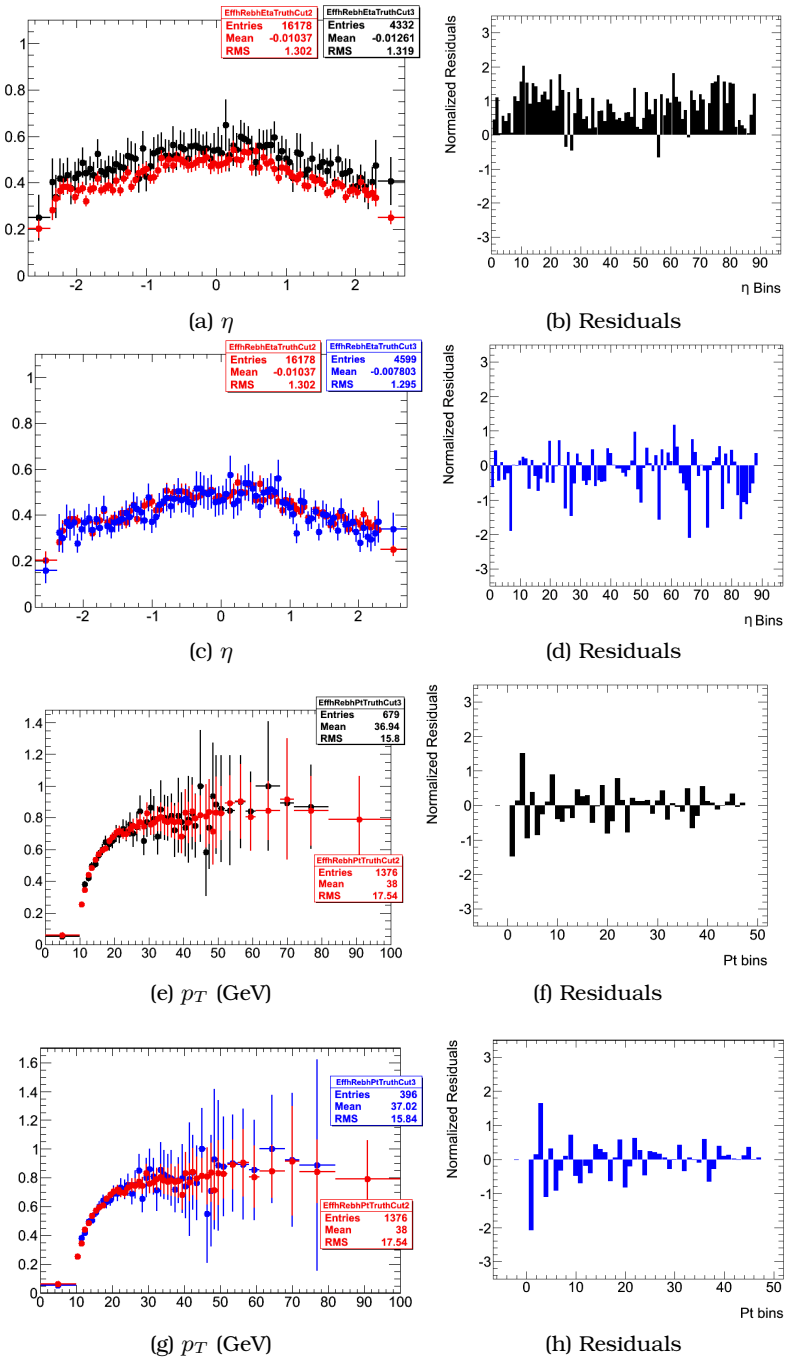

(a) η (b) Residuals

(c) η (d) Residuals

(e) p_T (GeV) (f) Residuals

(g) p_T (GeV) (h) Residuals

Figure A.8: η (a)-(d) and p_{T} (e)-(h) before (a), (b), (e), (f) and after (c), (d), (g), (h) the introduction of the corrections described in the text. The distributions are compared to the "reference" sample, and the residuals with respect to the latter are shown as well.

Calculation of η and p_T Weights

Since the previously described re-weighting method is iterative, particular attention has to be paid to the errors assigned to the final weights. In order to assure that all the sources of the statistical uncertainties and correlations have been taken into account, such as the errors of the sideband weights, the MC and real data distributions (properly propagating the errors), the normalization factors used for the weight extraction as well as those of the first order weights when they are used for the calculations of the second iteration, all ingredients used were represented with a custom made instances of a class where it took care for the correlations while making the needed calculus. The first and second iteration of the weights are calculated as follows:

$$W^1_{p_T} = \frac{\sum_\eta D_{\eta,p_T}}{\sum_{\eta,p_T} D_{\eta,p_T}} \frac{\sum_{\eta,p_T} MC_{\eta,p_T}}{\sum_\eta MC_{\eta,p_T}}$$

$$W^2_{p_T} = \frac{\sum_\eta D_{\eta,p_T}}{\sum_{\eta,p_T} D_{\eta,p_T}} \frac{\sum_{\eta,p_T} MC_{\eta,p_T} W^1_\eta W^1_{p_T}}{\sum_\eta MC_{\eta,p_T} W^1_\eta W^1_{p_T}}$$

(equivalent formulas hold for calculating the η weights.) The

$$\frac{\sum_{\eta,p_T} MC_{\eta,p_T}}{\sum_{\eta,p_T} D_{\eta,p_T}}$$

is the normalization factor for the first iteration while the

$$\frac{\sum_{\eta,p_T} D_{\eta,p_T}}{\sum_{\eta,p_T} MC_{\eta,p_T} W^1_\eta W^1_{p_T}}$$

is the normalization factor for the second iteration (taking into account the shape modification of the Monte Carlo distributions due to the re-weighting with the weights calculated in the first iteration). As mentioned above the weight applied to each event is: $W(p_T, \eta) = W_{p_T} \cdot W_\eta$.

Due to the nature of the iterative procedure, the final event weight used should be $W_{p_T} = W^1_{p_T} \cdot W^2_{p_T}$ for p_T and $W_\eta = W^1_\eta \cdot W^2_\eta$ for η, since the procedure converges fast and no more than two iterations are needed. This can clearly be seen in the two first rows of Figure A.9, where the second order weights are shown to be very close to one.

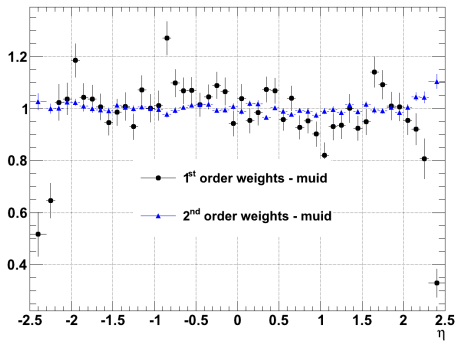

(a) η, muid weights

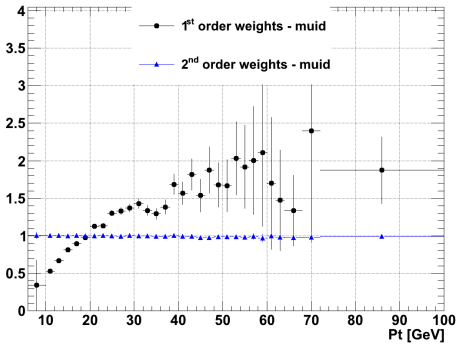

(b) p_T, muid weights

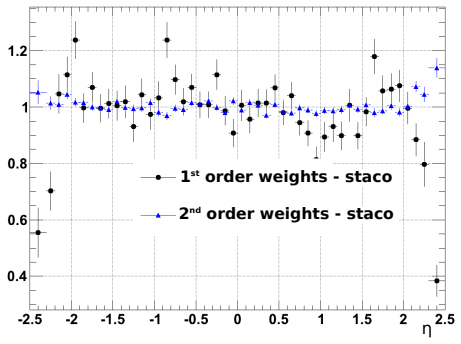

(c) η staco weights

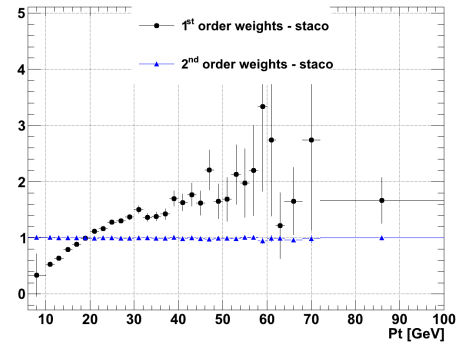

(d) p_T staco weights

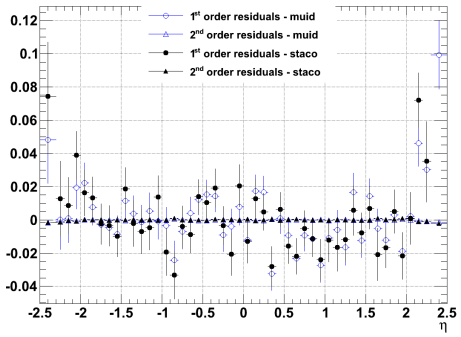

(e) η-dependent weights residuals

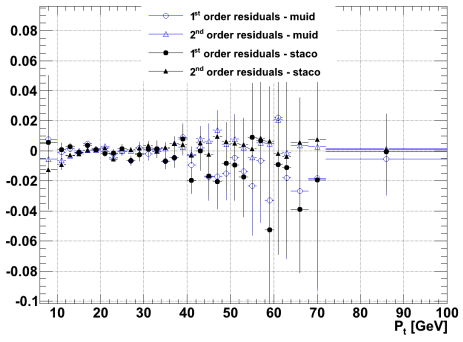

(f) p_T-dependent weight residuals

Figure A.9: 1^{st} and 2^{nd} order weights for η and p_T for both muid and staco [80]. Top row: muid muons used in reconstruction. Second row: staco muons used in the reconstruction. Third row: residuals for 1^{st} and 2^{nd} order weights, both muid and staco, for η and p_T.

A.2.4 Systematics

In order to check the systematic uncertainties that may come from the sideband subtraction, the weight sets calculated in different ways were compared. In particular three weight sample were studied:

- weights calculated using both sidebands
- weights calculated using only the left sideband
- weights calculated using only the right sideband.

As shown in Figures A.10 and A.11 all three weight sets converge, no significant differences have been observed and are compatible within the statistical uncertainty.

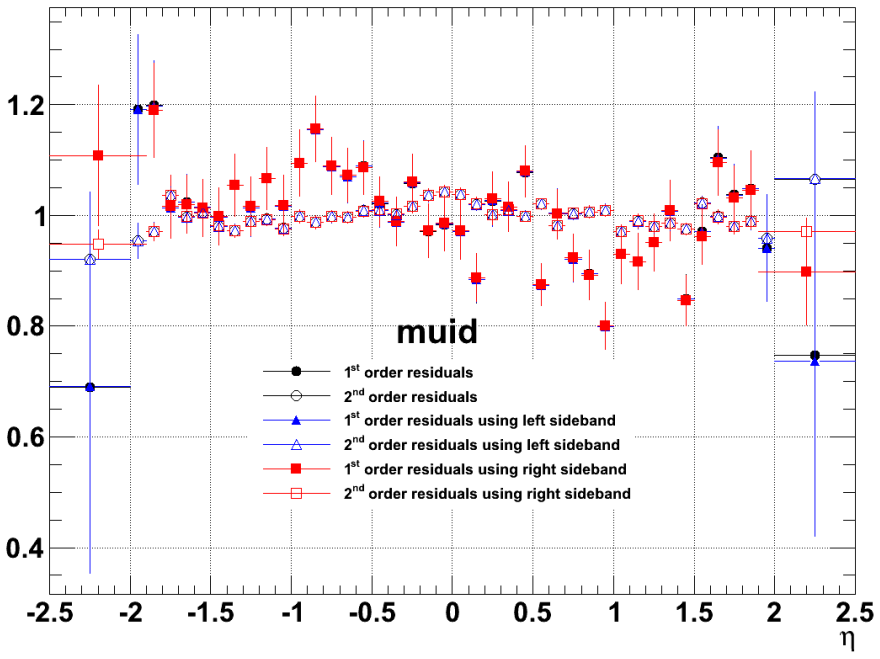

(a)

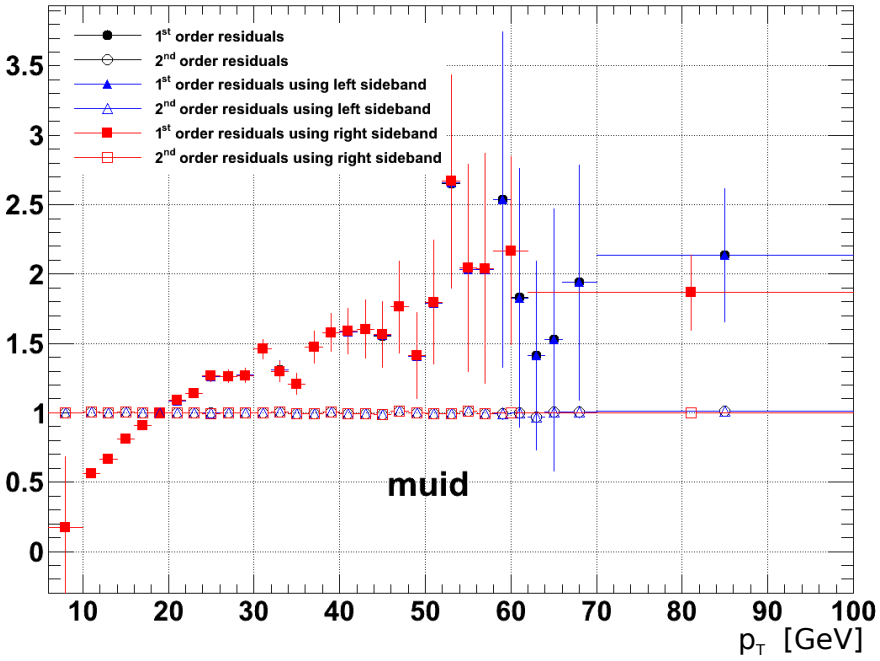

(b)

Figure A.10: The 1^{st} and 2^{nd} order weights for η and p_T (muid) using three different techniques for sideband subtraction weight calculation.

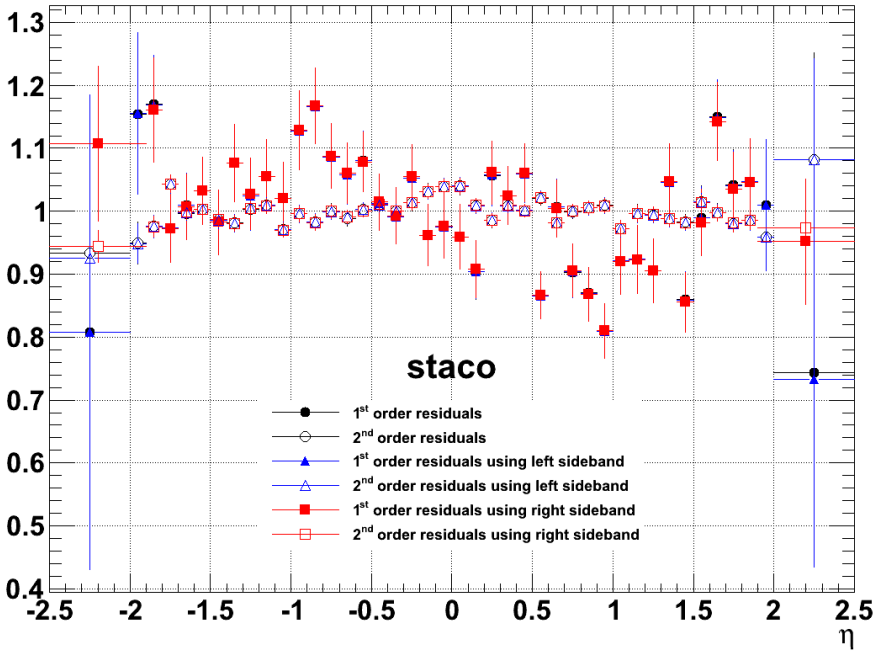

(a)

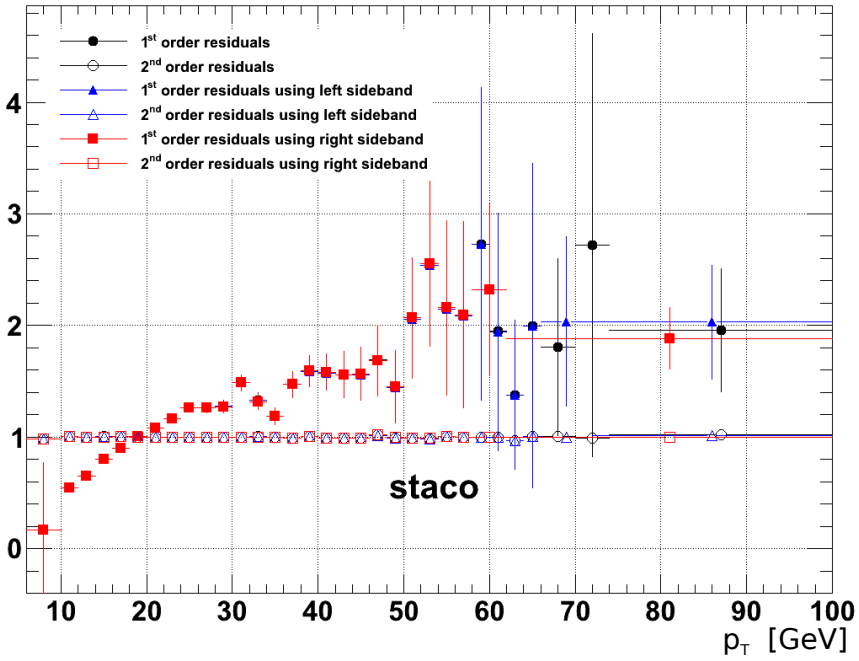

(b)

Figure A.11: The 1^{st} and 2^{nd} order weights for η and p_T (staco) using three different sideband subtraction weight calculation)

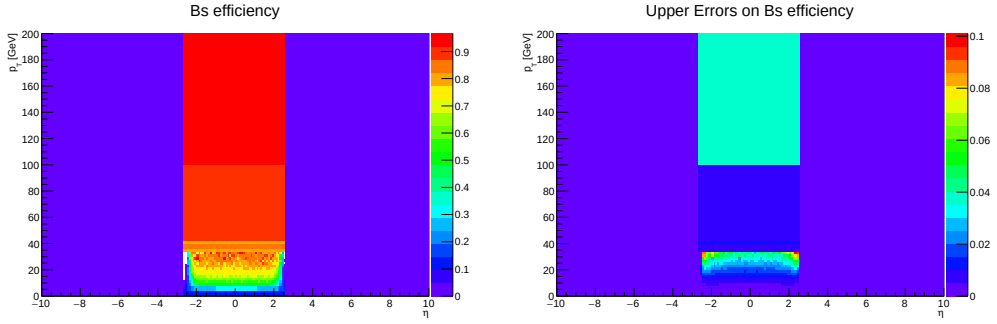

(a) Correction map (b) Correction map errors

Figure A.12: The generator level correction map and the corresponding errors for $B_s \to J/\psi\phi$ mode.

A.2.5 Studies on $B_s \to J/\psi\phi$

To further check the re-weighting procedure, weights have been calculated for the $B_s \to J/\psi\phi$ channel, following the exact same procedure as in the $B^{\pm}$ case.

The spectra are divided again in three regions, the signal region $[5331$ to $5391]$ MeV, the left sidebands $[5271$ to $5331]$ MeV and $[5391$ to $5451]$ MeV the right sideband. For this study (data driven weight calculation) only odd events from the data were used. With the final selection selection criteria, much tighter than the default used the in $J/\psi\phi$ analyses, we finally obtain about 2000 signal events (odd+even).

As in the previous study a generator level correction map is used to correct the Monte Carlo. The corresponding maps used for this part is shown in Figure A.12.

A.2.6 Data Driven Weights

The exact same method used for deriving the $B^+ \to J/\psi K^+$ weights, was also used for the weight set for the channel $B_s \to J/\psi\phi$. In Figure A.13 the first and the second order weights can be seen (for staco of B_s). Once again convergence of the iterative procedure is evident as second order weights are very close to one. The final weights estimated, are shown in Figure A.14.

Once the Data Driven Weights (DDW) set for the $B_s \to J/\psi\phi$ has been obtained, it has to be compared to the one calculated for $B^+ \to J/\psi K^+$. The data driven estimated weights for both channels ($B_s \to J/\psi\phi$ and $B^+ \to J/\psi K^+$) are shown in Figure A.15 for η and p_T. In order to properly compare the two sets of distributions the $B^+ \to J/\psi K^+$ weights were recalculated using the same binning as the $B_s \to J/\psi\phi$ channel.

A χ^2 test of the comparison of the re-binned weights for the two channels gave the following results:

	η	p_T
χ^2/NDF	1.68	0.756
Probability	0.0523	0.672

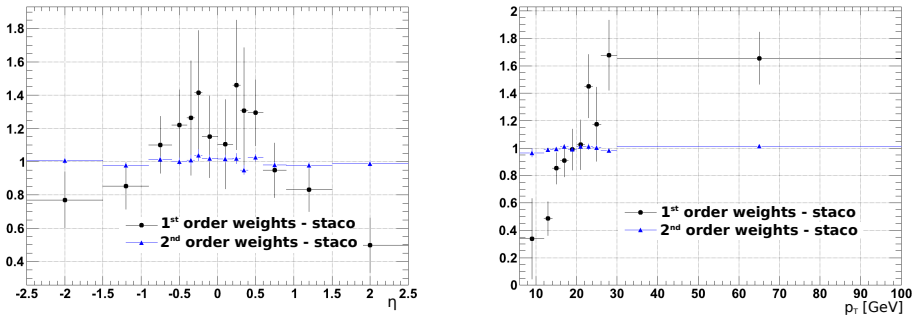

(a) (b)

Figure A.13: The 1^{st} and 2^{nd} order weights for η and p_T (staco).

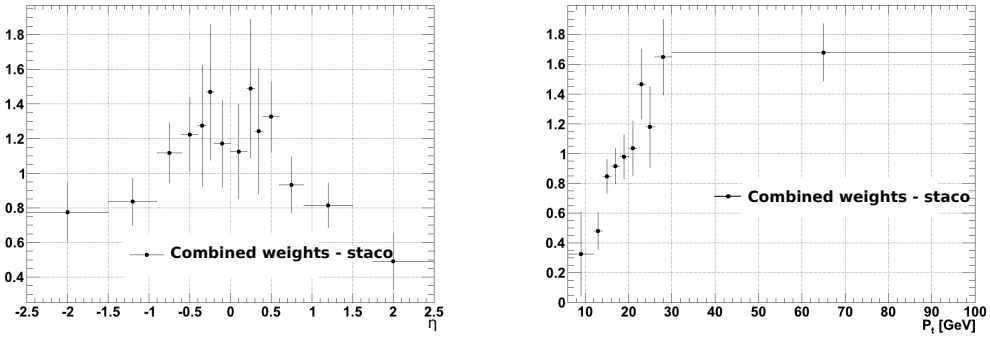

(a) (b)

Figure A.14: The combined weights for η and p_T, muid and staco.

The χ^2 test results indicates that the data driven weights extracted from $B^+ \to J/\psi\, K^+$ are compatible to the weights from the $B_s \to J/\psi\phi$.

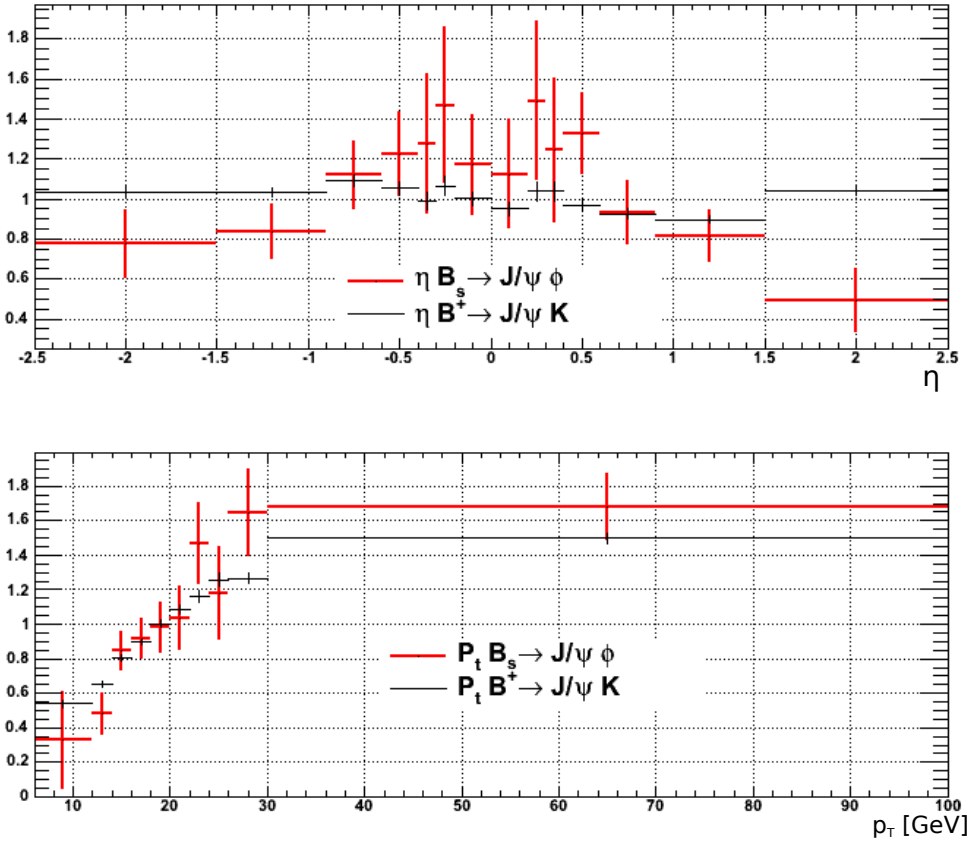

(a) Data driven weights comparison

Figure A.15: $B_s \to J/\psi\phi$ and $B^+ \to J/\psi K^+$ data driven weights for η and p_T.

A.3 Various Systematic Studies

In this subsection a brief description on various systematic studies that performed for the need of the $B_s \to \mu\mu$ analysis is given.

A.3.1 Granularity Study of GLC weights

The calculation of all the weights used in the present analysis (GLC and DDW) has been done with a discrete way using histograms to accumulate the involving quantities. The binning has the effect first to treat all the events inside the same bin with exactly the same manner and second to create step-wise behavior while changing regime (moving from one bin to a neighbor one).

In order to examine the effect of that we fit slices of the η vs p_T 2D map containing the combined correction (GLC and DDW) and the distributions of the fitted parameters in order to create the 2D model that is going to be used for the fit, were used. In Figure A.16 one can see the 2D map containing the combined weights, while the red continuous surface is the result of the fit.

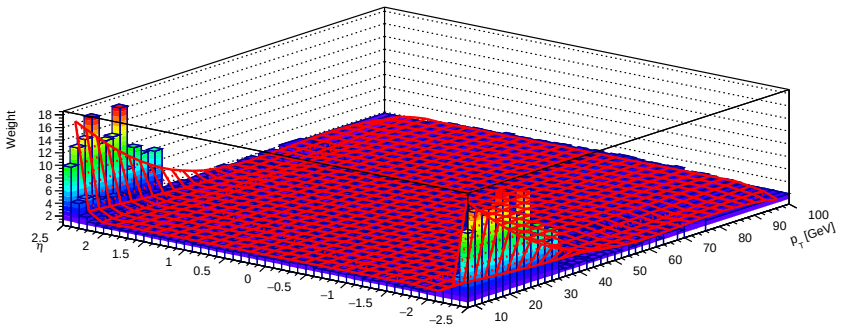

Figure A.16: Plot of the final weight map containing all weights and the 2D function that was used for the fitting of them (the red polygon surface).

As part of this study, the effect of using a continuous distribution (like a function) instead of a discrete (like a histogram) was estimated by performing the full calculations of efficiency times acceptance in two ways. Once by using as the assigned weight value of the corresponding bin for the given p_T and η and another time by evaluating the 2D function for the p_T and η of the candidate and comparing the results to each other.

In Figures A.17 one can find the results of the study mentioned above for the efficiency times acceptance of the B^+ channel as a function of η and p_T respectively. With the black histogram one can see the calculations performed using the 2D map (histogram) for the weight of each candidate while the red histogram is the result when the 2D function is used for the evaluation of the weight.

For a more immediate comparison of the results (Figures A.17) the difference of the two methods normalized to the nominal value (the one calculated using the

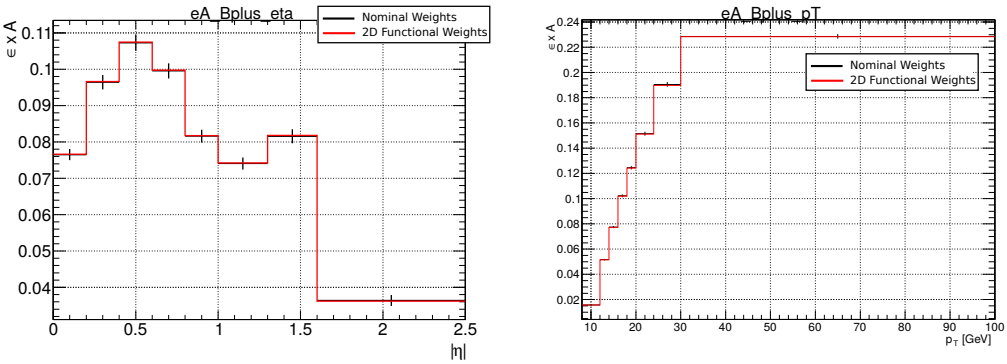

(a) Granularity effect versus η

(b) Granularity effect versus p_T

Figure A.17: Systematic study of the effect of the granularity of the weights in the calculation of the efficiency times acceptance for the B^+ channel as a function of η and as a function of p_T. With the black histogram one can see the calculations performed using the histogram by assigning the weight for each candidate, while with the red histogram one can see the calculations performed using the 2D function for the assigned weight.

histograms of the weights) of the efficiency times acceptance as a function of η and p_T respectively can be seen in Figures A.18. From these plots one can see that the differences are less than 0.5% and therefore are negligible.

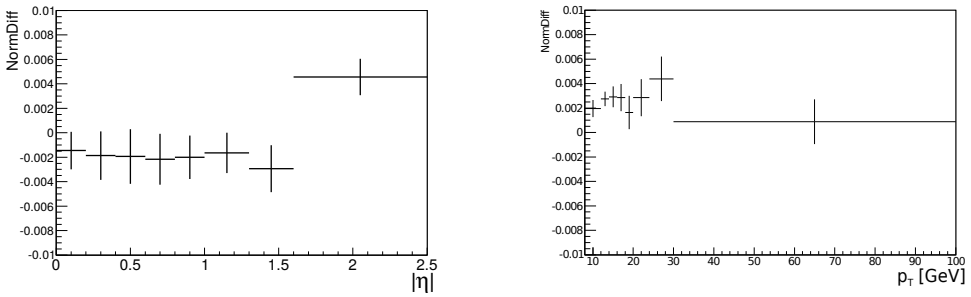

(a) Normalized difference versus η

(b) Normalized difference versus p_T

Figure A.18: Plot of the normalized difference of the two methods (one using the histogram for the weights and the other using the 2D graph interpolation) as a function of η and as a function of p_T.

A.3.2 Study on the triggers

In the middle of 2011 data taking, the trigger chain requirements were changed. Therefore, the 2011 data are split into two samples of roughly equal luminosities:

- Period A-K: EF_2mu4 (L1_2MU0 seed)
- Period L-M: EF_2mu4T (L1_2MU4 seed)

The EF_2mu4 chain was seeded at the Level 1 trigger from L1_2MU0 which has no p_T cut, while EF_2mu4T chain is seeded from L1_2MU4 which has a 4 GeV p_T cut already at Level 1.

The effect of this change was studied by comparing the number of events passing these triggers in the signal MC sample for the reference channel $B^{\pm} \to J/\psi K^{\pm}$. Figure A.19 and A.20 A.21 A.22 show the mass distributions obtained in this study: considering one single η bin, an effect of $(1.1 \pm 1.5)\%$ difference between the two triggers was observed. If instead, the three η ranges $[0, 1.0]$, $[1.0, 1.5]$, $[1.5, 2.5]$ were considered, the differences are $(2.7 \pm 2.0)\%$, $(1.4 \pm 3.0)\%$, and $(0.2 \pm 3.0)\%$ respectively. The effect is taken to be negligible. This has been confirmed by other ATLAS B-physics analyses.

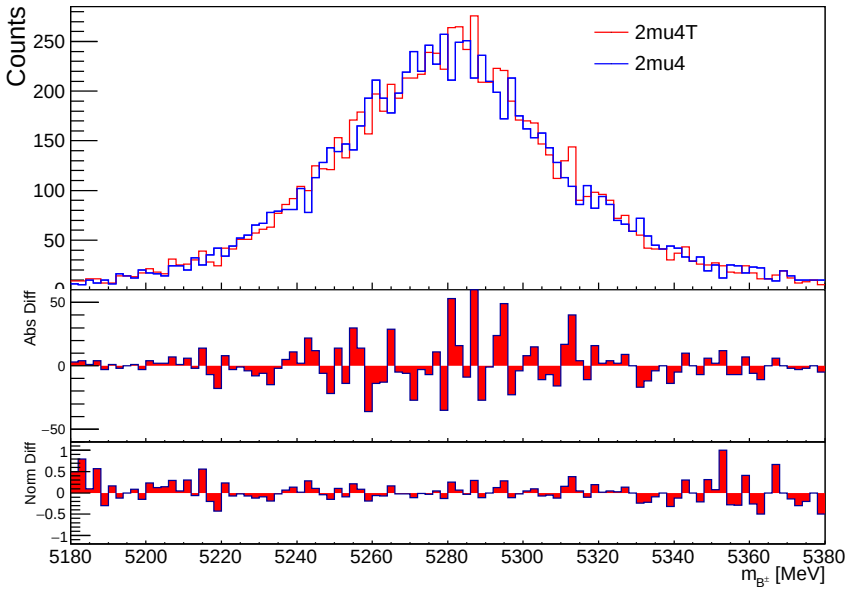

Figure A.19: Mass distributions for the selection of $B_s^0 \to \mu^+\mu^-$ decays with the `2mu4` or `2mu4T` trigger considering all the η_{MAX} (muon with the maximum absolute value of pseudorapidity) bins together.

In conclusion, no discrepancy between the two trigger chains found and it was decided to consider the entire 2011 data as a whole and consistent dataset.

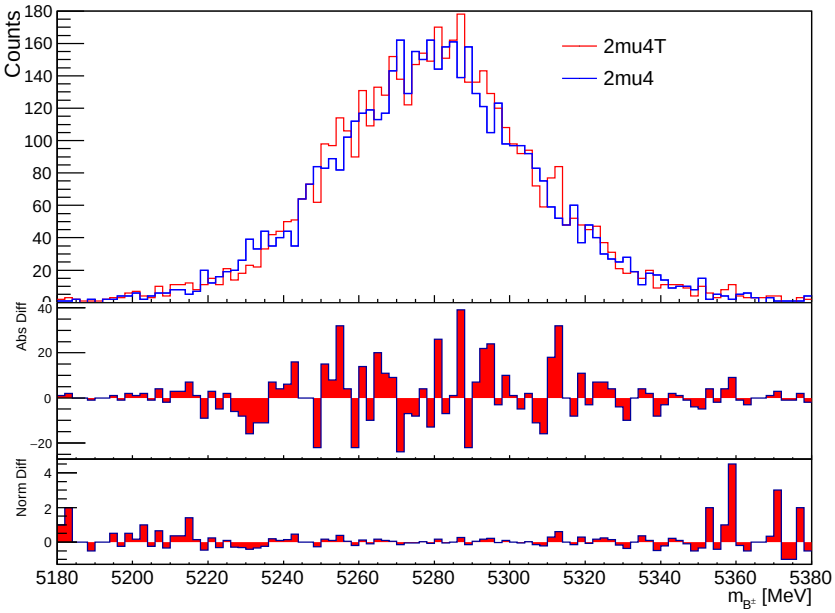

Figure A.20: Mass distributions for the selection of $B_s^0 \to \mu^+\mu^-$ decays with the `2mu4` or `2mu4T` trigger considering only events where the η_{MAX} (muon with the maximum absolute value of pseudorapidity) belongs to $[0,\ 1.0]$.

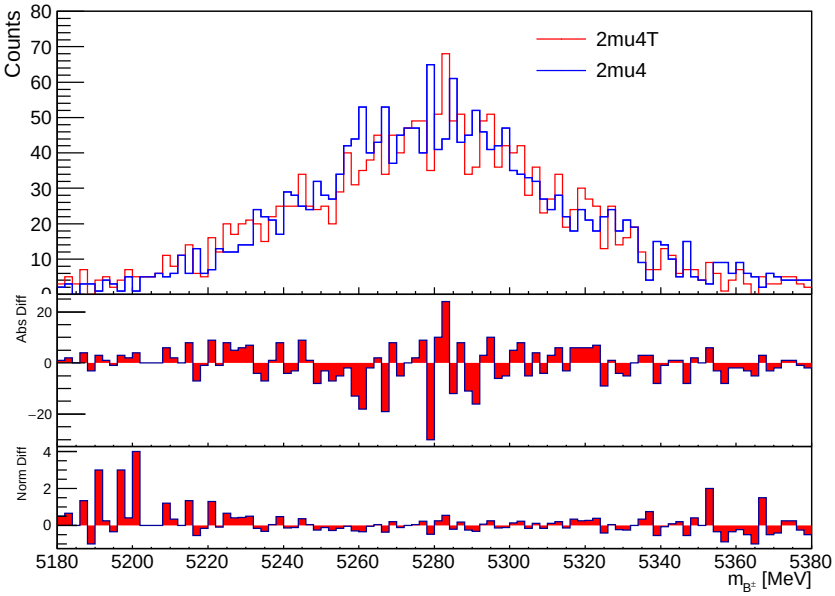

Figure A.21: Mass distributions for the selection of $B_s^0 \to \mu^+\mu^-$ decays with the `2mu4` or `2mu4T` trigger considering only events where the η_{MAX} (muon with the maximum absolute value of pseudorapidity) belongs to $[1.0,\ 1.5]$.

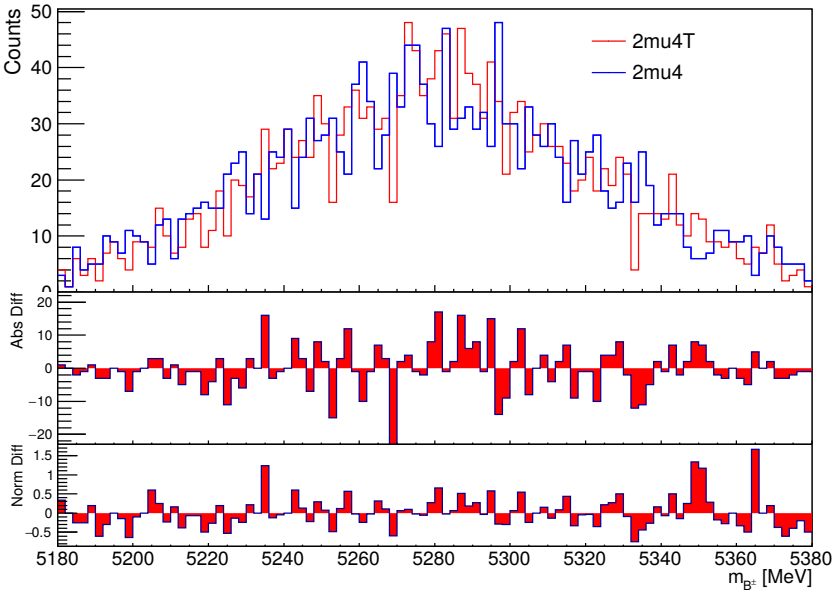

Figure A.22: Mass distributions for the selection of $B_s^0 \to \mu^+\mu^-$ decays with the `2mu4` or `2mu4T` trigger considering only events where the η_{MAX} (muon with the maximum absolute value of pseudorapidity) belongs to $[1.5,\ 2.5]$.

Appendix B

J/ψ and $\psi(2S)$

B.1 Datasets and event selection; supplementary information

B.1.1 The data selections

For the recorded data to be of sufficient quality to be considered for the analysis the Good Runs List data12_8TeV.periodAllYear_DetStatus-v61-pro14-02_DQDefects-00-01-00_PHYS_Standard
GRL_All_Good.xml was applied. Data from the BPhysics stream and the ONIA-MUMU_DAOD data format, using the software release 17.2.10.2 under processing grp14.

- Require at least two muons in the event.
- Both muons must have associated Inner Detector (ID) tracks.
- At least one muon must have combined information from ID and MS.
- The invariant mass (calculated from the ID track momenta and muon mass hypothesis) of at least one pair must satisfy 1.5 GeV $< M(\mu\mu) <$ 20 TeV.
- No explicit requirement on charge, kinematics or vertexing at this stage.

The skim criteria for the DAOD format are:

- data12_8TeV.periodC.physics_Bphysics.PhysCont.DAOD_JPSIMUMU.grp14_v03_p1425/
- data12_8TeV.periodD.physics_Bphysics.PhysCont.DAOD_JPSIMUMU.grp14_v04_p1425/
- data12_8TeV.periodE.physics_Bphysics.PhysCont.DAOD_JPSIMUMU.grp14_v03_p1425/
- data12_8TeV.periodG.physics_Bphysics.PhysCont.DAOD_JPSIMUMU.grp14_v03_p1425/
- data12_8TeV.periodH.physics_Bphysics.PhysCont.DAOD_JPSIMUMU.grp14_v03_p1425/
- data12_8TeV.periodI.physics_Bphysics.PhysCont.DAOD_JPSIMUMU.grp14_v03_p1425/

- data12_8TeV.periodJ.physics_Bphysics.PhysCont.DAOD_JPSIMUMU.grp14_v03_p1425/
- data12_8TeV.periodL.physics_Bphysics.PhysCont.DAOD_JPSIMUMU.grp14_v03_p1425/

The ROOT Ntuples are created from the standard B-Physics production and use the following datasets:

- user.achishol.data12_8TeV.periodC.physics_Bphysics.PhysCont.DAOD_JPSIMUMU.grp14_v04_p1425.Onia.Muons.v1/
- group.phys-beauty.user.achishol.data12_8TeV.periodD.physics_Bphysics.PhysCont.DAOD_JPSIMUMU.grp14_v04_p1425.Onia.Muons.v1/
- user.achishol.data12_8TeV.periodE.physics_Bphysics.PhysCont.DAOD_JPSIMUMU.grp14_v03_p1425.Onia.Muons.v1/
- user.achishol.data12_8TeV.periodG.physics_Bphysics.PhysCont.DAOD_JPSIMUMU.grp14_v03_p1425.Onia.Muons.v2/
- user.achishol.data12_8TeV.periodH.physics_Bphysics.PhysCont.DAOD_JPSIMUMU.grp14_v04_p1425.Onia.Muons.v1/
- user.achishol.data12_8TeV.periodI.physics_Bphysics.PhysCont.DAOD_JPSIMUMU.grp14_v03_p1425.Onia.Muons.v1/
- group.phys-beauty.user.achishol.data12_8TeV.periodJ.physics_Bphysics.PhysCont.DAOD_JPSIMUMU.grp14_v03_p1425.Onia.Muons.v1/
- group.phys-beauty.user.achishol.data12_8TeV.periodL.physics_Bphysics.PhysCont.DAOD_JPSIMUMU.grp14_v03_p1425.Onia.Muons.v1/

Trigger Selection

An event is considered if it passes the EF_2mu4T_Jpsimumu_L2StarB trigger, which was unprescaled for the majority of data taken between periods C6 – L. The L2StarB chains was implemented at period C6 (since run 206955) for all triggers in order to fix a bias affecting the pseudo proper lifetime estimation.

The EF_2mu4T_Jpsimumu_L2StarB trigger has a requirement of two muon regions of interest at Level 1 with $p_{\mathrm{T}} > 4$ GeV, plus a requirement of opposite-charged muons and an invariant mass between $2.5 < M(\mu\mu) < 4.2$ GeV. A breakdown of integrated luminosity by period is given in Table B.1. The uncertainty on the luminosity measurement is $\pm$ 2.8%. It is derived, following the same methodology as that detailed in Ref. [48], from a preliminary calibration of the luminosity scale derived from beam-separation scans performed in November 2012.

B.1.2 Event selections

Muons in events passing the selections above are sorted into pairs; each pair satisfying:

- They must be oppositely charged

Period	Runs	Eff. Luminosity (pb^{-1})
C6–C9	206955 – 207397	977.426
D	207447 – 209025	2929.86
E	209074 – 210308	2022.69
G	211620 – 212272	1059.63
H	212619 – 213359	1052.44
I	213431 – 213819	710.798
J	213900 – 215091	2051.2
L	215414 – 215643	632.578
Total		11436.622

Table B.1: Effective luminosity per period that was used in this analysis, collected with the EF_2mu4T_Jpsimumu_L2StarB trigger.

- They must both have associated "good" ID tracks passing the Muon CP group requirements:

  Number of pixel hits+number of crossed dead pixel sensors > 0

  Number of SCT hits+number of crossed dead SCT sensors > 4

  Number of pixel holes + number of SCT holes < 3

  A successful TRT extension where expected (i.e. in the eta acceptance of the TRT) An unsuccessful extension corresponds to either no TRT hit associated, or a set of TRT hits associated as outliers. The technical recommendation is therefore:

  Case 1 If nTRThits denote the number of TRT hits on the muon track, nTRToutliers the number of TRT outliers on the muon track, and n = nTRThits + nTRToutliers

  Case 2 $0.1 < |\eta| < 1.9$. Require n > 5 and nTRToutliers < 0.9 n

- Both muons must be combined muons (must have an associated ID track)
- Both muons must fall within a pseudorapidity region of $|\eta| < 2.3$
- The rapidity of the vertexed di-muon pair (onia candidate) must satisfy the rapidity requirement of $|y| < 2.0$
- The transverse momentum of the vertexed di-muon pair must satisfy the transverse momentum requirement of $p_T > 8.0$ GeV when the absolute rapidity is less than 0.75 while for the rest of di-muons the transverse momentum requirement is $p_T > 10.0$ GeV (the exclusion of this area is done due to a steeply changing low trigger efficiency and correlation effects at that area, which lead to an artificial fluctuation across rapidity of the measured cross sections)

- The invariant mass of an onia candidate, $M(\mu\mu)$, calculated from the ID track momenta and muon mass hypothesis must be within the range [2.6, 4.0] GeV.

B.1.3 Results in a tabular representation

Table B.2: Summary results for the cross section of prompt J/ψ for 8 TeV data. Uncertainties are statistical and systematic respectively.

p_T [GeV]	0.00–0.25	0.25–0.50	0.50–0.75	0.75–1.00
8.0 - 8.5	$3.25 \pm 0.01 \pm 0.42$	$3.19 \pm 0.01 \pm 0.46$	$3.38 \pm 0.01 \pm 0.33$	—
8.5 - 9.0	$2.59 \pm 0.00 \pm 0.28$	$2.52 \pm 0.01 \pm 0.31$	$2.70 \pm 0.01 \pm 0.21$	—
9.0 - 9.5	$2.00 \pm 0.00 \pm 0.20$	$1.96 \pm 0.00 \pm 0.22$	$2.03 \pm 0.00 \pm 0.17$	—
9.5 - 10.0	$1.49 \pm 0.00 \pm 0.15$	$1.50 \pm 0.00 \pm 0.17$	$1.55 \pm 0.00 \pm 0.13$	—
10.0 - 10.5	$1.14 \pm 0.00 \pm 0.11$	$1.16 \pm 0.00 \pm 0.13$	$1.19 \pm 0.00 \pm 0.10$	$1.07 \pm 0.00 \pm 0.05$
10.5 - 11.0	$(8.75 \pm 0.02 \pm 0.74) \cdot 10^{-1}$	$(9.13 \pm 0.02 \pm 0.93) \cdot 10^{-1}$	$(9.16 \pm 0.02 \pm 0.82) \cdot 10^{-1}$	$(8.29 \pm 0.02 \pm 0.43) \cdot 10^{-1}$
11.0 - 11.5	$(6.84 \pm 0.01 \pm 0.54) \cdot 10^{-1}$	$(7.22 \pm 0.01 \pm 0.71) \cdot 10^{-1}$	$(7.13 \pm 0.01 \pm 0.68) \cdot 10^{-1}$	$(6.53 \pm 0.01 \pm 0.39) \cdot 10^{-1}$
11.5 - 12.0	$(5.39 \pm 0.01 \pm 0.41) \cdot 10^{-1}$	$(5.78 \pm 0.01 \pm 0.55) \cdot 10^{-1}$	$(5.61 \pm 0.01 \pm 0.56) \cdot 10^{-1}$	$(5.14 \pm 0.01 \pm 0.33) \cdot 10^{-1}$
12.0 - 12.5	$(4.29 \pm 0.01 \pm 0.32) \cdot 10^{-1}$	$(4.65 \pm 0.01 \pm 0.42) \cdot 10^{-1}$	$(4.49 \pm 0.01 \pm 0.45) \cdot 10^{-1}$	$(4.10 \pm 0.01 \pm 0.26) \cdot 10^{-1}$
12.5 - 13.0	$(3.45 \pm 0.01 \pm 0.25) \cdot 10^{-1}$	$(3.79 \pm 0.01 \pm 0.33) \cdot 10^{-1}$	$(3.64 \pm 0.01 \pm 0.36) \cdot 10^{-1}$	$(3.33 \pm 0.01 \pm 0.21) \cdot 10^{-1}$
13.0 - 14.0	$(2.54 \pm 0.01 \pm 0.18) \cdot 10^{-1}$	$(2.81 \pm 0.00 \pm 0.23) \cdot 10^{-1}$	$(2.70 \pm 0.00 \pm 0.26) \cdot 10^{-1}$	$(2.45 \pm 0.01 \pm 0.14) \cdot 10^{-1}$
14.0 - 15.0	$(1.73 \pm 0.00 \pm 0.12) \cdot 10^{-1}$	$(1.94 \pm 0.00 \pm 0.14) \cdot 10^{-1}$	$(1.84 \pm 0.00 \pm 0.16) \cdot 10^{-1}$	$(1.66 \pm 0.02 \pm 0.10) \cdot 10^{-1}$
15.0 - 16.0	$(1.21 \pm 0.00 \pm 0.08) \cdot 10^{-1}$	$(1.35 \pm 0.00 \pm 0.09) \cdot 10^{-1}$	$(1.30 \pm 0.00 \pm 0.10) \cdot 10^{-1}$	$(1.15 \pm 0.00 \pm 0.07) \cdot 10^{-1}$
16.0 - 17.0	$(8.66 \pm 0.03 \pm 0.57) \cdot 10^{-2}$	$(9.74 \pm 0.03 \pm 0.62) \cdot 10^{-2}$	$(9.28 \pm 0.02 \pm 0.71) \cdot 10^{-2}$	$(8.15 \pm 0.03 \pm 0.50) \cdot 10^{-2}$
17.0 - 18.0	$(6.27 \pm 0.02 \pm 0.41) \cdot 10^{-2}$	$(7.06 \pm 0.02 \pm 0.46) \cdot 10^{-2}$	$(6.71 \pm 0.02 \pm 0.50) \cdot 10^{-2}$	$(5.86 \pm 0.02 \pm 0.39) \cdot 10^{-2}$
18.0 - 20.0	$(4.09 \pm 0.01 \pm 0.26) \cdot 10^{-2}$	$(4.55 \pm 0.01 \pm 0.30) \cdot 10^{-2}$	$(4.37 \pm 0.01 \pm 0.32) \cdot 10^{-2}$	$(3.73 \pm 0.01 \pm 0.27) \cdot 10^{-2}$
20.0 - 22.0	$(2.38 \pm 0.01 \pm 0.15) \cdot 10^{-2}$	$(2.64 \pm 0.01 \pm 0.17) \cdot 10^{-2}$	$(2.50 \pm 0.01 \pm 0.17) \cdot 10^{-2}$	$(2.17 \pm 0.01 \pm 0.17) \cdot 10^{-2}$
22.0 - 24.0	$(1.44 \pm 0.01 \pm 0.09) \cdot 10^{-2}$	$(1.59 \pm 0.01 \pm 0.10) \cdot 10^{-2}$	$(1.52 \pm 0.01 \pm 0.10) \cdot 10^{-2}$	$(1.31 \pm 0.01 \pm 0.10) \cdot 10^{-2}$
24.0 - 26.0	$(9.10 \pm 0.07 \pm 0.53) \cdot 10^{-3}$	$(1.01 \pm 0.01 \pm 0.06) \cdot 10^{-2}$	$(9.77 \pm 0.05 \pm 0.62) \cdot 10^{-3}$	$(8.34 \pm 0.05 \pm 0.66) \cdot 10^{-3}$
26.0 - 30.0	$(4.97 \pm 0.03 \pm 0.31) \cdot 10^{-3}$	$(5.53 \pm 0.03 \pm 0.35) \cdot 10^{-3}$	$(5.31 \pm 0.03 \pm 0.32) \cdot 10^{-3}$	$(4.60 \pm 0.03 \pm 0.37) \cdot 10^{-3}$
30.0 - 35.0	$(2.20 \pm 0.02 \pm 0.13) \cdot 10^{-3}$	$(2.45 \pm 0.02 \pm 0.16) \cdot 10^{-3}$	$(2.40 \pm 0.02 \pm 0.14) \cdot 10^{-3}$	$(2.04 \pm 0.02 \pm 0.17) \cdot 10^{-3}$
35.0 - 40.0	$(9.75 \pm 0.14 \pm 0.71) \cdot 10^{-4}$	$(1.08 \pm 0.01 \pm 0.07) \cdot 10^{-3}$	$(1.07 \pm 0.01 \pm 0.07) \cdot 10^{-3}$	$(9.23 \pm 0.11 \pm 0.82) \cdot 10^{-4}$
40.0 - 60.0	$(2.22 \pm 0.03 \pm 0.19) \cdot 10^{-4}$	$(2.60 \pm 0.03 \pm 0.22) \cdot 10^{-4}$	$(2.54 \pm 0.03 \pm 0.20) \cdot 10^{-4}$	$(2.31 \pm 0.03 \pm 0.26) \cdot 10^{-4}$
60.0 - 110.0	$(1.15 \pm 0.05 \pm 0.23) \cdot 10^{-5}$	$(1.29 \pm 0.05 \pm 0.26) \cdot 10^{-5}$	$(1.22 \pm 0.04 \pm 0.23) \cdot 10^{-5}$	$(1.33 \pm 0.05 \pm 0.31) \cdot 10^{-5}$
p_T [GeV]	1.00–1.25	1.25–1.50	1.50–1.75	1.75–2.00
8.0 - 8.5	—	—	—	—
8.5 - 9.0	—	—	—	—
9.0 - 9.5	—	—	—	—
9.5 - 10.0	—	—	—	—
10.0 - 10.5	$1.10 \pm 0.00 \pm 0.07$	$1.04 \pm 0.00 \pm 0.06$	$1.04 \pm 0.00 \pm 0.06$	$1.05 \pm 0.00 \pm 0.09$
10.5 - 11.0	$(8.63 \pm 0.02 \pm 0.50) \cdot 10^{-1}$	$(8.23 \pm 0.02 \pm 0.44) \cdot 10^{-1}$	$(8.13 \pm 0.02 \pm 0.52) \cdot 10^{-1}$	$(8.19 \pm 0.02 \pm 0.64) \cdot 10^{-1}$
11.0 - 11.5	$(6.88 \pm 0.02 \pm 0.39) \cdot 10^{-1}$	$(6.45 \pm 0.02 \pm 0.32) \cdot 10^{-1}$	$(6.42 \pm 0.01 \pm 0.44) \cdot 10^{-1}$	$(6.36 \pm 0.01 \pm 0.47) \cdot 10^{-1}$
11.5 - 12.0	$(5.48 \pm 0.01 \pm 0.30) \cdot 10^{-1}$	$(5.15 \pm 0.01 \pm 0.26) \cdot 10^{-1}$	$(5.07 \pm 0.01 \pm 0.36) \cdot 10^{-1}$	$(5.02 \pm 0.01 \pm 0.36) \cdot 10^{-1}$
12.0 - 12.5	$(4.40 \pm 0.01 \pm 0.24) \cdot 10^{-1}$	$(4.11 \pm 0.01 \pm 0.22) \cdot 10^{-1}$	$(4.07 \pm 0.01 \pm 0.30) \cdot 10^{-1}$	$(4.01 \pm 0.01 \pm 0.28) \cdot 10^{-1}$
12.5 - 13.0	$(3.53 \pm 0.01 \pm 0.20) \cdot 10^{-1}$	$(3.32 \pm 0.01 \pm 0.19) \cdot 10^{-1}$	$(3.25 \pm 0.01 \pm 0.25) \cdot 10^{-1}$	$(3.25 \pm 0.01 \pm 0.22) \cdot 10^{-1}$
13.0 - 14.0	$(2.60 \pm 0.01 \pm 0.14) \cdot 10^{-1}$	$(2.47 \pm 0.01 \pm 0.16) \cdot 10^{-1}$	$(2.40 \pm 0.00 \pm 0.19) \cdot 10^{-1}$	$(2.36 \pm 0.00 \pm 0.15) \cdot 10^{-1}$
14.0 - 15.0	$(1.74 \pm 0.00 \pm 0.10) \cdot 10^{-1}$	$(1.67 \pm 0.00 \pm 0.12) \cdot 10^{-1}$	$(1.61 \pm 0.00 \pm 0.13) \cdot 10^{-1}$	$(1.57 \pm 0.00 \pm 0.09) \cdot 10^{-1}$
15.0 - 16.0	$(1.19 \pm 0.00 \pm 0.07) \cdot 10^{-1}$	$(1.15 \pm 0.00 \pm 0.09) \cdot 10^{-1}$	$(1.10 \pm 0.00 \pm 0.09) \cdot 10^{-1}$	$(1.06 \pm 0.00 \pm 0.06) \cdot 10^{-1}$
16.0 - 17.0	$(8.40 \pm 0.03 \pm 0.56) \cdot 10^{-2}$	$(8.06 \pm 0.02 \pm 0.70) \cdot 10^{-2}$	$(7.71 \pm 0.02 \pm 0.60) \cdot 10^{-2}$	$(7.46 \pm 0.02 \pm 0.42) \cdot 10^{-2}$
17.0 - 18.0	$(6.00 \pm 0.02 \pm 0.43) \cdot 10^{-2}$	$(5.78 \pm 0.02 \pm 0.51) \cdot 10^{-2}$	$(5.54 \pm 0.02 \pm 0.43) \cdot 10^{-2}$	$(5.33 \pm 0.02 \pm 0.30) \cdot 10^{-2}$
18.0 - 20.0	$(3.81 \pm 0.01 \pm 0.29) \cdot 10^{-2}$	$(3.69 \pm 0.01 \pm 0.33) \cdot 10^{-2}$	$(3.53 \pm 0.01 \pm 0.28) \cdot 10^{-2}$	$(3.37 \pm 0.01 \pm 0.20) \cdot 10^{-2}$
20.0 - 22.0	$(2.19 \pm 0.01 \pm 0.18) \cdot 10^{-2}$	$(2.10 \pm 0.01 \pm 0.19) \cdot 10^{-2}$	$(1.99 \pm 0.01 \pm 0.16) \cdot 10^{-2}$	$(1.89 \pm 0.01 \pm 0.11) \cdot 10^{-2}$
22.0 - 24.0	$(1.31 \pm 0.01 \pm 0.12) \cdot 10^{-2}$	$(1.25 \pm 0.01 \pm 0.11) \cdot 10^{-2}$	$(1.18 \pm 0.01 \pm 0.09) \cdot 10^{-2}$	$(1.12 \pm 0.01 \pm 0.07) \cdot 10^{-2}$
24.0 - 26.0	$(8.19 \pm 0.05 \pm 0.75) \cdot 10^{-3}$	$(7.80 \pm 0.04 \pm 0.72) \cdot 10^{-3}$	$(7.34 \pm 0.04 \pm 0.59) \cdot 10^{-3}$	$(6.93 \pm 0.04 \pm 0.46) \cdot 10^{-3}$
26.0 - 30.0	$(4.41 \pm 0.03 \pm 0.41) \cdot 10^{-3}$	$(4.18 \pm 0.02 \pm 0.39) \cdot 10^{-3}$	$(4.05 \pm 0.02 \pm 0.33) \cdot 10^{-3}$	$(3.69 \pm 0.02 \pm 0.25) \cdot 10^{-3}$
30.0 - 35.0	$(1.94 \pm 0.02 \pm 0.19) \cdot 10^{-3}$	$(1.82 \pm 0.01 \pm 0.18) \cdot 10^{-3}$	$(1.72 \pm 0.01 \pm 0.14) \cdot 10^{-3}$	$(1.57 \pm 0.01 \pm 0.12) \cdot 10^{-3}$
35.0 - 40.0	$(8.71 \pm 0.10 \pm 0.89) \cdot 10^{-4}$	$(7.83 \pm 0.08 \pm 0.81) \cdot 10^{-4}$	$(7.49 \pm 0.08 \pm 0.67) \cdot 10^{-4}$	$(6.45 \pm 0.08 \pm 0.49) \cdot 10^{-4}$
40.0 - 60.0	$(2.16 \pm 0.03 \pm 0.23) \cdot 10^{-4}$	$(1.84 \pm 0.02 \pm 0.24) \cdot 10^{-4}$	$(1.74 \pm 0.02 \pm 0.20) \cdot 10^{-4}$	$(1.51 \pm 0.03 \pm 0.14) \cdot 10^{-4}$
60.0 - 110.0	$(1.18 \pm 0.04 \pm 0.21) \cdot 10^{-5}$	$(9.98 \pm 0.33 \pm 2.38) \cdot 10^{-6}$	$(8.56 \pm 0.33 \pm 1.92) \cdot 10^{-6}$	$(6.98 \pm 0.34 \pm 1.22) \cdot 10^{-6}$

Table B.3: Summary results for the cross section of non-prompt J/ψ for 8 TeV data. Uncertainties are statistical and systematic respectively.

p_T [GeV]	0.00–0.25	0.25–0.50	0.50–0.75	0.75–1.00
8.0 - 8.5	$1.24 \pm 0.01 \pm 0.16$	$1.21 \pm 0.01 \pm 0.17$	$1.26 \pm 0.01 \pm 0.13$	—-
8.5 - 9.0	$1.06 \pm 0.00 \pm 0.12$	$1.03 \pm 0.00 \pm 0.13$	$1.09 \pm 0.01 \pm 0.09$	—-
9.0 - 9.5	$(8.66 \pm 0.03 \pm 0.88) \cdot 10^{-1}$	$(8.55 \pm 0.03 \pm 0.98) \cdot 10^{-1}$	$(8.74 \pm 0.03 \pm 0.72) \cdot 10^{-1}$	—-
9.5 - 10.0	$(6.92 \pm 0.02 \pm 0.71) \cdot 10^{-1}$	$(6.96 \pm 0.02 \pm 0.79) \cdot 10^{-1}$	$(7.08 \pm 0.02 \pm 0.58) \cdot 10^{-1}$	—-
10.0 - 10.5	$(5.63 \pm 0.02 \pm 0.53) \cdot 10^{-1}$	$(5.71 \pm 0.02 \pm 0.62) \cdot 10^{-1}$	$(5.78 \pm 0.02 \pm 0.49) \cdot 10^{-1}$	$(5.22 \pm 0.02 \pm 0.23) \cdot 10^{-1}$
10.5 - 11.0	$(4.62 \pm 0.02 \pm 0.39) \cdot 10^{-1}$	$(4.78 \pm 0.02 \pm 0.49) \cdot 10^{-1}$	$(4.74 \pm 0.01 \pm 0.43) \cdot 10^{-1}$	$(4.31 \pm 0.02 \pm 0.22) \cdot 10^{-1}$
11.0 - 11.5	$(3.83 \pm 0.01 \pm 0.30) \cdot 10^{-1}$	$(4.04 \pm 0.01 \pm 0.40) \cdot 10^{-1}$	$(3.92 \pm 0.01 \pm 0.37) \cdot 10^{-1}$	$(3.56 \pm 0.01 \pm 0.21) \cdot 10^{-1}$
11.5 - 12.0	$(3.19 \pm 0.01 \pm 0.24) \cdot 10^{-1}$	$(3.40 \pm 0.01 \pm 0.32) \cdot 10^{-1}$	$(3.27 \pm 0.01 \pm 0.33) \cdot 10^{-1}$	$(2.99 \pm 0.01 \pm 0.19) \cdot 10^{-1}$
12.0 - 12.5	$(2.70 \pm 0.01 \pm 0.20) \cdot 10^{-1}$	$(2.91 \pm 0.01 \pm 0.26) \cdot 10^{-1}$	$(2.78 \pm 0.01 \pm 0.28) \cdot 10^{-1}$	$(2.53 \pm 0.01 \pm 0.16) \cdot 10^{-1}$
12.5 - 13.0	$(2.27 \pm 0.01 \pm 0.16) \cdot 10^{-1}$	$(2.49 \pm 0.01 \pm 0.21) \cdot 10^{-1}$	$(2.36 \pm 0.01 \pm 0.23) \cdot 10^{-1}$	$(2.14 \pm 0.01 \pm 0.13) \cdot 10^{-1}$
13.0 - 14.0	$(1.80 \pm 0.01 \pm 0.13) \cdot 10^{-1}$	$(2.00 \pm 0.00 \pm 0.16) \cdot 10^{-1}$	$(1.89 \pm 0.00 \pm 0.18) \cdot 10^{-1}$	$(1.71 \pm 0.01 \pm 0.10) \cdot 10^{-1}$
14.0 - 15.0	$(1.36 \pm 0.00 \pm 0.09) \cdot 10^{-1}$	$(1.50 \pm 0.00 \pm 0.11) \cdot 10^{-1}$	$(1.42 \pm 0.00 \pm 0.12) \cdot 10^{-1}$	$(1.28 \pm 0.01 \pm 0.07) \cdot 10^{-1}$
15.0 - 16.0	$(1.04 \pm 0.00 \pm 0.07) \cdot 10^{-1}$	$(1.15 \pm 0.00 \pm 0.07) \cdot 10^{-1}$	$(1.09 \pm 0.00 \pm 0.09) \cdot 10^{-1}$	$(9.62 \pm 0.03 \pm 0.56) \cdot 10^{-2}$
16.0 - 17.0	$(7.94 \pm 0.03 \pm 0.50) \cdot 10^{-2}$	$(8.87 \pm 0.03 \pm 0.55) \cdot 10^{-2}$	$(8.39 \pm 0.03 \pm 0.64) \cdot 10^{-2}$	$(7.31 \pm 0.03 \pm 0.45) \cdot 10^{-2}$
17.0 - 18.0	$(6.27 \pm 0.03 \pm 0.39) \cdot 10^{-2}$	$(6.90 \pm 0.02 \pm 0.43) \cdot 10^{-2}$	$(6.54 \pm 0.02 \pm 0.49) \cdot 10^{-2}$	$(5.67 \pm 0.02 \pm 0.38) \cdot 10^{-2}$
18.0 - 20.0	$(4.45 \pm 0.02 \pm 0.26) \cdot 10^{-2}$	$(4.89 \pm 0.01 \pm 0.31) \cdot 10^{-2}$	$(4.63 \pm 0.01 \pm 0.34) \cdot 10^{-2}$	$(3.99 \pm 0.01 \pm 0.29) \cdot 10^{-2}$
20.0 - 22.0	$(2.88 \pm 0.01 \pm 0.16) \cdot 10^{-2}$	$(3.15 \pm 0.01 \pm 0.19) \cdot 10^{-2}$	$(2.96 \pm 0.01 \pm 0.20) \cdot 10^{-2}$	$(2.55 \pm 0.01 \pm 0.19) \cdot 10^{-2}$
22.0 - 24.0	$(1.91 \pm 0.01 \pm 0.10) \cdot 10^{-2}$	$(2.09 \pm 0.01 \pm 0.13) \cdot 10^{-2}$	$(1.98 \pm 0.01 \pm 0.13) \cdot 10^{-2}$	$(1.69 \pm 0.01 \pm 0.13) \cdot 10^{-2}$
24.0 - 26.0	$(1.31 \pm 0.01 \pm 0.07) \cdot 10^{-2}$	$(1.44 \pm 0.01 \pm 0.09) \cdot 10^{-2}$	$(1.34 \pm 0.01 \pm 0.08) \cdot 10^{-2}$	$(1.15 \pm 0.01 \pm 0.09) \cdot 10^{-2}$
26.0 - 30.0	$(7.64 \pm 0.04 \pm 0.39) \cdot 10^{-3}$	$(8.48 \pm 0.03 \pm 0.50) \cdot 10^{-3}$	$(8.09 \pm 0.03 \pm 0.47) \cdot 10^{-3}$	$(6.92 \pm 0.03 \pm 0.56) \cdot 10^{-3}$
30.0 - 35.0	$(3.66 \pm 0.03 \pm 0.18) \cdot 10^{-3}$	$(4.12 \pm 0.02 \pm 0.24) \cdot 10^{-3}$	$(3.99 \pm 0.02 \pm 0.23) \cdot 10^{-3}$	$(3.44 \pm 0.02 \pm 0.29) \cdot 10^{-3}$
35.0 - 40.0	$(1.74 \pm 0.02 \pm 0.09) \cdot 10^{-3}$	$(2.01 \pm 0.01 \pm 0.13) \cdot 10^{-3}$	$(1.90 \pm 0.01 \pm 0.11) \cdot 10^{-3}$	$(1.70 \pm 0.01 \pm 0.15) \cdot 10^{-3}$
40.0 - 60.0	$(4.63 \pm 0.04 \pm 0.37) \cdot 10^{-4}$	$(5.23 \pm 0.04 \pm 0.44) \cdot 10^{-4}$	$(5.02 \pm 0.04 \pm 0.39) \cdot 10^{-4}$	$(4.55 \pm 0.04 \pm 0.51) \cdot 10^{-3}$
60.0 - 110.0	$(2.76 \pm 0.07 \pm 0.54) \cdot 10^{-5}$	$(3.05 \pm 0.06 \pm 0.62) \cdot 10^{-5}$	$(2.85 \pm 0.06 \pm 0.53) \cdot 10^{-5}$	$(2.91 \pm 0.06 \pm 0.67) \cdot 10^{-5}$
p_T [GeV]	1.00–1.25	1.25–1.50	1.50–1.75	1.75–2.00
8.0 - 8.5	—-	—-	—-	—-
8.5 - 9.0	—-	—-	—-	—-
9.0 - 9.5	—-	—-	—-	—-
9.5 - 10.0	—-	—-	—-	—-
10.0 - 10.5	$(5.28 \pm 0.02 \pm 0.33) \cdot 10^{-1}$	$(4.94 \pm 0.02 \pm 0.29) \cdot 10^{-1}$	$(4.91 \pm 0.02 \pm 0.30) \cdot 10^{-1}$	$(4.88 \pm 0.02 \pm 0.43) \cdot 10^{-1}$
10.5 - 11.0	$(4.41 \pm 0.02 \pm 0.26) \cdot 10^{-1}$	$(4.13 \pm 0.02 \pm 0.22) \cdot 10^{-1}$	$(4.09 \pm 0.01 \pm 0.26) \cdot 10^{-1}$	$(3.98 \pm 0.01 \pm 0.31) \cdot 10^{-1}$
11.0 - 11.5	$(3.75 \pm 0.02 \pm 0.21) \cdot 10^{-1}$	$(3.49 \pm 0.01 \pm 0.17) \cdot 10^{-1}$	$(3.42 \pm 0.01 \pm 0.23) \cdot 10^{-1}$	$(3.34 \pm 0.01 \pm 0.24) \cdot 10^{-1}$
11.5 - 12.0	$(3.14 \pm 0.01 \pm 0.17) \cdot 10^{-1}$	$(2.93 \pm 0.01 \pm 0.15) \cdot 10^{-1}$	$(2.88 \pm 0.01 \pm 0.20) \cdot 10^{-1}$	$(2.77 \pm 0.01 \pm 0.20) \cdot 10^{-1}$
12.0 - 12.5	$(2.65 \pm 0.01 \pm 0.15) \cdot 10^{-1}$	$(2.49 \pm 0.01 \pm 0.13) \cdot 10^{-1}$	$(2.41 \pm 0.01 \pm 0.18) \cdot 10^{-1}$	$(2.34 \pm 0.01 \pm 0.16) \cdot 10^{-1}$
12.5 - 13.0	$(2.27 \pm 0.01 \pm 0.13) \cdot 10^{-1}$	$(2.11 \pm 0.01 \pm 0.12) \cdot 10^{-1}$	$(2.05 \pm 0.01 \pm 0.15) \cdot 10^{-1}$	$(1.99 \pm 0.01 \pm 0.13) \cdot 10^{-1}$
13.0 - 14.0	$(1.80 \pm 0.01 \pm 0.10) \cdot 10^{-1}$	$(1.68 \pm 0.00 \pm 0.11) \cdot 10^{-1}$	$(1.63 \pm 0.00 \pm 0.12) \cdot 10^{-1}$	$(1.55 \pm 0.00 \pm 0.10) \cdot 10^{-1}$
14.0 - 15.0	$(1.32 \pm 0.00 \pm 0.08) \cdot 10^{-1}$	$(1.24 \pm 0.00 \pm 0.09) \cdot 10^{-1}$	$(1.19 \pm 0.00 \pm 0.09) \cdot 10^{-1}$	$(1.13 \pm 0.00 \pm 0.07) \cdot 10^{-1}$
15.0 - 16.0	$(9.88 \pm 0.03 \pm 0.61) \cdot 10^{-2}$	$(9.32 \pm 0.03 \pm 0.76) \cdot 10^{-2}$	$(8.86 \pm 0.03 \pm 0.68) \cdot 10^{-2}$	$(8.27 \pm 0.03 \pm 0.47) \cdot 10^{-2}$
16.0 - 17.0	$(7.41 \pm 0.03 \pm 0.49) \cdot 10^{-2}$	$(7.05 \pm 0.02 \pm 0.61) \cdot 10^{-2}$	$(6.70 \pm 0.02 \pm 0.52) \cdot 10^{-2}$	$(6.19 \pm 0.02 \pm 0.35) \cdot 10^{-2}$
17.0 - 18.0	$(5.70 \pm 0.03 \pm 0.41) \cdot 10^{-2}$	$(5.46 \pm 0.02 \pm 0.48) \cdot 10^{-2}$	$(5.17 \pm 0.02 \pm 0.40) \cdot 10^{-2}$	$(4.79 \pm 0.02 \pm 0.28) \cdot 10^{-2}$
18.0 - 20.0	$(3.97 \pm 0.01 \pm 0.31) \cdot 10^{-2}$	$(3.79 \pm 0.01 \pm 0.34) \cdot 10^{-2}$	$(3.55 \pm 0.01 \pm 0.28) \cdot 10^{-2}$	$(3.31 \pm 0.01 \pm 0.20) \cdot 10^{-2}$
20.0 - 22.0	$(2.51 \pm 0.01 \pm 0.21) \cdot 10^{-2}$	$(2.39 \pm 0.01 \pm 0.22) \cdot 10^{-2}$	$(2.21 \pm 0.01 \pm 0.18) \cdot 10^{-2}$	$(2.05 \pm 0.01 \pm 0.13) \cdot 10^{-2}$
22.0 - 24.0	$(1.66 \pm 0.01 \pm 0.15) \cdot 10^{-2}$	$(1.55 \pm 0.01 \pm 0.14) \cdot 10^{-2}$	$(1.43 \pm 0.01 \pm 0.11) \cdot 10^{-2}$	$(1.33 \pm 0.01 \pm 0.09) \cdot 10^{-2}$
24.0 - 26.0	$(1.11 \pm 0.01 \pm 0.10) \cdot 10^{-2}$	$(1.05 \pm 0.01 \pm 0.10) \cdot 10^{-2}$	$(9.71 \pm 0.05 \pm 0.80) \cdot 10^{-3}$	$(8.79 \pm 0.05 \pm 0.61) \cdot 10^{-3}$
26.0 - 30.0	$(6.51 \pm 0.03 \pm 0.61) \cdot 10^{-3}$	$(6.07 \pm 0.03 \pm 0.57) \cdot 10^{-3}$	$(5.61 \pm 0.03 \pm 0.46) \cdot 10^{-3}$	$(5.04 \pm 0.03 \pm 0.35) \cdot 10^{-3}$
30.0 - 35.0	$(3.14 \pm 0.02 \pm 0.31) \cdot 10^{-3}$	$(2.88 \pm 0.02 \pm 0.28) \cdot 10^{-3}$	$(2.67 \pm 0.02 \pm 0.22) \cdot 10^{-3}$	$(2.31 \pm 0.02 \pm 0.19) \cdot 10^{-3}$
35.0 - 40.0	$(1.51 \pm 0.01 \pm 0.15) \cdot 10^{-3}$	$(1.38 \pm 0.01 \pm 0.15) \cdot 10^{-3}$	$(1.25 \pm 0.01 \pm 0.11) \cdot 10^{-3}$	$(1.07 \pm 0.01 \pm 0.08) \cdot 10^{-3}$
40.0 - 60.0	$(4.09 \pm 0.03 \pm 0.45) \cdot 10^{-4}$	$(3.45 \pm 0.03 \pm 0.45) \cdot 10^{-4}$	$(3.04 \pm 0.03 \pm 0.36) \cdot 10^{-4}$	$(2.57 \pm 0.04 \pm 0.25) \cdot 10^{-4}$
60.0 - 110.0	$(2.56 \pm 0.05 \pm 0.46) \cdot 10^{-5}$	$(2.02 \pm 0.04 \pm 0.48) \cdot 10^{-5}$	$(1.67 \pm 0.04 \pm 0.38) \cdot 10^{-5}$	$(1.19 \pm 0.04 \pm 0.19) \cdot 10^{-5}$

Table B.4: Summary results for the cross section of prompt $\psi(2S)$ for 8 TeV data. Uncertainties are statistical and systematic respectively.

p_T [GeV]	0.00–0.25	0.25–0.50	0.50–0.75	0.75–1.00
8.0 - 8.5	$(1.11 \pm 0.03 \pm 0.16) \cdot 10^{-1}$	$(1.10 \pm 0.02 \pm 0.18) \cdot 10^{-1}$	$(1.13 \pm 0.02 \pm 0.14) \cdot 10^{-1}$	—
8.5 - 9.0	$(9.50 \pm 0.15 \pm 1.23) \cdot 10^{-2}$	$(8.60 \pm 0.16 \pm 1.23) \cdot 10^{-2}$	$(8.93 \pm 0.19 \pm 0.86) \cdot 10^{-2}$	—
9.0 - 9.5	$(7.18 \pm 0.10 \pm 0.85) \cdot 10^{-2}$	$(6.93 \pm 0.09 \pm 0.91) \cdot 10^{-2}$	$(7.08 \pm 0.10 \pm 0.75) \cdot 10^{-2}$	—
9.5 - 10.0	$(5.39 \pm 0.08 \pm 0.62) \cdot 10^{-2}$	$(5.28 \pm 0.07 \pm 0.69) \cdot 10^{-2}$	$(5.65 \pm 0.08 \pm 0.56) \cdot 10^{-2}$	—
10.0 - 10.5	$(4.29 \pm 0.06 \pm 0.47) \cdot 10^{-2}$	$(4.20 \pm 0.05 \pm 0.53) \cdot 10^{-2}$	$(4.43 \pm 0.06 \pm 0.46) \cdot 10^{-2}$	$(3.94 \pm 0.08 \pm 0.29) \cdot 10^{-2}$
10.5 - 11.0	$(3.39 \pm 0.05 \pm 0.34) \cdot 10^{-2}$	$(3.53 \pm 0.06 \pm 0.41) \cdot 10^{-2}$	$(3.53 \pm 0.05 \pm 0.36) \cdot 10^{-2}$	$(3.11 \pm 0.06 \pm 0.22) \cdot 10^{-2}$
11.0 - 11.5	$(2.71 \pm 0.04 \pm 0.25) \cdot 10^{-2}$	$(2.73 \pm 0.04 \pm 0.32) \cdot 10^{-2}$	$(2.66 \pm 0.04 \pm 0.29) \cdot 10^{-2}$	$(2.47 \pm 0.05 \pm 0.20) \cdot 10^{-2}$
11.5 - 12.0	$(2.15 \pm 0.04 \pm 0.19) \cdot 10^{-2}$	$(2.24 \pm 0.03 \pm 0.24) \cdot 10^{-2}$	$(2.27 \pm 0.03 \pm 0.25) \cdot 10^{-2}$	$(1.99 \pm 0.04 \pm 0.16) \cdot 10^{-2}$
12.0 - 12.5	$(1.74 \pm 0.03 \pm 0.15) \cdot 10^{-2}$	$(1.83 \pm 0.03 \pm 0.19) \cdot 10^{-2}$	$(1.77 \pm 0.03 \pm 0.20) \cdot 10^{-2}$	$(1.58 \pm 0.03 \pm 0.13) \cdot 10^{-2}$
12.5 - 13.0	$(1.44 \pm 0.03 \pm 0.13) \cdot 10^{-2}$	$(1.54 \pm 0.02 \pm 0.16) \cdot 10^{-2}$	$(1.47 \pm 0.02 \pm 0.16) \cdot 10^{-2}$	$(1.33 \pm 0.03 \pm 0.10) \cdot 10^{-2}$
13.0 - 14.0	$(1.07 \pm 0.02 \pm 0.09) \cdot 10^{-2}$	$(1.14 \pm 0.01 \pm 0.11) \cdot 10^{-2}$	$(1.12 \pm 0.01 \pm 0.12) \cdot 10^{-2}$	$(9.80 \pm 0.17 \pm 0.74) \cdot 10^{-3}$
14.0 - 15.0	$(7.47 \pm 0.13 \pm 0.61) \cdot 10^{-3}$	$(8.20 \pm 0.11 \pm 0.73) \cdot 10^{-3}$	$(7.63 \pm 0.11 \pm 0.76) \cdot 10^{-3}$	$(6.83 \pm 0.15 \pm 0.50) \cdot 10^{-3}$
15.0 - 16.0	$(5.25 \pm 0.10 \pm 0.45) \cdot 10^{-3}$	$(5.87 \pm 0.09 \pm 0.47) \cdot 10^{-3}$	$(5.65 \pm 0.09 \pm 0.54) \cdot 10^{-3}$	$(4.93 \pm 0.10 \pm 0.36) \cdot 10^{-3}$
16.0 - 17.0	$(3.77 \pm 0.09 \pm 0.31) \cdot 10^{-3}$	$(4.19 \pm 0.07 \pm 0.33) \cdot 10^{-3}$	$(3.97 \pm 0.08 \pm 0.35) \cdot 10^{-3}$	$(3.52 \pm 0.08 \pm 0.25) \cdot 10^{-3}$
17.0 - 18.0	$(2.76 \pm 0.07 \pm 0.23) \cdot 10^{-3}$	$(3.06 \pm 0.06 \pm 0.25) \cdot 10^{-3}$	$(2.91 \pm 0.06 \pm 0.26) \cdot 10^{-3}$	$(2.34 \pm 0.07 \pm 0.17) \cdot 10^{-3}$
18.0 - 20.0	$(1.90 \pm 0.04 \pm 0.14) \cdot 10^{-3}$	$(1.95 \pm 0.03 \pm 0.15) \cdot 10^{-3}$	$(1.86 \pm 0.03 \pm 0.16) \cdot 10^{-3}$	$(1.53 \pm 0.04 \pm 0.13) \cdot 10^{-3}$
20.0 - 22.0	$(1.09 \pm 0.03 \pm 0.09) \cdot 10^{-3}$	$(1.15 \pm 0.03 \pm 0.09) \cdot 10^{-3}$	$(1.12 \pm 0.03 \pm 0.09) \cdot 10^{-3}$	$(9.47 \pm 0.29 \pm 0.78) \cdot 10^{-4}$
22.0 - 24.0	$(6.39 \pm 0.25 \pm 0.49) \cdot 10^{-4}$	$(7.20 \pm 0.20 \pm 0.53) \cdot 10^{-4}$	$(6.95 \pm 0.20 \pm 0.53) \cdot 10^{-4}$	$(5.95 \pm 0.22 \pm 0.52) \cdot 10^{-4}$
24.0 - 26.0	$(4.22 \pm 0.20 \pm 0.30) \cdot 10^{-4}$	$(4.63 \pm 0.17 \pm 0.35) \cdot 10^{-4}$	$(4.25 \pm 0.16 \pm 0.34) \cdot 10^{-4}$	$(3.35 \pm 0.17 \pm 0.30) \cdot 10^{-4}$
26.0 - 30.0	$(2.27 \pm 0.11 \pm 0.17) \cdot 10^{-4}$	$(2.49 \pm 0.09 \pm 0.17) \cdot 10^{-4}$	$(2.56 \pm 0.09 \pm 0.18) \cdot 10^{-4}$	$(2.13 \pm 0.09 \pm 0.18) \cdot 10^{-4}$
30.0 - 35.0	$(9.06 \pm 0.64 \pm 0.81) \cdot 10^{-5}$	$(1.20 \pm 0.05 \pm 0.09) \cdot 10^{-4}$	$(1.11 \pm 0.06 \pm 0.08) \cdot 10^{-4}$	$(8.92 \pm 0.56 \pm 1.19) \cdot 10^{-5}$
35.0 - 40.0	$(4.93 \pm 0.45 \pm 0.38) \cdot 10^{-5}$	$(4.56 \pm 0.36 \pm 0.43) \cdot 10^{-5}$	$(5.20 \pm 0.38 \pm 0.33) \cdot 10^{-5}$	$(3.94 \pm 0.38 \pm 0.37) \cdot 10^{-5}$
40.0 - 60.0	$(1.19 \pm 0.12 \pm 0.10) \cdot 10^{-5}$	$(1.47 \pm 0.10 \pm 0.16) \cdot 10^{-5}$	$(1.19 \pm 0.10 \pm 0.10) \cdot 10^{-5}$	$(1.03 \pm 0.10 \pm 0.17) \cdot 10^{-5}$
60.0 - 110.0	$(5.32 \pm 1.68 \pm 0.95) \cdot 10^{-7}$	$(5.68 \pm 1.48 \pm 1.11) \cdot 10^{-7}$	$(4.03 \pm 1.44 \pm 0.71) \cdot 10^{-7}$	$(5.98 \pm 1.64 \pm 2.43) \cdot 10^{-7}$
p_T [GeV]	1.00–1.25	1.25–1.50	1.50–1.75	1.75–2.00
8.0 - 8.5	—	—	—	—
8.5 - 9.0	—	—	—	—
9.0 - 9.5	—	—	—	—
9.5 - 10.0	—	—	—	—
10.0 - 10.5	$(4.13 \pm 0.09 \pm 0.35) \cdot 10^{-2}$	$(3.84 \pm 0.08 \pm 0.29) \cdot 10^{-2}$	$(3.64 \pm 0.08 \pm 0.31) \cdot 10^{-2}$	$(3.34 \pm 0.08 \pm 0.45) \cdot 10^{-2}$
10.5 - 11.0	$(3.44 \pm 0.07 \pm 0.26) \cdot 10^{-2}$	$(3.05 \pm 0.07 \pm 0.22) \cdot 10^{-2}$	$(2.87 \pm 0.06 \pm 0.23) \cdot 10^{-2}$	$(2.57 \pm 0.06 \pm 0.40) \cdot 10^{-2}$
11.0 - 11.5	$(2.65 \pm 0.06 \pm 0.22) \cdot 10^{-2}$	$(2.49 \pm 0.06 \pm 0.17) \cdot 10^{-2}$	$(2.27 \pm 0.05 \pm 0.18) \cdot 10^{-2}$	$(1.99 \pm 0.05 \pm 0.24) \cdot 10^{-2}$
11.5 - 12.0	$(2.13 \pm 0.05 \pm 0.17) \cdot 10^{-2}$	$(2.02 \pm 0.05 \pm 0.14) \cdot 10^{-2}$	$(1.89 \pm 0.04 \pm 0.16) \cdot 10^{-2}$	$(1.68 \pm 0.04 \pm 0.26) \cdot 10^{-2}$
12.0 - 12.5	$(1.70 \pm 0.05 \pm 0.13) \cdot 10^{-2}$	$(1.63 \pm 0.04 \pm 0.12) \cdot 10^{-2}$	$(1.54 \pm 0.03 \pm 0.15) \cdot 10^{-2}$	$(1.42 \pm 0.04 \pm 0.27) \cdot 10^{-2}$
12.5 - 13.0	$(1.35 \pm 0.03 \pm 0.10) \cdot 10^{-2}$	$(1.31 \pm 0.03 \pm 0.10) \cdot 10^{-2}$	$(1.18 \pm 0.03 \pm 0.11) \cdot 10^{-2}$	$(1.17 \pm 0.03 \pm 0.16) \cdot 10^{-2}$
13.0 - 14.0	$(1.05 \pm 0.02 \pm 0.08) \cdot 10^{-2}$	$(9.95 \pm 0.18 \pm 0.74) \cdot 10^{-3}$	$(9.28 \pm 0.16 \pm 0.96) \cdot 10^{-3}$	$(8.11 \pm 0.18 \pm 1.33) \cdot 10^{-3}$
14.0 - 15.0	$(7.02 \pm 0.14 \pm 0.54) \cdot 10^{-3}$	$(6.58 \pm 0.13 \pm 0.56) \cdot 10^{-3}$	$(6.21 \pm 0.12 \pm 0.66) \cdot 10^{-3}$	$(5.63 \pm 0.13 \pm 1.03) \cdot 10^{-3}$
15.0 - 16.0	$(4.95 \pm 0.11 \pm 0.39) \cdot 10^{-3}$	$(4.89 \pm 0.10 \pm 0.45) \cdot 10^{-3}$	$(4.19 \pm 0.10 \pm 0.43) \cdot 10^{-3}$	$(3.81 \pm 0.10 \pm 0.71) \cdot 10^{-3}$
16.0 - 17.0	$(3.42 \pm 0.10 \pm 0.28) \cdot 10^{-3}$	$(3.43 \pm 0.08 \pm 0.33) \cdot 10^{-3}$	$(3.00 \pm 0.08 \pm 0.40) \cdot 10^{-3}$	$(2.91 \pm 0.09 \pm 0.57) \cdot 10^{-3}$
17.0 - 18.0	$(2.64 \pm 0.09 \pm 0.22) \cdot 10^{-3}$	$(2.46 \pm 0.07 \pm 0.24) \cdot 10^{-3}$	$(2.20 \pm 0.06 \pm 0.29) \cdot 10^{-3}$	$(1.83 \pm 0.07 \pm 0.46) \cdot 10^{-3}$
18.0 - 20.0	$(1.67 \pm 0.04 \pm 0.16) \cdot 10^{-3}$	$(1.61 \pm 0.04 \pm 0.16) \cdot 10^{-3}$	$(1.40 \pm 0.04 \pm 0.18) \cdot 10^{-3}$	$(1.22 \pm 0.04 \pm 0.30) \cdot 10^{-3}$
20.0 - 22.0	$(9.78 \pm 0.30 \pm 0.87) \cdot 10^{-4}$	$(9.38 \pm 0.26 \pm 0.98) \cdot 10^{-4}$	$(8.07 \pm 0.26 \pm 1.54) \cdot 10^{-4}$	$(7.87 \pm 0.32 \pm 1.63) \cdot 10^{-4}$
22.0 - 24.0	$(5.64 \pm 0.27 \pm 0.57) \cdot 10^{-4}$	$(5.34 \pm 0.20 \pm 0.66) \cdot 10^{-4}$	$(4.95 \pm 0.24 \pm 0.72) \cdot 10^{-4}$	$(4.30 \pm 0.24 \pm 1.04) \cdot 10^{-4}$
24.0 - 26.0	$(3.49 \pm 0.18 \pm 0.41) \cdot 10^{-4}$	$(3.46 \pm 0.15 \pm 0.61) \cdot 10^{-4}$	$(2.66 \pm 0.15 \pm 0.65) \cdot 10^{-4}$	$(2.53 \pm 0.17 \pm 0.70) \cdot 10^{-4}$
26.0 - 30.0	$(1.93 \pm 0.09 \pm 0.27) \cdot 10^{-4}$	$(1.75 \pm 0.08 \pm 0.32) \cdot 10^{-4}$	$(1.70 \pm 0.08 \pm 0.35) \cdot 10^{-4}$	$(1.52 \pm 0.10 \pm 0.40) \cdot 10^{-4}$
30.0 - 35.0	$(8.85 \pm 0.56 \pm 1.41) \cdot 10^{-5}$	$(8.36 \pm 0.48 \pm 1.65) \cdot 10^{-5}$	$(7.68 \pm 0.53 \pm 1.43) \cdot 10^{-5}$	$(5.99 \pm 0.59 \pm 2.09) \cdot 10^{-5}$
35.0 - 40.0	$(4.30 \pm 0.39 \pm 0.60) \cdot 10^{-5}$	$(3.68 \pm 0.32 \pm 0.74) \cdot 10^{-5}$	$(3.31 \pm 0.36 \pm 0.53) \cdot 10^{-5}$	$(3.28 \pm 0.40 \pm 0.88) \cdot 10^{-5}$
40.0 - 60.0	$(8.99 \pm 1.06 \pm 2.18) \cdot 10^{-6}$	$(8.75 \pm 0.84 \pm 2.11) \cdot 10^{-6}$	$(6.09 \pm 1.13 \pm 1.90) \cdot 10^{-6}$	$(6.66 \pm 1.73 \pm 3.20) \cdot 10^{-6}$
60.0 - 110.0	$(6.55 \pm 1.58 \pm 1.51) \cdot 10^{-7}$	$(3.79 \pm 1.16 \pm 1.14) \cdot 10^{-7}$	$(5.52 \pm 1.32 \pm 1.24) \cdot 10^{-7}$	$(7.24 \pm 1.76 \pm 6.31) \cdot 10^{-7}$

Table B.5: Summary results for the cross section of non-prompt $\psi(2S)$ for 8 TeV data. Uncertainties are statistical and systematic respectively.

p_T [GeV]	0.00–0.25	0.25–0.50	0.50–0.75	0.75–1.00
8.0 - 8.5	$(5.00 \pm 0.21 \pm 0.76) \cdot 10^{-2}$	$(4.42 \pm 0.17 \pm 0.73) \cdot 10^{-2}$	$(4.55 \pm 0.19 \pm 0.60) \cdot 10^{-2}$	—-
8.5 - 9.0	$(4.27 \pm 0.12 \pm 0.56) \cdot 10^{-2}$	$(3.93 \pm 0.13 \pm 0.58) \cdot 10^{-2}$	$(4.11 \pm 0.15 \pm 0.47) \cdot 10^{-2}$	—-
9.0 - 9.5	$(3.33 \pm 0.09 \pm 0.40) \cdot 10^{-2}$	$(3.21 \pm 0.07 \pm 0.43) \cdot 10^{-2}$	$(3.27 \pm 0.08 \pm 0.37) \cdot 10^{-2}$	—-
9.5 - 10.0	$(2.76 \pm 0.07 \pm 0.32) \cdot 10^{-2}$	$(2.77 \pm 0.06 \pm 0.36) \cdot 10^{-2}$	$(2.81 \pm 0.06 \pm 0.30) \cdot 10^{-2}$	—-
10.0 - 10.5	$(2.34 \pm 0.05 \pm 0.25) \cdot 10^{-2}$	$(2.25 \pm 0.05 \pm 0.27) \cdot 10^{-2}$	$(2.24 \pm 0.05 \pm 0.23) \cdot 10^{-2}$	$(2.10 \pm 0.07 \pm 0.16) \cdot 10^{-2}$
10.5 - 11.0	$(1.92 \pm 0.04 \pm 0.18) \cdot 10^{-2}$	$(1.90 \pm 0.05 \pm 0.21) \cdot 10^{-2}$	$(1.94 \pm 0.04 \pm 0.20) \cdot 10^{-2}$	$(1.79 \pm 0.05 \pm 0.13) \cdot 10^{-2}$
11.0 - 11.5	$(1.58 \pm 0.04 \pm 0.14) \cdot 10^{-2}$	$(1.58 \pm 0.03 \pm 0.17) \cdot 10^{-2}$	$(1.61 \pm 0.03 \pm 0.17) \cdot 10^{-2}$	$(1.42 \pm 0.04 \pm 0.11) \cdot 10^{-2}$
11.5 - 12.0	$(1.36 \pm 0.03 \pm 0.11) \cdot 10^{-2}$	$(1.38 \pm 0.03 \pm 0.14) \cdot 10^{-2}$	$(1.33 \pm 0.03 \pm 0.14) \cdot 10^{-2}$	$(1.20 \pm 0.04 \pm 0.09) \cdot 10^{-2}$
12.0 - 12.5	$(1.15 \pm 0.03 \pm 0.09) \cdot 10^{-2}$	$(1.21 \pm 0.02 \pm 0.12) \cdot 10^{-2}$	$(1.17 \pm 0.03 \pm 0.12) \cdot 10^{-2}$	$(1.04 \pm 0.03 \pm 0.08) \cdot 10^{-2}$
12.5 - 13.0	$(9.84 \pm 0.25 \pm 0.76) \cdot 10^{-3}$	$(1.03 \pm 0.02 \pm 0.09) \cdot 10^{-2}$	$(9.63 \pm 0.22 \pm 0.98) \cdot 10^{-3}$	$(8.42 \pm 0.27 \pm 0.66) \cdot 10^{-3}$
13.0 - 14.0	$(7.60 \pm 0.15 \pm 0.58) \cdot 10^{-3}$	$(7.92 \pm 0.13 \pm 0.68) \cdot 10^{-3}$	$(7.74 \pm 0.13 \pm 0.75) \cdot 10^{-3}$	$(7.03 \pm 0.16 \pm 0.47) \cdot 10^{-3}$
14.0 - 15.0	$(5.99 \pm 0.13 \pm 0.44) \cdot 10^{-3}$	$(6.30 \pm 0.11 \pm 0.50) \cdot 10^{-3}$	$(5.80 \pm 0.11 \pm 0.53) \cdot 10^{-3}$	$(5.07 \pm 0.13 \pm 0.34) \cdot 10^{-3}$
15.0 - 16.0	$(4.34 \pm 0.11 \pm 0.32) \cdot 10^{-3}$	$(4.73 \pm 0.09 \pm 0.34) \cdot 10^{-3}$	$(4.58 \pm 0.09 \pm 0.38) \cdot 10^{-3}$	$(3.69 \pm 0.10 \pm 0.23) \cdot 10^{-3}$
16.0 - 17.0	$(3.71 \pm 0.09 \pm 0.26) \cdot 10^{-3}$	$(3.85 \pm 0.08 \pm 0.27) \cdot 10^{-3}$	$(3.61 \pm 0.08 \pm 0.29) \cdot 10^{-3}$	$(2.93 \pm 0.09 \pm 0.22) \cdot 10^{-3}$
17.0 - 18.0	$(2.85 \pm 0.08 \pm 0.20) \cdot 10^{-3}$	$(2.98 \pm 0.07 \pm 0.21) \cdot 10^{-3}$	$(2.65 \pm 0.07 \pm 0.22) \cdot 10^{-3}$	$(2.20 \pm 0.07 \pm 0.18) \cdot 10^{-3}$
18.0 - 20.0	$(1.99 \pm 0.05 \pm 0.14) \cdot 10^{-3}$	$(2.17 \pm 0.04 \pm 0.15) \cdot 10^{-3}$	$(1.97 \pm 0.04 \pm 0.15) \cdot 10^{-3}$	$(1.69 \pm 0.04 \pm 0.14) \cdot 10^{-3}$
20.0 - 22.0	$(1.36 \pm 0.04 \pm 0.09) \cdot 10^{-3}$	$(1.40 \pm 0.03 \pm 0.10) \cdot 10^{-3}$	$(1.27 \pm 0.03 \pm 0.11) \cdot 10^{-3}$	$(1.02 \pm 0.03 \pm 0.10) \cdot 10^{-3}$
22.0 - 24.0	$(8.37 \pm 0.30 \pm 0.50) \cdot 10^{-4}$	$(9.16 \pm 0.24 \pm 0.61) \cdot 10^{-4}$	$(8.73 \pm 0.24 \pm 0.62) \cdot 10^{-4}$	$(6.95 \pm 0.25 \pm 0.95) \cdot 10^{-4}$
24.0 - 26.0	$(6.04 \pm 0.24 \pm 0.39) \cdot 10^{-4}$	$(6.43 \pm 0.20 \pm 0.43) \cdot 10^{-4}$	$(5.75 \pm 0.20 \pm 0.44) \cdot 10^{-4}$	$(4.92 \pm 0.20 \pm 0.60) \cdot 10^{-4}$
26.0 - 30.0	$(3.50 \pm 0.13 \pm 0.21) \cdot 10^{-4}$	$(3.69 \pm 0.11 \pm 0.25) \cdot 10^{-4}$	$(3.54 \pm 0.11 \pm 0.24) \cdot 10^{-4}$	$(2.88 \pm 0.11 \pm 0.31) \cdot 10^{-4}$
30.0 - 35.0	$(1.75 \pm 0.09 \pm 0.09) \cdot 10^{-4}$	$(1.94 \pm 0.07 \pm 0.16) \cdot 10^{-4}$	$(1.90 \pm 0.07 \pm 0.11) \cdot 10^{-4}$	$(1.56 \pm 0.07 \pm 0.28) \cdot 10^{-4}$
35.0 - 40.0	$(8.97 \pm 0.58 \pm 0.71) \cdot 10^{-5}$	$(9.94 \pm 0.51 \pm 0.64) \cdot 10^{-5}$	$(8.24 \pm 0.48 \pm 0.50) \cdot 10^{-5}$	$(7.43 \pm 0.50 \pm 1.00) \cdot 10^{-5}$
40.0 - 60.0	$(2.21 \pm 0.15 \pm 0.24) \cdot 10^{-5}$	$(2.46 \pm 0.13 \pm 0.37) \cdot 10^{-5}$	$(2.51 \pm 0.14 \pm 0.32) \cdot 10^{-5}$	$(1.97 \pm 0.13 \pm 0.45) \cdot 10^{-5}$
60.0 - 110.0	$(1.65 \pm 0.21 \pm 0.27) \cdot 10^{-6}$	$(1.73 \pm 0.19 \pm 0.28) \cdot 10^{-6}$	$(1.55 \pm 0.18 \pm 0.23) \cdot 10^{-6}$	$(1.44 \pm 0.18 \pm 0.28) \cdot 10^{-6}$
p_T [GeV]	1.00–1.25	1.25–1.50	1.50–1.75	1.75–2.00
8.0 - 8.5	—-	—-	—-	—-
8.5 - 9.0	—-	—-	—-	—-
9.0 - 9.5	—-	—-	—-	—-
9.5 - 10.0	—-	—-	—-	—-
10.0 - 10.5	$(2.12 \pm 0.08 \pm 0.19) \cdot 10^{-2}$	$(1.80 \pm 0.07 \pm 0.20) \cdot 10^{-2}$	$(1.69 \pm 0.06 \pm 0.24) \cdot 10^{-2}$	$(1.36 \pm 0.05 \pm 0.29) \cdot 10^{-2}$
10.5 - 11.0	$(1.61 \pm 0.06 \pm 0.13) \cdot 10^{-2}$	$(1.58 \pm 0.06 \pm 0.14) \cdot 10^{-2}$	$(1.44 \pm 0.05 \pm 0.19) \cdot 10^{-2}$	$(1.27 \pm 0.05 \pm 0.28) \cdot 10^{-2}$
11.0 - 11.5	$(1.42 \pm 0.05 \pm 0.10) \cdot 10^{-2}$	$(1.33 \pm 0.05 \pm 0.13) \cdot 10^{-2}$	$(1.20 \pm 0.04 \pm 0.15) \cdot 10^{-2}$	$(1.01 \pm 0.04 \pm 0.19) \cdot 10^{-2}$
11.5 - 12.0	$(1.16 \pm 0.04 \pm 0.08) \cdot 10^{-2}$	$(1.15 \pm 0.04 \pm 0.10) \cdot 10^{-2}$	$(9.99 \pm 0.32 \pm 1.44) \cdot 10^{-3}$	$(7.90 \pm 0.32 \pm 1.85) \cdot 10^{-3}$
12.0 - 12.5	$(1.00 \pm 0.04 \pm 0.08) \cdot 10^{-2}$	$(1.01 \pm 0.03 \pm 0.09) \cdot 10^{-2}$	$(8.48 \pm 0.28 \pm 1.35) \cdot 10^{-3}$	$(6.99 \pm 0.29 \pm 1.83) \cdot 10^{-3}$
12.5 - 13.0	$(8.75 \pm 0.32 \pm 0.68) \cdot 10^{-3}$	$(8.30 \pm 0.29 \pm 0.76) \cdot 10^{-3}$	$(7.65 \pm 0.24 \pm 1.06) \cdot 10^{-3}$	$(6.03 \pm 0.25 \pm 1.39) \cdot 10^{-3}$
13.0 - 14.0	$(7.14 \pm 0.18 \pm 0.63) \cdot 10^{-3}$	$(6.54 \pm 0.17 \pm 0.77) \cdot 10^{-3}$	$(5.84 \pm 0.14 \pm 0.97) \cdot 10^{-3}$	$(4.47 \pm 0.15 \pm 1.12) \cdot 10^{-3}$
14.0 - 15.0	$(5.34 \pm 0.14 \pm 0.45) \cdot 10^{-3}$	$(4.72 \pm 0.13 \pm 0.61) \cdot 10^{-3}$	$(4.30 \pm 0.12 \pm 0.75) \cdot 10^{-3}$	$(3.53 \pm 0.12 \pm 0.91) \cdot 10^{-3}$
15.0 - 16.0	$(4.01 \pm 0.12 \pm 0.37) \cdot 10^{-3}$	$(3.65 \pm 0.10 \pm 0.52) \cdot 10^{-3}$	$(3.15 \pm 0.09 \pm 0.52) \cdot 10^{-3}$	$(2.76 \pm 0.10 \pm 0.66) \cdot 10^{-3}$
16.0 - 17.0	$(2.91 \pm 0.11 \pm 0.23) \cdot 10^{-3}$	$(2.89 \pm 0.08 \pm 0.40) \cdot 10^{-3}$	$(2.42 \pm 0.08 \pm 0.47) \cdot 10^{-3}$	$(2.02 \pm 0.08 \pm 0.55) \cdot 10^{-3}$
17.0 - 18.0	$(2.30 \pm 0.09 \pm 0.25) \cdot 10^{-3}$	$(2.21 \pm 0.07 \pm 0.31) \cdot 10^{-3}$	$(1.89 \pm 0.07 \pm 0.39) \cdot 10^{-3}$	$(1.40 \pm 0.07 \pm 0.44) \cdot 10^{-3}$
18.0 - 20.0	$(1.69 \pm 0.05 \pm 0.21) \cdot 10^{-3}$	$(1.52 \pm 0.04 \pm 0.22) \cdot 10^{-3}$	$(1.37 \pm 0.04 \pm 0.26) \cdot 10^{-3}$	$(1.13 \pm 0.04 \pm 0.36) \cdot 10^{-3}$
20.0 - 22.0	$(1.09 \pm 0.04 \pm 0.12) \cdot 10^{-3}$	$(9.26 \pm 0.29 \pm 1.50) \cdot 10^{-4}$	$(8.21 \pm 0.28 \pm 2.05) \cdot 10^{-4}$	$(7.22 \pm 0.34 \pm 2.18) \cdot 10^{-4}$
22.0 - 24.0	$(6.67 \pm 0.32 \pm 0.87) \cdot 10^{-4}$	$(6.11 \pm 0.23 \pm 1.17) \cdot 10^{-4}$	$(5.39 \pm 0.26 \pm 1.12) \cdot 10^{-4}$	$(4.85 \pm 0.26 \pm 1.48) \cdot 10^{-4}$
24.0 - 26.0	$(4.76 \pm 0.22 \pm 0.78) \cdot 10^{-4}$	$(4.47 \pm 0.19 \pm 1.07) \cdot 10^{-4}$	$(3.67 \pm 0.18 \pm 1.08) \cdot 10^{-4}$	$(2.98 \pm 0.20 \pm 1.03) \cdot 10^{-4}$
26.0 - 30.0	$(2.84 \pm 0.12 \pm 0.54) \cdot 10^{-4}$	$(2.60 \pm 0.09 \pm 0.64) \cdot 10^{-4}$	$(2.21 \pm 0.10 \pm 0.61) \cdot 10^{-4}$	$(1.79 \pm 0.13 \pm 0.60) \cdot 10^{-4}$
30.0 - 35.0	$(1.41 \pm 0.07 \pm 0.31) \cdot 10^{-4}$	$(1.27 \pm 0.06 \pm 0.33) \cdot 10^{-4}$	$(1.04 \pm 0.07 \pm 0.33) \cdot 10^{-4}$	$(8.45 \pm 0.74 \pm 3.17) \cdot 10^{-5}$
35.0 - 40.0	$(6.39 \pm 0.52 \pm 1.54) \cdot 10^{-5}$	$(6.26 \pm 0.41 \pm 1.80) \cdot 10^{-5}$	$(5.25 \pm 0.47 \pm 1.20) \cdot 10^{-5}$	$(3.27 \pm 0.46 \pm 1.26) \cdot 10^{-5}$
40.0 - 60.0	$(1.90 \pm 0.15 \pm 0.65) \cdot 10^{-5}$	$(1.38 \pm 0.11 \pm 0.46) \cdot 10^{-5}$	$(1.25 \pm 0.14 \pm 0.48) \cdot 10^{-5}$	$(1.10 \pm 0.23 \pm 0.60) \cdot 10^{-5}$
60.0 - 110.0	$(1.04 \pm 0.17 \pm 0.16) \cdot 10^{-6}$	$(9.61 \pm 1.22 \pm 2.04) \cdot 10^{-7}$	$(5.43 \pm 1.23 \pm 1.37) \cdot 10^{-7}$	$(7.36 \pm 1.39 \pm 4.47) \cdot 10^{-7}$

Table B.6: Summary results for the non-prompt fraction of J/ψ as a percentage for 8 TeV data. Uncertainties are statistical and systematic respectively.

p_T [GeV]	0.00–0.25	0.25–0.50	0.50–0.75	0.75–1.00
8.0 - 8.5	27.70 ± 0.14 ± 1.00	27.50 ± 0.12 ± 0.90	27.24 ± 0.13 ± 0.85	—-
8.5 - 9.0	29.08 ± 0.10 ± 1.20	28.96 ± 0.12 ± 1.09	28.68 ± 0.13 ± 0.95	—-
9.0 - 9.5	30.23 ± 0.10 ± 1.25	30.40 ± 0.09 ± 1.10	30.11 ± 0.09 ± 0.90	—-
9.5 - 10.0	31.70 ± 0.10 ± 1.30	31.74 ± 0.09 ± 1.10	31.32 ± 0.09 ± 0.98	—-
10.0 - 10.5	33.17 ± 0.10 ± 1.31	32.94 ± 0.09 ± 1.14	32.72 ± 0.09 ± 0.97	32.73 ± 0.12 ± 0.76
10.5 - 11.0	34.56 ± 0.10 ± 1.35	34.36 ± 0.11 ± 1.13	34.09 ± 0.09 ± 0.95	34.22 ± 0.12 ± 0.77
11.0 - 11.5	35.91 ± 0.11 ± 1.34	35.85 ± 0.10 ± 1.17	35.49 ± 0.10 ± 0.93	35.32 ± 0.12 ± 0.76
11.5 - 12.0	37.20 ± 0.12 ± 1.31	37.02 ± 0.10 ± 1.14	36.85 ± 0.10 ± 0.94	36.76 ± 0.13 ± 0.73
12.0 - 12.5	38.60 ± 0.13 ± 1.42	38.48 ± 0.10 ± 1.17	38.28 ± 0.11 ± 0.93	38.12 ± 0.13 ± 0.73
12.5 - 13.0	39.69 ± 0.13 ± 1.32	39.70 ± 0.11 ± 1.17	39.36 ± 0.11 ± 0.90	39.15 ± 0.14 ± 0.73
13.0 - 14.0	41.56 ± 0.11 ± 1.32	41.56 ± 0.09 ± 1.14	41.19 ± 0.09 ± 0.94	41.16 ± 0.11 ± 0.70
14.0 - 15.0	43.98 ± 0.12 ± 1.33	43.61 ± 0.10 ± 1.15	43.61 ± 0.10 ± 0.91	43.48 ± 0.14 ± 0.69
15.0 - 16.0	46.08 ± 0.14 ± 1.35	45.97 ± 0.11 ± 1.14	45.78 ± 0.11 ± 0.90	45.45 ± 0.13 ± 0.70
16.0 - 17.0	47.84 ± 0.16 ± 1.34	47.68 ± 0.12 ± 1.12	47.49 ± 0.12 ± 0.88	47.27 ± 0.15 ± 0.66
17.0 - 18.0	50.02 ± 0.18 ± 1.32	49.44 ± 0.13 ± 1.14	49.34 ± 0.14 ± 0.87	49.15 ± 0.16 ± 0.71
18.0 - 20.0	52.11 ± 0.15 ± 1.36	51.85 ± 0.11 ± 1.14	51.47 ± 0.11 ± 0.88	51.67 ± 0.14 ± 0.64
20.0 - 22.0	54.74 ± 0.19 ± 1.32	54.35 ± 0.14 ± 1.11	54.22 ± 0.14 ± 0.85	54.06 ± 0.17 ± 0.65
22.0 - 24.0	57.04 ± 0.23 ± 1.29	56.70 ± 0.17 ± 1.03	56.47 ± 0.17 ± 0.85	56.37 ± 0.20 ± 0.65
24.0 - 26.0	58.94 ± 0.27 ± 1.26	58.70 ± 0.20 ± 1.07	57.84 ± 0.21 ± 0.83	57.93 ± 0.24 ± 0.61
26.0 - 30.0	60.62 ± 0.25 ± 1.43	60.53 ± 0.19 ± 1.08	60.36 ± 0.19 ± 0.86	60.03 ± 0.22 ± 0.69
30.0 - 35.0	62.42 ± 0.33 ± 1.27	62.78 ± 0.24 ± 1.11	62.39 ± 0.24 ± 0.86	62.74 ± 0.27 ± 0.72
35.0 - 40.0	64.07 ± 0.47 ± 1.57	65.15 ± 0.35 ± 1.12	64.01 ± 0.35 ± 0.86	64.77 ± 0.38 ± 0.57
40.0 - 60.0	67.58 ± 0.46 ± 1.14	66.77 ± 0.35 ± 0.90	66.41 ± 0.35 ± 0.94	66.30 ± 0.38 ± 0.65
60.0 - 110.0	70.67 ± 1.20 ± 0.85	70.31 ± 0.96 ± 0.99	69.93 ± 0.96 ± 0.96	68.61 ± 0.99 ± 1.54
p_T [GeV]	1.00–1.25	1.25–1.50	1.50–1.75	1.75–2.00
8.0 - 8.5	—-	—-	—-	—-
8.5 - 9.0	—-	—-	—-	—-
9.0 - 9.5	—-	—-	—-	—-
9.5 - 10.0	—-	—-	—-	—-
10.0 - 10.5	32.51 ± 0.13 ± 0.67	32.28 ± 0.12 ± 0.67	32.13 ± 0.11 ± 0.69	31.78 ± 0.10 ± 0.74
10.5 - 11.0	33.79 ± 0.13 ± 0.67	33.44 ± 0.13 ± 0.66	33.47 ± 0.11 ± 0.68	32.69 ± 0.10 ± 0.74
11.0 - 11.5	35.26 ± 0.13 ± 0.63	35.12 ± 0.13 ± 0.63	34.77 ± 0.11 ± 0.67	34.45 ± 0.11 ± 0.71
11.5 - 12.0	36.48 ± 0.13 ± 0.64	36.28 ± 0.13 ± 0.61	36.19 ± 0.11 ± 0.64	35.60 ± 0.11 ± 0.70
12.0 - 12.5	37.62 ± 0.15 ± 0.64	37.69 ± 0.13 ± 0.60	37.22 ± 0.12 ± 0.64	36.84 ± 0.12 ± 0.66
12.5 - 13.0	39.09 ± 0.14 ± 0.57	38.85 ± 0.14 ± 0.60	38.68 ± 0.12 ± 0.62	37.96 ± 0.12 ± 0.69
13.0 - 14.0	40.94 ± 0.11 ± 0.61	40.52 ± 0.10 ± 0.60	40.39 ± 0.09 ± 0.61	39.57 ± 0.10 ± 0.67
14.0 - 15.0	43.13 ± 0.12 ± 0.56	42.65 ± 0.11 ± 0.56	42.46 ± 0.10 ± 0.60	41.83 ± 0.11 ± 0.63
15.0 - 16.0	45.30 ± 0.13 ± 0.54	44.75 ± 0.12 ± 0.56	44.53 ± 0.12 ± 0.59	43.89 ± 0.12 ± 0.63
16.0 - 17.0	46.86 ± 0.16 ± 0.57	46.69 ± 0.13 ± 0.52	46.47 ± 0.13 ± 0.57	45.35 ± 0.14 ± 0.61
17.0 - 18.0	48.73 ± 0.18 ± 0.55	48.55 ± 0.15 ± 0.54	48.29 ± 0.14 ± 0.57	47.32 ± 0.15 ± 0.64
18.0 - 20.0	51.02 ± 0.14 ± 0.53	50.70 ± 0.12 ± 0.53	50.14 ± 0.12 ± 0.57	49.54 ± 0.13 ± 0.61
20.0 - 22.0	53.40 ± 0.17 ± 0.48	53.21 ± 0.15 ± 0.54	52.59 ± 0.15 ± 0.56	52.09 ± 0.16 ± 0.62
22.0 - 24.0	55.85 ± 0.22 ± 0.51	55.30 ± 0.18 ± 0.52	54.71 ± 0.20 ± 0.57	54.22 ± 0.20 ± 0.62
24.0 - 26.0	57.59 ± 0.24 ± 0.50	57.32 ± 0.22 ± 0.43	56.95 ± 0.22 ± 0.53	55.91 ± 0.24 ± 0.63
26.0 - 30.0	59.61 ± 0.22 ± 0.53	59.19 ± 0.20 ± 0.45	58.09 ± 0.20 ± 0.55	57.75 ± 0.22 ± 0.63
30.0 - 35.0	61.79 ± 0.28 ± 0.52	61.32 ± 0.25 ± 0.43	60.78 ± 0.26 ± 0.56	59.51 ± 0.29 ± 0.69
35.0 - 40.0	63.41 ± 0.40 ± 0.52	63.84 ± 0.35 ± 0.47	62.61 ± 0.38 ± 0.57	62.39 ± 0.43 ± 0.69
40.0 - 60.0	65.46 ± 0.38 ± 0.49	65.16 ± 0.35 ± 0.52	63.61 ± 0.41 ± 0.58	63.04 ± 0.46 ± 0.71
60.0 - 110.0	68.54 ± 1.01 ± 0.67	66.91 ± 0.98 ± 0.60	66.05 ± 1.15 ± 0.72	63.04 ± 1.48 ± 1.97

Table B.7: Summary results for the non-prompt fraction of $\psi(2S)$ as a percentage for 8 TeV data. Uncertainties are statistical and systematic respectively.

p_T [GeV]	0.00–0.25	0.25–0.50	0.50–0.75	0.75–1.00
8.0 - 8.5	$30.99 \pm 1.06 \pm 1.67$	$28.68 \pm 0.89 \pm 2.08$	$28.71 \pm 1.00 \pm 2.15$	—-
8.5 - 9.0	$31.02 \pm 0.70 \pm 1.83$	$31.37 \pm 0.83 \pm 2.02$	$31.49 \pm 0.95 \pm 2.02$	—-
9.0 - 9.5	$31.72 \pm 0.67 \pm 1.79$	$31.64 \pm 0.60 \pm 1.88$	$31.57 \pm 0.64 \pm 1.98$	—-
9.5 - 10.0	$33.84 \pm 0.66 \pm 1.81$	$34.47 \pm 0.59 \pm 1.94$	$33.21 \pm 0.58 \pm 1.95$	—-
10.0 - 10.5	$35.23 \pm 0.65 \pm 1.70$	$34.86 \pm 0.57 \pm 1.74$	$33.58 \pm 0.58 \pm 1.92$	$34.78 \pm 0.86 \pm 2.10$
10.5 - 11.0	$36.15 \pm 0.67 \pm 1.65$	$34.94 \pm 0.72 \pm 1.75$	$35.43 \pm 0.58 \pm 1.82$	$36.52 \pm 0.84 \pm 1.97$
11.0 - 11.5	$36.80 \pm 0.70 \pm 1.60$	$36.67 \pm 0.61 \pm 1.78$	$37.67 \pm 0.61 \pm 1.78$	$36.59 \pm 0.85 \pm 2.14$
11.5 - 12.0	$38.67 \pm 0.73 \pm 1.53$	$38.22 \pm 0.61 \pm 1.68$	$36.90 \pm 0.63 \pm 1.88$	$37.54 \pm 0.86 \pm 1.97$
12.0 - 12.5	$39.84 \pm 0.78 \pm 1.61$	$39.70 \pm 0.63 \pm 1.63$	$39.73 \pm 0.66 \pm 1.79$	$39.61 \pm 0.89 \pm 2.01$
12.5 - 13.0	$40.52 \pm 0.80 \pm 1.63$	$40.06 \pm 0.66 \pm 1.70$	$39.57 \pm 0.70 \pm 1.81$	$38.77 \pm 0.93 \pm 2.03$
13.0 - 14.0	$41.58 \pm 0.63 \pm 1.48$	$41.07 \pm 0.51 \pm 1.57$	$40.96 \pm 0.53 \pm 1.70$	$41.76 \pm 0.71 \pm 2.00$
14.0 - 15.0	$44.51 \pm 0.71 \pm 1.49$	$43.45 \pm 0.56 \pm 1.57$	$43.19 \pm 0.60 \pm 1.72$	$42.60 \pm 0.80 \pm 1.96$
15.0 - 16.0	$45.26 \pm 0.81 \pm 1.54$	$44.60 \pm 0.63 \pm 1.48$	$44.76 \pm 0.66 \pm 1.72$	$42.77 \pm 0.88 \pm 1.94$
16.0 - 17.0	$49.59 \pm 0.90 \pm 1.42$	$47.90 \pm 0.70 \pm 1.50$	$47.60 \pm 0.73 \pm 1.68$	$45.48 \pm 0.94 \pm 1.80$
17.0 - 18.0	$50.79 \pm 1.02 \pm 1.38$	$49.38 \pm 0.78 \pm 1.49$	$47.63 \pm 0.84 \pm 1.63$	$48.44 \pm 1.09 \pm 1.85$
18.0 - 20.0	$51.24 \pm 0.84 \pm 1.43$	$52.57 \pm 0.65 \pm 1.43$	$51.52 \pm 0.69 \pm 1.53$	$52.45 \pm 0.87 \pm 1.65$
20.0 - 22.0	$55.34 \pm 1.05 \pm 1.33$	$54.75 \pm 0.81 \pm 1.33$	$53.08 \pm 0.85 \pm 1.36$	$51.83 \pm 1.10 \pm 1.83$
22.0 - 24.0	$56.71 \pm 1.34 \pm 1.28$	$56.00 \pm 0.97 \pm 1.33$	$55.69 \pm 1.01 \pm 1.38$	$53.88 \pm 1.28 \pm 1.82$
24.0 - 26.0	$58.86 \pm 1.57 \pm 1.25$	$58.18 \pm 1.19 \pm 1.43$	$57.50 \pm 1.28 \pm 1.48$	$59.47 \pm 1.56 \pm 1.25$
26.0 - 30.0	$60.65 \pm 1.48 \pm 1.38$	$59.77 \pm 1.12 \pm 1.33$	$58.03 \pm 1.14 \pm 1.38$	$57.51 \pm 1.41 \pm 1.67$
30.0 - 35.0	$65.94 \pm 1.96 \pm 1.52$	$61.82 \pm 1.37 \pm 1.15$	$63.08 \pm 1.45 \pm 1.44$	$63.63 \pm 1.76 \pm 1.08$
35.0 - 40.0	$64.53 \pm 2.64 \pm 1.05$	$68.57 \pm 2.04 \pm 1.30$	$61.28 \pm 2.22 \pm 1.48$	$65.35 \pm 2.59 \pm 1.29$
40.0 - 60.0	$64.96 \pm 2.71 \pm 1.70$	$62.61 \pm 2.05 \pm 1.09$	$67.89 \pm 2.24 \pm 1.26$	$65.69 \pm 2.63 \pm 5.09$
60.0 - 110.0	$75.63 \pm 6.35 \pm 1.88$	$75.25 \pm 5.32 \pm 1.69$	$79.36 \pm 6.21 \pm 1.55$	$70.67 \pm 6.33 \pm 6.33$
p_T [GeV]	1.00–1.25	1.25–1.50	1.50–1.75	1.75–2.00
8.0 - 8.5	—-	—-	—-	—-
8.5 - 9.0	—-	—-	—-	—-
9.0 - 9.5	—-	—-	—-	—-
9.5 - 10.0	—-	—-	—-	—-
10.0 - 10.5	$33.89 \pm 0.99 \pm 2.30$	$31.91 \pm 0.99 \pm 2.02$	$31.75 \pm 0.86 \pm 2.07$	$28.92 \pm 0.92 \pm 2.69$
10.5 - 11.0	$31.90 \pm 0.99 \pm 2.08$	$34.11 \pm 1.02 \pm 2.08$	$33.43 \pm 0.84 \pm 1.87$	$33.11 \pm 0.92 \pm 2.37$
11.0 - 11.5	$34.93 \pm 1.00 \pm 2.29$	$34.88 \pm 0.97 \pm 1.98$	$34.62 \pm 0.84 \pm 1.81$	$33.66 \pm 0.98 \pm 2.04$
11.5 - 12.0	$35.27 \pm 0.99 \pm 2.29$	$36.25 \pm 1.00 \pm 2.20$	$34.54 \pm 0.85 \pm 1.67$	$32.03 \pm 1.00 \pm 1.63$
12.0 - 12.5	$37.09 \pm 1.15 \pm 1.87$	$38.23 \pm 0.96 \pm 1.90$	$35.51 \pm 0.89 \pm 1.80$	$32.94 \pm 1.04 \pm 1.89$
12.5 - 13.0	$39.25 \pm 1.05 \pm 2.18$	$38.88 \pm 0.99 \pm 1.85$	$39.44 \pm 0.90 \pm 1.58$	$33.99 \pm 1.06 \pm 1.93$
13.0 - 14.0	$40.48 \pm 0.77 \pm 1.82$	$39.66 \pm 0.74 \pm 1.96$	$38.63 \pm 0.69 \pm 1.86$	$35.55 \pm 0.87 \pm 1.81$
14.0 - 15.0	$43.24 \pm 0.83 \pm 1.93$	$41.80 \pm 0.81 \pm 1.77$	$40.95 \pm 0.79 \pm 1.85$	$38.54 \pm 0.93 \pm 1.52$
15.0 - 16.0	$44.73 \pm 0.91 \pm 1.90$	$42.73 \pm 0.82 \pm 1.82$	$42.92 \pm 0.87 \pm 1.75$	$42.03 \pm 1.01 \pm 1.69$
16.0 - 17.0	$45.96 \pm 1.16 \pm 1.87$	$45.74 \pm 0.89 \pm 1.61$	$44.60 \pm 0.97 \pm 1.53$	$40.98 \pm 1.15 \pm 1.65$
17.0 - 18.0	$46.60 \pm 1.28 \pm 1.58$	$47.31 \pm 1.04 \pm 1.64$	$46.30 \pm 1.10 \pm 1.81$	$43.25 \pm 1.43 \pm 1.31$
18.0 - 20.0	$50.27 \pm 0.89 \pm 1.64$	$48.60 \pm 0.84 \pm 1.77$	$49.37 \pm 0.90 \pm 1.55$	$48.20 \pm 1.11 \pm 1.45$
20.0 - 22.0	$52.67 \pm 1.09 \pm 1.87$	$49.68 \pm 1.03 \pm 1.90$	$50.46 \pm 1.11 \pm 1.35$	$47.86 \pm 1.37 \pm 2.00$
22.0 - 24.0	$54.19 \pm 1.59 \pm 1.78$	$53.35 \pm 1.30 \pm 1.87$	$52.13 \pm 1.52 \pm 1.54$	$52.99 \pm 1.69 \pm 1.45$
24.0 - 26.0	$57.69 \pm 1.63 \pm 1.41$	$56.35 \pm 1.43 \pm 1.43$	$58.00 \pm 1.79 \pm 1.02$	$54.08 \pm 2.12 \pm 1.40$
26.0 - 30.0	$59.51 \pm 1.46 \pm 1.33$	$59.77 \pm 1.34 \pm 6.46$	$56.55 \pm 1.51 \pm 1.49$	$54.20 \pm 2.05 \pm 1.35$
30.0 - 35.0	$61.42 \pm 1.91 \pm 1.39$	$60.28 \pm 1.69 \pm 6.14$	$57.45 \pm 2.10 \pm 2.73$	$58.53 \pm 2.64 \pm 1.16$
35.0 - 40.0	$59.81 \pm 2.79 \pm 2.44$	$63.00 \pm 2.42 \pm 1.81$	$61.36 \pm 2.97 \pm 1.51$	$49.96 \pm 4.08 \pm 2.40$
40.0 - 60.0	$67.89 \pm 2.97 \pm 1.78$	$61.29 \pm 2.78 \pm 6.47$	$67.23 \pm 4.08 \pm 1.40$	$62.32 \pm 4.62 \pm 2.57$
60.0 - 110.0	$61.37 \pm 6.92 \pm 3.75$	$71.71 \pm 6.79 \pm 4.17$	$49.59 \pm 8.35 \pm 4.59$	$50.41 \pm 7.79 \pm 25.47$

Table B.8: Summary results for the prompt ratio as a percentage for 8 TeV data. Uncertainties are statistical and systematic respectively.

p_T [GeV]	0.00–0.25	0.25–0.50	0.50–0.75	0.75–1.00
8.0 - 8.5	$3.43 \pm 0.08 \pm 0.16$	$3.44 \pm 0.06 \pm 0.21$	$3.35 \pm 0.07 \pm 0.19$	—-
8.5 - 9.0	$3.66 \pm 0.06 \pm 0.20$	$3.41 \pm 0.06 \pm 0.19$	$3.30 \pm 0.07 \pm 0.15$	—-
9.0 - 9.5	$3.59 \pm 0.05 \pm 0.18$	$3.54 \pm 0.05 \pm 0.18$	$3.49 \pm 0.05 \pm 0.18$	—-
9.5 - 10.0	$3.62 \pm 0.05 \pm 0.15$	$3.52 \pm 0.05 \pm 0.18$	$3.64 \pm 0.05 \pm 0.16$	—-
10.0 - 10.5	$3.78 \pm 0.06 \pm 0.17$	$3.62 \pm 0.05 \pm 0.18$	$3.73 \pm 0.05 \pm 0.17$	$3.67 \pm 0.07 \pm 0.18$
10.5 - 11.0	$3.87 \pm 0.06 \pm 0.16$	$3.87 \pm 0.06 \pm 0.17$	$3.86 \pm 0.05 \pm 0.15$	$3.75 \pm 0.07 \pm 0.14$
11.0 - 11.5	$3.96 \pm 0.06 \pm 0.15$	$3.78 \pm 0.05 \pm 0.18$	$3.74 \pm 0.05 \pm 0.13$	$3.78 \pm 0.07 \pm 0.16$
11.5 - 12.0	$3.99 \pm 0.07 \pm 0.15$	$3.87 \pm 0.06 \pm 0.15$	$4.05 \pm 0.06 \pm 0.16$	$3.87 \pm 0.08 \pm 0.15$
12.0 - 12.5	$4.04 \pm 0.07 \pm 0.14$	$3.95 \pm 0.06 \pm 0.14$	$3.94 \pm 0.06 \pm 0.15$	$3.87 \pm 0.08 \pm 0.13$
12.5 - 13.0	$4.19 \pm 0.08 \pm 0.16$	$4.07 \pm 0.06 \pm 0.16$	$4.05 \pm 0.07 \pm 0.12$	$4.00 \pm 0.09 \pm 0.12$
13.0 - 14.0	$4.21 \pm 0.06 \pm 0.15$	$4.05 \pm 0.05 \pm 0.15$	$4.13 \pm 0.05 \pm 0.13$	$4.00 \pm 0.07 \pm 0.14$
14.0 - 15.0	$4.32 \pm 0.07 \pm 0.13$	$4.23 \pm 0.06 \pm 0.16$	$4.14 \pm 0.06 \pm 0.13$	$4.12 \pm 0.12 \pm 0.13$
15.0 - 16.0	$4.33 \pm 0.09 \pm 0.18$	$4.34 \pm 0.07 \pm 0.14$	$4.36 \pm 0.07 \pm 0.16$	$4.27 \pm 0.09 \pm 0.15$
16.0 - 17.0	$4.36 \pm 0.10 \pm 0.15$	$4.30 \pm 0.08 \pm 0.14$	$4.28 \pm 0.08 \pm 0.14$	$4.31 \pm 0.10 \pm 0.10$
17.0 - 18.0	$4.40 \pm 0.12 \pm 0.16$	$4.33 \pm 0.09 \pm 0.17$	$4.34 \pm 0.09 \pm 0.15$	$4.00 \pm 0.11 \pm 0.08$
18.0 - 20.0	$4.63 \pm 0.10 \pm 0.17$	$4.30 \pm 0.08 \pm 0.12$	$4.25 \pm 0.08 \pm 0.13$	$4.11 \pm 0.10 \pm 0.11$
20.0 - 22.0	$4.60 \pm 0.14 \pm 0.19$	$4.37 \pm 0.10 \pm 0.16$	$4.48 \pm 0.11 \pm 0.15$	$4.37 \pm 0.13 \pm 0.09$
22.0 - 24.0	$4.43 \pm 0.17 \pm 0.18$	$4.52 \pm 0.13 \pm 0.13$	$4.56 \pm 0.13 \pm 0.11$	$4.54 \pm 0.16 \pm 0.16$
24.0 - 26.0	$4.64 \pm 0.22 \pm 0.14$	$4.57 \pm 0.16 \pm 0.15$	$4.35 \pm 0.17 \pm 0.17$	$4.02 \pm 0.20 \pm 0.15$
26.0 - 30.0	$4.58 \pm 0.21 \pm 0.17$	$4.49 \pm 0.16 \pm 0.11$	$4.81 \pm 0.17 \pm 0.14$	$4.62 \pm 0.20 \pm 0.07$
30.0 - 35.0	$4.11 \pm 0.29 \pm 0.25$	$4.90 \pm 0.22 \pm 0.16$	$4.63 \pm 0.23 \pm 0.14$	$4.37 \pm 0.27 \pm 0.41$
35.0 - 40.0	$5.06 \pm 0.46 \pm 0.23$	$4.24 \pm 0.33 \pm 0.25$	$4.88 \pm 0.36 \pm 0.14$	$4.27 \pm 0.41 \pm 0.19$
40.0 - 60.0	$5.36 \pm 0.52 \pm 0.20$	$5.65 \pm 0.40 \pm 0.39$	$4.67 \pm 0.41 \pm 0.25$	$4.45 \pm 0.44 \pm 0.52$
60.0 - 110.0	$4.64 \pm 1.52 \pm 0.36$	$4.40 \pm 1.19 \pm 0.33$	$3.29 \pm 1.21 \pm 0.32$	$4.50 \pm 1.28 \pm 1.66$
p_T [GeV]	1.00–1.25	1.25–1.50	1.50–1.75	1.75–2.00
8.0 - 8.5	—-	—-	—-	—-
8.5 - 9.0	—-	—-	—-	—-
9.0 - 9.5	—-	—-	—-	—-
9.5 - 10.0	—-	—-	—-	—-
10.0 - 10.5	$3.77 \pm 0.08 \pm 0.16$	$3.70 \pm 0.08 \pm 0.15$	$3.51 \pm 0.07 \pm 0.18$	$3.19 \pm 0.07 \pm 0.31$
10.5 - 11.0	$3.98 \pm 0.08 \pm 0.15$	$3.70 \pm 0.09 \pm 0.14$	$3.53 \pm 0.07 \pm 0.17$	$3.13 \pm 0.07 \pm 0.40$
11.0 - 11.5	$3.85 \pm 0.09 \pm 0.19$	$3.86 \pm 0.09 \pm 0.14$	$3.54 \pm 0.07 \pm 0.15$	$3.13 \pm 0.08 \pm 0.29$
11.5 - 12.0	$3.89 \pm 0.09 \pm 0.17$	$3.92 \pm 0.09 \pm 0.14$	$3.73 \pm 0.08 \pm 0.17$	$3.34 \pm 0.08 \pm 0.43$
12.0 - 12.5	$3.86 \pm 0.11 \pm 0.15$	$3.96 \pm 0.09 \pm 0.15$	$3.78 \pm 0.08 \pm 0.22$	$3.55 \pm 0.09 \pm 0.57$
12.5 - 13.0	$3.83 \pm 0.09 \pm 0.12$	$3.94 \pm 0.09 \pm 0.15$	$3.62 \pm 0.09 \pm 0.20$	$3.60 \pm 0.09 \pm 0.41$
13.0 - 14.0	$4.03 \pm 0.07 \pm 0.13$	$4.02 \pm 0.07 \pm 0.13$	$3.86 \pm 0.07 \pm 0.24$	$3.44 \pm 0.07 \pm 0.48$
14.0 - 15.0	$4.02 \pm 0.08 \pm 0.14$	$3.94 \pm 0.08 \pm 0.16$	$3.86 \pm 0.08 \pm 0.26$	$3.59 \pm 0.08 \pm 0.57$
15.0 - 16.0	$4.15 \pm 0.09 \pm 0.13$	$4.25 \pm 0.08 \pm 0.16$	$3.80 \pm 0.09 \pm 0.25$	$3.60 \pm 0.10 \pm 0.59$
16.0 - 17.0	$4.07 \pm 0.12 \pm 0.13$	$4.26 \pm 0.10 \pm 0.17$	$3.89 \pm 0.10 \pm 0.39$	$3.90 \pm 0.12 \pm 0.66$
17.0 - 18.0	$4.40 \pm 0.14 \pm 0.12$	$4.26 \pm 0.12 \pm 0.16$	$3.97 \pm 0.11 \pm 0.39$	$3.44 \pm 0.13 \pm 0.76$
18.0 - 20.0	$4.39 \pm 0.11 \pm 0.17$	$4.35 \pm 0.10 \pm 0.17$	$3.96 \pm 0.10 \pm 0.37$	$3.61 \pm 0.11 \pm 0.79$
20.0 - 22.0	$4.46 \pm 0.14 \pm 0.12$	$4.46 \pm 0.12 \pm 0.22$	$4.05 \pm 0.13 \pm 0.63$	$4.17 \pm 0.17 \pm 0.75$
22.0 - 24.0	$4.31 \pm 0.20 \pm 0.15$	$4.27 \pm 0.16 \pm 0.34$	$4.18 \pm 0.20 \pm 0.47$	$3.84 \pm 0.21 \pm 0.82$
24.0 - 26.0	$4.26 \pm 0.22 \pm 0.29$	$4.44 \pm 0.19 \pm 0.59$	$3.62 \pm 0.20 \pm 0.76$	$3.65 \pm 0.24 \pm 0.89$
26.0 - 30.0	$4.38 \pm 0.20 \pm 0.41$	$4.19 \pm 0.18 \pm 0.60$	$4.20 \pm 0.20 \pm 0.72$	$4.11 \pm 0.28 \pm 0.95$
30.0 - 35.0	$4.56 \pm 0.29 \pm 0.51$	$4.60 \pm 0.26 \pm 0.70$	$4.46 \pm 0.30 \pm 0.68$	$3.81 \pm 0.37 \pm 1.13$
35.0 - 40.0	$4.93 \pm 0.45 \pm 0.43$	$4.70 \pm 0.40 \pm 0.73$	$4.42 \pm 0.48 \pm 0.56$	$5.08 \pm 0.61 \pm 1.15$
40.0 - 60.0	$4.17 \pm 0.49 \pm 0.79$	$4.75 \pm 0.45 \pm 0.86$	$3.50 \pm 0.64 \pm 0.93$	$4.41 \pm 1.11 \pm 1.92$
60.0 - 110.0	$5.56 \pm 1.40 \pm 1.10$	$3.80 \pm 1.20 \pm 0.80$	$6.44 \pm 1.62 \pm 0.60$	$10.38 \pm 2.74 \pm 8.90$

Table B.9: Summary results for the non-prompt ratio as a percentage for 8 TeV data. Uncertainties are statistical and systematic respectively.

p_T [GeV]	0.00–0.25	0.25–0.50	0.50–0.75	0.75–1.00
8.0 - 8.5	$4.02 \pm 0.16 \pm 0.32$	$3.65 \pm 0.14 \pm 0.31$	$3.60 \pm 0.15 \pm 0.31$	—-
8.5 - 9.0	$4.02 \pm 0.11 \pm 0.30$	$3.82 \pm 0.12 \pm 0.30$	$3.78 \pm 0.14 \pm 0.32$	—-
9.0 - 9.5	$3.85 \pm 0.10 \pm 0.28$	$3.75 \pm 0.09 \pm 0.28$	$3.74 \pm 0.09 \pm 0.29$	—-
9.5 - 10.0	$3.99 \pm 0.09 \pm 0.24$	$3.99 \pm 0.09 \pm 0.27$	$3.97 \pm 0.09 \pm 0.29$	—-
10.0 - 10.5	$4.15 \pm 0.09 \pm 0.26$	$3.94 \pm 0.08 \pm 0.24$	$3.87 \pm 0.08 \pm 0.25$	$4.02 \pm 0.13 \pm 0.27$
10.5 - 11.0	$4.15 \pm 0.10 \pm 0.23$	$3.97 \pm 0.10 \pm 0.22$	$4.09 \pm 0.08 \pm 0.23$	$4.15 \pm 0.12 \pm 0.25$
11.0 - 11.5	$4.12 \pm 0.10 \pm 0.22$	$3.92 \pm 0.08 \pm 0.21$	$4.11 \pm 0.09 \pm 0.21$	$3.99 \pm 0.12 \pm 0.23$
11.5 - 12.0	$4.25 \pm 0.10 \pm 0.20$	$4.07 \pm 0.08 \pm 0.20$	$4.06 \pm 0.09 \pm 0.19$	$4.00 \pm 0.12 \pm 0.18$
12.0 - 12.5	$4.26 \pm 0.11 \pm 0.20$	$4.15 \pm 0.09 \pm 0.17$	$4.19 \pm 0.09 \pm 0.18$	$4.12 \pm 0.12 \pm 0.23$
12.5 - 13.0	$4.34 \pm 0.11 \pm 0.17$	$4.13 \pm 0.09 \pm 0.16$	$4.08 \pm 0.09 \pm 0.19$	$3.93 \pm 0.12 \pm 0.24$
13.0 - 14.0	$4.21 \pm 0.08 \pm 0.16$	$3.96 \pm 0.06 \pm 0.15$	$4.09 \pm 0.07 \pm 0.15$	$4.11 \pm 0.09 \pm 0.19$
14.0 - 15.0	$4.42 \pm 0.09 \pm 0.16$	$4.21 \pm 0.07 \pm 0.14$	$4.07 \pm 0.08 \pm 0.18$	$3.97 \pm 0.11 \pm 0.20$
15.0 - 16.0	$4.19 \pm 0.10 \pm 0.14$	$4.11 \pm 0.08 \pm 0.12$	$4.18 \pm 0.08 \pm 0.19$	$3.83 \pm 0.11 \pm 0.17$
16.0 - 17.0	$4.67 \pm 0.12 \pm 0.13$	$4.34 \pm 0.09 \pm 0.13$	$4.30 \pm 0.09 \pm 0.15$	$4.01 \pm 0.12 \pm 0.23$
17.0 - 18.0	$4.54 \pm 0.13 \pm 0.14$	$4.32 \pm 0.10 \pm 0.11$	$4.05 \pm 0.10 \pm 0.20$	$3.88 \pm 0.13 \pm 0.22$
18.0 - 20.0	$4.48 \pm 0.11 \pm 0.10$	$4.43 \pm 0.08 \pm 0.14$	$4.26 \pm 0.08 \pm 0.19$	$4.24 \pm 0.10 \pm 0.22$
20.0 - 22.0	$4.71 \pm 0.13 \pm 0.18$	$4.44 \pm 0.10 \pm 0.17$	$4.28 \pm 0.10 \pm 0.24$	$3.99 \pm 0.13 \pm 0.28$
22.0 - 24.0	$4.38 \pm 0.16 \pm 0.10$	$4.39 \pm 0.12 \pm 0.15$	$4.42 \pm 0.12 \pm 0.20$	$4.10 \pm 0.15 \pm 0.45$
24.0 - 26.0	$4.63 \pm 0.19 \pm 0.24$	$4.47 \pm 0.14 \pm 0.19$	$4.29 \pm 0.15 \pm 0.25$	$4.28 \pm 0.18 \pm 0.38$
26.0 - 30.0	$4.59 \pm 0.17 \pm 0.20$	$4.35 \pm 0.13 \pm 0.15$	$4.37 \pm 0.13 \pm 0.21$	$4.16 \pm 0.16 \pm 0.31$
30.0 - 35.0	$4.79 \pm 0.23 \pm 0.15$	$4.70 \pm 0.17 \pm 0.30$	$4.76 \pm 0.18 \pm 0.20$	$4.54 \pm 0.21 \pm 0.64$
35.0 - 40.0	$5.16 \pm 0.34 \pm 0.33$	$4.95 \pm 0.25 \pm 0.10$	$4.34 \pm 0.25 \pm 0.18$	$4.38 \pm 0.29 \pm 0.44$
40.0 - 60.0	$4.77 \pm 0.32 \pm 0.42$	$4.71 \pm 0.25 \pm 0.56$	$4.99 \pm 0.27 \pm 0.53$	$4.33 \pm 0.28 \pm 0.83$
60.0 - 110.0	$5.98 \pm 0.81 \pm 0.22$	$5.65 \pm 0.65 \pm 0.21$	$5.44 \pm 0.66 \pm 0.21$	$4.96 \pm 0.65 \pm 0.22$
p_T [GeV]	1.00–1.25	1.25–1.50	1.50–1.75	1.75–2.00
8.0 - 8.5	—-	—-	—-	—-
8.5 - 9.0	—-	—-	—-	—-
9.0 - 9.5	—-	—-	—-	—-
9.5 - 10.0	—-	—-	—-	—-
10.0 - 10.5	$4.01 \pm 0.15 \pm 0.27$	$3.64 \pm 0.14 \pm 0.34$	$3.45 \pm 0.12 \pm 0.43$	$2.79 \pm 0.11 \pm 0.51$
10.5 - 11.0	$3.65 \pm 0.14 \pm 0.21$	$3.82 \pm 0.15 \pm 0.31$	$3.52 \pm 0.11 \pm 0.40$	$3.19 \pm 0.11 \pm 0.61$
11.0 - 11.5	$3.79 \pm 0.14 \pm 0.20$	$3.83 \pm 0.14 \pm 0.33$	$3.52 \pm 0.11 \pm 0.37$	$3.02 \pm 0.11 \pm 0.49$
11.5 - 12.0	$3.70 \pm 0.13 \pm 0.21$	$3.92 \pm 0.14 \pm 0.29$	$3.47 \pm 0.11 \pm 0.42$	$2.85 \pm 0.11 \pm 0.59$
12.0 - 12.5	$3.77 \pm 0.15 \pm 0.24$	$4.05 \pm 0.13 \pm 0.31$	$3.51 \pm 0.12 \pm 0.48$	$2.99 \pm 0.12 \pm 0.70$
12.5 - 13.0	$3.86 \pm 0.14 \pm 0.25$	$3.94 \pm 0.14 \pm 0.29$	$3.73 \pm 0.11 \pm 0.42$	$3.03 \pm 0.12 \pm 0.62$
13.0 - 14.0	$3.96 \pm 0.10 \pm 0.29$	$3.88 \pm 0.10 \pm 0.39$	$3.59 \pm 0.09 \pm 0.50$	$2.89 \pm 0.10 \pm 0.65$
14.0 - 15.0	$4.04 \pm 0.11 \pm 0.27$	$3.81 \pm 0.10 \pm 0.40$	$3.63 \pm 0.10 \pm 0.54$	$3.13 \pm 0.11 \pm 0.72$
15.0 - 16.0	$4.05 \pm 0.12 \pm 0.30$	$3.92 \pm 0.10 \pm 0.45$	$3.56 \pm 0.10 \pm 0.49$	$3.34 \pm 0.11 \pm 0.71$
16.0 - 17.0	$3.93 \pm 0.14 \pm 0.21$	$4.10 \pm 0.11 \pm 0.43$	$3.61 \pm 0.11 \pm 0.60$	$3.26 \pm 0.13 \pm 0.79$
17.0 - 18.0	$4.04 \pm 0.16 \pm 0.33$	$4.06 \pm 0.13 \pm 0.43$	$3.66 \pm 0.13 \pm 0.64$	$2.92 \pm 0.14 \pm 0.82$
18.0 - 20.0	$4.26 \pm 0.11 \pm 0.40$	$4.00 \pm 0.10 \pm 0.44$	$3.84 \pm 0.11 \pm 0.61$	$3.42 \pm 0.12 \pm 0.96$
20.0 - 22.0	$4.33 \pm 0.14 \pm 0.31$	$3.87 \pm 0.12 \pm 0.49$	$3.72 \pm 0.12 \pm 0.79$	$3.52 \pm 0.16 \pm 0.94$
22.0 - 24.0	$4.03 \pm 0.19 \pm 0.39$	$3.94 \pm 0.15 \pm 0.62$	$3.77 \pm 0.18 \pm 0.66$	$3.66 \pm 0.19 \pm 0.99$
24.0 - 26.0	$4.28 \pm 0.19 \pm 0.55$	$4.27 \pm 0.18 \pm 0.83$	$3.78 \pm 0.19 \pm 0.95$	$3.38 \pm 0.22 \pm 1.03$
26.0 - 30.0	$4.36 \pm 0.18 \pm 0.66$	$4.29 \pm 0.15 \pm 0.95$	$3.95 \pm 0.17 \pm 0.92$	$3.56 \pm 0.24 \pm 1.03$
30.0 - 35.0	$4.49 \pm 0.23 \pm 0.77$	$4.41 \pm 0.20 \pm 0.92$	$3.89 \pm 0.25 \pm 1.09$	$3.66 \pm 0.31 \pm 1.15$
35.0 - 40.0	$4.24 \pm 0.34 \pm 0.84$	$4.53 \pm 0.29 \pm 1.09$	$4.19 \pm 0.36 \pm 0.80$	$3.06 \pm 0.42 \pm 1.02$
40.0 - 60.0	$4.65 \pm 0.35 \pm 1.33$	$4.02 \pm 0.31 \pm 1.09$	$4.10 \pm 0.45 \pm 1.33$	$4.28 \pm 0.85 \pm 2.04$
60.0 - 110.0	$4.05 \pm 0.66 \pm 0.26$	$4.76 \pm 0.63 \pm 0.17$	$3.26 \pm 0.76 \pm 0.54$	$6.19 \pm 1.22 \pm 3.63$

Appendix C

Contributions

In this section the contributions of the author on various fields during to his Ph.D. period on the faculty of Physics at the National Technical University of Athens are going to be mentioned.

- Participation on all test beam periods working on both technical setup and data analysis for MAMMA collaboration.
- Developed the first version of offline event builder and viewer for the data acquired with the micromegas detectors using various front-end electronics for the MAMMA collaboration, including data grouping and clustering.
- Contribute to the building of the first version of the program for the initialization (SDC) of the VMM electronics.
- Took and analyzed the first measurements of the crosstalk for the micromegas detector.
- Participates in RD51 test beam periods helping with the common tools and infrastructure.
- Developed an automated complete system (slow control system) which would control and monitor the high voltage channels of the detectors for the needs of the test beams.
- In parallel, tools have been developed in order to provide offline analysis with the data accumulated through the test beam periods.
- An updated version of the slow control system is being prepared including additional useful (i.e. environmental) information gathered by external connected microcontrolers like Arduino.
- A fast and robust tracking software package was developed for the RD51 telescopes in order to provide a user-friendly program with a smooth graphical user interface.

- Contribution to the development of the official ATLAS simulation by implementing the standalone code for the full simulation of the micromegas detectors into the ATLAS reconstruction software (ATHENA).
- Development of new and supporting and maintaining of the existing tools and panels for the ATLAS DCS of the Muon Spectrometer.
- Performed the J/ψ and $\psi(2S)$ measurement using 2012 ATLAS data and carried out all the comparisons with the 2011 data part of the analysis of the joined paper.
- The study of the decay $\chi_b \to J/\psi J/\psi$.
- Contributed to the $B_s \to \mu\mu$ analysis performing the MC tuning, calculating the acceptance term and by performing various cross checks and closure tests.
- Providing ntuples for both data and MC as well as performed closure tests and calculating the J/ψ cross-section participate on other analyses than those described in this dissertation like "A Study of prompt pair production of J/ψ mesons at ATLAS" of the B-Physics work group of ATLAS.